Non-instantaneous polarization in perovskite-like ferroelectrics revealed by correlated (ultra)fast luminescence and absorption spectroscopy
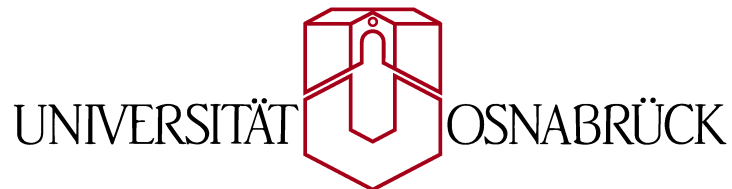
On the formation of self-trapped excitons in lithium niobate
and their relation to small electron and hole polaron pairs

**Kumulative Dissertation
zur Erlangung des Grades
eines Doktors der Naturwissenschaften**

von

Andreas Krampf

genehmigt durch den Fachbereich Physik der

UNIVERSITÄT OSNABRÜCK

Osnabrück, im Juli 2020

Contents

1 Introduction

Non-instantaneous polarization in the form of polaronic effects [1] is known to determine the optical and transport properties of a wide range of technically relevant oxide dielectrics. For example, transient absorption and luminescence of SiO_2 [2–4], TiO_2 [5–7], and other wide gap oxide materials [8, 9] are associated with the formation of small polarons and self-trapped excitons (STEs). Of particular interest are the ABO_3 perovskite-like dielectrics such as alkali and alkaline earth metal titanates [10–15], tantalates [16–18], and niobates [19–23]. They are important materials in the fields of optical frequency conversion [24], holographic data storage [25, 26], THz pulse generation [27] or promise advancements in photovoltaics [28], oxide electronics [29], and electroluminescent devices [30].

Among these materials, the ferroelectric lithium niobate ($LiNbO_3$, LN) occupies a prominent position. Due to its pronounced electro-optical, piezoelectric, photoelastic, and nonlinear optical properties [31, 32], LN is used in a variety of (technical) applications such as electro-, acousto-, and nonlinear-optical devices [33], optical waveguides [34] or as versatile harmonic nanoparticle labels for microscopic imaging of biological samples [35]. Some of the observed light-induced phenomena are again associated with small polaron formation and transport. Prominent and intensively studied examples are transient absorption features [36–51] and the bulk photovoltaic effect [52], which leads to photorefraction used for holographic data storage [53–55].

Only recently the observed blue-green (photo)luminescence of LN has been described in the framework of small polarons as well, i.e., by geminate annihilation of oppositely-charged small polaron pairs [56, 57]. This work, however, reveals strong indications that this microscopic picture is inaccurate. The first correlated temperature-dependent photoluminescence and absorption spectroscopy measurements on LN are presented, which reveal that photoluminescence and small polaron absorption decay on time scales differing by orders of magnitude. A mathematical formulation describing both optical responses with a common physical origin results in contradictory temperature behaviors of the extracted parameters. To resolve these disagreements an alternative microscopic picture is revived, which has been proposed over thirty years ago by the group of George Blasse: radiative decay of self-trapped excitons located at NbO_6 octahedra is assumed to be responsible for the emission of light [58–62].

Absorption and emission features of self-trapped excitons in LN are uncovered and characterized by means of transient photoluminescence and absorption spectroscopy showing that an influence of self-trapped exciton formation on the light-matter interaction can per se no longer be neglected. For example, long-lived excitonic absorption

centers in the blue spectral range are revealed in Fe-doped specimens. Since they last for seconds up to hours, they are expected to possess a major influence on light-induced damage of the material. This should be the case especially for illumination with continuous wave lasers or short laser pulses at high repetition rates. It is further shown that the occurrence of these transients can be tailored by chemical reduction of the crystals and by changing the pump light intensity and photon energy. Long-lived excitonic states are proposed to be responsible for the observed long-lived transient absorption and luminescence in Mg-doped samples as well.

Based on the new data and reviewing (contradictory) published observations of luminescence and absorption features of LN crystals with different stoichiometry and doping, a comprehensive microscopic picture is developed describing the decay of these transient phenomena in LN. In addition to the commonly used model including only strong-coupling electron and hole polarons, it considers self-trapped exciton hopping and pinning on defect sites. The latter mechanism is proposed to result in the long-lived absorption features of Fe- and Mg-doped samples. Detailed atomistic models of self-trapped exciton hopping and pinning are given. A mathematical description of (pinned) self-trapped exciton decay based on rate equations is able to resolve the aforementioned contradictory temporal behavior of extracted fitting parameters.

The parallel existence of self-trapped excitons and small polarons in LN raises the question whether both species are independent or coupled quasi-particles. It is conceivable that pairs of oppositely-charged small polarons merge into self-trapped excitons or that STEs break into small polaron pairs. To address this question the formation and decay of both species has to be examined. Formation times of (free) small polarons in lithium niobate are in the range of 1–300 fs [40, 51]. It may therefore be expected that self-trapped excitons form on the time scale of a few hundred femtoseconds as well. Transient luminescence spectrometers offering such high temporal resolutions are commonly based on the fluorescence upconversion technique [63]. There, the fluorescence is mixed with a train of short gate laser pulses in a nonlinear optical crystal. The gate pulses convert a temporal (and spectral) 'slice' of the fluorescence light to higher energies. The intensity of this generated sum-frequency is then proportional to the intensity of the fluorescence 'slice' and the temporal resolution is on the order of the gate pulse duration. Since experiments of this kind with sub-200 fs temporal resolution are not available as commercial 'turn-key' solutions, a corresponding experiment is designed. It largely follows the femtosecond broadband upconversion spectrometer (FLUPS) introduced by Ernsting *et al.* [64–67], but is modified to meet the special requirements of measuring weakly luminescent solids: in order to prevent a deterioration of the temporal resolution due to the large group velocity dispersion in LN, the luminescence is collected in reflection geometry using a custom-built Cassegrain reflector. A comparison of photoluminescence and absorption build-up and decay strongly suggest that self-trapped excitons and small polarons in LN are not correlated. Non of these quasi-particles species seem to be a precursor of the other.

2 Fundamentals

This chapter briefly reviews the theoretical concepts used in this work. It is limited to the basics that are not covered by the attached publications. The first section deals with the description of nonlinear light-matter interaction and in particular with sum-frequency mixing based on a nonlinear polarization of second order. A second section describing the propagation of light pulses in media is followed by an introduction of small polarons and self-trapped excitons. The chapter ends with a short survey of the studied material lithium niobate.

2.1 Nonlinear light-matter interaction

The field of optics is concerned with the interaction of light with matter manifesting in multifarious linear and nonlinear optical responses. In linear optics material properties are independent of the light intensity and familiar effects such as (linear) refraction, diffraction, and absorption occur. At sufficiently high electric field strengths, however, a mutual interaction between the light waves and the medium is observed. In this nonlinear optical regime, material properties like, e.g., the index of refraction or the absorption coefficient, can be changed and even controlled by the incoming light field.

The following chapter follows the descriptions in *Nonlinear Optics* by Robert Boyd [68] and *The Elements of Nonlinear Optics* by Paul Butcher and David Cotter [69]. Subsection 2.1.3 is based on Ref. [68] and *Applied Nonlinear Optics* by Frits Zernike and John Midwinter [70].

2.1.1 Nonlinear polarization of second order

A dielectric material can be regarded as a conglomeration of charged particles, i.e., electrons and ions, elastically bound together. If an external electric field is applied, both charged particles are displaced from their equilibrium positions inducing a small electric dipole-moment. Combined, these microscopic dipoles form a macroscopic polarization. In case of light waves, the electric field oscillates at a given frequency

$$E(t) = \frac{1}{2}\mathcal{E}\left(\exp(-i\omega t) + \exp(i\omega t)\right). \tag{2.1}$$

For optical frequencies (10^{13}-10^{17} Hz), the heavy ions cannot follow the varying electric field and only the electrons' motions have to be considered. They can be thought of

as classical, damped, anharmonic oscillators driven by the external electric field. The equation of motion for the electron displacement x is then

$$m\left(\frac{d^2x}{dt^2} + 2\Gamma\frac{dx}{dt} + \omega_0^2 x + \left(\xi^{(2)}x^2 + \xi^{(3)}x^3 + ...\right)\right) = -eE(t), \tag{2.2}$$

where ω_0 is the resonance frequency, Γ a damping constant, $-m\omega_0^2 x - m(\xi^{(2)}x^2 + \xi^{(3)}x^3 + ...)$ the restoring and $-eE(t)$ the driving force. The prefactors $\xi^{(n)}$ characterize the strength of the anharmonic contributions.

Neglecting these anharmonic terms and considering an oscillating electric field given by Eq. (2.1), the solution of Eq. (2.2), i.e., the time-dependent displacement, is

$$x(t) = \frac{-e\mathcal{E}}{2m}\frac{\exp(-i\omega t)}{\omega_0^2 - \omega^2 - 2i\Gamma\omega} + c.c., \tag{2.3}$$

with $c.c.$ being the complex conjugate. The induced macroscopic polarization P is equal to the number density of dipoles per unit volume N multiplied with their dipole moment

$$P(t) = -Nex(t). \tag{2.4}$$

From Eq. (2.3) follows that in case of a harmonic oscillation the polarization depends linearly on the electric field

$$P^{(1)} = \frac{1}{2}\epsilon_0\chi(\omega)\mathcal{E}\exp(-i\omega t) + c.c., \tag{2.5}$$

with the permittivity of free space ϵ_0 and the linear susceptibility

$$\chi(\omega) = \frac{Ne^2}{\epsilon_0 m}\frac{1}{\omega_0^2 - \omega^2 - 2i\Gamma\omega} = \frac{Ne^2}{\epsilon_0 m}\left(\frac{\omega_0^2 - \omega^2}{(\omega_0^2 - \omega^2)^2 + 4\Gamma^2\omega^2} + i\frac{2\Gamma\omega}{(\omega_0^2 - \omega^2)^2 + 4\Gamma^2\omega^2}\right). \tag{2.6}$$

Obviously, in the linear case, the induced polarization oscillates with the same frequency ω as the driving electric field. The oscillating dipoles in turn, thus, emit waves with this frequency. If the oscillating electric field is part of an electromagnetic wave, this changes the way the wave propagates through the medium. In fact, the real part of Eq. (2.6) gives qualitatively the refractive index of the material. The imaginary part in contrast describes qualitatively the absorption of the material. Both are depicted in Fig. 2.1. The region, in which the real part of the susceptibility and therefore the index of refraction rises with increasing frequency, is called region of normal dispersion. Around the resonance frequency ω_0, where the imaginary part (absorption) has its maximum, the refractive index decreases with increasing frequency. This region (blue area) having a width given by the damping constant Γ is called region of anomalous dispersion.

The restoring force appearing in Eq. (2.2) corresponds to a potential energy function

$$U(x) = -\int F_{\text{restoring}}\,dx = \frac{1}{2}m\omega_0^2 x^2 + \frac{1}{3}m\xi^{(2)}x^3 + \frac{1}{4}m\xi^{(3)}x^4 + ... \tag{2.7}$$
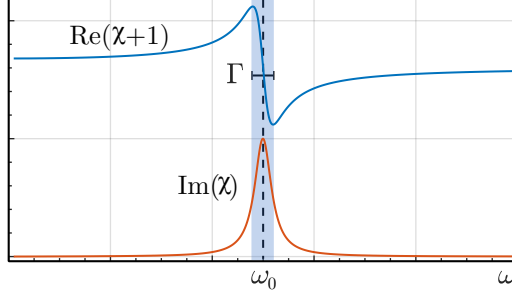
Figure 2.1 – Real (blue) and imaginary (red) part of the linear susceptibility (Eq. (2.6)) as a function of frequency.

In centrosymmetric media only terms proportional to even powers of x appear because the potential energy has to reflect the symmetry $U(x) = U(-x)$. However, as in this work only non-centrosymmetric nonlinear optical materials appear, this case is treated exclusively in the following description.

In contrast to the linear case described above, no analytical solution of the general form of Eq. (2.2) including anharmonic contributions has been found. Nevertheless, if these contributions are small compared to the harmonic one, they can be treated as perturbations and $x(t)$ can be expanded as a power series in E. An equivalent treatment is the expansion of the polarization as a power series. If for a more general description, the vector character of the electric field and the polarization is considered, the i-th component of the polarization reads

$$P_i = \epsilon_0 \left(\chi_{ij}^{(1)} E_j + 2\,\chi_{ijk}^{(2)}\,E_j\,E_k + 4\,\chi_{ijkl}^{(3)}\,E_j\,E_k\,E_l + ... \right), \tag{2.8}$$

where $i,j,k,l,...$ are Cartesian coordinates and $\chi^{(n)}$ denote the nonlinear susceptibilities of n-th order being a tensor of the rank $n+1$. The notation makes use of the Einstein notation.

An external electric field containing two frequency components ω_1 and ω_2 given by

$$E_j(t) = \mathcal{E}_{1j}\,e^{-i\omega_1 t} + \mathcal{E}_{2j}\,e^{-i\omega_2 t} + c.c. \tag{2.9}$$

inserted in Eq. (2.8) leads to a nonlinear polarization of second order

$$P_i^{(2)}(t) = 2\epsilon_0 \chi_{ijk}^{(2)} \Bigg(\mathcal{E}_{1j}\,\mathcal{E}_{1k}^* + \mathcal{E}_{2j}\,\mathcal{E}_{2k}^* + \mathcal{E}_{1j}\,\mathcal{E}_{1k}\,e^{-2i\omega_1 t} + \mathcal{E}_{2j}\,\mathcal{E}_{2k}\,e^{-2i\omega_2 t}$$

$$+ \left(\mathcal{E}_{1j}\,\mathcal{E}_{2k}^* + \mathcal{E}_{2j}^*\,\mathcal{E}_{1k} \right) e^{-i(\omega_1 - \omega_2)t} + \left(\mathcal{E}_{1j}\,\mathcal{E}_{2k} + \mathcal{E}_{2j}\,\mathcal{E}_{1k} \right) e^{-i(\omega_1 + \omega_2)t} + c.c. \Bigg). \tag{2.10}$$

If for convenience the nonlinear polarization is written as

$$P^{(2)}(t) = \sum_n P^{(2)}(\omega_n)\,e^{-i\omega_n t}, \tag{2.11}$$

9

the frequency components of the nonlinear polarization from Eq. (2.10) (see Fig. 2.2) are given by

$$
\begin{aligned}
P^{(2)}(0) &= 2\epsilon_0 \chi_{ijk}^{(2)} (\mathcal{E}_{1j}\,\mathcal{E}_{1k}^* + \mathcal{E}_{2j}\,\mathcal{E}_{2k}^*) & \text{(OR)}, \\
P^{(2)}(2\omega_1) &= 2\epsilon_0 \chi_{ijk}^{(2)} \mathcal{E}_{1j}\,\mathcal{E}_{1k} & \text{(SHG)}, \\
P^{(2)}(2\omega_2) &= 2\epsilon_0 \chi_{ijk}^{(2)} \mathcal{E}_{2j}\,\mathcal{E}_{2k} & \text{(SHG)}, \\
P^{(2)}(\omega_1 - \omega_2) &= 2\epsilon_0 \chi_{ijk}^{(2)} (\mathcal{E}_{1j}\,\mathcal{E}_{2k}^* + \mathcal{E}_{2j}^*\,\mathcal{E}_{1k}) & \text{(DFG)}, \\
P^{(2)}(\omega_1 + \omega_2) &= 2\epsilon_0 \chi_{ijk}^{(2)} (\mathcal{E}_{1j}\,\mathcal{E}_{2k} + \mathcal{E}_{2j}\,\mathcal{E}_{1k}) & \text{(SFG)}.
\end{aligned}
\tag{2.12}
$$

The first term describing a static polarization (and thus a static electric field in the
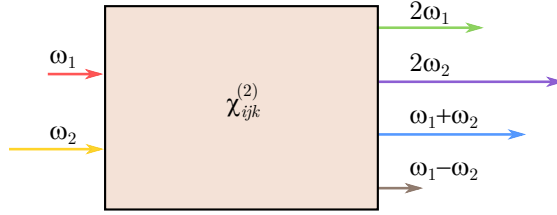
Figure 2.2 – Frequency mixing in a nonlinear optical medium caused by $\chi^{(2)}$. A driving electromagnetic field with the frequency components ω_1 and ω_2 induces frequency components of the polarization with frequencies $2\omega_1$, $2\omega_2$, $\omega_1 + \omega_2$, and $\omega_1 - \omega_2$. Electromagnetic waves with these frequencies are emitted. The input frequency components are omitted at the exit plane of the medium for the sake of clarity.

medium) is called *optical rectification* (OR). The process of *second harmonic generation* (SHG) denotes the occurrence of frequency components oscillating with twice the frequency of the input fields. It can be regarded as a special case of *sum-frequency generation* (SFG), identifying the appearance of components with the frequency $(\omega_1 + \omega_2)$. The fourth and last frequency mixing process induced by the nonlinear response of second order is *difference frequency generation* (DFG) denoting components with the frequency $(\omega_1 - \omega_2)$. It should be noted that in this notation, the contributions with negative frequencies arising from the complex conjugation have been omitted for clarity.

As sum-frequency generation plays a major role in a large part of this thesis, it is examined in more detail. So far, a frequency dependence of the nonlinear susceptibility has been neglected. In a more general description including dispersion, the nonlinear polarization of second order for sum-frequency generation reads

$$
P_i^{(2)}(\omega_n + \omega_m) = \epsilon_0 \sum_{jk} \sum_{(nm)} \chi_{ijk}^{(2)}(\omega_n + \omega_m, \omega_n, \omega_m)\, \mathcal{E}_j(\omega_n)\, \mathcal{E}_k(\omega_m),
\tag{2.13}
$$

where the notation (nm) indicates that $\omega_n + \omega_m$ is kept fix whereas ω_n and ω_m can vary. The frequency dependency of the nonlinear susceptibility is given by

$$
\chi^{(2)}(\omega_n + \omega_m, \omega_n, \omega_m) = \frac{\epsilon_0^2 m \xi^{(2)}}{N^2 e^3} \chi^{(1)}(\omega_n + \omega_m)\chi^{(1)}(\omega_n)\chi^{(1)}(\omega_m)
\tag{2.14}
$$

with the linear susceptibilities from Eq. (2.6).

The summations in Eq. (2.13) lead to an overall number of 324 different complex tensor elements. However, considering symmetries this number can be largely reduced. First of all, as the electric field as well as the polarization are real physical quantities, the frequency components of the susceptibility have to obey

$$\chi_{ijk}^{(2)}(-\omega_n - \omega_m, -\omega_n, -\omega_m) = \chi_{ijk}^{(2)}(\omega_n + \omega_m, \omega_n, \omega_m)^*. \tag{2.15}$$

A further simplification exploits the fact that changing the order of the electric fields in the products $\mathcal{E}_j(\omega_n)\,\mathcal{E}_k(\omega_m)$ cannot change the underlying physics. Thus, the polarization has to be invariant for simultaneous interchanging of n with m and j with k (intrinsic permutation symmetry)

$$\chi_{ijk}^{(2)}(\omega_n + \omega_m, \omega_n, \omega_m) = \chi_{ikj}^{(2)}(\omega_n + \omega_m, \omega_m, \omega_n). \tag{2.16}$$

In case of frequency conversion, the nonlinear optical medium is transparent in the relevant frequency range, i.e., the light-matter interaction is regarded as lossless. The frequencies involved hence lie far away from the resonance frequency of the anharmonic oscillator and from the Eqs. (2.6) and (2.14) follows that the susceptibility is a real quantity. This leads to a full permutation symmetry meaning that the frequency arguments can be freely interchanged providing that the associated Cartesian indices are interchanged simultaneously.

Moreover, often the dispersion of the susceptibility is small and the indices can be permuted without changing the frequency argument. If this so-called Kleinman symmetry is valid, the last two indices of the susceptibility tensor are symmetric. They can be merged to

$$xx = 1, \quad yy = 2, \quad zz = 3$$
$$yz = zy = 4, \quad xz = zx = 5, \quad xy = yx = 6, \tag{2.17}$$

where x, y, and z again denote the Cartesian coordinates. The susceptibility tensor in its contracted form then reads

$$d_{ij} = \begin{pmatrix} d_{11} & d_{12} & d_{13} & d_{14} & d_{15} & d_{16} \\ d_{21} & d_{22} & d_{23} & d_{24} & d_{25} & d_{26} \\ d_{31} & d_{32} & d_{33} & d_{34} & d_{35} & d_{36} \end{pmatrix}. \tag{2.18}$$

Here $(1/2)\chi_{ij}^{(2)}$ is replaced by d_{ij} for convenience. If Kleinman's symmetry is fully exploited, the number of independent tensor elements further reduces to 10 [71]. Sum-frequency generation ($\omega_3 = \omega_1 + \omega_2$) can then be expressed by

$$\begin{pmatrix} P_x^{(2)}(\omega_3) \\ P_y^{(2)}(\omega_3) \\ P_z^{(2)}(\omega_3) \end{pmatrix} = 4\epsilon_0 \begin{pmatrix} d_{11} & d_{12} & d_{13} & d_{14} & d_{15} & d_{16} \\ d_{16} & d_{22} & d_{23} & d_{24} & d_{14} & d_{12} \\ d_{15} & d_{24} & d_{33} & d_{23} & d_{13} & d_{14} \end{pmatrix} \begin{pmatrix} \mathcal{E}_x(\omega_1)\,\mathcal{E}_x(\omega_2) \\ \mathcal{E}_y(\omega_1)\,\mathcal{E}_y(\omega_2) \\ \mathcal{E}_z(\omega_1)\,\mathcal{E}_z(\omega_2) \\ \mathcal{E}_y(\omega_1)\,\mathcal{E}_z(\omega_2) + \mathcal{E}_z(\omega_1)\,\mathcal{E}_y(\omega_2) \\ \mathcal{E}_x(\omega_1)\,\mathcal{E}_z(\omega_2) + \mathcal{E}_z(\omega_1)\,\mathcal{E}_x(\omega_2) \\ \mathcal{E}_x(\omega_1)\,\mathcal{E}_y(\omega_2) + \mathcal{E}_y(\omega_1)\,\mathcal{E}_x(\omega_2) \end{pmatrix}. \tag{2.19}$$

The additional factor 2 stems from the summation over n and m. Equation (2.19) can be reduced to a one-dimensional problem if a fixed geometry, i.e., fixed propagation and polarization directions, is used. The relation between the nonlinear polarization and the applied electric fields is then governed by an effective susceptibility

$$P^{(2)}(\omega_3) = 4\epsilon_0 d_{\text{eff}} \mathcal{E}(\omega_1) \mathcal{E}(\omega_2).$$ (2.20)

A concrete procedure to calculate d_{eff} is given in section 2.1.3.

2.1.2 The coupled wave equations for sum-frequency mixing

In the previous section the nonlinear interaction of electromagnetic waves with a medium was reviewed by regarding only its oscillating electric field. A full description, however, requires to consider the temporal and spatial evolution of the electric field governed by a wave equation, which can be derived from Maxwell's equations. In case of charge- and current-free, nonmagnetic media, Faraday's law of induction and Ampère's circuital law (with Maxwell's addition) have the form

$$\nabla \times \mathbf{E}(\mathbf{r},t) = -\frac{\partial}{\partial t}\Big(\mu_0 \mathbf{H}(\mathbf{r},t)\Big)$$ (2.21)

and

$$\nabla \times \mathbf{H}(\mathbf{r},t) = \frac{\partial}{\partial t}\Big(\epsilon_0 \mathbf{E}(\mathbf{r},t) + \mathbf{P}(\mathbf{r},t)\Big).$$ (2.22)

Here, $\mathbf{E}(\mathbf{r},t)$ and $\mathbf{H}(\mathbf{r},t)$ denote the electric and magnetic field vectors and ϵ_0 and μ_0 are the permittivity and permeability of free space, respectively. The curl of Eq. (2.21) together with Eq. (2.22) leads to the wave equation in its general form

$$\nabla \times \Big(\nabla \times \mathbf{E}(\mathbf{r},t)\Big) + \mu_0 \epsilon_0 \frac{\partial^2}{\partial t^2}\mathbf{E}(\mathbf{r},t) = -\mu_0 \frac{\partial^2}{\partial t^2}\mathbf{P}(\mathbf{r},t),$$ (2.23)

where the polarization $\mathbf{P}(\mathbf{r},t)$ serves as a source term in this differential equation.

In a first step the wave equation is simplified exploiting the 'identity' $\nabla \times (\nabla \times \mathbf{E}) = \nabla(\nabla \mathbf{E}) - \nabla^2 \mathbf{E} = -\nabla^2 \mathbf{E}$. It should be noted that the second identity is not generally valid as Gauss's law for charge-free space $\nabla \mathbf{D} = 0$ with $\mathbf{D} = \epsilon_0 \mathbf{E} + \mathbf{P}$ does not necessarily lead to $\nabla \mathbf{E} = 0$. However, this term is negligible in case that the slowly-varying envelope approximation is valid [68]. The wave equation has then the form

$$\left(\nabla^2 - \frac{1}{c^2}\frac{\partial^2}{\partial t^2}\right) \mathbf{E}(\mathbf{r},t) = \mu_0 \frac{\partial^2}{\partial t^2} \mathbf{P}(\mathbf{r},t),$$ (2.24)

where $\epsilon_0 \mu_0 = 1/c^2$ is used.

As before the polarization can be divided into linear and non-linear contributions

$$\mathbf{P}(\mathbf{r},t) = \mathbf{P}^{(1)}(\mathbf{r},t) + \mathbf{P}^{(2)}(\mathbf{r},t) + \mathbf{P}^{(3)}(\mathbf{r},t) + ... = \mathbf{P}^{(1)}(\mathbf{r},t) + \mathbf{P}^{\text{NL}}(\mathbf{r},t).$$ (2.25)

In a similar manner the electric displacement can be split into a linear and a nonlinear part

$$\mathbf{D} = \mathbf{D}^{(1)} + \mathbf{P}^{\mathrm{NL}} \quad \text{with} \quad \mathbf{D}^{(1)} = \epsilon_0 \mathbf{E} + \mathbf{P}^{(1)}. \tag{2.26}$$

The wave equation then reads

$$\nabla^2 \mathbf{E}(\mathbf{r},t) - \mu_0 \frac{\partial^2}{\partial t^2} \mathbf{D}^{(1)}(\mathbf{r},t) = \mu_0 \frac{\partial^2}{\partial t^2} \mathbf{P}^{\mathrm{NL}}(\mathbf{r},t). \tag{2.27}$$

In the quite general case of a lossless but dispersive medium, each frequency component of the fields has to be taken into account separately. Expressing the fields as sums of their frequency components

$$\mathbf{E}(\mathbf{r},t) = \sum_n \mathbf{E}_n(\mathbf{r},t) \quad \text{with} \quad \mathbf{E}_n(\mathbf{r},t) = \mathcal{E}_n(\mathbf{r})e^{-i\omega_n t} + c.c. \tag{2.28}$$

$$\mathbf{D}^{(1)}(\mathbf{r},t) = \sum_n \mathbf{D}_n^{(1)}(\mathbf{r},t) \quad \text{with} \quad \mathbf{D}_n^{(1)}(\mathbf{r},t) = \mathcal{D}_n^{(1)}(\mathbf{r})e^{-i\omega_n t} + c.c. \tag{2.29}$$

$$\mathbf{P}^{\mathrm{NL}}(\mathbf{r},t) = \sum_n \mathbf{P}_n^{\mathrm{NL}}(\mathbf{r},t) \quad \text{with} \quad \mathbf{P}_n^{\mathrm{NL}}(\mathbf{r},t) = \mathcal{P}_n^{\mathrm{NL}}(\mathbf{r})e^{-i\omega_n t} + c.c. \tag{2.30}$$

and using the relation between the electric field and displacement given by the dielectric tensor $\epsilon^{(1)}(\omega_n) = 1 + \chi^{(1)}$

$$\mathbf{D}_n^{(1)}(\mathbf{r},t) = \epsilon_o \epsilon^{(1)}(\omega_n) \cdot \mathbf{E}_n(\mathbf{r},t) \tag{2.31}$$

leads to a wave equation for each frequency component

$$\nabla^2 \mathbf{E}_n(\mathbf{r},t) - \frac{\epsilon^{(1)}(\omega_n)}{c^2} \frac{\partial^2}{\partial t^2} \mathbf{E}_n(\mathbf{r},t) = \frac{1}{\epsilon_0 c^2} \frac{\partial^2}{\partial t^2} \mathbf{P}_n^{\mathrm{NL}}(\mathbf{r},t). \tag{2.32}$$

In the simplest case of a nonlinear interaction only the contributions of second order are considered, the applied waves with the frequencies ω_1 and ω_2 propagate collinearly in the z direction, and enter the nonlinear optical material at normal incidence (cf. Fig. 2.2). Since the wave equation (2.32) has to be fulfilled for every frequency component, it is also valid for the generated frequency ω_3. If the source term, i.e., the nonlinear polarization, is small, the solution of the wave equation should not differ too much from the one of the homogeneous form in absence of a nonlinear term, which reads

$$E_3(z,t) = \mathcal{E}_3(z)e^{-i\omega_3 t} + c.c. = A_3 e^{i(k_3 z - \omega_3 t)} + c.c. \quad \text{with} \quad k_3 = \frac{n_3 \omega_3}{c}, \quad n_3^2 = \epsilon^{(1)}(\omega_3). \tag{2.33}$$

In this solution A_3 is a constant. If the small source term is considered, the solution has the same form except that A_3 is now a slowly varying function of z. The source term of Eq. (2.32) is written as

$$P_3^{(2)}(z,t) = \mathcal{P}_3^{(2)}(z)e^{-i\omega_3 t} + c.c., \tag{2.34}$$

where, according to Eq. (2.20), $\mathcal{P}_3^{(2)}(z)$ is given by

$$\mathcal{P}_3^{(2)}(z) = 4\epsilon_0 d_{\text{eff}} \mathcal{E}_1(z) \mathcal{E}_2(z). \tag{2.35}$$

If the applied electric fields are again represented by

$$E_i(z,t) = \mathcal{E}_i(z)e^{-i\omega_i t} + c.c. \quad \text{with} \quad \mathcal{E}_i(z) = A_i e^{ik_i z}, \tag{2.36}$$

the amplitude of the nonlinear polarization reads

$$\mathcal{P}_3^{(2)}(z) = 4\epsilon_0 d_{\text{eff}} A_1 A_2 e^{i(k_1+k_2)z}. \tag{2.37}$$

This relation, together with Eq. (2.34) and the trial solution Eq. (2.33) with an amplitude A_3 slowly varying as a function of z, can now be included in the wave equation (2.32). As the fields are only considered to vary in z, ∇^2 can be replaced by $\frac{\partial^2}{\partial z^2}$ and the wave equation

$$\left(\frac{\partial^2 A_3}{\partial z^2} + 2ik_3 \frac{\partial A_3}{\partial z} - k_3^2 A_3 + \frac{\epsilon^{(1)}(\omega_3)\omega_3^2 A_3}{c^2} \right) e^{i(k_3 z - \omega_3 t)} + c.c.$$
$$= \frac{-4d_{\text{eff}}\omega_3^2}{c^2} A_1 A_2 e^{i[(k_1+k_2)z - \omega_3 t]} + c.c. \tag{2.38}$$

is obtained. From Eq. (2.33) it is immediately clear that the third and fourth term on the left-hand side cancel out. Multiplying both sides with $e^{i(k_3 z - \omega_3 t)}$ and dropping the complex conjugate leads to the simpler equation

$$\frac{\partial^2 A_3}{\partial z^2} + 2ik_3 \frac{\partial A_3}{\partial z} = \frac{-4d_{\text{eff}}\omega_3^2}{c^2} A_1 A_2 e^{i(k_1+k_2-k_3)z}. \tag{2.39}$$

Usually the first term on the left-hand side is much smaller than the second and can be neglected. Repeating the same derivation for the other two frequency components results in a set of wave equations coupled via the effective nonlinear susceptibility

$$\frac{\partial A_1}{\partial z} = \frac{2id_{\text{eff}}\omega_1^2}{k_1 c^2} A_3 A_2^* e^{-i\Delta kz} \tag{2.40}$$

$$\frac{\partial A_2}{\partial z} = \frac{2id_{\text{eff}}\omega_2^2}{k_2 c^2} A_3 A_1^* e^{-i\Delta kz} \tag{2.41}$$

$$\frac{\partial A_3}{\partial z} = \frac{2id_{\text{eff}}\omega_3^2}{k_3 c^2} A_1 A_2 e^{i\Delta kz}. \tag{2.42}$$

Here, the phase mismatch $\Delta k = k_1 + k_2 - k_3$ is introduced. These equations describe how the amplitudes of the frequency components change during propagation through the medium as a result of their coupling to the other two components. Since the medium is assumed to be lossless in the relevant frequency range, the full permutation symmetry is applied justifying the same susceptibility value in the three differential equations.

In case of small conversion efficiency, the input fields can be considered as constant meaning that $\frac{\partial A_1}{\partial z} = \frac{\partial A_2}{\partial z} \approx 0$. Then, Eq. (2.42) can be easily solved. Integrating the

equation from $z = 0$ to $z = L$ gives the amplitude of the sum frequency A_3 at the exit plane of the medium

$$A_3(L) = \frac{2id_{\mathrm{eff}}\omega_3^2 A_1 A_2}{k_3 c^2} \int_0^L e^{i\Delta kz} \mathrm{d}z = \frac{2id_{\mathrm{eff}}\omega_3^2 A_1 A_2}{k_3 c^2} \left(\frac{e^{i\Delta kL} - 1}{i\Delta k} \right). \tag{2.43}$$

The intensity of a field is given by

$$I = 2n\epsilon_0 c |A|^2, \tag{2.44}$$

so that the intensity of the generated field is

$$I_3 = \frac{2d_{\mathrm{eff}}^2 \omega_3^2 I_1 I_2}{\epsilon_0 c^3 n_1 n_2 n_3} L^2 \left(\frac{\sin(\Delta kL/2)}{\Delta kL/2} \right)^2. \tag{2.45}$$

The energy conversion from the input fields to the generated one allows a small mismatch of the wave vectors. The effect on the conversion efficiency is entirely determined by the factor $\sin^2(\Delta kL/2)/(\Delta kL/2)^2$, which is plotted in Fig. 2.3 (a). With increasing $|\Delta k|L$ the efficiency decreases drastically. This means that for an efficient frequency conversion either the phase matching condition has to be fulfilled or the crystal length must be short.
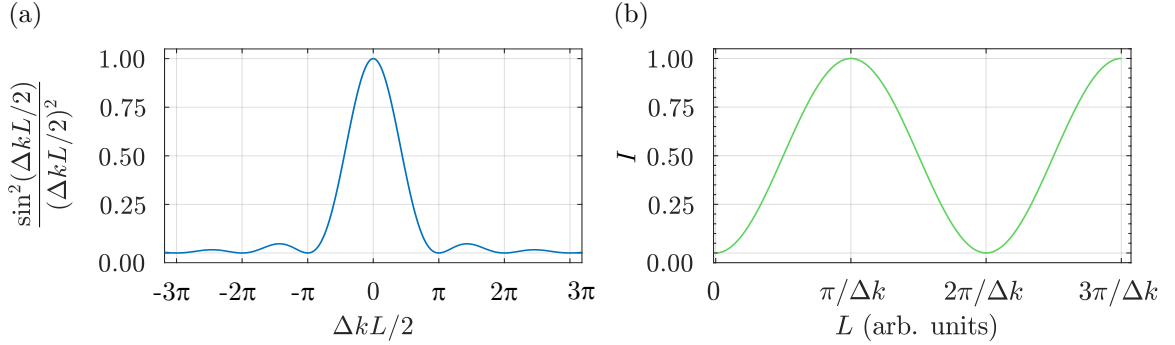
Figure 2.3 – **(a)** Conversion efficiency as a function of phase mismatch Δk. **(b)** Intensity of the generated sum-frequency as a function of propagation distance L.

The effect of the phase mismatch can be understood returning to the microscopic picture of driven anharmonic oscillators. The driving waves move through the medium with the velocities ω/k. For the sake of simplicity, these two velocities are assumed to be approximately equal for the moment. The coherent optical field induces a conglomeration of coherently oscillating dipoles forming a macroscopic polarization. The phase fronts of this polarization move through the crystal with the same velocity as the driving waves. The generated sum frequency, however, moves with the velocity ω_3/k_3. If $\Delta k = 0$, the polarization wave and the sum frequency wave will move synchronously with a fixed phase difference of 90° through the medium. Each sum-frequency wave emitted from a microscopic dipole will constructively interfere with all waves emitted from the other dipoles and a net intensity of the generated wave is obtained at the exit of the medium.

If in contrast $\Delta k \neq 0$, the polarization wave and the sum-frequency wave will move asynchronously and gain phase with respect to each other. After a propagation distance of $L_c = |\pi/\Delta k|$ they are out of phase by 180° and the sum-frequency waves emitted from the dipole at $z = 0$ and $z = L_c$ interfere destructively, as schematically shown in Fig. 2.4. The sum-frequency amplitude has thus reached its maximum and decreases for larger propagation distance z. The sign of the power flow changes and the power is now coupled from the electromagnetic wave to the polarization wave until it is completely transferred back at $z = 2L_c$ (cf. Fig. 2.3 (b)). The length L_c is called coherence length. For non phase-matched frequency mixing the maximum amplitude gained is the signal from one coherence length independent from the actual medium thickness.
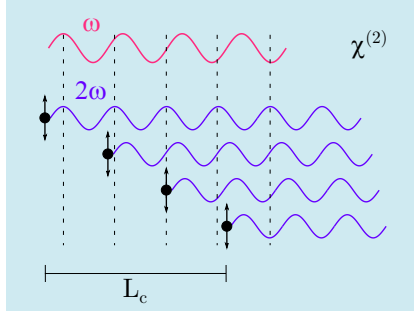
Figure 2.4 – Superposition of generated sum-frequency waves in presence of phase mismatch. Fundamental driving waves (red) with the same frequency ω induce dipoles (black) emitting waves with double frequency (blue). In presence of phase mismatch the fundamental and harmonic waves propagate through the medium with different velocities. As a result, for increasing starting positions the harmonic waves gain phase with respect to each other. Waves emitted from dipoles with a distance of $L_c = |\pi/\Delta k|$ are out of phase by 180° and interfere destructively.

As mentioned above, this derivation is based on a collinear geometry. For the more general case of non-collinear sum-frequency mixing, which is used in section 3.2.4, the phase mismatch has to be written in the vectorial form

$$\Delta \mathbf{k} = \mathbf{k}_1 + \mathbf{k}_2 - \mathbf{k}_3. \tag{2.46}$$

2.1.3 Phase matching in birefringent crystals

In the last section, the effect of a phase mismatch between the waves involved in frequency conversion was reviewed. The origin of such a mismatch is the dispersion of the index of refraction leading to different phase velocities for electromagnetic waves oscillating at different frequencies. From Eq. (2.33) follows that the phase matching condition for sum-frequency generation can be written as

$$n_3 = \frac{n_1\omega_1 + n_2\omega_2}{\omega_3}. \tag{2.47}$$

The difference between n_3 and n_2 is therefore

$$n_3 - n_2 = (n_1 - n_2)\frac{\omega_1}{\omega_3}. \tag{2.48}$$

Usually, the index of refraction of a material is a monotonically increasing function of the frequency, which is called normal dispersion. The left- and right-hand side of Eq. (2.48) thus have different signs showing that phase matching is impossible in materials with normal dispersion.
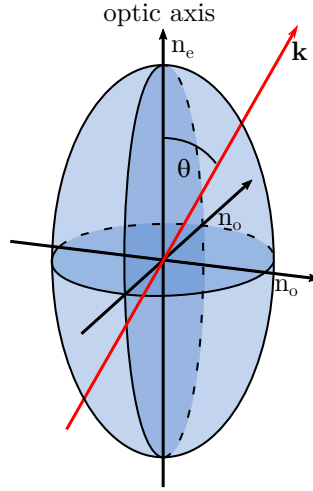
Figure 2.5 – Refractive index of a birefringent uniaxial medium. Rays (k) with a polarization perpendicular to the symmetry axis (optic axis) are called ordinary rays. They experience the angle-independent ordinary refractive index n_o. Rays having a polarization component parallel to the optic axis are called extraordinary rays. The refractive index then depends on the angle θ to the optic axis and is given by Eq. (2.49).

Phase matching is usually achieved by employing birefringent, nonlinear optical crystals for frequency mixing. Birefringence is the property of a material that the index of refraction depends on the light polarization, i.e., the direction of the oscillating electric field vector. In the easiest case a uniaxial symmetry is found, where the symmetry axis is called optic axis (see Fig. 2.5). A ray having a polarization perpendicular to the optic axis is called ordinary ray (or ordinarily polarized). The index of refraction 'seen' by these rays is n_o. All rays with a polarization, which has a component in the direction of the optic axis, are called extraordinary rays. In these cases the index of refraction depends on the angle θ enclosed by the wave vector and the optic axis

$$n_e(\theta) = \frac{n_o n_e}{\sqrt{n_o^2 \sin^2(\theta) + n_e^2 \cos^2(\theta)}}, \tag{2.49}$$

where n_e is the principal value of the extraordinary refractive index being equal to $n_e(\theta = 90°)$. For $\theta = 0°$ the refractive index is trivially n_o. Thus, by varying θ, the index of refraction can be tuned to values between n_e and n_o. Two different groups of uniaxial birefringent crystals are found. In negative uniaxial crystals $n_e < n_o$, whereas

correspondingly in positive uniaxial crystals $n_{\mathrm{e}} > n_{\mathrm{o}}$. For phase matching, the polarization of the wave with the highest frequency has to be chosen to experience the smaller of the possible refractive indices. For the other two waves, two combinations are possible: if both have the same polarization the phase matching is called type I, if their polarizations are orthogonal it is called type II.
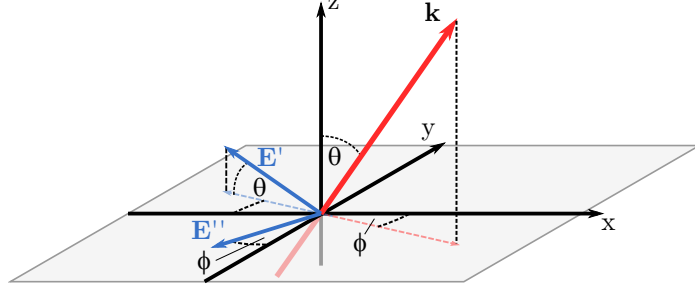
Figure 2.6 – Coordinate system used to convert the electric field vectors from Cartesian to spherical coordinates via equation (2.50).

In section 2.1.1 the effective susceptibility has been introduced, which can be calculated for a given set of polarizations and propagation directions. In case of uniaxial crystals, it is convenient to express the applied electric field vectors and the resulting polarization in spherical coordinates (cf. Fig. 2.6). The optic axis is set along the z-coordinate. Again, θ is the polar angle enclosed by the wave vector k and the optic axis. A rotation around the symmetry axis is given by the azimuthal angle ϕ. If the electric field vectors of an ordinarily and extraordinarily polarized wave are denoted with E'' and E', respectively, their components can be expressed by

$$
\begin{aligned}
E'_x &= E'\cos(\theta')\cos(\phi') & E''_x &= -E''\sin(\phi'') \\
E'_y &= E'\cos(\theta')\sin(\phi') & E''_y &= E''\cos(\phi'') \\
E'_z &= -E'\sin(\theta') & E''_z &= 0.
\end{aligned}
\tag{2.50}
$$

The polarization generating the sum-frequency is generally either parallel or perpendicularly polarized with respect to the incoming wave. For convenience, the polarization can be expressed as

$$
\begin{aligned}
P^{(2)}_\perp &= P^{(2)}_x\sin(\phi''') - P^{(2)}_y\cos(\phi''') \\
P^{(2)}_\parallel &= -(P^{(2)}_x\cos(\phi''') + P^{(2)}_y\sin(\phi'''))\cos(\theta''') + P^{(2)}_z\sin(\theta''').
\end{aligned}
\tag{2.51}
$$

For a given geometry, the effective susceptibility is now obtained by first calculating the nonlinear polarization vector according to Eq. (2.19). Then the Cartesian coordinates are transferred via Eqs. (2.50) and (2.51). In section 3.2.4 the effective susceptibility is calculated for non-collinear sum-frequency mixing in BBO with type II phase matching.

2.2 Propagation of light pulses in media

In the following section the propagation of light pulses in media is shortly reviewed following the description in *Ultrashort Laser Pulse Phenomena* by J.-C. Diels and W. Rudolph [72].

2.2.1 Mathematical description of light pulses

Laser pulses are intense electromagnetic wave packets, i.e., short bursts of electromagnetic field elongation propagating through space. As such, they can be thought of as superposition of a set of sinusoidal waves with different frequencies, which interfere destructively except for a small region in time (cf. Fig. 2.7). Thus, the electric field of a light pulse can be fully described in the time or alternatively in the frequency domain. In the latter case the spectrum built from the involved frequencies is used. Both representations are connected via the Fourier transform

$$\tilde{E}(\Omega) = \int_{-\infty}^{\infty} E(t)e^{-i\Omega t}\mathrm{d}t$$
$$E(t) = \frac{1}{2\pi}\int_{-\infty}^{\infty} \tilde{E}(\Omega)e^{i\Omega t}\mathrm{d}\Omega. \tag{2.52}$$

From the real electric field $E(t)$ a complex spectrum $\tilde{E}(\Omega)$ is obtained, which contains

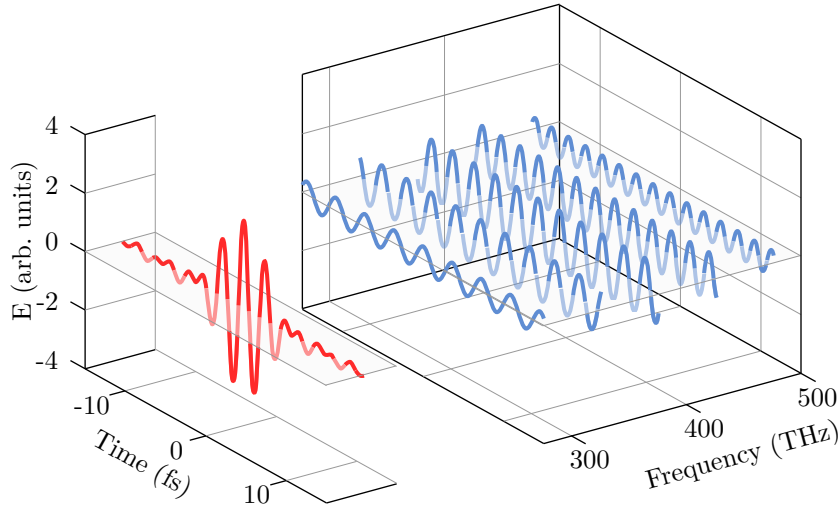**Figure 2.7** – Superposition of a set of sinusoidal waves with different frequencies (blue). As a function of frequency their amplitudes follow a Gaussian distribution. Constructive interference is observed only in a small region of time (red).

positive and negative frequencies. It can, however, be more practical to express the electric field in the time domain by a complex function with a corresponding spectrum

without nonzero negative frequency components

$$\tilde{E}^+(t) = \frac{1}{2\pi}\int_{-\infty}^{\infty}\tilde{E}^+(\Omega)e^{i\Omega t}\mathrm{d}\Omega \quad \text{with} \quad \tilde{E}^+(\Omega) = |\tilde{E}(\Omega)|e^{i\Phi(\Omega)} = \begin{cases} \tilde{E}(\Omega) & \text{for } \Omega \geq 0 \\ 0 & \text{for } \Omega < 0. \end{cases}$$
(2.53)

Again, both functions are connected by the Fourier transform similar to Eq. (2.52). Correspondingly the complex quantities $\tilde{E}^-(t)$ and $\tilde{E}^-(\Omega)$ can be defined. The real electric field $E(t)$ and its complex Fourier transform $\tilde{E}(\Omega)$ are obtained from the newly defined functions via

$$E(t) = \tilde{E}^+(t) + \tilde{E}^-(t)$$
$$\tilde{E}(\Omega) = \tilde{E}^+(\Omega) + \tilde{E}^-(\Omega).$$
(2.54)

The complex electric field $\tilde{E}^+(t)$ in the time domain can be described by the product of a time-dependent amplitude and a phase term

$$\tilde{E}^+(t) = \frac{1}{2}\mathcal{E}(t)e^{i\Gamma(t)}.$$
(2.55)

It should be noted that the amplitude function $\mathcal{E}(t)$ should not be confused with the quantity $\mathcal{E}(\mathbf{r})$ used in Eq. (2.28) to separate the temporal and spatial variation of an electric field. Centering the spectral amplitude around a carrier frequency ω_l and assuming that only frequencies from a bandwidth small compared to the carrier frequency contribute to the electric field leads to the expression

$$\tilde{E}^+(t) = \frac{1}{2}\mathcal{E}(t)e^{i\phi_0}e^{i\phi(t)}e^{i\omega_l t} = \frac{1}{2}\tilde{\mathcal{E}}(t)e^{i\omega_l t}.$$
(2.56)

Here, $\phi(t)$ is a time-dependent phase and $\mathcal{E}(t)$ and $\tilde{\mathcal{E}}(t)$ are called the real and complex field envelope, respectively. The constant phase term, the carrier to envelope phase, ϕ_0 can be neglected within the framework of this thesis and also in most of the other practical cases.

The quantities essential for this work are the envelope functions in the time and frequency domain, which give the temporal pulse shape and the pulse spectrum. The temporal and spectral complex envelopes are connected with the electric fields via

$$\tilde{\mathcal{E}}(t) = \frac{1}{2\pi}\int_{-\infty}^{\infty}2\tilde{E}^+(\Omega + \omega_l)e^{i\Omega t}\mathrm{d}\Omega$$
$$\tilde{\mathcal{E}}(\Omega) = \int_{-\infty}^{\infty}\tilde{\mathcal{E}}(t)e^{-i\Omega t}\mathrm{d}t = 2\int_{-\infty}^{\infty}\tilde{E}^+(t)e^{-i(\Omega+\omega_l)t}\mathrm{d}t = 2\tilde{E}^+(\Omega + \omega_l),$$
(2.57)

where ω_l is chosen that $\tilde{\mathcal{E}}(\Omega)$ is centered at $\Omega = 0$. They are depicted in Fig. 2.8 (a) and (b). Experimentally, not the electric field amplitude itself but the intensity proportional to the squared amplitude is accessible. The spectral intensity $S(\Omega)$ measured by a spectrometer is given by

$$S(\Omega) \propto |\tilde{E}^+(\Omega)|^2 = |\tilde{\mathcal{E}}(\Omega - \omega_l)|^2.$$
(2.58)

(a)

(b)
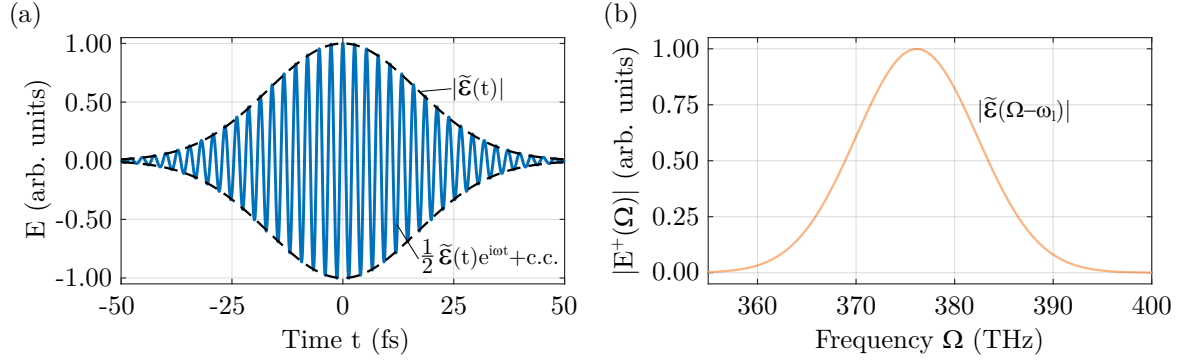
Figure 2.8 – Electric field of a short light pulse shown in the **(a)** time and **(b)** frequency domain.

It can thus be related with the temporal intensity $I(t) \propto |\tilde{\mathcal{E}}(t)|^2$ via Fourier transformation.

It has already been stated that the temporal and spectral features of an electromagnetic wave packet are connected via Fourier transformation. Therefore, the pulse duration τ defined as the full width at half maximum (FWHM) of the intensity function $I(t) \propto |\tilde{\mathcal{E}}(t)|^2$ and the spectral width $\Delta\omega$, which is the FWHM of the spectral intensity $S(\Omega)$, depend on each other. From the Fourier transformation a minimum duration-bandwidth product is obtained

$$\Delta\omega\,\tau = 2\pi\Delta\nu\,\tau \geq 2\pi c_{\mathrm{B}}, \tag{2.59}$$

where c_{B} is a constant depending on the actual pulse or spectral shape, respectively. It is 0.441 for a Gaussian-shaped pulse. In case of equality of the equation the pulses are called bandwidth or Fourier limited. These pulses have the minimum pulse duration for a given spectrum.

Until now the time-dependent phase term $e^{i\phi(t)}$ in Eq. (2.56) has been hidden in the complex envelope function. By taking the time-derivative of the phase factor, a time-dependent carrier frequency $\omega(t)$, which is called instantaneous frequency, can be defined

$$\omega(t) = \omega_l + \frac{\mathrm{d}\phi(t)}{\mathrm{d}t}. \tag{2.60}$$

If the temporal change of the phase term is constant, the instantaneous frequency is just shifted with respect to the formerly defined carrier-frequency. If $\mathrm{d}\phi(t)/\mathrm{d}t$, however, is a function of time, the frequency ω varies with time. The pulse is then called *chirped*. The electric field as a function of time for a pulse with a linear chirp is shown in Fig. 2.9 (a). The corresponding instantaneous frequency is shown in Fig. 2.9 (b).

2.2.2 Pulse propagation

In section 2.1.2 the propagation of electromagnetic waves in a medium has been reviewed focusing on the nonlinear light-matter interaction of second order. The propagation of
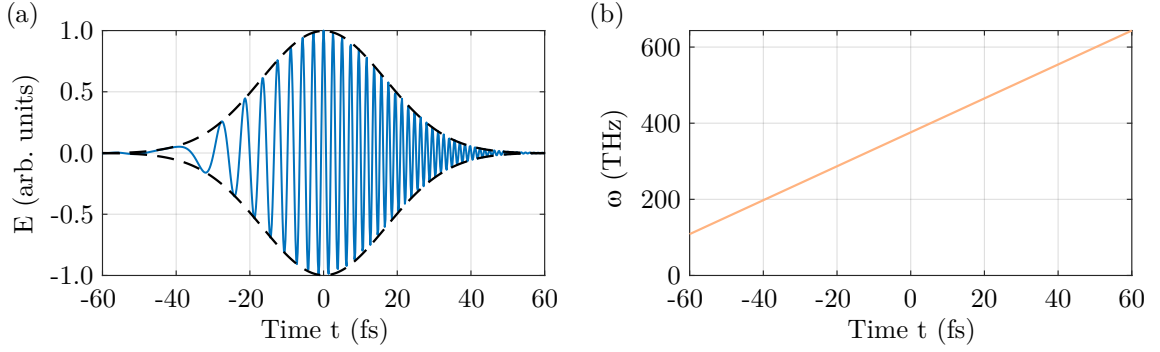
Figure 2.9 – **(a)** Time-dependent electric field of a short light pulse with linear chirp. **(b)** Instantaneous frequency of the chirped light pulse shown in the left panel.

short light pulses in the linear regime is again described by a wave equation such as Eq. (2.24). The polarization serving as source term of the differential equation has already been divided into a linear and a nonlinear part in Eq. (2.25). Here, only the linear part is considered. For simplicity, the pulse is considered as superposition of infinite plane waves propagating in the z-direction. This leads to the reduced wave equation

$$\left(\frac{\partial^2}{\partial z^2} - \frac{1}{c^2}\frac{\partial^2}{\partial t^2} \right) E(z,t) = \mu_0 \frac{\partial^2}{\partial t^2} P^{(1)}(z,t). \tag{2.61}$$

From Eqs. (2.26) and (2.31) the linear polarization in the frequency domain

$$P^{(1)}(\Omega,z) = \epsilon_0 \left(\epsilon^{(1)}(\Omega) - 1 \right) \tilde{E}(\Omega,z) \tag{2.62}$$

can be found. The Fourier transform of the reduced wave equation (2.61) is then given by

$$\left(\frac{\partial^2}{\partial z^2} + \Omega^2 \epsilon^{(1)}(\Omega)\mu_0 \right) \tilde{E}(\Omega,z) = 0, \tag{2.63}$$

with the solution

$$\tilde{E}(\Omega,z) = \tilde{E}(\Omega,0)e^{-ik(\Omega)z}. \tag{2.64}$$

The wave vector k has already been introduced in Eq. (2.33) being

$$k^2(\Omega) = \frac{\Omega^2}{c^2}n^2(\Omega). \tag{2.65}$$

Whereas in section 2.1.2 the frequency dependence of the wave vector was considered for monochromatic waves with different frequencies, here its effect on the envelope of a single pulse is the subject. For this purpose, the wave vector is expanded around the carrier frequency of the pulse

$$k(\Omega) = k(\omega_l) + \delta k, \tag{2.66}$$

where

$$\delta k = \left.\frac{\mathrm{d}k}{\mathrm{d}\Omega}\right|_{\omega_l}(\Omega - \omega_l) + \frac{1}{2}\left.\frac{\mathrm{d}^2 k}{\mathrm{d}\Omega^2}\right|_{\omega_l}(\Omega - \omega_l)^2 + ...\,. \tag{2.67}$$

Using this expression, the solution of the reduced wave equation is rewritten as

$$\tilde{E}(\Omega,z) = \tilde{E}(\Omega,0)e^{-ik_l z}e^{-i\delta k z} \quad \text{with} \quad k_l^2 = \omega_l^2 n^2(\omega_l)/c^2. \tag{2.68}$$

In the time domain, Eq. (2.68) corresponds to

$$\tilde{E}(t,z) = \frac{1}{2}\tilde{\mathcal{E}}(t,z)e^{i(\omega_l t - k_l z)}, \tag{2.69}$$

where $\tilde{\mathcal{E}}(t,z)$ is now slowly varying in space and time. An envelope function slowly varying in the spatial coordinate can be defined as

$$\tilde{\mathcal{E}}(\Omega,z) = \tilde{E}(\Omega + \omega_l,0)e^{-i\delta k z}. \tag{2.70}$$

After some calculation [72], a wave equation for this envelope function can be found. For this purpose, the susceptibility $\epsilon^{(1)}$ and therefore the polarization is also expanded around the carrier frequency ω_l and the coordinate system is transferred to a frame of reference moving at the *group velocity*

$$v_{\mathrm{g}} = \left(\left.\frac{\mathrm{d}k}{\mathrm{d}\Omega}\right|_{\omega_l}\right)^{-1}. \tag{2.71}$$

This frame of reference is reached introducing the new coordinates

$$\xi = z \quad \text{and} \quad \eta = t - \frac{z}{v_{\mathrm{g}}} \tag{2.72}$$

and partial derivatives

$$\frac{\partial}{\partial z} = \frac{\partial}{\partial \xi} - \frac{1}{v_{\mathrm{g}}}\frac{\partial}{\partial \eta} \quad \text{and} \quad \frac{\partial}{\partial t} = \frac{\partial}{\partial \eta}. \tag{2.73}$$

In this frame of reference, the reduced wave equation reads

$$\frac{\partial}{\partial \xi}\tilde{\mathcal{E}}(\eta,\xi) - \frac{i}{2}k_l''\frac{\partial^2}{\partial \eta^2}\tilde{\mathcal{E}}(\eta,\xi) + \mathcal{O} = -\frac{i}{2k_l}\frac{\partial}{\partial \xi}\left(\frac{\partial}{\partial \xi} - \frac{2}{v_{\mathrm{g}}}\frac{\partial}{\partial \eta}\right)\tilde{\mathcal{E}}(\eta,\xi). \tag{2.74}$$

The quantity k_l'' is the second derivative of k (cf. second term in Eq. (2.67)) and is called *group velocity dispersion (GVD)*. The term $\mathcal{O}$ summarizes contributions from dispersion of higher order. Neglecting these higher terms and once more applying the slowly varying envelope approximation leads to a much simpler wave equation for the complex envelope function

$$\frac{\partial}{\partial \xi}\tilde{\mathcal{E}}(\eta,\xi) - \frac{i}{2}k_l''\frac{\partial^2}{\partial \eta^2}\tilde{\mathcal{E}}(\eta,\xi) = 0. \tag{2.75}$$

Obviously, in absence of GVD ($k_l'' = 0$), the envelope propagates at group velocity without any change. The group velocity from Eq. (2.71) can be used to define the group index

$$n_{\mathrm{g}}(\Omega) = \frac{c}{v_{\mathrm{g}}} = c\frac{\partial k}{\partial \Omega} = n(\Omega) + \Omega\frac{\partial n}{\partial \Omega}. \tag{2.76}$$

If GVD is present (and no further higher orders), the complex envelope function is given by

$$\tilde{\mathcal{E}}(\Omega,z) = \tilde{\mathcal{E}}(\Omega,0)\exp\left(-\frac{i}{2}k_l''\Omega^2 z\right). \tag{2.77}$$

While the spectral amplitudes remain unaffected, the propagation leads to a quadratic gain of spectral phase, which leads to the pulse chirp introduced earlier. It is easy to realize that in the time domain an originally Fourier-limited pulse continuously broadens propagating though a dispersive medium.

2.3 Polarons and self-trapped excitons

The concept of *self-trapping* of charge carriers or excitons in a polarizable medium can be traced back to the year 1933, when Landau described an electron localized in a potential well induced by itself [1]. The presence of the electron alters the surrounding atoms' equilibrium positions forming a potential well, in which the electron is finally trapped. The charge carrier together with the induced lattice distortion is called *polaron*. In this work only the subcategory of *small polarons* is considered as they are the relevant quasi-particles occurring in the samples under study. These polarons are characterized by a coupling of the charge carrier to the lattice, or strictly speaking to the phonons, strong enough to limit their charge carrier to a single lattice site [73] (cf. Fig. 2.10 (a)).
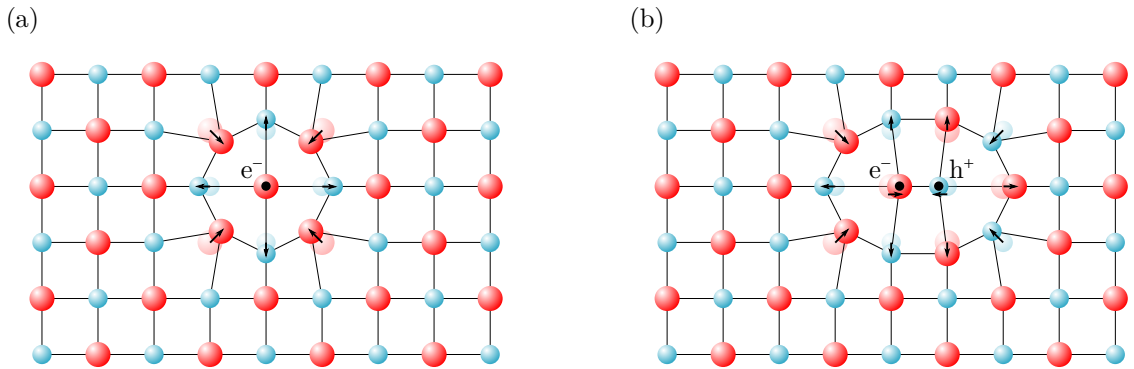
(a) (b)

Figure 2.10 – Schematic representation of the lattice distortion induced by **(a)** an electron and **(b)** an exciton. Adjacent atoms are shifted with respect to their undisturbed equilibrium positions. A potential well is induced, which is deep enough to localize the charge carrier or the exciton at a lattice site.

A net additional charge 'placed' in the crystal is not the prerequisite for self-trapping to occur. A similar phenomenon is observed in case of excitons, i.e., elementary excitations of nonmetallic condensed matter. These electron-hole pairs are bound via their mutual Coulomb attraction and are neutral quasi-particles, if their internal coordinates can be neglected. Again a coupling to phonon modes leading to self-trapping in a deformed lattice can be observed (cf. Fig. 2.10 (b)). The localized exciton with its accompanying atomic relaxation is called *self-trapped exciton (STE)* [74].

Small polarons and self-trapped excitons exhibit characteristic transport, absorption, and luminescence features. As these quasi-particles are localized, i.e., their electronic transfer energy is small, they respond to a classical motion of the lattice atoms with an incoherent transport [73]. They move via phonon-assisted jumps, which is called hopping transport. The strong coupling to phonons also predominantly determines the absorption and luminescence features of such quasi-particles. Instead of sharp absorption and emission lines, broad spectra are observed.

All of these characteristica are further discussed in the next subsections. But first, the formation of these quasi-particles is examined in more detail. For the sake of convenience, the terms charge carrier and small polaron are used synonymously for excitons and self-trapped excitons. This is justified as coupling of charge carriers and excitons to the lattice can be treated identically leading to similar results [75]. They will only be distinguished whenever qualitative differences of their behavior are observed.

2.3.1 Self-trapping in a deformable continuum

The following subsection is a recapitulation of the elaborate work on this topic by David Emin, which is summarized in his book on polarons [73]. Similar results are obtained by Yutaka Toyozawa using a different mathematical approach [76].

The ground state of a charge carrier placed in a deformable lattice can often be calculated within the adiabatic approximation. There, the motion of the light charge carriers is assumed to be sufficiently rapid to instantly follow changing positions of the orders of magnitude heavier atoms. For a qualitative description their interaction with phonon modes can be simplified treating the lattice as a deformable continuum [73]. The presence of the charge carrier then induces a deformation of the continuum $\Delta(\mathbf{u})$ at a position $\mathbf{u}$ lowering the charge carrier's potential energy at position $\mathbf{r}$ by

$$V(\mathbf{r}) = \int d\mathbf{u} Z(\mathbf{r} - \mathbf{u})\Delta(\mathbf{u}), \qquad (2.78)$$

where $Z(\mathbf{r} - \mathbf{u})$ denotes the strength and range of the (linear) charge carrier-continuum, i.e., charge carrier-phonon, interaction. For a further simplification, self-trapping is treated in the limit of large atomic masses meaning that atoms are regarded as infinitely massive while the medium's stiffness remains finite. The kinetic energy of the atoms can then be neglected and polaron motion is suppressed.

Within these approximations, the adiabatic energy of the system V_{ad} is the sum of the charge carrier's energy W_{n}, which is a function of the dilation Δ, and the strain

energy of the continuum [77]

$$V_{\mathrm{ad}} = W_{\mathrm{n}} + V_{\mathrm{strain}} \quad \text{with} \quad V_{\mathrm{strain}} = \frac{\zeta}{2} \int \mathrm{d}\mathbf{u}\Delta^2(\mathbf{u}), \tag{2.79}$$

where ζ denotes the continuum's stiffness constant. The potential energy of the system is schematically depicted in Fig. 2.11. The strain energy of the continuum without additional charge carrier is a quadratic function of the deformation with its minimum at zero dilation Δ (grey). The charge carrier's potential energy decreases linearly with increasing deformation (blue). The net potential energy (black) has a minimum at the new equilibrium deformation Δ_{eq}, which is called polaron/self-trapped exciton binding energy E_{B}. The lowering of the electronic/excitonic potential energy is twice the binding energy. This result will later be of importance dealing with polaronic optical absorption.
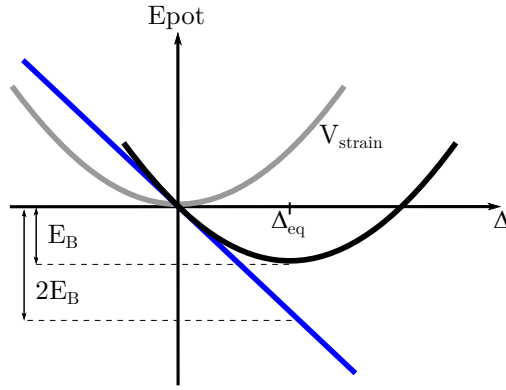
Figure 2.11 – Net potential energy of a polaron/self-trapped exciton (black) and its contributions from strain energy (grey) and linear charge carrier/exciton-lattice interaction (blue). A net minimum energy E_{B} is found for an equilibrium deformation Δ_{eq}.

For a more concrete description of self-trapping in a deformable continuum as a result of different charge carrier-lattice interactions, the adiabatic energy can be calculated in a semi-classical approach. The charge carrier's energy W_{n} is the expectation value of the electronic Hamiltonian

$$H_{\mathrm{e}} = -\frac{\hbar^2}{2m}\nabla_r^2 + \int \mathrm{d}\mathbf{u}Z(\mathbf{r} - \mathbf{u})\Delta(\mathbf{u}), \tag{2.80}$$

where the first term gives the kinetic energy and the second term the potential defined in Eq. (2.78). Calculating the electronic ground state means finding the equilibrium dilation $\Delta_{\mathrm{eq}}(\mathbf{u})$, which minimizes the system's adiabatic energy

$$\frac{\partial V_{\mathrm{strain}}}{\partial \Delta(\mathbf{u})} + \frac{\partial W_{\mathrm{n}}}{\partial \Delta(\mathbf{u})} = \frac{\partial}{\partial \Delta(\mathbf{u})}\frac{\zeta}{2}\int \mathrm{d}\mathbf{u}\Delta^2(\mathbf{u}) + \langle \psi_n(\mathbf{r},\Delta(\mathbf{u})) \left| \frac{\partial H_{\mathrm{e}}}{\partial \Delta(\mathbf{u})} \right| \psi_n(\mathbf{r},\Delta(\mathbf{u})) \rangle$$

$$= \zeta\Delta(\mathbf{u}) + \int \mathrm{d}\mathbf{r}|\psi_n(\mathbf{r},\Delta(\mathbf{u}))|^2 Z(\mathbf{r} - \mathbf{u}) = 0. \tag{2.81}$$

The equilibrium deformation thus depends on the magnitude of the charge carrier-phonon coupling, the stiffness constant, and the spatial extent of the self-trapped charge carrier

$$\Delta_{\text{eq}}(\mathbf{u}) = -\frac{1}{\zeta} \int d\mathbf{r} \, |\psi_n(\mathbf{r}, \Delta_{\text{eq}}(\mathbf{u}))|^2 \, Z(\mathbf{r} - \mathbf{u}). \tag{2.82}$$

Inserting this expression into the electronic Hamiltonian gives the nonlinear eigenvalue equation

$$\left[-\frac{\hbar^2}{2m} \nabla_r^2 - \frac{1}{\zeta} \int d\mathbf{r}' \, |\psi_n(\mathbf{r}')|^2 \int d\mathbf{u} Z(\mathbf{r} - \mathbf{u}) \, Z(\mathbf{r}' - \mathbf{u}) \right] \psi_n(\mathbf{r}) = W_n \psi_n(\mathbf{r}) \tag{2.83}$$

with the ground state's electronic energy

$$\begin{aligned}
W_n &= \frac{\hbar^2}{2m} \int d\mathbf{r} \, |\nabla_r \psi_n(\mathbf{r})|^2 + V_{\text{int}} \\
&= \frac{\hbar^2}{2m} \int d\mathbf{r} \, |\nabla_r \psi_n(\mathbf{r})|^2 - \frac{1}{\zeta} \int d\mathbf{r} \, |\psi_n(\mathbf{r})|^2 \int d\mathbf{r}' \, |\psi_n(\mathbf{r}')|^2 \int d\mathbf{u} Z(\mathbf{r} - \mathbf{u}) \, Z(\mathbf{r}' - \mathbf{u}).
\end{aligned} \tag{2.84}$$

To produce the equilibrium deformation the strain energy

$$V_{\text{strain}} = \frac{\zeta}{2} \int d\mathbf{u} \Delta_{\text{eq}}^2(\mathbf{u}) = \frac{1}{2} V_{\text{int}} \tag{2.85}$$

had to be invested, which is half the charge carrier's potential energy. Combining these two contributions the minimum of the adiabatic energy reads

$$V_{\text{ad}}^{\text{min}} = \frac{\hbar^2}{2m} \int d\mathbf{r} \, |\nabla_r \psi_n(\mathbf{r})|^2 - \int d\mathbf{r} \, |\psi_n(\mathbf{r})|^2 \int d\mathbf{r}' \, |\psi_n(\mathbf{r}')|^2 \, I(\mathbf{r}, \mathbf{r}'). \tag{2.86}$$

The second term is the net polaron binding energy, which has been denoted with E_{B} in Fig. 2.11. From Eqs. (2.84) and (2.85) again follows that the lowering of the electronic energy is twice the net polaron binding energy. The general expression for the charge carrier-phonon interaction $I(\mathbf{r}, \mathbf{r}') = \frac{1}{2\zeta} \int d\mathbf{u} Z(\mathbf{r} - \mathbf{u}) Z(\mathbf{r}' - \mathbf{u})$ will now be specified for typical long- and short-range interactions.

Ionic displacements in response to an additional charge carrier placed in a deformable continuum lead to a (Fröhlich) long-range charge carrier-phonon interaction of the form

$$I_{\text{LR}}(\mathbf{r}, \mathbf{r}') = \left(\frac{1}{\epsilon_\infty} - \frac{1}{\epsilon_0} \right) \frac{e^2}{2|\mathbf{r} - \mathbf{r}'|}, \tag{2.87}$$

where ϵ_0 and ϵ_∞ denote the static and high-frequency dielectric constants of the medium. The dc polarization of a material given by displacement of ions and electrons is proportional to $1 - 1/\epsilon_0$. As only the electrons are fast enough to follow electric fields oscillating at high frequencies, the optical polarization proportional to $1 - 1/\epsilon_\infty$ only considers the

electronic contribution. The prefactor $1/\epsilon_\infty - 1/\epsilon_0$ thus gives the dielectric polarization energy due to ionic displacements. The ratio of the dielectric constants $\epsilon_0/\epsilon_\infty$ therefore determines the strength of a long-range contribution to the charge carrier-phonon interaction. Whereas the long-range interaction is very small in covalent materials ($\epsilon_0 \approx \epsilon_\infty$) it is pronounced in ferroelectric and polar materials. In perovskite-like materials, e.g., lithium niobate, often having unusually displaceable ions $\epsilon_0 \gg \epsilon_\infty$. In contrast to charge carriers excitons can be approximately regarded as neutral particles. They are thus often described exhibiting negligible long-range interaction. However, this is not generally true. If the effective masses of the hole and the electron largely differ, they do not fully screen each other and a long-range interaction is observed. The heavier mass then determines whether the exciton resembles a hole or an electron polaron.

Short range charge carrier-phonon interaction is not limited to polar or ionic media or a net charge of the quasi-particle. It appears when strain at the charge carrier's site changes its energy. Being a contact interaction it has the form

$$I_{\mathrm{SR}}(\mathbf{r},\mathbf{r}') = \frac{F^2}{2\zeta}\delta(\mathbf{r} - \mathbf{r}'), \tag{2.88}$$

where F is a constant having the dimension of a force. Acoustic as well as optical phonons contribute to the short-range interaction [78–80].

In the general case, a charge carrier exhibits a short- and long-range interaction with the continuum. The minimum adiabatic energy of Eq. (2.86) then reads

$$
\begin{aligned}
V_{\mathrm{ad}}^{\mathrm{min}} =& \frac{\hbar^2}{2m} \int \mathrm{d}\mathbf{r}\, |\nabla_r \psi_n(\mathbf{r})|^2 \\
&- \frac{e^2}{2}\left(\frac{1}{\epsilon_\infty} - \frac{1}{\epsilon_0}\right) \int \mathrm{d}\mathbf{r} \int \mathrm{d}\mathbf{r}' \frac{|\psi_n(\mathbf{r})|^2 |\psi_n(\mathbf{r}')|^2}{|\mathbf{r} - \mathbf{r}'|} - \frac{F^2}{2\zeta} \int \mathrm{d}\mathbf{r}\, |\psi_n(\mathbf{r})|^4 .
\end{aligned}
\tag{2.89}
$$

Here, a cross term between the short- and long-range interaction, describing the long-range interaction at the position of the charge carrier, has been omitted [77] as its contribution is usually small [81].

Instead of finding an explicit solution for the wave function of the self-trapped charge carrier, Emin and Holstein introduced a scaling approach to qualitatively investigate self-trapping in presence of linear long- and short-range interactions [77]. In detail, they replaced $\mathbf{r}$ by $\mathbf{r}/L$ and $\psi_n(\mathbf{r})$ by $L^{-d/2}\psi_n(\mathbf{r}/L)$, where d is the dimensionality of the charge carrier. Changing the extension of the wave function $\psi(\mathbf{r})$ will increase the total energy, as the energy of Eq. (2.89) is by construction already the minimum energy of the system. The minimum will thus again be obtained for $L = 1$. A large value $L \to \infty$ corresponds to a free charge carrier/exciton. Small values in contrast $L \to 0$ denote a severely localized state. Now, the adiabatic energy of Eq. (2.89) can be investigated as a function of charge carrier localization L

$$E(L) = \frac{T_{\mathrm{e}}}{L^2} - \frac{V_{\mathrm{L}}}{L} - \frac{V_{\mathrm{SR}}}{L^d}, \tag{2.90}$$

where T_e, V_L, and V_{SR} are the three contributions to Eq. (2.89). Obviously, the energy $E(L)$ is largely influenced by the dimensionality of the system d. Here, only the three-dimensional case $d = 3$ will be studied. The peculiarities of one- and two-dimensional systems are discussed in [73, 74, 76]. To study the effect of the long- and short-range interaction on the localization of a charge carrier in a three-dimensional continuum, three different cases can be distinguished. First, allowing only a long-range interaction ($V_{SR} = 0$), the energy functional has a single minimum at a finite radius, which is called *large polaron* (cf. Fig. 2.12 (a)).
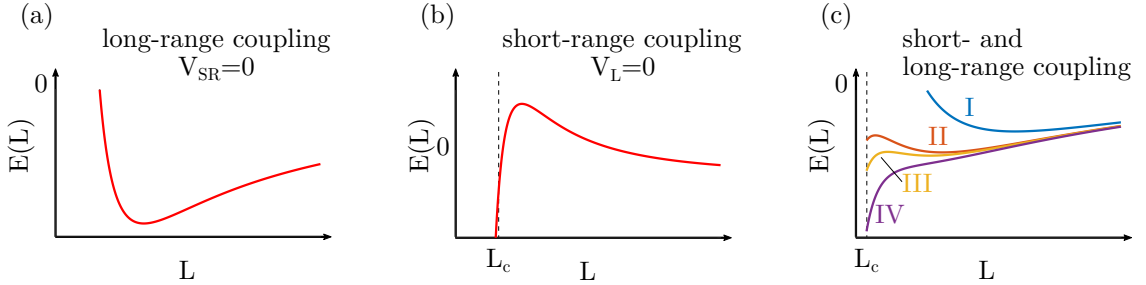

Figure 2.12 – Adiabatic energy of a charge carrier/exciton as a function of wave function localization L for **(a)** long-range coupling, **(b)** short-range coupling, and **(c)** combined coupling of both interactions with different strength ratio. The expression for the adiabatic energy is given by Eq. (2.90). The three dimensional case ($d = 3$) is considered.

If in contrast only a short-range interaction is present ($V_L = 0$) two minima for $L \to \infty$ and $L \to 0$ are found, which are separated by an energy barrier (cf. Fig. 2.12 (b)). The charge carrier can thus either remain free or collapse into a severely localized state. The barrier between these minima is called barrier to self-trapping. It means that a minimum distortion of the lattice is needed to create a potential well sufficiently high to commence self-trapping [80]. It is responsible for delayed small polaron formation times [82]. Other than indicated by the adiabatic continuum model, the polaron or self-trapped exciton radius cannot shrink to infinitely small values. The collapse stops when the potential well, in which the charge carrier is trapped, reaches the size of atomic distances. This is indicated in Fig. 2.12 (b) and (c) by the cut-off value L_c. The quasi-particle with the energy $E(L_c)$ is then called small polaron or self-trapped exciton.

In the more general case of simultaneous long- and short-range interaction the appearance of energetic minima largely depends on the relative strength of the two contributions (cf. Fig. 2.12 (c)). Starting from a situation where the short-range interaction is negligible, again a large polaron minimum is observed (I). If now the strength of the short-range interaction is increased (II), an additional meta-stable small polaron minimum occurs at $L = L_c$, which is stabilized for further increased short-range interaction (III). A pronounced short-range interaction can lead to a stable small polaron state without any energy barrier to self-trapping and the large polaron minimum disappears (IV). It can thus be seen that a considerable short-range contribution is mandatory for small polaron/self-trapped exciton formation. However, a long-range interaction - if not too strong - facilitates the collapse to a single site.

2.3.2 Absorption and emission spectra in presence of strong charge carrier-/ exciton-phonon coupling

Absorption and emission features of charge carriers and excitons coupling to phonon modes with different coupling strengths has been studied extensively by Yutaka Toyozawa in the last 60 years. A few of the results, which are described in detail in his book [76], are summarized in this subsection. Polaronic absorption, which is related to photon-induced hopping, is again reviewed based on the findings by David Emin [73].
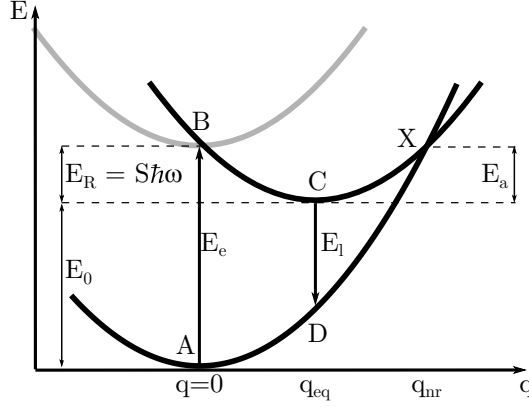
Figure 2.13 – Configuration coordinate model of an excitation with linear coupling to the lattice. Absorption of a photon with the energy E_e leads to a Franck-Condon transition from the ground state (A) to an excited state (B). The excited system relaxes by the energy E_R to the upper black energy sheet with the new equilibrium configuration q_{eq}. From the minimum (C) the residual added energy can be dissipated via photon (C to D) or thermally activated via phonon emission (X to A).

Generation and recombination of electron-hole pairs with strong coupling to the lattice can be described using the configuration coordinate model [76, 83]. Figure 2.13 shows the energy of a deformable medium as a function of the configuration coordinate q, which is basically the deformation parameter Δ used before. The lower curve depicts the energy of the ground state with its minimum (A) at zero deformation $q = 0$. The upper grey curve is the energy of the deformable medium after excitation of an electron-hole pair, but without the response of the medium in form of a relaxation. The grey curve is therefore equivalent to the grey curve in Fig. 2.11. The excitation without changing the configuration coordinate, i.e., a Franck-Condon transition from point A to B, requires the excitation energy E_e. As in Fig. 2.11 the system rapidly relaxes via phonon emission to the energy curve depicted by the upper black curve. The minimum of the excited state (C) appears lowered by the relaxation energy E_R and at a new equilibrium deformation q_{eq}. The electron-hole pair now has become a pair of oppositely-charged polarons or a self-trapped exciton.

From the minimum at (C) the system can return to the ground state via emission of a photon with the energy E_l (Franck-Condon transition from C to D) and subsequent emission of phonons (D to A). The crossing point X of the upper and lower curve offers a

second, non-radiative recombination channel. The excitation energy is dissipated solely via emission of phonons. For this to happen enough thermal energy has to be present to produce a transient deformation of the lattice q_{nr} enabling to surpass the energy barrier E_a. Obviously, the strength of the charge carrier lattice interaction determines the lattice relaxation (cf. Eq. (2.91)) and therefore the energy barrier for non-radiative relaxation. The stronger the relaxation the smaller the energy barrier and the more probable non-radiative transitions become. In this way, the configuration-coordinate model explains qualitatively why some localized centers show luminescence and some do not [83]. In fact, luminescence is quenched if the point B lies above the crossing point X. This is the case when the ratio $\Lambda = E_R/E_e$ is $> 1/4$ [84], which follows from simple calculations. Figure 2.13 shows the situation where $\Lambda = 1/4$ and radiative as well as non-radiative relaxations are both possible.

The shape of the absorption feature is also determined by the charge carrier lattice interaction. According to Toyozawa [76], the influence of the charge carrier-phonon coupling on the vibrational structure in the absorption spectra can be exemplified treating the nuclear motions quantum mechanically as one-dimensional harmonic oscillators at $T = 0\,\mathrm{K}$, where only the lowest vibrational state is populated. Figure 2.14 (a) depicts the same situation as Fig. 2.13 adding the vibrational states. The intensity of the vibra-
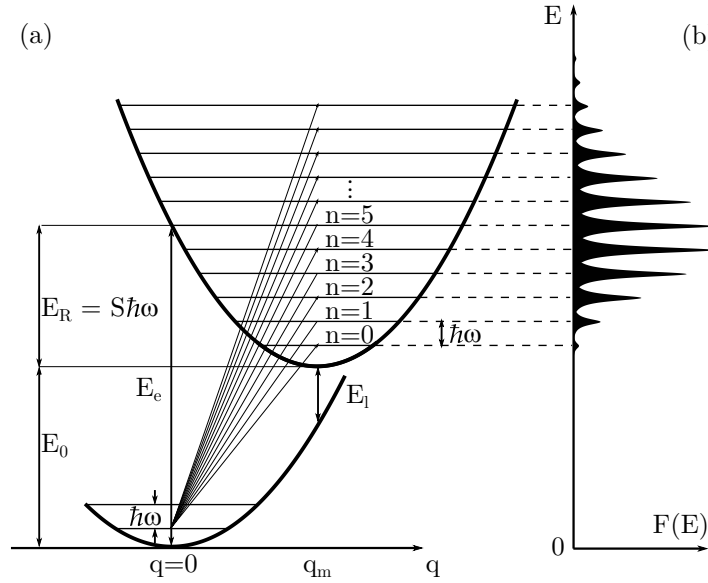
Figure 2.14 – **(a)** Configuration Coordinate model for a one-dimensional harmonic oscillation linearly coupled to a charge carrier following [76]. **(b)** Normalized absorption spectrum. The spectral lines are schematically depicted with homogeneous broadening.

tional absorption lines (Fig. 2.14 (b)) caused by transitions from the vibrational ground state to an excited state n follows a Poisson distribution

$$I_n = \exp(-S)\frac{S^n}{n!} \quad \text{with} \quad S = \frac{E_R}{\hbar\omega}, \tag{2.91}$$

where S measures the coupling strength and ω is the frequency of the coupling phonon

mode. This distribution is depicted in Fig. 2.15 for different coupling strength values. For weak coupling ($S \leq 1$, figure part (a)) mainly transitions with zero or one phonon(s) involved are observed. With increasing coupling strength more and more lines with higher n appear and the zero-phonon line decreases. In the strong-coupling regime $S \geq 20$ [85] the envelope of the distribution is given by a Gaussian function (cf. Fig. 2.15 (c)). The mean value of the distribution $\langle n \rangle$ given by Eq. (2.91) is found to be equal to S and the mean absorption energy is then $\langle E \rangle = E_0 + \langle n \rangle \hbar\omega = E_0 + E_{\mathrm{R}} = E_{\mathrm{e}}$.
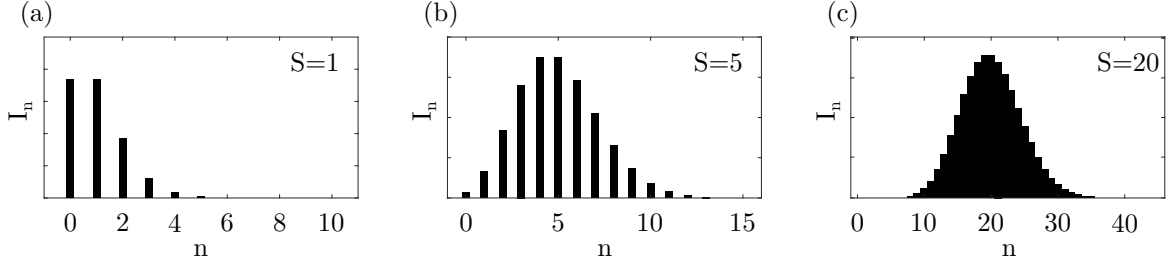
Figure 2.15 – Intensity distribution of the vibrational absorption lines at $T = 0\,\mathrm{K}$ given by Eq. (2.91) for different coupling strength values S.

From Eq. (2.91) follows that the normalized absorption spectrum is

$$F(E) = \exp(-S) \sum_n \frac{S^n}{n!} \delta(E_0 + n\hbar\omega - E). \qquad (2.92)$$

However, even at $T = 0\,\mathrm{K}$ the absorption lines are not perfectly sharp but homogeneously broadened (cf. Fig. 2.14 (b)). For high temperatures and strong coupling the absorption lines hence merge into a structureless Gaussian absorption band. The derivation of the absorption feature in three dimensions, although much more complicated, leads to the same result for strong coupling. The absorption spectrum is then given by a Gaussian function [76]

$$F(E) = \frac{1}{\sqrt{2\pi D^2}} \exp\left(-\frac{(E - E_{\mathrm{e}})^2}{2D^2}\right) \quad \text{with} \quad D^2 = 2E_{\mathrm{R}} k_{\mathrm{B}} T. \qquad (2.93)$$

The shape of the emission spectrum for the transition C to D is again determined by the charge carrier lattice interaction and is derived in a similar manner to be

$$G(E) \propto E^3 \exp\left(-\frac{(E - E_{\mathrm{l}})^2}{2D^2}\right) \quad \text{with} \quad E_{\mathrm{l}} = E_{\mathrm{e}} - 2E_{\mathrm{R}}. \qquad (2.94)$$

Apart from the factor E^3 it has also a Gaussian shape with the same width parameter D as the absorption spectrum, but is shifted by the Stoke's shift $2E_{\mathrm{R}} = 2S\hbar\omega$.

It should be mentioned that the symmetric Gaussian shape is a consequence of linear charge carrier-phonon interaction and harmonic potential approximation. For nonlinear electron-phonon coupling considerably skewed band shapes are observed [86]. Suzuki *et al.* extended the approach to quadratic coupling ultimately leading to asymmetric bands,

which are of Gaussian shape on the high energy side but have an increased low-energy tail [87].

Luminescence emitted from recombination of excitons, self-trapped excitons, and oppositely-charged small polarons differ in their energy. Excitonic luminescence has the highest energy and the shortest lifetime because of the strong overlap of the electron and the hole. Due to the relaxation of the lattice, self-trapped exciton luminescence appears more red-shifted. The recombination is considerably slower as the self-trapping barrier has to be surpassed. Geminate small polaron recombination tends to be the slowest process with the lowest energy as the overlap is relatively weak [73].
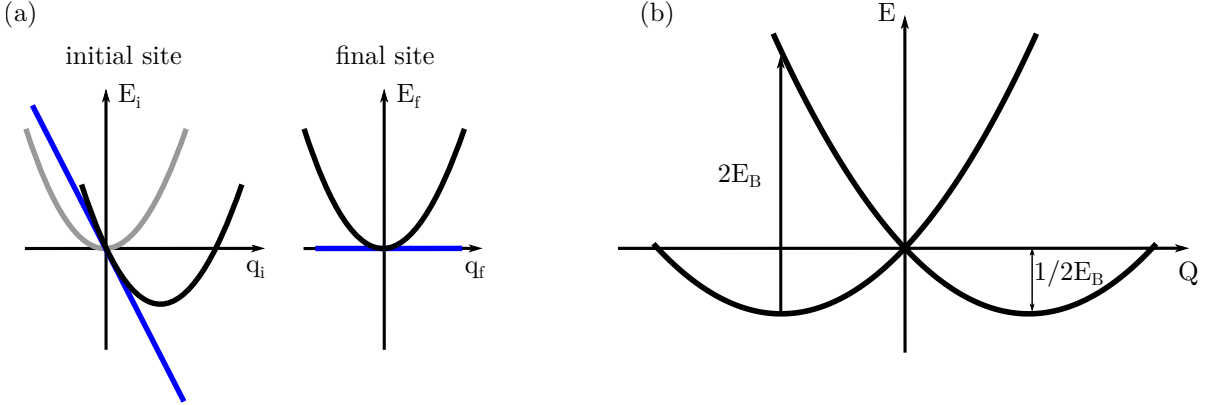
Figure 2.16 – **(a)** Potential energy of a polaron/self-trapped exciton located at the initial site (left) and of an initially unoccupied site (right). **(b)** Symmetrized representation of the left panel emphasizing the equivalence of a polaron located at the two different sites.

The absorption and luminescence features described so far reflect excitation and recombination from and to the ground state, respectively. However, small polarons and self-trapped excitons already formed exhibit absorption features, which are related to *photon-assisted hopping*. These absorption processes are essentially excitations of the self-trapped charge carrier or exciton constituent from their localized state at one site q_i to a localized state at an equivalent neighboring final site q_f [37, 43, 73]. The energies of the involved sites are depicted in Fig. 2.16 (a). Whereas the strain energy equals for both sites, the electronic energy (blue) is zero for the initially unoccupied final site. After the transition the potential energies at the final and initial sites are interchanged. As now two sites are involved, a description as in Fig. 2.14 using the configuration coordinate of one site would yield misleading results. Instead, the site-centered coordinates q_i and q_f are transformed to new coordinates, which highlight the equivalence of the initial and final sites [37, 43]

$$Q = q_i - q_f \quad \text{and} \quad q_s = q_i + q_f. \tag{2.95}$$

The resulting potential sheets in this symmetrized representation are depicted in Fig. 2.16 (b). Using the nomenclature of Figs. 2.13 and 2.14 the relaxation energy is now $E_R = 2E_B$. The absorption spectrum according to Eq. 2.93 but based on photon-induced

hopping therefore reads [43, 88]

$$F_{\text{hop}}(E) = \frac{1}{\sqrt{2\pi D^2}}\exp\left(-\frac{(E - 2E_{\text{B}})^2}{2D^2}\right) \quad \text{with} \quad D^2 = 4E_{\text{B}}k_{\text{B}}T. \tag{2.96}$$

Another argument explaining the peak energy of the absorption spectrum has already been given in Fig. 2.11 and Eq. (2.85). The electronic part of the polaron binding energy is $2E_{\text{B}}$. To liberate the charge carrier from its fixed potential well thus requires twice the polaron binding energy. Since the strain energy at the final site after the hop will be the same as at the initial site before the transition, no net energy changing the strain has to be invested.

Figure 2.16 (b) additionally suggests that photon-induced polaron hopping does not lead to emission of luminescence. This is also clear from the criterion introduced earlier: since the final state is again a relaxed polaron/self-trapped exciton, the ratio of the excitation and relaxation energy equals 1 [43]. Luminescence as a process to dissipate the added energy is fully suppressed.

2.3.3 Semiclassical hopping transport and small polaron recombination

Softening the condition of infinitely massed atoms allows a self-trapped quasi-particle's thermally-induced motion. In contrast to free or weakly coupling charge carriers/ excitons, small polaron and self-trapped exciton transport is incoherent. The following subsection dealing with incoherent small polaron and self-trapped exciton transport, which is called *hopping transport*, follows the elaborate description by David Emin and his book *Polarons* [73]. It generalizes the molecular crystal model by Holstein [79, 89]. The atomic movement is thereby treated as classical. Again, polarons and self-trapped excitons are not distinguished. However, it should be noted that in case of small polaron transport a real charge transport is observed. In case of (self-trapped) excitons only excitation energy propagates through the medium.

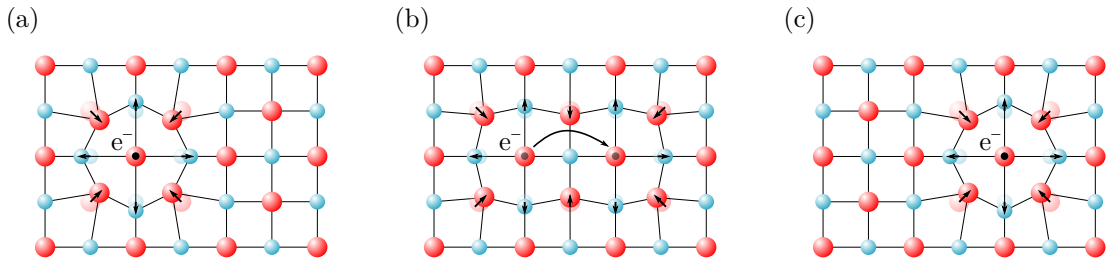**Figure 2.17** – Schematic representation of a small polaron hop. **(a)** A small polaron located at an initial site. **(b)** At a coincidence event large (thermal) fluctuations of the atomic displacements create an energetic environment being equal at the initial and final sites. The electron at the initial site is halfway liberated from its self-trapped state. **(c)** After a hop to the final site the large displacements relax.

Self-trapped charge carriers can only move through a crystal by hopping from one site to another. As they are trapped in a potential well formed by a self-induced lattice distortion, they cannot move 'on their own volition'. Instead, the atomic displacement forming the potential well, in which the charge carrier is trapped, has to move as well. Basically, a small polaron hop can be described by a three step process (cf. Fig. 2.17). Large fluctuations of the atoms positions occur near the self-trapped charge carrier creating an energetic environment, which enables the carrier to move to another site. The large displacement then relaxes and the energy is dissipated to the surrounding lattice. The polaron is now located at the adjacent site. At elevated temperatures this is naturally the case due to the thermal vibration of the system. The hopping occurs via absorption and emission of (multiple) phonons and is thus called phonon-assisted hopping.

In detail, the atomic displacement pattern has to change in such way that the potential wells at the initial site, where the polaron is located, and the final site are equal. This situation is called *coincidence event* [79]. The minimum energy needed for such an coincidence lifts the electrons energy approximately halfway to liberation from the self-trapped state and simultaneously creates a potential well with the same energy at the final site. If this energy is larger than the electronic transfer energy t, the following electronic motion will be incoherent. Two different hopping types are found, which differ in whether the electron moves rapidly enough to follow the atomic motion or not. The latter is called non-adiabatic hopping. In this case the hopping rate is determined by the velocity, with which the electron moves between the sites, and the time, in which the coincidence event is present given by the vibration frequency.
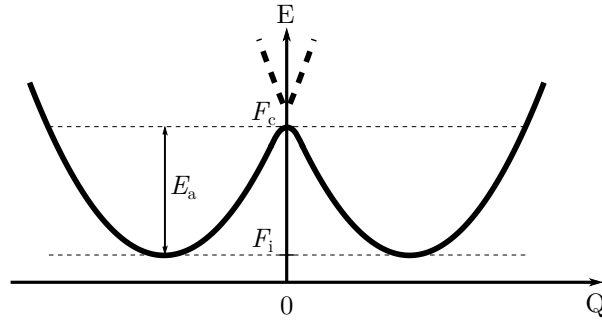
Figure 2.18 – Two-side adiabatic potential plotted against the relative atomic displacements $Q = q_i - q_f$, where q_i and q_f are the displacements at the initial and final sites, respectively. The free energy of the system with the polaron at the initial site is F_i. During the coincidence event, where the atomic displacements are equal ($Q = 0$), the free energy is F_c. The activation energy for a thermally induced hop is E_a.

However, usually the charge carrier is able to follow the atomic motion and hopping transport is adiabatic [73]. The two-side adiabatic potential is plotted in Fig. 2.18, which is essentially equal to Fig. 2.16 (b). The left potential well relates to a carrier occupying the initial site. The right one then corresponds to the carrier being trapped at the final site. An adiabatic hop can now be described by a trajectory of a fictitious

particle moving from the initial to the final site on this potential curve. The maximum at $q_i - q_f = 0$ corresponds to the coincidence event. This barrier has to be surpassed for an adiabatic hop to occur and the high-temperature hopping rate between equivalent sites is then given by [90]

$$R(T) = \nu \, W_t(1,2) \exp\left(-\frac{F_c - F_i}{k_B T}\right) \tag{2.97}$$

with the vibration frequency ν. $W_t(1,2)$ is the probability that the charge carrier avails itself of the opportunity to hop during a coincidence event. In the non-adiabatic case this probability is very small [79]. In the adiabatic limit, however, it is approximately one [75, 79] provided that the atomic relaxation is fast enough to prevent the charge carrier/exciton from hopping back. Otherwise it will shuttle back and forth between the initial and final sites until the lattice relaxes. The probability then reduces to one half [91, 92]. The system's free energy with a polaron at the initial site is

$$F_i = \left(\frac{T_e}{R_i^2} - \frac{V_{SR}}{R_i^3} - \frac{V_L}{R_i}\right) + f_i, \tag{2.98}$$

which is basically Eq. (2.90) with renamed extension parameter $R = L$ indicating the polaron radius. The additional contribution f_i rises from the softened condition of infinitely massed atoms and is the free energy of the atoms oscillating about the displaced equilibrium positions. The system's free energy at the coincidence event with minimum energy is [81]

$$F_c = \left(\frac{T_e}{R_c^2} - \frac{V_{SR}}{2R_c^3} - \frac{V_L}{2}\left(\frac{1}{R_c} + \frac{1}{s}\right)\right) - |t(s)| + f_c. \tag{2.99}$$

Here, s is the separation of the two sites. Note that the fact that the charge carrier at the coincidence event is shared between the two sites [81] is considered by the factors 1/2 occurring in the contributions of the charge carrier-phonon coupling. For the same reason the confinement energy is lowered by the transfer energy $t(s)$. Using the expressions Eqs. (2.98) and (2.99) the adiabatic hopping rate for elevated temperatures is given by

$$R(T) = \nu \exp\left(\frac{f_i - f_c}{k_B T}\right) \exp\left(-\frac{E_a}{k_B T}\right) \tag{2.100}$$

with the activation energy

$$E_a = T_e\left(\frac{1}{R_c^2} - \frac{1}{R_i^2}\right) - V_{SR}\left(\frac{1}{2R_c^3} - \frac{1}{R_i^3}\right) - V_L\left(\frac{1}{2R_c} + \frac{1}{2s} - \frac{1}{R_i}\right) - |t(s)|. \tag{2.101}$$

Usually the radii at the initial site and the coincidence event are assumed to be equal $R_i = R_c = R$, simplifying the action energy to

$$E_a \approx \frac{V_{SR}}{2R^3} + \frac{V_L}{2}\left(\frac{1}{R} - \frac{1}{s}\right) - |t(s)|. \tag{2.102}$$

The contribution of the transfer energy $t(s)$ can also often be neglected [90]. Obviously, in case of vanishing long-range interaction and large separations $s \gg R$, the activation energy is half the polaron binding energy.

The free energies of atomic vibrations $f_{i,c}$ in Eq. (2.100) associated with vibrations about the displaced equilibrium positions in the initial state and the coincidence configuration are generally not equal. The stiffness constant is usually decreased by the charge carrier moving in response to the atomic vibration since the charge carrier's wave function changes [81]. This reduces the vibration's free energy. As the carrier changes sites, this carrier-induced softening/energy lowering is especially large at the coincidence event [90]. It can be shown that the factor in Eq. (2.100) considering the change of free energy can be expressed as $\Delta f / k_B T = (E_a + t)/t$ leading to the adiabatic hopping rate [73, 90]

$$R(T) \cong \nu \exp\left(\frac{E_a}{t}\right) \exp\left(-\frac{E_a}{k_B T}\right). \tag{2.103}$$

At elevated temperatures, the phonon-assisted hopping rate of small polarons and self-trapped excitons thus follow an Arrhenius behavior with an activation energy E_a. In the case of equivalent sites this energy is essentially half the polaron binding energy. The concept can however be extended to inequivalent sites [93].

If the temperature is reduced, less and less phonons are available for an assisted jump. In this so-called multiphonon-freezeout regime the temperature dependent hopping rate then starts to deviate from the Arrhenius behavior and can be described by

$$R(T) \cong \nu \exp\left(-\left(\frac{2E_b}{h\nu}\right) \tanh\left(\frac{h\nu}{4k_B T}\right)\right). \tag{2.104}$$

Here, a more and more significant contribution to the coincidence event is given by atomic tunneling processes. These tunneling processes should not be confused with a tunneling transport of atoms through the crystal. The atoms move from their equilibrium position via tunneling eventually establishing a distortion pattern at the final site, which corresponds to the displacement needed for polaron formation. The electron then gets trapped at the new site and the atomic displacements of the former unoccupied site tunnel to the formerly occupied one. This process is much slower and temperature independent. With decreasing temperature the hopping rate hence starts to deviate from the Arrhenius behavior to lower rates until a temperature-independent hopping rate is found for low temperatures.

In Eq. (2.97) the pre-exponential factor ν has been called vibration frequency. In the adiabatic limit, where the charge carrier can follow atomic motion, the high temperature hopping rate indeed tends to the vibration frequency of the atoms. In case the charge carrier couples to a single phonon mode, ν can be identified with the phonon frequency. However, charge carriers - especially with strong interaction with the lattice - couple to various phonon modes. The frequency factor is then an average of different vibration frequencies weighted with their contribution to the activation energy [94]. It should be

noted that the statements above are true if the relaxation of the lattice is not too slow and the polaron hops are independent from each other. In some cases the relaxation of the lattice appears to be too slow to prevent a polaron from hopping back or even to further sites within a single coincidence event. The frequency factor is then smaller than a typical phonon frequency and the polaron hops are correlated [91].
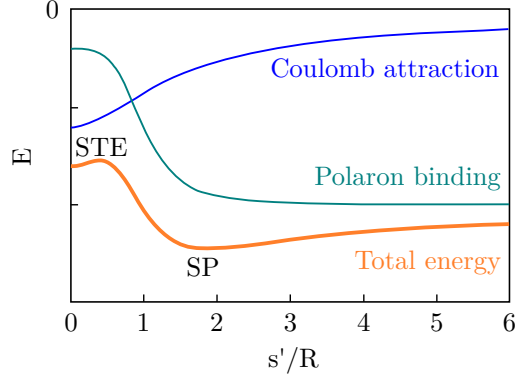
Figure 2.19 – Energy of two oppositely-charged small polarons as a function of their distance s'. The total energy is the sum of Coulomb attraction and polaron binding energy, which is repulsive for smaller separations. The total energy exhibits a minimum for finite separation of the two polarons (SP). A shallow, metastable minimum is found for zero separation denoting a self-trapped exciton state (STE). Redrawn from [73].

Small polarons are often generated via excitation with super-bandgap photons. An electron-hole-pair is induced, which can then relax into oppositely-charged polarons. As the polarons interact with each other via Coulomb attraction and indirectly via interference of their induced distortion patterns, the energy of the polarons depends on their separation s' (not to be confused with the hopping distance s). In contrast to the Coulomb attraction the indirect interaction is repulsive [75,95] as the charge carriers compete to displace the atoms in different directions. This destructive interference of the displacement pattern raises the net energy of the polarons as their separation is reduced (cf. Fig. 2.19). A minimum net energy is found for finite separation of the polarons with s' being larger than the polaron radius. The repulsion increases dramatically as the separation is on the order of the small polaron radius. For zero separation of the charges a shallow minimum is found, which is the self-trapped exciton state.

2.4 Lithium niobate

Lithium niobate ($LiNbO_3$, LN) is a prominent representative of perovskite-like oxide ferroelectrics and is known for its pronounced electro-optic and nonlinear optical properties [32]. Below the Curie-temperature, which lies between 1040–1200°C for different stoichiometries [96], its crystal structure has a trigonal space group R3c and the point group 3m. Distorted oxygen octahedra with oxygen planes aligned along the symmetry axis are a third filled with Li ions, Nb ions or are empty, respectively (cf. Fig. 2.20 (a)).

The stacking order in direction of the symmetry axis is ...Li-Nb-□...Li-Nb-□, where □ denotes an empty octahedron. The Li ions are shifted with respect to the oxygen planes along the symmetry axis, whereas the Nb ions are slightly shifted from the octahedra centers. This symmetry break induces as spontaneous polarization leading to the material's ferroelectricity. Commonly, the threefold symmetry axis is called z-axis, whereas the y-axis lies perpendicularly to the z-axis in the mirror plane. The x-axis is then chosen to be orthogonal to both of these axes. Whereas the z- and y-axes are polar, the x-axis is non-polar. The z-axis is additionally pyroelectric.
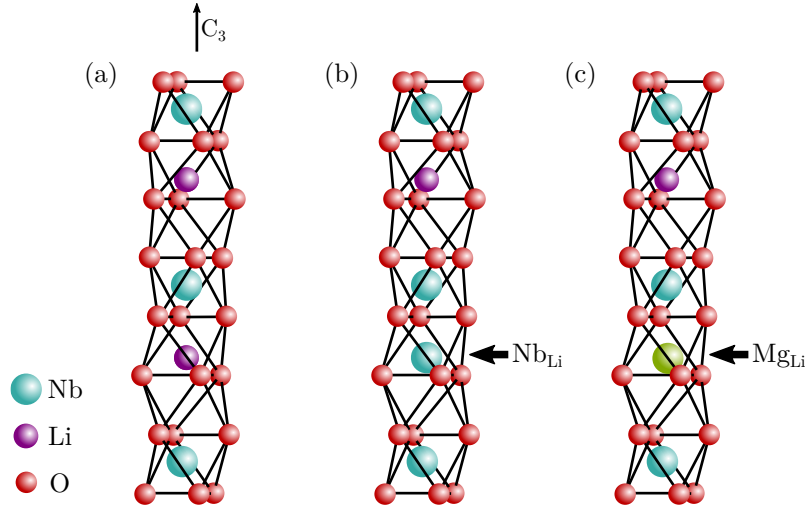
Figure 2.20 – Structure of lithium niobate with **(a)** regular stacking order, **(b)** isolated Nb_{Li} antisite, and **(c)** Mg_{Li} defect.

LN crystals are transparent in the spectral range from $0.32 - 5\mu m$ and negatively birefringent with a large refractive index ($n_o(\lambda = 633\,\text{nm})$= 2.286, $n_e(\lambda = 633\,\text{nm})$= 2.202 [97]). The chemically stable crystals have a high melting point at 1,255 °C.

Usually, LN crystals are grown via the Czochralski technique with a congruently melting composition ([Li]/[Li]+Nb] = 0.4845). Since in this case the solid crystal and the melt, from which it is pulled, have the same composition, the highest crystal quality is achieved. Stoichiometric samples, however, cannot be obtained from this preparation method. For this purpose, different alternative techniques have been developed. One of the them is a post-growth method called vapor transport equilibration (VTE), where crystals of congruent composition together with a powder with a Li concentration higher than in the crystal are placed in a Pt crucible and heated to temperatures above 1,000 °C [98]. Diffusion of Li then increases the [Li]/[Nb] ratio. Usually, this technique is limited to samples with only a few millimeters of thickness. Alternatively, crystals with near-stoichiometric composition can be grown with the top seeded solution growth method. Adding K_2O to the melt leads to the surprising result that near-stoichiometric crystals are obtained while the amount of K incorporated in the crystal is negligible [99]. A third alternative is the so-called double crucible Czochralski method, where the crystal is pulled from an inner crucible with a Li-rich melt connected with an outer crucible

containing a stoichiometric melt, which is automatically refilled [100].

As already mentioned above, usually LN crystals are grown by the Czochralski method leading to congruently melting compositions having a ratio [Li]/[Nb] = 0.94. This means that the crystal lattice contains a quite large concentration of intrinsic defects. In fact, one percent of the Li sites are occupied by Nb^{5+} ions (cf. Fig. 2.20 (b)). These Nb_{Li} defects, which are called antisite defects, are fourfold charged with respect to the regular Li^+ ion. The surplus charge is then compensated for by four percent of the Li sites being empty, which are then called Li vacancies V_{Li} [101]. It should be noted that the near-stoichiometric crystals still contain antisite defects at a small concentration.
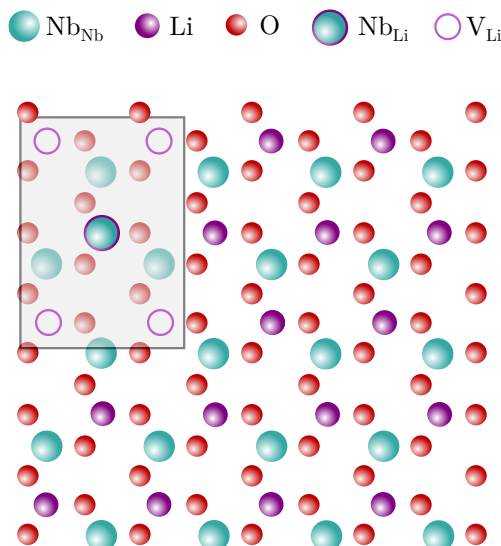
Figure 2.21 – Lithium niobate structure projected onto the (001) plane with one intrinsic Nb_{Li} antisite defect and four charge compensating V_{Li} vacancies.

In order to improve the optical stability of lithium niobate for applications, where high optical intensities are present, the crystals are doped with optical damage resistant impurity ions such as Mg [102], Zn [103, 104] or Hf [105, 106]. They are known to be incorporated on Li sites reducing the antisite defect concentration, which increases the photo-conductivity. Magnesium was the first dopant and is still the most prominent one. Iyi *et al.* studied the composition of Mg-doped crystals in detail and proposed a two step incorporation process [107]. First, Mg ions are incorporated on regular Li sites reducing the antisite concentration in the crystal and forming Mg_{Li} defects (cf. Fig. 2.20 (c)). Above a threshold value no antisite defects are observed anymore. From this point on further Mg ions replace Li ions and additional lithium vacancies are produced to compensate for the additional charge. Above a second threshold concentration Mg ions are also incorporated on regular Nb sites leading to Mg_{Nb} defect sites. The first threshold level is experimentally observed at about $5\,mol\%$ Mg in the melt.

Different properties of LN such as the optical response, i.e., blue/green-induced infrared absorption [108, 109], photorefraction [52], photoluminescence [58–62], etc., can be described in the framework of strong coupling polarons and excitons. The rich defect

structure of the crystals, which is very sensitive to growing techniques, parameters or post-growth treatments, largely influences the occurrence of different intrinsic small polaron and exciton species in the material. In antisite defect-free crystals, electrons are self-trapped at regular Nb ions, which are then called Nb_{Nb}^{4+} free polarons. In case of interband excitation of electrons, small hole polarons located at oxygen ions near a lithium vacancy (O^--V_{Li}) are formed. If antisite defects are present, the optical response is predominantly determined by electrons self-trapped at the defect sites, which are called Nb_{Li}^{4+} bound polarons. In chemically reduced crystals Nb_{Nb}^{4+}−Nb_{Li}^{4+} bipolarons are found. As typical for strong-coupling polarons, all of these transients show a broad asymmetric absorption peak.

Similar to the properties of small polarons, the photoluminescence of lithium niobate is very sensitive to crystal stoichiometry and doping and occurs on very different time scales. The fastest emission feature reported in literature is the rather weak green luminescence observed in congruent LN single crystals or Li-deficient LN powder. Its decay time is estimated to ≈ 80 ns at 5 K [59,110] and ≈ 50 ns at 70 K [111]. Having an excitation band near 305 nm its emission band peaks around 520 nm [59]. Based on the model of radiative recombination of self-trapped excitons located at NbO_6-octahedra, this fast decay was attributed to self-trapped excitons annihilating in octahedra near an antisite defect [58, 60–62]. In absence of antisite defects like in Li-enriched LN powder, a considerably more intense luminescence is observed with a decay time of $\approx 130 \mu$s. At 5 K this broad luminescence band peaks in the blue spectral range near 440 nm with an excitation spectrum around 260 nm. This photoluminescence band was attributed to self-trapped excitons in regular NbO_6 octahedra [59, 61]. A similar luminescence band is observed in crystals doped with magnesium above the photorefractive threshold eliminating antisite defects [110, 111] (see Fig. 2.22). As expected for phenomena based on strong-coupling transients, a pronounced shift of the peak position and a considerable broadening is observed, which is shown in section 4.1. The temperature dependence of this luminescence decay induced by ns and fs laser pulses will be discussed in chapter 4 as well. In 7 mol% Mg-doped LN crystals a second, much slower decay component has been observed [56, 57]. Its decay time is in the range of 0.2-2 s between 200 K and 100 K. The authors assigned the two decay components to geminate small polaron annihilation [56]. However, in chapter 4 experimental and mathematical results are presented, which indicate that this microscopic picture is inadequate. A way more detailed review of the luminescence properties of lithium niobate single crystals with different stoichiometries and dopings is given in section 4.4.

Figure 2.22 – Luminescence of an Mg-doped congruent LN crystal ($c_{Mg} = 6.5$ mol%) induced by intense ultrashort fs-laser pulses with a central wavelength of 400 nm. The crystal is cooled down to 10 K in a closed-cycle cryostat.

3 Broadband Femtosecond Fluorescence Upconversion Spectroscopy

In this chapter the new fluorescence upconversion spectroscopy (FLUPS) setup adapted for solid sample inspection, which is used and briefly described in section 5.2, is presented and characterized in detail. After a short introduction of this ultrafast measurement technique and an overview of the experimental setup, different crucial components are discussed. These are the custom-built Cassegrain reflector used for luminescence collection and the gate pulse front tilt. Finally, photometric and temporal correction procedures are presented. The first is an extension of an already introduced scheme and turns out to be very robust.

3.1 FLUPS Principle

A large number of experimental methods are available for the investigation of excited states. Most of them probe different properties of the induced transients. Time-resolved fluorescence measurements for example provide insight to radiative and/or non-radiative decay channels and are a powerful tool especially if absorption features are weak or lie outside of a conveniently detectable wavelength range. Evaluating kinetic traces and (time-dependent) spectral properties of the luminescence helps to find a proper microscopic model describing the structure and relaxation of the exited states.

Whereas a direct measurement of the luminescence kinetics is limited to time scales above 100 ps, i.e., the detection limit of modern electronics, different 'indirect' measurement techniques have been developed providing much better temporal resolutions (for an overview see Ref. [112]). Commonly, shorter kinetics in the ps time range are detected via time-correlated single photon counting [113–115] or Streak cameras. Although the latter can reach resolutions of a few hundred fs, laser pulse based pump-probe experiments are the techniques of choice in the sub-ps time range [112].

The highest temporal resolutions are achieved via fluorescence upconversion, which has been established over 40 years ago by Mahr and Hirsch [63]. The principle is schematically shown in Fig. 3.1. The fluorescence - excited by a short laser pulse - is superposed with a train of short laser pulses (gate pulses) in a nonlinear optical medium, where the sum(difference)-frequency of the input waves is generated. Trivially, upconversion only

occurs when the short gate pulse propagates through the nonlinear optical medium. In the ideal case the upconverted signal thus has approximately the same temporal shape as the gate pulse leading theoretically to a temporal resolution given by the gate pulse duration. In this way, a minimum temporal resolution of 40 fs has been achieved [116]. As the intensity of this sum-frequency pulse is proportional to the number of fluorescence photons involved in the upconversion process, the generated sum-frequency pulse train retraces the fluorescence kinetics (right panel of Fig. 3.1).
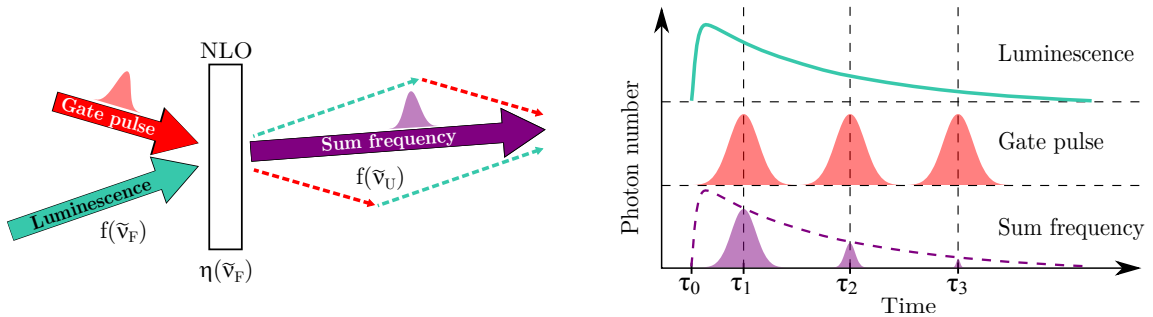
Figure 3.1 – Schematic picture of fluorescence upconversion. Fluorescence and gate pulses are superposed in a nonlinear optical medium, in which the sum-frequency of the incoming waves is generated. The intensity of the sum-frequency pulses is proportional to the number of fluorescence photons involved in the sum-frequency generation. A pulse train of gate pulses therefore retraces the fluorescence kinetics.

In the conventional scheme of such a fluorescence upconversion experiment fluorescence and gate pulse are superposed collinearly in a nonlinear optical crystal [63, 116–125]. Phase matching and therefore efficient sum-frequency generation (SFG) is achieved in a small fluorescence spectral bandwidth. The fluorescence spectrum is then obtained by tuning the crystal angle and reconstructing the spectra from the single kinetic traces via normalization. For this purpose, the kinetic traces are integrated and compared with the corresponding intensity values of the steady state fluorescence spectra [126, 127].

Meanwhile modifications of this technique enabling broadband detection have been introduced. For instance, upconverted spectra at fixed time delays are obtained rotating the crystal with a constant angular speed during the integration time of a CCD camera [128–132]. Alternatively, the phase matching condition is softened by using a very thin nonlinear optical crystal and a non-collinear SFG geometry. In these cases the conventional measuring routine is reversed: fluorescence spectra are recorded for fixed time delays and then merged into kinetics traces. At the expense of conversion efficiency the second approach benefits from a reduced background signal, a faster detection and a robust photometric correction procedure [64–67, 133]. The latter is calculated in the next but one subsection based on phase matching considerations including geometry and gate pulse parameters.

3.2 Experimental Setup

3.2.1 Overview
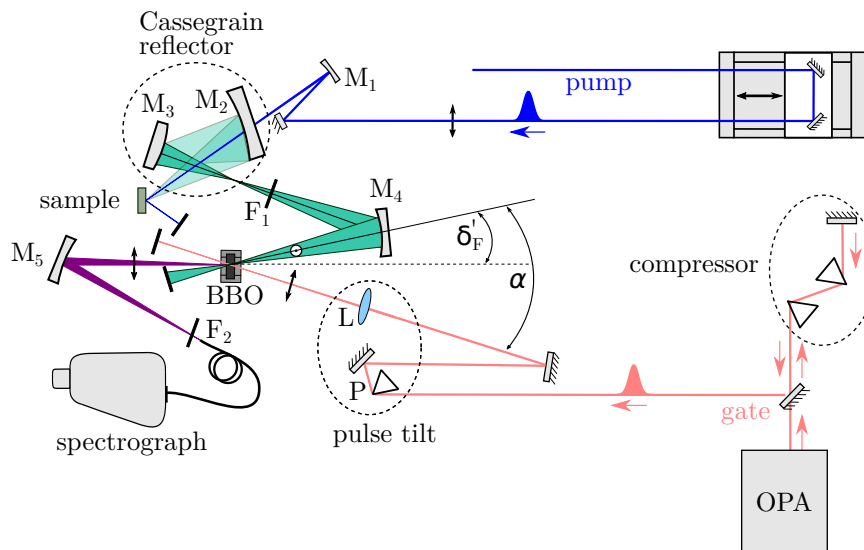
Figure 3.2 – Broadband fluorescence upconversion spectrometer used for single crystal measurements in reflection geometry. A sample is excited with fs-laser pulses ($\lambda = 400\,\text{nm}$, $\tau = 60\,\text{fs}$), which can be delayed by a motorized translation stage. The emitted luminescence is collected and imaged onto a BBO crystal using an off-axis Cassegrain reflector built of two spherical mirrors. There it is mixed with compressed and tilted gate pulses, which enclose an angle of α with the central ray of the luminescence cone. Another spherical mirror images the generated sum-frequency onto the entrance of an optical fiber connected to a spectrograph. **F:** filter, **M:** spherical mirror, **L:** lens, **P:** prism. Reproduced and modified from Krampf *et al.* Scientific Reports **10**, 11397 (2020); the complete manuscript can be found in appendix A.5.

The experimental setup to investigate ultrafast luminescence kinetics of solid samples is based on the broadband fs-fluorescence upconversion setup introduced by N. P. Ernsting to measure luminescence of solved molecules [64, 65, 67]. Ultrashort intense laser pulses ($\lambda = 800\,\text{nm}$, $\tau = 35\,\text{fs}$) are delivered with a maximum repetition rate of $1\,\text{kHz}$ by a regeneratively amplified Ti-Sapphire laser (Coherent Inc. type *Astrella*). The pulses pass a Galilei telescope for beam size reduction before being frequency-doubled using a standard BBO crystal ($d = 200\,\mu\text{m}$, EKSMA Optics). After passing a linear translation stage they are focused onto the sample by a concave mirror with a protected aluminum coating (M_1, $R = -500\,\text{mm}$).

A pair of spherical mirrors forming an off-axis Cassegrain reflector (M_2, $R = -150\,\text{mm}$, M_3, $R = 258.4\,\text{mm}$, magnification ≈ 3) collects the luminescence under a full angle of $\approx 15°$ and $\approx 32°$ in the horizontal and vertical plane, respectively. The Cassegrain reflector is described in more detail in the next subsection. In contrast to the reference setup the larger mirror of the reflector has a hole drilled in its center to enable

excitation in a reflective configuration. Together with a two-photon process to excite the sample limiting the emitting volume to a thin subsurface layer, this geometry reduces a deterioration of the temporal resolution caused by the large group velocity dispersion in the samples under study. The sample is mounted on an x-y-axis dovetail translation stage to adjust the position for perfect imaging. The magnified image of the luminescing area is reimaged by another concave mirror (M_4, R = $-300\,\text{mm}$) without further magnification onto a customized BBO crystal (d = $130\,\mu\text{m}$, $\theta_N = 40°$, $\Phi = 0°$, front p-coating @ 400–1300 nm, backside p-coating @ 300–450 nm, Altechna). This additional imaging is used to increase the distance between the Cassegrain reflector and the BBO crystal for a more convenient installation. A longpass filter with a cut-on wavelength of 422 nm (F_1, Asahi Spectra USA Inc. *ZUL422*) in the optical path of the luminescence suppresses pump scatter. The specularly reflected pump beam is blocked with a beam dump.

Luminescence and gate pulses ($\lambda = 1340\,\text{nm}$, $\tau = 45\,\text{fs}$, $E = 50\,\mu\text{J}$) delivered by an optical parametric amplifier (Light Conversion type *TOPAS Prime*) are mixed in the BBO crystal under non-collinear Type II phase matching condition, where the luminescence is ordinarily and the gate pulses are extraordinarily polarized. The uniaxial symmetry of the BBO crystal allows for two different geometric configurations differing in the obtained conversion efficiency and bandwidth. For a higher conversion efficiency at the expense of a reduced bandwidth, 'Case A' from Ref. [67] is chosen. The angle enclosed by the luminescence central ray and the gate pulse propagation direction is set to $\alpha \approx 19°$. This is a compromise between an increased conversion bandwidth, that is larger for large angles, and a deterioration of the temporal resolution, which decreases with larger angles due to geometric reasons [67]. The latter, called phase front mismatch [134], can be compensated for by tilting the gate pulse front. For this purpose an equilateral N-SF11 prism (P) tilts the gate pulse fronts by $\approx 3.2°$. To increase the tilt angle, the gate beam profile is imaged with a convex lens (L, f = 100 mm) onto the BBO crystal with a ≈ 6.5-fold demagnification stretching the angle to $\approx 20°$. A detailed calculation for the tilt procedure is given below. A pulse broadening due to group velocity dispersion in the N-SF11 prism is compensated for by a prism compressor.

As it will be discussed further below, the angles of incidence of the waves involved in the SFG process are crucial parameters determining the achieved spectral conversion efficiency curve. In fact, the spectral region of efficient conversion can be tuned by rotating the BBO crystal while the angle α is kept fixed. Thus, it is mandatory to determine and control the used angles as precisely as possible. Therefore, the BBO crystal is mounted on a high precision motorized rotation table (Newport *(M-) URM*). The angle α can now be determined (and later controlled) with an easy routine. First, the rotation table is turned until the fraction of the gate pulse reflected from the BBO surface directs back to the incidence direction marking the gate angle zero. A potential tilt of the BBO crystal surface relative to the crystal mount is then already compensated for. If now the crystal is rotated by $\alpha/2$, the reflected gate pulse passes the Cassegrain reflector in 'reversed' direction and overlaps with the pump beam spot on the sample surface. Setting the rotation table to α gives the fluorescence angle $\delta'_F = 0$.

The generated sum-frequency is imaged with a UV-reflectance enhanced concave aluminum mirror (M_5, R $= -200\,\text{mm}$) onto the entrance of an optical fiber with 19 fiber cores ($200\,\mu\text{m}$), which are aligned on the backside of the fiber. This maintains the high spectral resolution of the connected spectrograph with a thermoelectrically cooled CCD (Roper Scientific, type *IsoPlane* and *PIXIS 2K*). The spectrograph is designed for enhanced performance in the UV-spectral range. The non-collinear geometry allows for a spatial filtering of the residual luminescence and gate pulse photons, which are blocked by beam dumps. If necessary, an additional longpass filter (F_2, Schott *WG335*) is placed in front of the optical fiber to suppress upconverted scattered pump light occurring around time zero. The latter is used to define time zero and the apparatus response function of the experimental setup.

3.2.2 Luminescence collection with an off-axis Cassegrain reflector

The samples under study exhibit a large index of refraction as well as a large group velocity dispersion. A transmission geometry as in the reference system (cf. Ref. [67]) would suffer from a deterioration of the achievable temporal resolution if relatively thick samples are examined. In order not to be limited to extremely thin samples a reflection geometry is established. An optical system used for luminescence collection in an upconversion setup has to meet two conditions: (i) a maximum fraction of the emitted light has to be directed to the nonlinear optical crystal, while (ii) the high temporal resolution is maintained. Both requirements can be satisfied with an off-axis Cassegrain reflector.

The first demand is of special importance when weakly luminescing solid samples are studied. From Eq. (2.45) it follows that the generated sum-frequency signal depends linearly on the fluorescence intensity. This simplified statement, however, is misleading, since it tempts to collect a large fluorescence cone, which is then focused onto the nonlinear optical crystal as tightly as possible. It neglects that only a certain angular bandwidth contributes to the frequency mixing process via tolerance phasematching. This means that the intensity of the luminescence in the BBO crystal is *not* the essential quantity for efficient upconversion but its power per area *and angle*. The relevant quantity is therefore the *etendue* assigned to the SFG process in the BBO crystal. It is given by the product of the luminescence spot on the BBO crystal and the solid acceptance angle of the SFG process. Every optical element of a more complex system has its own etendue. Since this quantity can in principle not be increased, the overall etendue of an optical system is limited by the smallest value occurring. In the present case the acceptance angle of the SFG process is therefore the first limiting factor. For the given crystal (material, thickness, cut angle, orientation), phase matching condition (Type II), and angle α, the acceptance angle in the horizontal plane is $\pm 2.5°$, while practically no limitations occur in the vertical plane [67].

In contrast to the solid angle the image size remains a free parameter. However, the fluorescence and gate pulse image should have equal sizes on the BBO crystal. A small diameter of $\approx 500\,\mu\text{m}$ is chosen to ensure a high gate pulse intensity. It should

be noted that the gate pulse divergence can be neglected. At this point, the etendue of the optical system is fully determined. The last degree of freedom with respect to the conversion efficiency maximization is the choice of the image magnification. For an efficient luminescence excitation, a high pump intensity is needed (two-photon absorption process) suggesting a magnifying optical system. As the etendue is conserved, a magnification reduces the solid angle by the same factor as the area is increased. A convenient compromise between object size and mirror diameters, distances, and commercially available focus lengths is a magnification of $M \approx 3$. The first mirror of the setup therefore collects a full angle in the horizontal plane of $\approx 15°$.
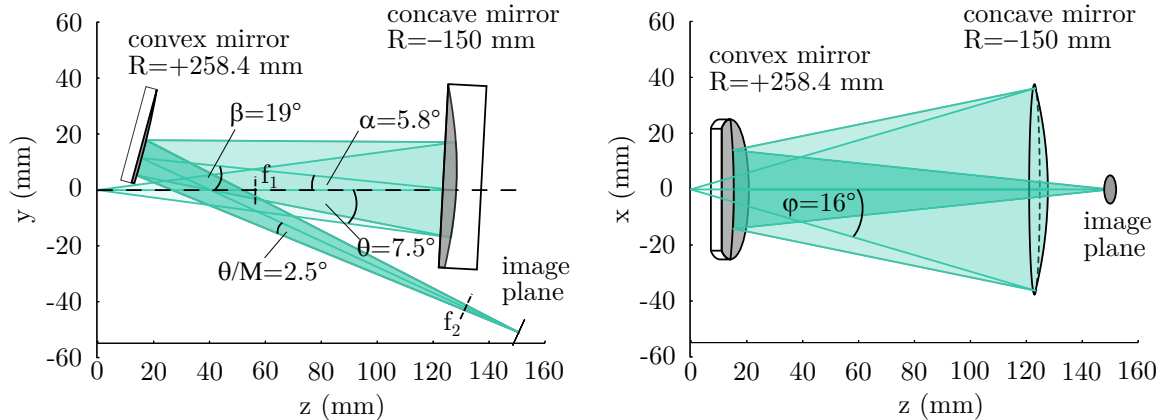
Figure 3.3 – Off-axis Cassegrain reflector for luminescence imaging modeled with a ray tracer and depicted in the z-y-plane **(left)** and z-x-plane **(right)**. It consists of two spherical mirrors with aluminum coating and radii of R = -150 mm and R = 258.4 mm, respectively. According to the acceptance angles for sum-frequency generation, the first, concave mirror (D=3") collects cones of fluorescence with the solid angles of $\approx 15°$ and $\approx 32°$, respectively. The magnification of the system is $M \approx 3$.

In order to not reduce the etendue any further, an off-axis Cassegrain reflector geometry is chosen. An on-axis configuration suffers from relatively large losses as the collected luminescence has to be led through the center of the first, larger mirror. Figure 3.3 shows the Cassegrain reflector used in the experiment, modeled with a ray tracing software (Stellar Software *Beam4*). To reduce astigmatism, the tilt angles of the mirrors are kept as small as possible by cutting the parts of the mirrors, which are not reached by the rays included in the accepted angular region. The first mirror with aluminum coating has a diameter of 3" and is placed in a distance of ≈ 127 mm from the sample. In contrast to the horizontal plane, there is practically no limitation to the acceptance angle in the vertical plane. The whole luminescence cone reaching the mirror with a full angle of $\approx 32°$ contributes to SFG. An even larger mirror would therefore further increase the conversion efficiency independent from the limitations in the horizontal plane. Luminescence collection in reflection geometry is enabled by a small hole drilled in the center of the first mirror, through which the pump pulse is led.

The quality of optical imaging and therefore its effect on the achievable temporal resolution of the experimental setup is studied with the ray tracing software. Figure 3.4
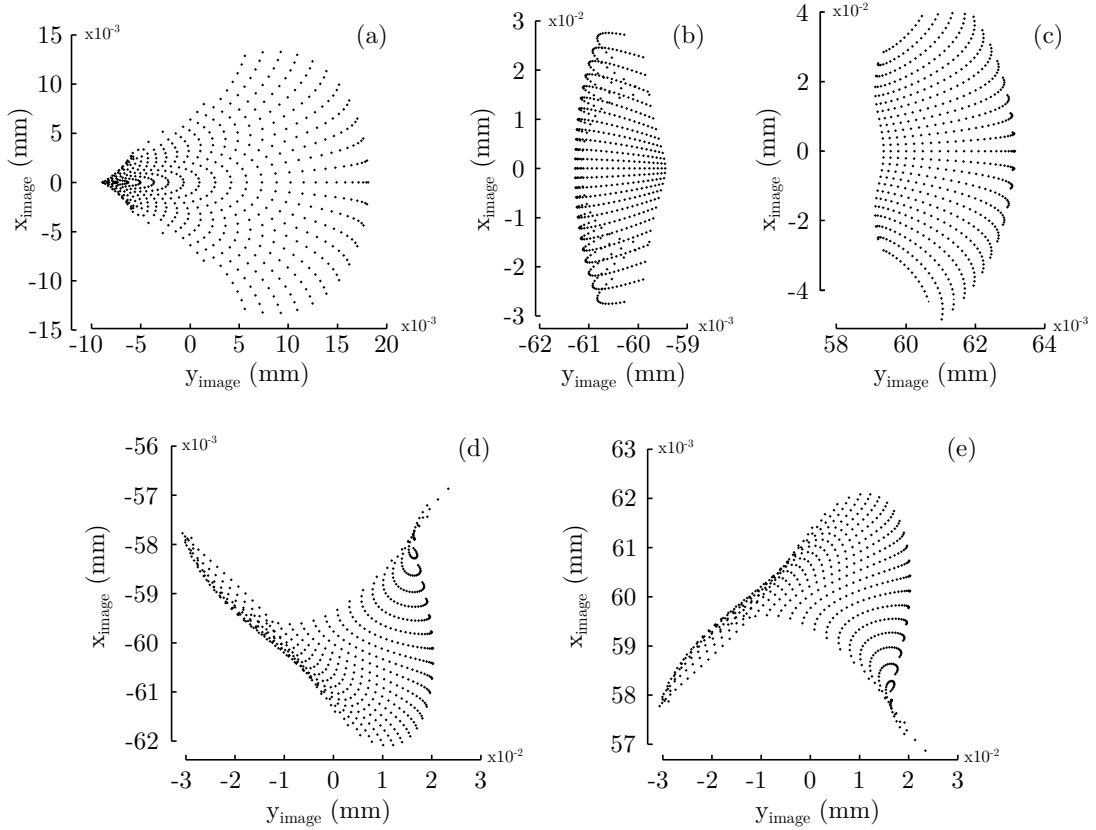
Figure 3.4 – Arrival coordinates in the image plane of rays starting from point sources **(a)** at the center of the luminescing spot and shifted by **(b,c)** ∓ 0.2 mm in the y-, and **(d,e)** x-direction. The ray paths are modeled with a ray tracing software.

shows the arrival coordinates in the image plane of rays starting from point sources at the center of the luminescing spot and shifted by ± 0.2 mm in the x- and y-direction, respectively. From each point source rays start under the full angles discussed above. For perfect imaging all rays would be reunited in single points in the image plane having a threefold distance to each other. As can be seen, quite complex structures are observed in the image plane caused by a nontrivial interplay between spherical aberration, astigmatism, and coma. However, the deviations are small as they occur on a μm scale.

In order to study the effect on the achievable temporal resolution of the experimental setup, the path lengths of the light rays from the sample to the image plane are traced. From these values the relative time differences needed for the different rays to reach the image plane are calculated. This gives an impression, how much the temporal resolution of the experimental setup is affected by the observed aberrations. Figure 3.5 (a) shows the time difference for rays in the horizontal plane, i.e., for different angles θ. The blue curve represents rays starting from the center of the luminescing spot. Only a very small delay of ≤ 1 fs relative to the central ray is observed. The red and yellow curves display rays starting ± 0.2 mm shifted in y-direction from the central ray, corresponding to an image on the BBO with 1.2 mm diameter. The here obtained relative delay of ≤ 5 fs is

(a)

(b)

Figure 3.5 – Temporal difference of the fluorescence ray 'passing time' through the Cassegrain reflector. The values are calculated from optical path lengths for individual rays forming the fluorescence light cones depicted in Fig. 3.3. The two ext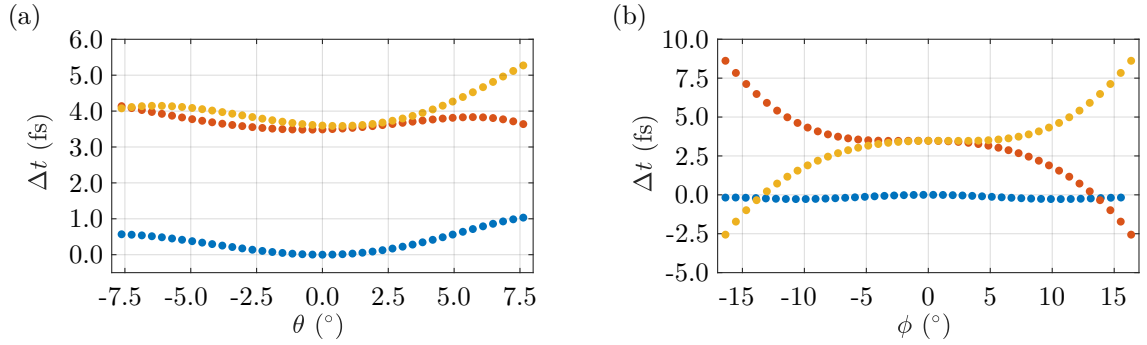reme cases of rays lying in the horizontal plane **(a)** and vertical plane **(b)** are shown. Rays starting from the center of the luminescence spot are marked with blue dots, whereas red and yellow dots show rays starting at $y = \pm 0.2$ mm.

therefore even larger than the actual deterioration in the experiment. The asymmetric character of all the curves nicely reflects the off-axis geometry. In the vertical plane much larger angles are collected. Accordingly, the relative delay is larger as well, but is still ≤ 10 fs (cf. Fig. 3.5 (b)). As expected, in the vertical plane axially symmetric curves are observed.

3.2.3 Gate pulse front tilt

As already mentioned in one of the previous sections, a tilt of the pulse fronts has to be performed in order to achieve a high temporal resolution in the experiment. The tilt introduced by a prism can easily be calculated from geometrical considerations. The calculation and visualization (Fig. 3.6) presented here follow the descriptions given in Refs. [64] and [72].

According to Fermat's principle passing the prism the wavefront AA' is transformed into the wavefront BB' in such a way that corresponding points on the wavefronts cover the same optical distances. This means that, e.g., the optical distances AB and A'B' are equal. From this statement one finds

$$\frac{2L_{\text{left}}}{c} = \frac{2L_{\text{right}}}{v_{\text{ph}}}, \tag{3.1}$$

where v_{ph} is the phase velocity in the prism. Since the phase and pulse velocities are approximately equal in air, the wavefront and the pulse front take the same time to pass the distance $\overline{AOB}$. In contrast, traveling through the prism material, the pulse is delayed with respect to the phase. This delay increases linearly with the amount of medium passed, leading to pulse fronts tilted by the angle Φ. The temporal difference between the outer parts of the pulse front after passing the distances $2L_{\text{right}}$ and $2L_{\text{left}}$,

respectively, is

$$\Delta t = \frac{2L_{\text{right}}}{v_{\text{g}}} - \frac{2L_{\text{left}}}{c} \tag{3.2}$$

with the group velocity in the prism v_{g}. In this time the outer left part of the pulse front covers the distance $\overline{B'E}$, which is according to Eq. (3.1) and (3.2)

$$\overline{B'E} = c\Delta t = 2nL_{\text{right}}\left(\frac{v_{\text{ph}}}{v_{\text{g}}} - 1\right), \tag{3.3}$$

where n is the index of refraction of the prism material. If the angle of incidence is chosen so that a minimum angle of deviation is obtained, i.e., a symmetric optical path in the prism is achieved, one finds

$$L_{\text{right}} = d_0 \frac{\sin\left(\frac{\gamma}{2}\right)}{\sqrt{1 - n^2\sin^2\left(\frac{\gamma}{2}\right)}} \tag{3.4}$$

with the apex angle of the prism γ. From Fig. 3.6 then follows that the tilt angle is given by

$$\Phi = \arctan\left(\frac{\overline{B'E}}{d_0}\right) = \arctan\left(\frac{2n\sin\left(\frac{\gamma}{2}\right)}{\sqrt{1 - n^2\sin^2\left(\frac{\gamma}{2}\right)}}\left(\frac{n_{\text{g}}}{n} - 1\right)\right). \tag{3.5}$$

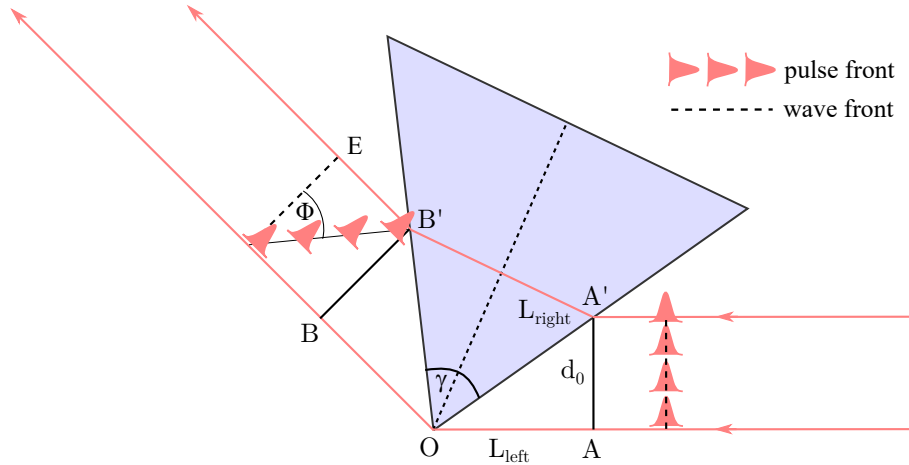**Figure 3.6** – Pulse front tilt induced by a prism. Before entering the prism the pulse front (red) and wavefront AA' are parallel to each other and perpendicular to the propagation direction. In the prism the pulse is delayed with respect to the phase. After passing the prism the wavefront BB' is still perpendicular to the propagation direction, the pulse front in contrast is tilted by the angle Φ.

In the experimental setup a high dispersive prism (Schott N-SF11 glass) with an apex angle of $\gamma = 60°$ is used for pulse front tilting. According to Eq. (3.5) the pulse fronts are then tilted by $\Phi \approx 3.2°$. In order to compensate for the large angle $\alpha \approx 19°$, this small tilt angle has to be stretched. For this purpose, the gate pulse spot on the entrance of the prism is imaged with a demagnification onto the BBO crystal. The principle of this stretching procedure can be sketched as follows: a demagnification only acts on the beam diameter d_0, which will be reduced by the factor M. The distance $\overline{B'E}$, however, remains constant. For the desired demagnification M one finds

$$M = \frac{\tan(\Phi')}{\tan(\Phi)},\tag{3.6}$$

with the new, larger tilt angle Φ'. The new tilt angle should be $\approx 20°$ leading to a desired magnification of $M \approx 6.5$. With the focal length of the imaging lens ($f = 100\,\text{mm}$) and the magnification, it is easy to calculate the distance between the prism and the lens s_1 and between the lens and the BBO crystal s_2

$$s_1 = f(1 + M) \quad \text{and} \quad s_2 = s_1/M.\tag{3.7}$$

Figure 3.7 shows the Gaussian-shaped cross-correlation signal between pump light scattered at the sample surface and the gate pulse (blue dots). This signal reflects the apparatus response function having a full width at half maximum of $\leq 160\,\text{fs}$. For comparison, the calculated cross-correlation signal for a collinear geometry is depicted as well (dashed black line) assuming pump and gate pulse durations of 60 fs and 45 fs, respectively. As can be seen, the deterioration of the temporal resolution due to the non-collinear geometry is small considering the quite large angle α.
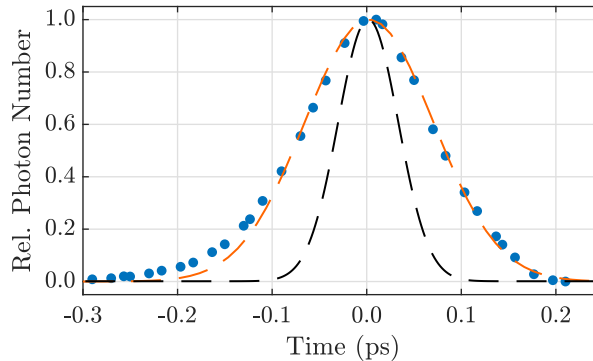
Figure 3.7 – Measured cross-correlation signal of scattered pump light and gate pulses (blue dots). Fitting a Gaussian function to the data (red line) leads to a full width at half maximum of $\leq 160\,\text{fs}$. For comparison the signal for a collinear geometry (black line) is calculated considering the same pulse durations as in the experiment (60 fs and 45 fs).

3.2.4 Photometric correction

As already mentioned above, in the broadband upconversion scheme using a fixed non-collinear geometry for SFG, the phase matching condition is broadened enabling the

detection of fluorescence spectra for fixed delay times. However, the spectral efficiency has still a finite bandwidth and thus, a recorded spectrum represents not only a temporal but also spectral 'slice' of the overall luminescence decay. To reconstruct the original fluorescence spectrum from the measured data, a photometric correction has to be performed.

State-of-the-art correction procedure

As in every fluorescence measurement, the spectral transfer function of the detection system has to be determined to correct the spectra. In an upconversion spectrometer the spectral efficiency curve for SFG is the crucial contribution to the transfer function. However, as in conventional fluorimetry the influence of the spectrograph and the optical fiber $T(\lambda_\mathrm{F})$ has also to be taken into account. For this purpose a standard lamp (Ben-
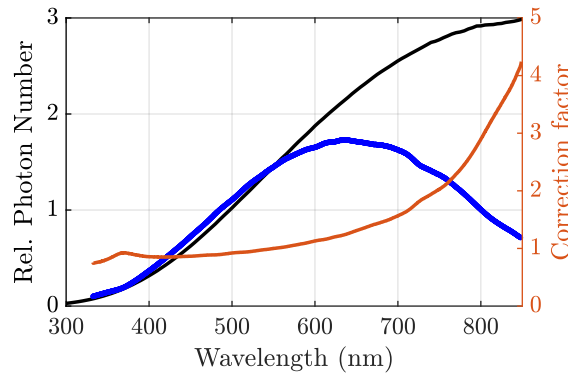
Figure 3.8 – Measured (blue) and expected (black) spectra of a standard lamp used to calibrate the spectrograph. The correction curve (orange) is obtained by pointwise division of the expected and measured spectra.

tham *CAL_CL2_100W*) is used to calibrate the spectrograph. Figure 3.8 shows the measured (blue) and expected (black) spectra. Pointwise division of these curves gives the correction function (orange), which is later used to correct the measured upconverted UV-spectra.

The more crucial contribution to the overall transfer function is the spectral efficiency curve of the SFG. An experimental determination of this curve is not as trivial as for the spectrograph [67]. However, as it is demonstrated in this work (cf. section 5.2), a photometric correction performed in silico leads to very good results provided that all experimental parameters relevant for efficient SFG are determined very thoroughly. Gerecke *et al.* gave a simple mathematical description to calculate the phase mismatch for non-collinear SFG [67] using the angles outside the nonlinear optical crystal, which are the ones used in the descriptions earlier. Now, the task is to calculate for a given set of parameters the length of the k-vector of the generated sum-frequency by momentum and energy conservation, respectively. The difference between these values is then the phase mismatch.

For convenience the primed angles of incidence defined with respect to the surface
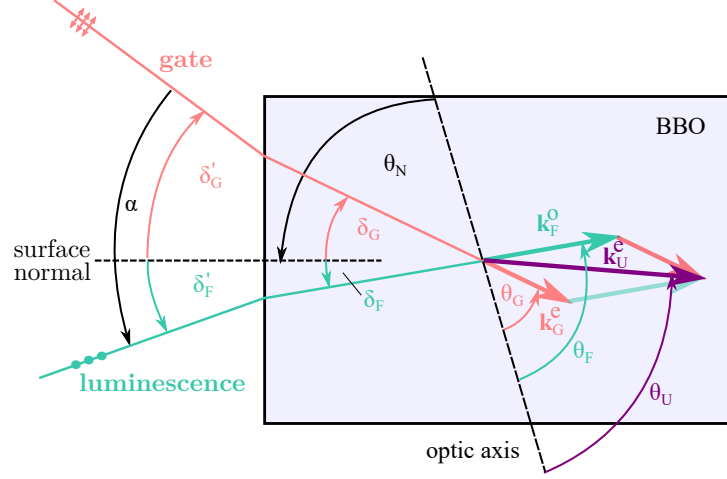
Figure 3.9 – Coordinate system and angles used in the phase matching calculation. The primed angles and α are defined in the laboratory system, i.e., with respect to the surface normal of the BBO crystal. These are related with the angles θ relative to the optic axis of the crystal via the equations (3.8)–(3.10).

normal, hereinafter referred to as laboratory frame of reference, are used as input parameters as they represent directly accessible quantities. These have to be transferred to angles θ relative to the optic axis in the following denoted as crystal frame of reference. The relation between the two frames of reference are depicted in Fig. 3.9. Obviously, the angles δ inside the crystal in the laboratory frame of reference are connected with the angles θ via the simple relation

$$\theta = \theta_N - \delta, \tag{3.8}$$

where θ_N denotes the cutting angle, i.e., the angle enclosed by the surface normal and the optic axis.

First, the angles δ inside the crystal have to be calculated via Snell's law, which is in case of ordinary polarization simply given by

$$\sin(\delta'_F) = n_{oF} \sin(\delta_F), \tag{3.9}$$

where n is the index of refraction. In case of the extraordinarily polarized gate pulse, the index of refraction depends on $\theta_G = \theta_N - \delta_G$. Therefore the equation

$$\sin(\delta'_G) = n_G(\theta_G) \sin(\delta_G) = \frac{n_{oG}n_{eG}}{\sqrt{n_{oG}^2\sin^2(\theta_N - \delta_G) + n_{eG}^2\cos^2(\theta_N - \delta_G)}} \sin(\delta_G) \tag{3.10}$$

has to be solved. The quantities n_{oG} and n_{eG} are the refractive indices for ordinary and extraordinary polarization, i.e., $\theta_G = 0°$ and $\theta_G = 90°$, respectively.

In a second step, the wave vector $\mathbf{k}_U^e$ of the generated sum-frequency resulting from a set of angles and wavelengths is calculated from a momentum conservation argument

$$\mathbf{k}_U^e = \mathbf{k}_G^e + \mathbf{k}_F^o = 2\pi\tilde{\nu}_G n_{eG}(\theta_G)\begin{pmatrix}\cos(\theta_G)\\\sin(\theta_G)\end{pmatrix} + 2\pi\tilde{\nu}_F n_{oF}\begin{pmatrix}\cos(\theta_F)\\\sin(\theta_F)\end{pmatrix}. \tag{3.11}$$

Projecting $\mathbf{k}_U^e$ on the optic axis gives the angle θ_U enclosed by the k-vector of the sum-frequency and the optic axis

$$\theta_U = \arccos\left(\frac{\mathbf{k}_U^e \cdot \binom{1}{0}}{|\mathbf{k}_U^e|}\right). \tag{3.12}$$

The phase mismatch Δk is now given by the difference between the length of $\mathbf{k}_U^e$ obtained from Eq. (3.11) and from energy conservation ($\tilde{\nu}_U = \tilde{\nu}_F + \tilde{\nu}_G$)

$$\Delta k = |\mathbf{k}_U^e| - 2\pi\tilde{\nu}_U n_U^e(\theta_U). \tag{3.13}$$

As the gate pulse intensity exceeds the luminescence intensity by orders of magnitude, the conversion efficiency can be approximated by Eq. (2.45), which now reads

$$\eta = \frac{I_U}{I_F} = \frac{8\pi^2\tilde{\nu}_U^2 d_{\text{eff}}^2 I_G}{\epsilon_0\, c\, n_{\text{eG}}(\theta_G)\, n_{\text{eU}}(\theta_U)\, n_{\text{oL}}} L^2 \left(\frac{\sin\left(\frac{\Delta k L}{2}\right)}{\frac{\Delta K L}{2}}\right)^2, \tag{3.14}$$

where d_{eff} denotes the effective nonlinear optical susceptibility, which can be deduced from the phase matching condition and crystal symmetry. First of all, the susceptibility tensor given in Eq. (2.19) can be simplified considering the symmetry of the used BBO crystal. For its crystal class 3m only four different tensor elements remain and the tensor has the easier form

$$d_{il} = \begin{pmatrix} 0 & 0 & 0 & 0 & d_{15} & -d_{22} \\ -d_{22} & d_{22} & 0 & d_{15} & 0 & 0 \\ d_{31} & d_{31} & d_{33} & 0 & 0 & 0 \end{pmatrix}. \tag{3.15}$$

According to Eq. (2.19), the nonlinear polarization generating the sum-frequency is then given by

$$\begin{pmatrix} P_x^{(2)} \\ P_y^{(2)} \\ P_z^{(2)} \end{pmatrix} = \begin{pmatrix} d_{15}E_z^G E_x^F - d_{22}\left(E_x^G E_y^F + E_y^G E_x^F\right) \\ d_{15}E_z^G E_y^F + d_{22}\left(E_y^G E_y^F - E_x^G E_x^F\right) \\ d_{31}\left(E_x^G E_x^F + E_y^G E_y^F\right) \end{pmatrix}. \tag{3.16}$$

Here, the fact that E^F lies in the x-y-plane, i.e., $E_z^F = 0$ is used for further simplification. As the generated sum-frequency and the gate waves are both extraordinarily polarized, Eq. (2.51) together with trigonometric identities leads to

$$\begin{aligned} P_\parallel^{(2)} = E^G E^F[(&-d_{15}\sin(\theta_G)\cos(\theta_U)\sin(\phi_L - \phi_U) \\ &+ d_{22}\cos(\theta_G)\cos(\theta_U)\cos(\phi_G + \phi_F + \phi_U) \\ &+ d_{31}\cos(\theta_G)\sin(\theta_U)\sin(\phi_G - \phi_F)]. \end{aligned} \tag{3.17}$$

Since all angles ϕ are very small, the effective nonlinear dielectric tensor can be approximated by

$$d_{\text{eff}} = d_{22}\cos(\theta_U)\cos(\theta_G). \tag{3.18}$$

The tensor element d_{22} corresponds to d_{yyy}, which can be determined following Miller's rule [135]

$$\chi_{yyy}^{(2)} = \chi_{yy}^{(1)} \chi_{yy}^{(1)} \chi_{yy}^{(1)} \Delta_{yyy}. \tag{3.19}$$

The linear susceptibilities in turn can be calculated from the index of refraction. If the optic axis is again aligned with the z-axis, this leads to

$$\chi_{yy}^{(1)} = n_{\mathrm{o}}^2 - 1. \tag{3.20}$$

The factor $\Delta yyy = 7.79 \cdot 10^{-13}\,\mathrm{pmV}^{-1}$ can be deduced from second harmonic generation measurements [136].

The spectral efficiency curve calculated so far is valid only for a single fluorescence angle δ_{F}'. However, the luminescence is collected over a large solid angle (cf. Fig. 3.3) and the divergence of the incoming luminescence light has to be taken into account. The net spectral efficiency curve of the sum-frequency generation is thus calculated by averaging over all fluorescence angles included in the fluorescence light cone described in Fig. 3.3. It should be noted that the narrower light cone after magnification has to be used in the calculation. In BBO with its uniaxial crystal symmetry the effective susceptibility and the index of refraction do not depend on the angle ϕ. It is therefore sufficient to only consider angles θ in the horizontal plane. Effectively only a small cone of angles in this plane contributes to SFG. Typically angles on the order of $\pm 2.5\,^\circ$ can be used via angular tolerance phase matching [67].

Extension of the spectral efficiency calculation

Up to now the conversion efficiency of two perfectly monochromatic waves has been calculated and averaged over different fluorescence angles. For a more realistic estimation of the spectral efficiency an additional contribution has to be considered as well: the finite spectral bandwidth of the gate pulses. For each spectral part perfect phase matching is achieved for a different fluorescence wavenumber and/or angle. Figure 3.10 shows the spectral efficiency curve of non-collinear sum-frequency generation for different distinct gate pulse wavenumbers. Changing the gate wavenumber by $\pm 130\,\mathrm{cm}^{-1}$ already shifts the maximum of conversion efficiency by more than $\pm 900\,\mathrm{cm}^{-1}$.

To account for the different frequencies of a real short laser pulse, the spectral efficiency curve has to be calculated not only for every fluorescence angle, but also for every gate pulse wavenumber. The contribution of one gate pulse frequency has to be weighted with its fraction of the total gate pulse energy. Figure 3.11 shows the Gaussian-shaped spectrum of the gate pulses used in this work having a central wavenumber $\tilde{\nu} = 7{,}469\,\mathrm{cm}^{-1}$ ($\lambda = 1340\,\mathrm{nm}$) and a full width at half maximum of $268\,\mathrm{cm}^{-1}$ ($\approx 48\,\mathrm{nm}$). Accordingly, the different frequencies of the gate pulse are weighted with a function

$$g(\tilde{\nu}_{\mathrm{G},i}) = \exp\left(-\frac{(\tilde{\nu}_{\mathrm{G}} - \tilde{\nu}_{\mathrm{G0}})^2}{2\sigma^2}\right). \tag{3.21}$$

55
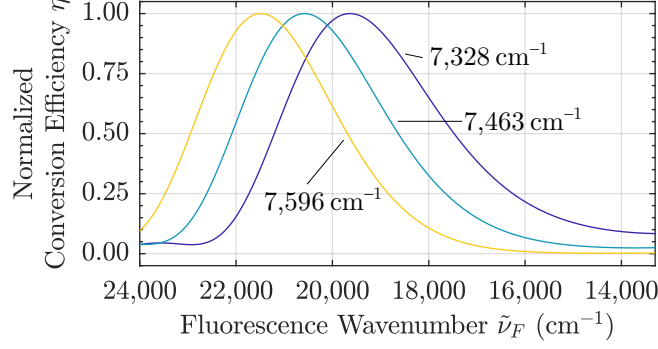
Figure 3.10 – Normalized spectral conversion efficiencies of sum-frequency generation in a thin BBO crystal ($L = 130\,\mu$m, $\theta_N = 40°$, $\phi = 0°$) set to $\delta'_F = 2.5°$ for different gate wavenumbers ($7{,}328\,\mathrm{cm}^{-1}$, $7{,}463\,\mathrm{cm}^{-1}$, and $7{,}596\,\mathrm{cm}^{-1}$). The external angle enclosed by the fluorescence and the gate pulse is $\alpha = 19°$. Type II phase matching is used.
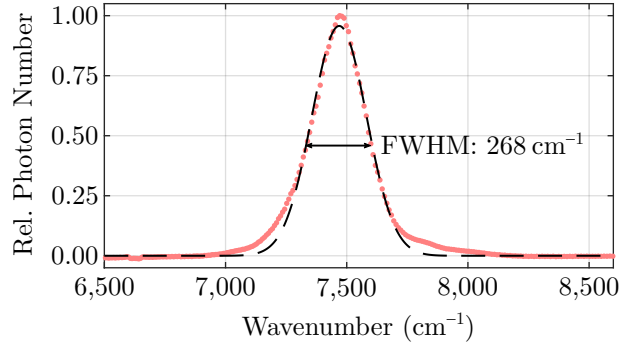
Figure 3.11 – Spectrum of the gate pulses involved in luminescence upconversion. The spectrum is fitted with a Gaussian function according to Eq. (3.21).

The effective efficiency curve is then obtained by averaging over all combinations of gate wavelengths and fluorescence angles

$$\eta_{\mathrm{eff}}(\tilde{\nu}_{\mathrm{F}}) = \frac{1}{N_{\tilde{\nu}}} \frac{1}{N_{\delta'}} \sum_{i=1}^{N_{\tilde{\nu}}} \sum_{j=1}^{N_{\delta'}} \eta(\tilde{\nu}_{\mathrm{F}}, \tilde{\nu}_{\mathrm{G},i}, \delta'_{\mathrm{F},j}) g(\tilde{\nu}_{\mathrm{G},i}), \qquad (3.22)$$

where $N_{\tilde{\nu}}$ and $N_{\delta'}$ are the numbers of discrete wavenumbers and angles used in the calculation. Figure 3.12 compares spectral efficiency curves with and without consideration of the gate pulse bandwidth for two differently thick BBO crystals. In both cases the angle enclosed by the gate pulse and the central ray of the fluorescence cone is $\alpha = 19°$, the fluorescence angle is set to $\delta'_F = 2.5°$ and the divergence of the fluorescence light cone is $\pm 2.5°$. In case of a very thin BBO crystal ($d = 130\,\mu$m, Fig. 3.12 (a)) the maximum of the efficiency curve lies at $20{,}600\,\mathrm{cm}^{-1}$. Without considering the gate pulse bandwidth and taking 30% of the maximum value as reference, efficient upconversion is possible in a range from $18{,}060\,\mathrm{cm}^{-1} - 22{,}350\,\mathrm{cm}^{-1}$. If the extended calculation is used, the expected range broadens by $670\,\mathrm{cm}^{-1}$. In case of a thicker crystal ($d = 500\,\mu$m,

Fig. 3.12 (b)), the difference becomes much more crucial. Whereas the 'monochromatic' calculation leads to a range for efficient upconversion from $19{,}730\,\mathrm{cm}^{-1} - 21{,}150\,\mathrm{cm}^{-1}$, the different frequencies in the gate pulse increase this range by a factor of two. Thus, without considering the gate pulse bandwidth, the photometric correction can lead to very large errors regarding the obtained spectral width of the measured luminescence.
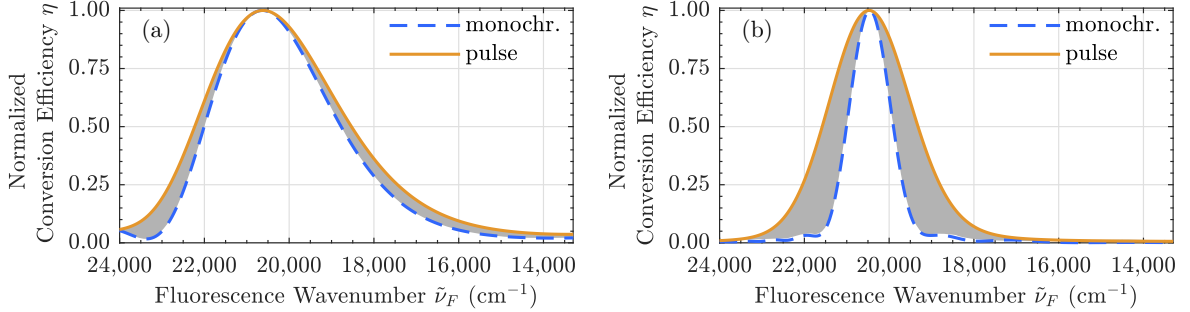
Figure 3.12 – Normalized spectral conversion efficiencies of a thin BBO crystal ($\theta_{\mathrm{N}} = 40°$, $\phi = 0°$) set to $\delta'_{\mathrm{F}} = 2.5°$ with (orange) and without (dashed blue) consideration of the gate pulse bandwidth of $48\,\mathrm{nm}$ (central wavelength $1340\,\mathrm{nm}$). Both are normalized to their respective maximum. The external angle enclosed by the fluorescence and the gate pulse is $\alpha = 19°$. Type II phase matching is used. The influence of the gate pulse spectral bandwidth is calculated for the two BBO crystal thicknesses **(a)** L = $130\,\mu\mathrm{m}$ and **(b)** L = $500\,\mu\mathrm{m}$. Figure part (a) is reproduced from Krampf *et al.* Scientific Reports **10**, 11397 (2020); the complete manuscript can be found in appendix A.5.

Now that a realistic spectral efficiency curve is at hand, the distribution of UV-photons measured with the experimental setup and the fluorescence spectrum emitted from the sample can be converted into each other via

$$f(\tilde{\nu}_{\mathrm{U}}) = f(\tilde{\nu}_{\mathrm{F}}) \circ \eta_{\mathrm{eff}}(\tilde{\nu}_{\mathrm{F}}) \circ T(\tilde{\nu}_{\mathrm{F}}), \tag{3.23}$$

where $\circ$ denotes the Hadamard, i.e., pointwise product of the vectors. If necessary, the transfer function of a filter used in the beam path can be added to Eq. (3.23) as well. A measurement on a standard sample (Coumarin 153 solved in dimethyl-sulfoxide) is presented and discussed in section 5.2 proving that the experimental setup works as expected. This additionally shows that for such an experiment a theoretically obtained correction function is sufficient.

3.2.5 Group velocity dispersion correction

In the experimental setup shown in Fig. 3.2 only reflective optical elements are used to image the luminescence onto the BBO crystal. In this way, a deterioration of the achievable temporal resolution due to group velocity dispersion is avoided. However, a thin fused silica longpass filter is placed in the optical path of the luminescence to suppress scattered pump light. Due to group velocity dispersion the spectral components of the fluorescence experience different group indices passing the longpass filter. Their
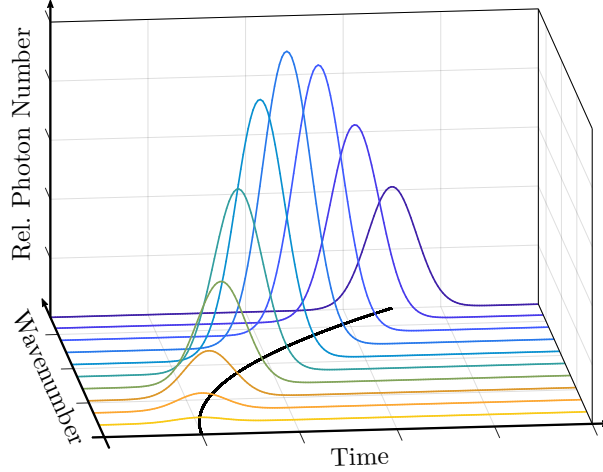
Figure 3.13 – Schematic representation of the temporal delay of different luminescence wavenumbers caused by group velocity dispersion. In media with normal dispersion spectral components with larger wavenumber propagate slower. Their temporal peak therefore appears later on the temporal axis.

respective optical path lengths from the sample to the BBO crystal thus slightly differ. This means that although emitted at the exact same time, they do not arrive at the BBO crystal simultaneously. As a result, even in absence of a temporal Stoke's shift, the respective maxima of the kinetic traces of single wavenumbers appear at different times in the measurement (cf. Fig. 3.13). To compensate for this effect the temporal delay induced by group velocity dispersion has to be determined. In a first step, the index of refraction n for the spectral region of the emitted luminescence is calculated using the Sellmeier equation

$$n = \sqrt{1 + \frac{A\lambda^2}{\lambda^2 - B^2} + \frac{C\lambda^2}{\lambda^2 - D^2} + \frac{E\lambda^2}{\lambda^2 - F^2}} \qquad (3.24)$$

with the experimentally determined constants for fused silica [137]

$$A = 0.6961663 \quad B = 0.0684043 \quad C = 0.4079426$$
$$D = 0.1162414 \quad E = 0.8974794 \quad F = 9.896161. \qquad (3.25)$$

The dispersion of the refractive index is shown in Fig. 3.14 (a) as a red line. From this the group index n_g (blue line) can be calculated via

$$n_\mathrm{g}(\tilde{\nu}) = n(\tilde{\nu}) + \tilde{\nu}\frac{\mathrm{d}n}{\mathrm{d}\tilde{\nu}}. \qquad (3.26)$$

The temporal difference between spectral components passing the filter can then be calculated from their different optical path lengths

$$\Delta t = \frac{d\Delta n_\mathrm{g}}{c}, \qquad (3.27)$$

(a)

(b)
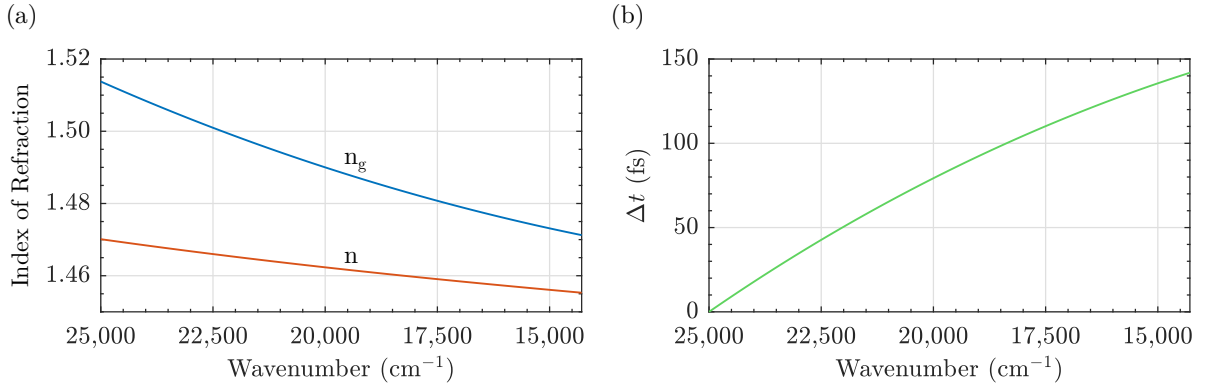
Figure 3.14 – **(a)** Refractive index n (red) and group index n_g (blue) of fused silica as a function of wavenumber. **(b)** Temporal delay of spectral components introduced by group velocity dispersion in a $1\,\mathrm{mm}$ thick fused silica filter in the optical path of the luminescence. The delay is calculated with respect to the optical path of the pump pulse central wavenumber at $25{,}000\,\mathrm{cm}^{-1}$.

where d is the thickness of the filter. As in the experiment scattered pump light is used to define time zero, the delay of the spectral components is calculated relative to the optical path length of the pump pulse central wavenumber at $25{,}000\,\mathrm{cm}^{-1}$. As shown in Fig. 3.14 (b) the temporal delay is on the order of a few tens of fs.

A measured upconversion signal nicely showing the calculated temporal delay is given in Fig. 3.15. Here, the temporal evolution of the upconverted luminescence spectrum of an Mg-doped lithium niobate crystal is shown. For short times a pronounced peak is observed for every spectral component. Obviously, these maxima are observed at different points in time. Their relative temporal delay exactly follows the calculated time delay introduced by group velocity dispersion in the fused silica longpass filter (red dashed line).
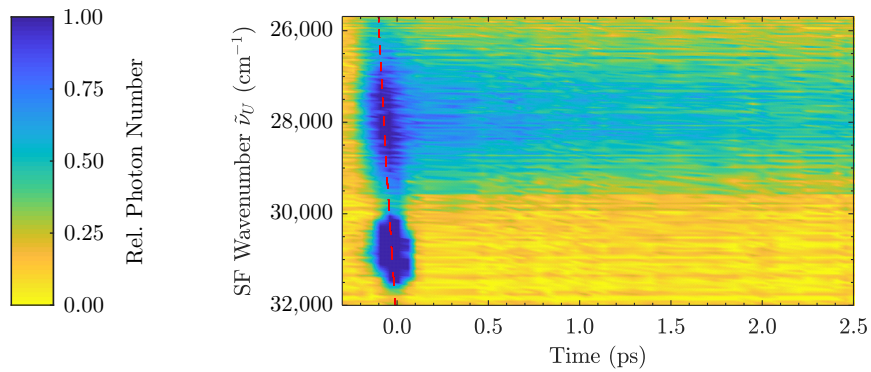
Figure 3.15 – Upconverted luminescence spectra of $6.5\,\mathrm{mol\%}$ Mg-doped LN as a function of time up to $2.5\,\mathrm{ps}$. The red dashed line illustrates the temporal delay between the luminescence kinetic traces at different wavenumbers introduced by their different group velocities in the long pass filter given in Fig. 3.14. The extraordinarily polarized part of the fluorescence is used (with respect to the sample's optical axis).

59

4 Luminescence and absorption of self-trapped excitons in lithium niobate

Whereas the formation, transport, and relaxation of strong-coupling polarons in LN has been investigated extensively in the last decades, a comprehensive microscopic picture describing the blue-green (photo)luminescence of these crystals has not been established so far. Early findings of Blasse *et al.* suggested electron-hole pairs localized at niobium-oxygen-octahedra at the origin [58–62]. They assigned the blueish low-temperature luminescence to the regular octahedra and the greenish to the presence of antisite defects. However, a deeper microscopic picture has not been developed until recently temperature and stoichiometry dependent measurements after ns-pulse exposure have been conducted [56, 57]. A microscopic picture tracing the photoluminescence back to geminate small polaron recombination has been proposed by the authors. While this assumption could be justified by the sheer success of the small polaron theory to explain many features of lithium niobate, there are strong arguments against it. This chapter will show that the established small polarons in LN cannot be at the origin of the luminescence. Instead, Blasse's self-trapped exciton hypothesis is revived. In fact, a considerable contribution of self-trapped excitons to the transient absorption of lithium niobate is found. Both luminescence and absorption phenomena of crystals with different stoichiometry and doping are explained with a microscopic picture based on self-trapped exciton hopping, pinning, and relaxation.

This chapter starts with first hints indicating that geminate small polaron recombination cannot be at the origin of the photoluminescence of lithium niobate crystals and can in fact also not be neglected in transient absorption as well. In the second section the incomplete argumentation proposing self-trapped excitons rather than small polarons at the origin of the luminescence is supported by further experimental investigations and modeling. Section 4.3 fosters the idea of pinned excitons being responsible for the already known long-lived absorption in the blue spectral range in iron-doped lithium niobate and determines its spectral fingerprint and absorption cross section. The last section 4.4 reviews literature on luminescence and transient absorption to resolve contradictory assignments of small polarons to certain optical properties of LN. A detailed atomistic model is proposed consistently describing luminescence and absorption phenomena in lithium niobate with the formation of small polarons *and* (pinned) self-trapped excitons.

4.1 The role of self-trapped excitons in polaronic recombination processes in lithium niobate

The author contributed to the paper *The role of self-trapped excitons in polaronic recombination processes in lithium niobate.* The abstract is printed with friendly permission of IOP Publishing Ltd. The complete article can be found in the appendix A.1.

- Simon Messerschmidt, Andreas Krampf, Felix Freytag, Mirco Imlau, Laura Vittadello, Marco Bazzan, and Gábor Corradi
The role of self-trapped excitons in polaronic recombination processes in lithium niobate

Abstract: Transient absorption and photoluminescence are experimentally investigated in the polaronic reference system lithium niobate, $LiNbO_3$ (LN), with the aim to refine the microscopic model of small polaron dynamics in materials with strong electron-phonon coupling. As a unique feature, our study is performed by using two different spectroscopic methods, in crystals with dopants enhancing photorefraction or damage resistance, and over a broad temperature range from $15 - 400\,K$. Although being self-consistent for particular experimental conditions, the hitherto used microscopic polaronic models reveal inconsistencies when applied to this larger data set. We show that comprehensive modeling is unlocked by the inclusion of an additional type of polaronic state with the following characteristics: (i) strongly temperature- and dopant-dependent relaxation times, (ii) an absorption feature in the blue-green spectral range, and (iii) a Kohlrausch-Williams-Watts decay shape with a temperature-dependent stretching factor $\beta(T)$ showing a behavior contrary to that of small, strong-coupling polarons. The hypothesis of self-trapped excitons (STEs, i.e., bound electron-hole pairs strongly coupled to Nb^{5+} and O^{2-} within a niobium-oxygen octahedron) and their pinning on defects as the microscopic origin of these characteristics is supported by a spectroscopic linkage of photoluminescence at low ($15\,K$) and elevated ($300\,K$) temperatures and explains the long-lifetime components in transient absorption as due to pinned STEs.

4.2 Microscopic origin of photoluminescence in lithium niobate - small polarons or self-trapped excitons?

In the previous section, inconsistencies in the temperature-dependent transient absorption of iron-doped LN samples were discovered and discussed. A correlation of the temperature behavior of the stretching factor extracted from transient photoluminescence and absorption measurements was used to attribute both phenomena to a similar microscopic cause. A contrary temperature behavior was found to be known for small polarons in LN. Since an explanation of the observation using the known small polarons was not possible, the hypothesis of radiatively decaying STEs at the origin of luminescence was revived. The unassigned transient absorption feature in the blue-green spectral range was then attributed to STEs pinned on defects. The initial suspicion raised in this publication contradicts the hypothesis of geminate recombination of small polarons as the cause of luminescence, previously published by Kämpfe *et al.* [56]. Since the argumentation so far has been incomplete, this section will present further measurements and modeling of the data that support the hypothesis.

4.2.1 Temperature-dependent correlated transient absorption and emission spectroscopy

Correlated transient absorption and photoluminescence measurements on Mg-doped lithium niobate ($c_{Mg} = 6.5\,mol\%$) for time scales $\geq 100\,ns$ are shown in Fig. 4.1. The luminescence data are part of the publication 5.2, whereas the transient absorption (TA) measurements have been performed by Tobias Nörenberg in the context of his master's thesis. It is immediately clear that both transient phenomena occur on time scales differing by orders of magnitude. Between $50\,K$ and $175\,K$ the photoluminescence disappears within milli- and microseconds, respectively. The transient absorption on the other hand lasts for a few hundred microseconds up to several thousands of seconds. Therefore, at elevated temperatures, say above 170 K, the decay times differ by 'only' two orders of magnitude, while the difference increases drastically as the sample is cooled to low temperatures (< 100 K). At 50 K the transient absorption decays at least eight orders of magnitude more slowly than the luminescence.

Figure 4.2 compares the mean decay time of the transient photoluminescence and absorption signal. As already discussed in section 4.1 and Ref. [56], in lithium niobate the decay of the small polaron number density often follows a stretched-exponential behavior

$$N(t) = N_0 \exp\left[-(t/\tau)^\beta\right], \tag{4.1}$$

where the stretching factor lies between zero and one ($0 < \beta \leq 1$). Kämpfe *et al.* proposed that the photoluminescence stems from geminate small polaron recombination. Assuming only a single radiative decay channel, they argued that the transient
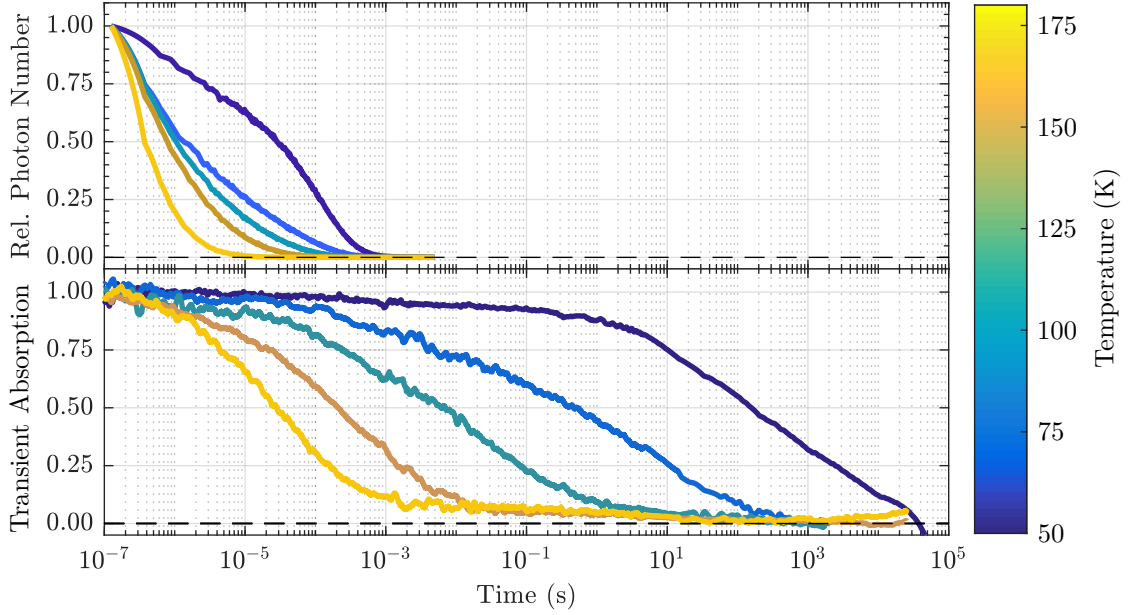
Figure 4.1 – Comparison of the photoluminescence (upper panel) and transient absorption (lower panel) decay of a magnesium-doped lithium niobate sample ($c_{Mg} = 6.5\,\text{mol\%}$) for different temperatures between $50\,\text{K}$ and $180\,\text{K}$. Only selected temperatures are shown for clarity. The photoluminescence is induced by irradiation with fs laser pulses ($\lambda = 400\,\text{nm}$, $\tau = 60\,\text{fs}$, $I = 140\,\text{TWm}^{-2}$) and detected at $\lambda_{em} = 440\,\text{nm}$, whereas the transient absorption signal probed at a wavelength of $785\,\text{nm}$ is excited by ns laser pulses ($\lambda = 532\,\text{nm}$, $\tau = 8\,\text{ns}$, $I \approx 1.7\,\text{TWm}^{-2}$). The data are also part of the publications A.3 (luminescence and absorption) and A.5 (luminescence).

luminescence signal is given by the first derivative of the small polaron number density

$$I_{\text{lum}}(t) \propto -\frac{\mathrm{d}N(t)}{\mathrm{d}t} = \beta\tau^{-\beta}t^{\beta-1}N(t) = N_0\beta\tau^{-\beta}t^{\beta-1}\exp\left[-(t/\tau)^{\beta}\right]. \qquad (4.2)$$

As it will be discussed in section 4.4, if additional channels are present, this approach leads to incorrect results. However, to test the microscopic model of small polarons at the origin of both signals in more detail, the transient absorption and emission data presented in Fig. 4.1 are fitted with Eqs. (4.1) and (4.2). The transient absorption data are fitted with Eq. (4.1) as they are proportional to the number density of absorbing particles. Since $\beta \leq 1$ the average decay time is

$$\langle\tau\rangle = (1/N_0)\int_0^\infty N(t)\mathrm{d}t = \tau\Gamma(1 + 1/\beta), \qquad (4.3)$$

where $\Gamma(...)$ is the gamma function. The mean decay times of the number densities are shown in Fig. 4.2 for different temperatures. Again it is found that both decays take place on very different time scales. While transient absorption and luminescence signals probing the same particle do not necessarily decay on the exact same time scale, especially if the radiative decay probability is time-dependent, both signals *cannot* be
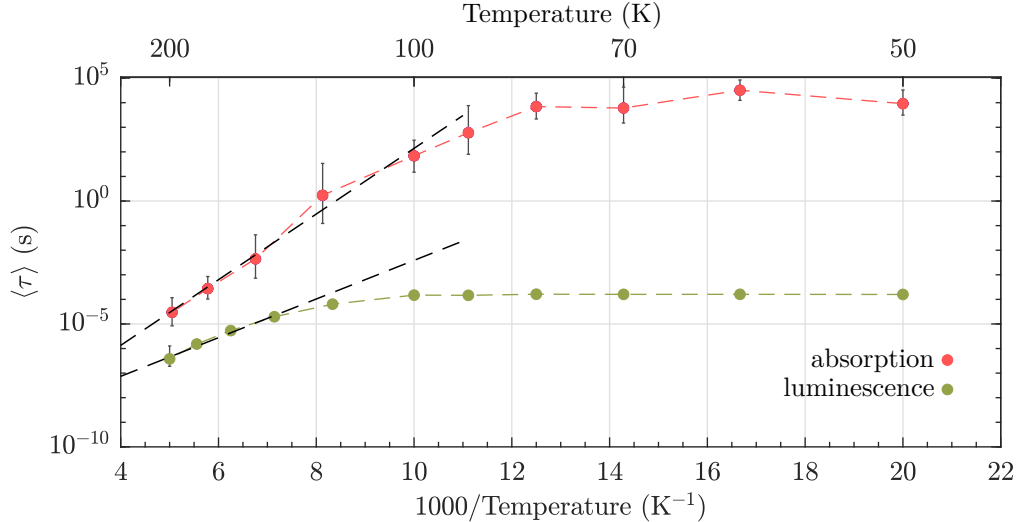
Figure 4.2 – Temperature-dependent mean decay time of transient absorption (red) and photoluminescence (green) of a magnesium-doped lithium niobate sample (c_{Mg} = $6.5\,\mathrm{mol}\%$). Eqs. (4.1) and (4.2) are fitted to the absorption and luminescence data partly shown in Fig. 4.1. Activation energies are obtained by fitting Arrhenius functions to the data (dashed black lines).

described by a common set of decay parameters and certainly do not share the same microscopic mechanism. This is also supported by the activation energies deduced from both data sets. From transient absorption an activation energy of $E_{A,\mathrm{Abs}} = (0.26 \pm 0.06)\,\mathrm{eV}$ is found, whereas evaluating the luminescence data leads to $E_{A,\mathrm{Lum}} = (0.16 \pm 0.05)\,\mathrm{eV}$.

Additional correlated transient absorption and emission measurements are performed as well at room temperature using ultrafast spectroscopy techniques. The results, which support the conclusions here, are presented and discussed in section 5.2.

4.2.2 Fs- and ns-pulse induced transient photoluminescence

Further experimental observations that can provide information about whether geminate small polaron recombination lead to the photoluminescence of LN are intensity dependent measurements of the luminescence decay. Two-particle processes, such as small polaron recombination, typically show a dependence of the decay parameters on the particle number density, i.e., correspondingly on the intensity of the pump light. In particular, a shortening of the decay time is observed for higher number densities. For example, Beyer *et al.* found that by increasing the pump pulse intensity from about $400\,\mathrm{TWm}^{-2}$ to $2.25\,\mathrm{PWm}^{-2}$, the decay constant of small bound polarons decreases by two orders of magnitude [44]. Kämpfe *et al.* observed no change of the luminescence decay parameters in ns-pulse-induced processes over a pump pulse intensity range of two orders of magnitude (average pump power $40\,\mathrm{GWm}^{-2}$) [56]. To extend this moderate range without increasing the average power above the damage threshold of the material,

64

temperature-dependent transient photoluminescence induced by ns- and fs-laser pulses are compared. The pump intensities are $100\,\mathrm{GWm}^{-2}$ (ns pulse) and $140\,\mathrm{TWm}^{-2}$ (fs pulse), hence differing by three orders of magnitude. Both measurements are shown in Fig. 4.3 for temperatures between $24\,\mathrm{K}$ and $160\,\mathrm{K}$. Apart from a clearly increased signal-to-noise ratio in case of the fs-pulse induced measurements, there is no deviation at first glance. For a more detailed analysis, the data are again fitted with Eq. (4.2). The fit parameters τ and β are shown in Fig. 4.4. Obviously, a detailed examination of the fitting parameters does not reveal any significant deviations either. Although this is another indication that the luminescence is not caused by a two-particle process, it should be noted that the pump intensities used here are orders of magnitude smaller than in Ref. [44]. It may be possible that a certain intensity and therefore number density threshold has to be surpassed before a detectable decrease is observed. However, the data presented in Ref. [44] do not indicate such threshold in the low TWm^{-2} regime.
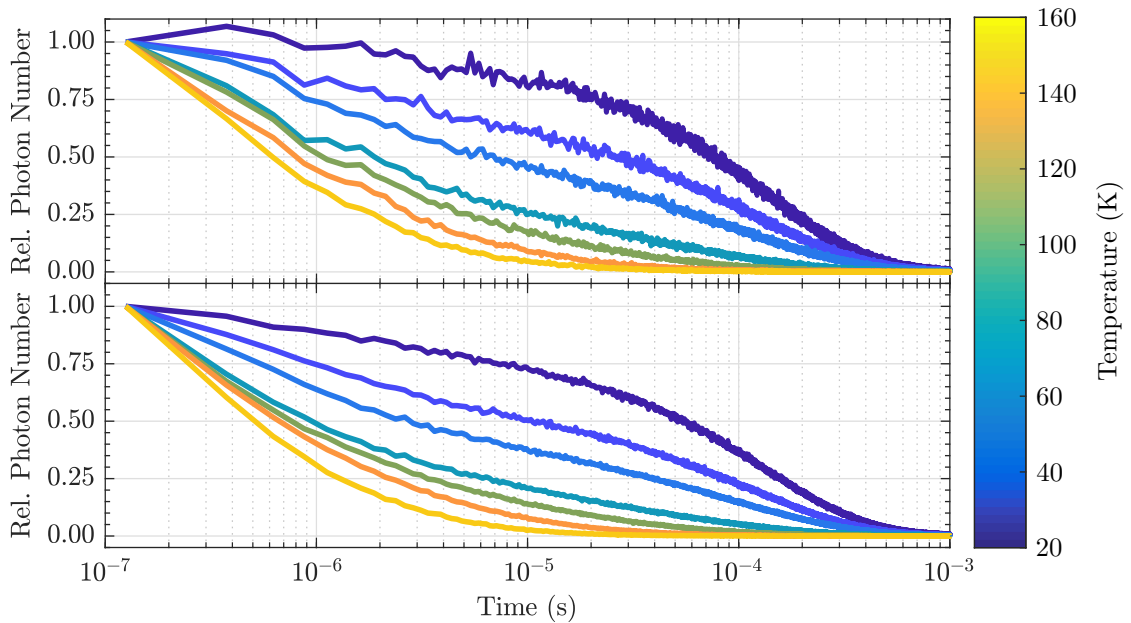
Figure 4.3 – Comparison of the transient photoluminescence of a magnesium-doped lithium niobate sample ($\mathrm{c_{Mg}} = 6.5\,\mathrm{mol\%}$) induced by ns laser pulses ($\tau = 8\,\mathrm{ns}$, $\lambda = 355\,\mathrm{nm}$, $I \approx 100\,\mathrm{GWm}^{-2}$, upper panel) and fs laser pulses ($\tau = 60\,\mathrm{fs}$, $\lambda = 400\,\mathrm{nm}$, $I = 140\,\mathrm{TWm}^{-2}$, lower panel) for different temperatures between $24\,\mathrm{K}$ and $160\,\mathrm{K}$. The photoluminescence is measured with a photomultiplier and a gated photon counter at an emission wavelength of $\lambda_{\mathrm{em}} = 460\,\mathrm{nm}$. Both are recorded at a laser pulse repetition rate of $10\,\mathrm{Hz}$. The luminescence data induced by ns-laser pulses can be found in the publication A.1.

4.2.3 Temperature dependence of the decay shape

The third indication, which contradicts the theory of geminate small polaron recombination at the origin of photoluminescence in LN, is the temperature behavior of the
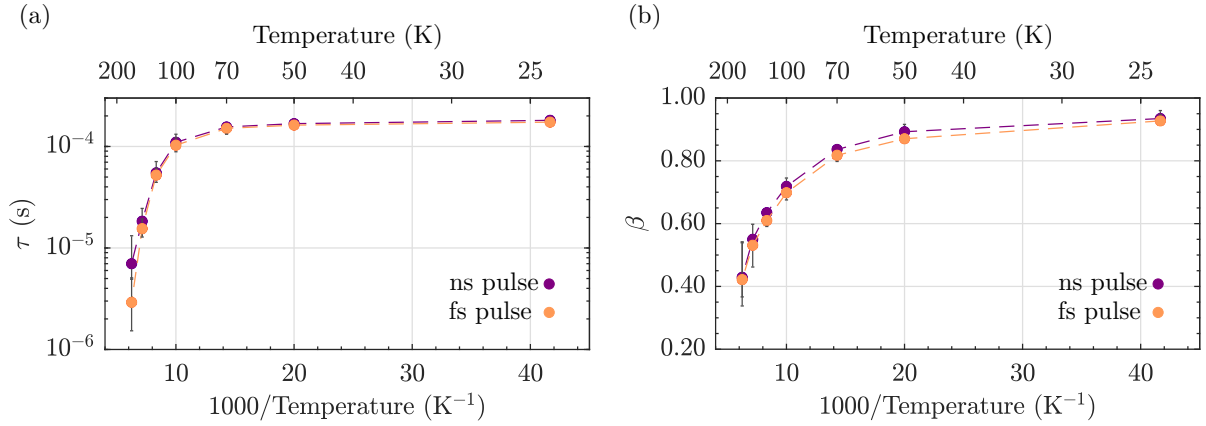
Figure 4.4 – Parameters obtained from fitting Eq. (4.2) to the data partly shown in Fig. 4.3.

stretching factor β already mentioned in section 4.1 and shown in Fig. 4.4 (b). First of all, a stretched-exponential decay can be considered as the superposition of exponential decays with different decay constants. The stretching factor β thereby measures the width of this decay constant distribution: the smaller beta is, the wider the distribution, i.e., the more different decay constants underlie the measured decay. In the context of ordered solid state systems, the appearance of stretched-exponential decays is a general feature of hopping transport with randomly distributed mobile particles and traps in the lattice [138]. For example in case of trap saturation, a random walk-type hopping transport of small polarons leads to a stretched-exponential decay of their number density even in absence of energetic or structural disorder [139].

For small polarons in LN it has been observed that the stretching factor increases with increasing temperature (e.g. section 4.1 and Ref. [39]). Thus, it appears that the distribution of the decay constants becomes narrower. This may be interpreted as an increased mobility of the polarons [39]. However, as shown in section 4.1, Fig. 4.4 and Ref. [56], an opposite temperature behavior of the stretching factor is observed, when extracted from luminescence data via Eq. (4.2). This contradicts the polaron recombination hypothesis, as in two different measurements, the same particle appears more and less mobile simultaneously.

As an alternative scenario, the radiative decay of STEs is proposed as the cause of luminescence (cf. section 4.1). Since both recombination partners move through the material as a unit, this intrinsic recombination should lead to an exponential decay of the luminescence signal. The stretched-exponential behavior that is observed is then attributed to pinning at defect centers, where a nonradiative recombination takes place. This model qualitatively reflects the observed temperature-dependent stretching factor: at low temperatures a value near one is observed. It is interpreted by a very low mobility of the STEs, which remain at one site and decay there radiatively. With increasing temperatures, the particles become increasingly mobile and start to hop through the lattice. Pinned on a defect site they can no longer recombine radiatively. The fraction

of the population which reaches a pinning center follows a stretched-exponential decay. As the portion of hopping and pinned STEs increases with higher temperature, the decay appears increasingly stretched and the effective β value decreases. Accordingly, this model argues with the temperature behavior of the stretching factor known for random walk hopping, which is implicitly 'subtracted' from the intrinsic $\beta = 1$ value.

Based on the described model, a mathematical representation of the number density can be found, explicitly considering the two decay channels. The starting point is the first-order differential equation

$$\frac{\mathrm{d}N}{\mathrm{d}t} = \gamma(t)N(t), \tag{4.4}$$

where $N(t)$ is the number density (or concentration) of the self-trapped excitons and $\gamma(t)$ is their time-dependent decay rate. The latter is the sum of contributions from the radiative and non-radiative decay channels

$$\gamma(t) = \gamma_{\mathrm{r}} + \gamma_{\mathrm{nr}}(t). \tag{4.5}$$

The indices r and nr denote the two channels. The radiative one is local and time-independent, whereas the non-radiative channel, describing the hopping and pinning of the excitons, is time-dependent

$$\begin{aligned} \gamma_{\mathrm{r}} &= \tau_{\mathrm{r}}^{-1} \\ \gamma_{\mathrm{nr}} &= \beta\, t^{\beta-1} \tau_{\mathrm{nr}}^{-\beta}. \end{aligned} \tag{4.6}$$

The non-radiative decay rate is defined in such a way that this channel alone would again result in a Kohlrausch-Williams-Watts stretched-exponential function for the number density according to Eq. (4.1). With these decay rates the first-order rate equation (4.4) reads

$$\frac{\mathrm{d}N}{\mathrm{d}t} = (\gamma_{\mathrm{r}} + \gamma_{\mathrm{nr}}(t))N(t) = \left(\tau_{\mathrm{r}}^{-1} + \beta t^{\beta-1}\tau_{\mathrm{nr}}^{-\beta}\right)N(t), \tag{4.7}$$

which is easily solved leading to the time-dependent number density

$$N(t) = N_0 \exp\left[-\left(\frac{t}{\tau_{\mathrm{r}}}\right) - \left(\frac{t}{\tau_{\mathrm{nr}}}\right)^{\beta}\right] \tag{4.8}$$

with $N_0 = N(0)$. A special case of this function, i.e., with $\beta = 1/3$, has already been used to describe 1D diffusion of polaronic excitons to quenching centers in emissive conjugated polymers [140].

The approximation used in section 4.1 and Ref. [56] linking the measured luminescence intensity with the temporal derivative of the particle number density is valid if only a single (radiative) decay channel exists or if both channels exhibit the same time dependence. The latter case will be discussed in detail in section 4.4. Since here recombination paths with different decay rates are present, the general formula

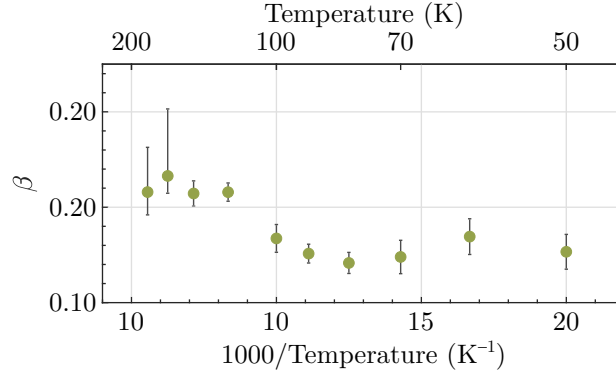$$I_{\mathrm{lum}}(t) \propto \gamma_{\mathrm{r}} N(t) \tag{4.9}$$

Figure 4.5 – Temperature-dependent stretching factor β obtained by fitting Eq. (4.10) to transient photoluminescence data partly shown in the upper panel of Fig. 4.1. The values are also presented in the publication A.3.

has to be used. With the number density of self-trapped excitons given by Eq. (4.8), the luminescence intensity reads

$$I_{\text{lum}}(t) \propto \tau_{\text{r}}^{-1} N_0 \exp\left[-\left(\frac{t}{\tau_{\text{r}}}\right) - \left(\frac{t}{\tau_{\text{nr}}}\right)^{\beta} \right]. \tag{4.10}$$

The transient photoluminescence data induced by fs-laser pulse irradiation partly shown in the upper panel of Fig. 4.1 are fitted with Eq. (4.10). The fits are presented in section 4.4 for selected temperatures. The stretching coefficients obtained from the fitting procedure are shown in Fig. 4.5. Now the stretching factor exhibits the temperature behavior known for hopping transport in LN, i.e., an increase of β with increasing temperatures. The trivial reason for this observation is that the local decay is now mathematically separated from the non-radiative hopping and pinning process.

Again, the mean decay time of the luminescing particles can be calculated. Since the easy expression Eq. (4.3) is not valid anymore, the general relation

$$\langle \tau \rangle = \frac{1}{N_0} \int_0^\infty N(t)\mathrm{d}t \tag{4.11}$$

is used. The result is shown in Fig. 4.6 together with the values already presented in Fig. 4.2. It is striking that the mean decay times deduced from fitting Eqs. (4.2) and (4.10) to the luminescence data differ by more than one order of magnitude for elevated temperatures, although the fitting quality is almost identical. This observation appears even more surprising considering the functions describing the particle number densities. Especially at elevated temperatures, where $\tau_{\text{nr}} \ll \tau_{\text{r}}$, Eqs. (4.1) and (4.8) are practically identical (cf. section 5.2). So how can the mean decay times calculated from these similar number density functions be so different, although the luminescence fits are more or less indistinguishable? The reason is the pre-exponential factor $t^{\beta-1}$ in Eq. (4.2). Since $\beta \leq 1$, this factor describes a power law decay. For short times this contribution increases sharply and even diverges for $t \to 0$. Accordingly, the decay

already introduced by this contribution is compensated for by a larger decay time τ compared to τ_{nr} obtained from Eq. (4.10). This is in agreement with the observation that the difference between the mean decay times increases with increasing temperatures. The stretching factor in the power law decreases, which in turn increases the exponent and thus its influence on the decay time. The choice of the model approach therefore does not only have a significant impact on the temperature behavior of the stretching factor, but also on the resulting particle lifetimes.

In section 5.2 the mean decay times obtained by fitting Eq. 4.10 to the data are extended by the room temperature value in order to deduce a more robust value for the activation energy. The radiative decay time can be determined up to $120\,\mathrm{K}$. It appears to have a temperature-independent value of $\approx 220\,\mu\mathrm{s}$. Above $120\,\mathrm{K}$ $\tau_{nr} \ll \tau_r$ and τ_r can be neglected.

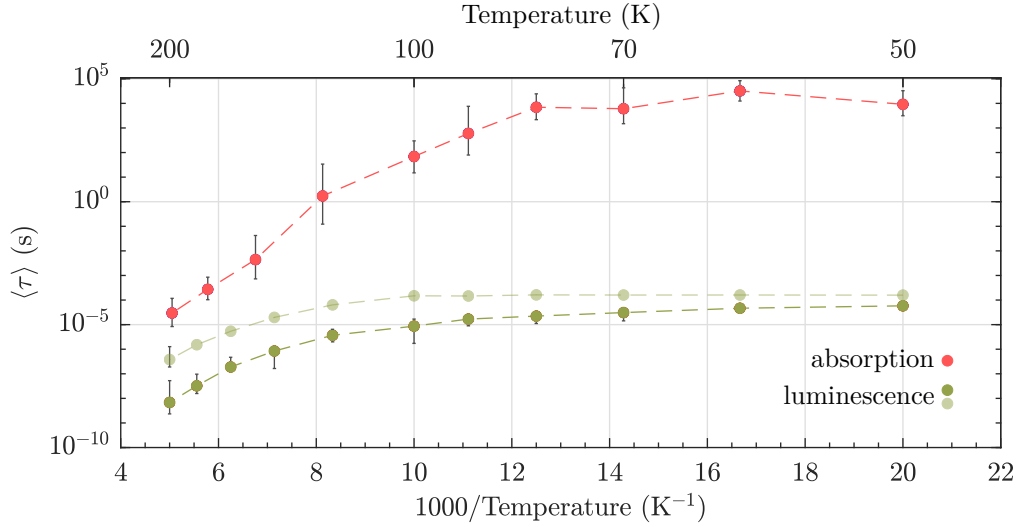**Figure 4.6** – Temperature-dependent mean decay time of transient absorption and photoluminescence of a magnesium-doped lithium niobate sample ($c_{Mg} = 6.5\,\mathrm{mol\%}$). The mean decay times are calculated via Eq. (4.11) with parameters obtained by fitting Eq. (4.1) to the absorption data (red) and Eqs. (4.2) (light green) and (4.10) (green) to the luminescence data partly shown in Fig. (4.1).

4.3 Pulse-induced transient blue absorption related with long-lived excitonic states in iron-doped lithium niobate

The author contributed to the paper *Pulse-induced transient blue absorption related with long-lived excitonic states in iron-doped lithium niobate.* The abstract is printed with friendly permission of the Optical Society of America (OSA). The complete article can be found in the appendix A.2.

- Simon Messerschmidt, Bjoern Bourdon, David Brinkmann, Andreas Krampf, Laura Vittadello, and Mirco Imlau
  Pulse-induced transient blue absorption related with long-lived excitonic states in iron-doped lithium niobate
  Opt. Mater. Express **9**, 2748-2760 (2019); doi: 10.1364/OME.9.002748

  Abstract: Transient absorption is studied in Fe-doped lithium niobate single crystals with the goal to control and probe a blue absorption feature related with excitonic states bound to Fe_{Li} defect centers. The exciton absorption is deduced from the comparison of ns-pump, supercontinuum-probe spectra obtained in crystals with different Fe-concentration and $Fe_{Li}^{2+/3+}$-ratio, at different pulse peak and photon energies as well as by signal separation taking well-known small polaron absorption bands into account. As a result, a broad-band absorption feature is deduced being characterized by an absorption cross-section of up to $\sigma^{max}(2.85\,\mathrm{eV}) = (4 \pm 2) \cdot 10^{-22}\,\mathrm{m^2}$. The band peaks at about $2.85\,\mathrm{eV}$ and can be reconstructed by the sum of two Gaussians centered at $2.2\,\mathrm{eV}$ (width $\approx 0.5\,\mathrm{eV}$) and $2.9\,\mathrm{eV}$ (width $\approx 0.4\,\mathrm{eV}$), respectively. The appropriate build-up and decay properties strongly depend on the crystals' composition as well as the incident pulse parameters. All findings are comprehensively analyzed and discussed within the model of $Fe_{Li}^{2+} - O^{-} - V_{Li}$ excitonic states.

4.4 Excitonic hopping-pinning scenarios in lithium niobate based on atomistic models

The author contributed to the paper *Excitonic hopping-pinning scenarios in lithium niobate based on atomistic models: different kinds of stretched exponential kinetics in the same system.* The abstract is printed with friendly permission of IOP Publishing Ltd. The submitted manuscript can be found in the appendix A.3.

- Gábor Corradi, Andreas Krampf, Simon Messerschmidt, Laura Vittadello and Mirco Imlau

Abstract: Based on a model of coupled processes with differently time-dependent decay kinetics we present a critical review on photoluminescence (PL) and transient absorption (TA) experiments in undoped and Mg or Fe-doped $LiNbO_3$, together with a comprehensive interpretation of visible radiative and parallel non-radiative decay processes on timescales ranging from 50 ns up to minutes. Analogies and peculiarities of the kinetics of mobile self-trapped and pinned excitons are investigated and compared with those of hopping polarons in the same system. Exciton hopping with an activation energy of $\approx$0.18 eV is shown to govern the lifetime and quenching of the short PL component above 100 K. Strong interaction between excitons and dipolar pinning defects explains the exorbitant lifetimes and large depinning energies characterizing delayed TA components in doped $LiNbO_3$, while restricted hopping of the pinned excitons is proposed to play a role in strongly delayed PL in $LiNbO_3$:Mg exhibiting a narrowed emission band due to locally reduced electron-phonon coupling. Atomistic models of pinned excitons are proposed corresponding to charge-compensated dipolar defects predicted by theories of dopant incorporation in $LiNbO_3$ and are systematically assigned to absorption bands observed near the UV edge. Excitation in these bands is shown to lead directly to pinned exciton states confirming also the previously proposed two-step exciton-decay scenario in $LiNbO_3$:Fe. Weak intrinsic sub-80 ns luminescence in congruent $LiNbO_3$ is explained as an opposite effect of enhanced electron-phonon coupling for excitons pinned on Nb_{Li} antisite defects. The comparison of the different observed stretching behaviors in the paradigmatic system $LiNbO_3$ provides an intuitive picture of the underlying physical processes. The findings are relevant not only for holographic and non-linear optical applications of $LiNbO_3$ but are of general interest also for the treatment of stretched exponential or other time-dependent kinetics in complex condensed systems ranging from nanocrystals and polymers to liquids and biophysical systems.

5 Self-trapped excitons and small polarons in lithium niobate: independent species?

One unsolved question arising from the existence of self-trapped excitons is whether their formation and disappearance is related to the established small electron and hole polarons in lithium niobate. As sketched in section 2.3.3 and especially in Fig. 2.19, a pair of oppositely-charged small polarons and a self-trapped exciton are quite similar quasi-particles and differ mainly in the separation of their charges. It is thus not trivial whether small polarons and self-trapped excitons in LN are independent, decoupled transients. Two different, simple formation models linking both species are thinkable: (i) self-trapped excitons form in response to electron-hole pair generation and subsequently break into a small polaron pair or (ii) separated small polarons form and merge into a self-trapped exciton. To address this question the formation and decay times of (free) Nb_{Nb}^{4+} small polarons and self-trapped excitons are determined experimentally and compared using (ultra)fast transient absorption and luminescence spectroscopy, respectively.

The recombination of small polarons and self-trapped excitons has already been discussed in the previous chapter. From Fig. 4.1 it is obvious that no change of transient absorption is observed during the decay of the luminescence signal. As already mentioned in the previous sections, an absorption features of mobile self-trapped excitons has not been observed in the visible or near-infrared spectral range. A decreasing absorption signal parallel to the luminescence decay is therefore not expected. However, if STE decay led to a considerable increase of the number density of small polarons, a rising absorption signal would be detected. Of course, there is a very low probability that the absorption cross sections of self-trapped excitons and pairs of electron and hole polarons coincide hiding a conversion process in the measurement. Apart from this improbable coincidence, the investigations indicate that for times much later than the formation of small polarons and self-trapped excitons, which will be discussed in detail in the next two sections, a substantial formation of further small polarons due to STE decay does not occur. In section 5.3 a possible additional luminescence signal from hot electron-hole pairs is discussed. A refined microscopic picture of strong-coupling quasi-particle formation in magnesium-doped lithium niobate closes this chapter.

5.1 Picosecond near-to-mid-infrared absorption of pulse-injected small polarons in magnesium doped lithium niobate

The author contributed to the paper *Picosecond near-to-mid-infrared absorption of pulse-injected small polarons in magnesium doped lithium niobate.* The abstract is printed with the friendly permission of the Optical Society of America (OSA). The complete article can be found in the appendix A.4.

- Felix Freytag, Phillip Booker, Gábor Corradi, Simon Messerschmidt, Andreas Krampf, and Mirco Imlau
  Picosecond near-to-mid-infrared absorption of pulse-injected small polarons in magnesium doped lithium niobate
  Opt. Mater. Express **8**, 1505-1514 (2018); doi: 10.1364/OME.8.001505

  Abstract: Femtosecond-pulse-induced ($E_{\text{pump}} = 2.5\,\text{eV}$) picosecond infrared absorption is studied in the spectral region between $0.30\,\text{eV}$ and $1.05\,\text{eV}$ in LiNbO_3:Mg. We find a non-instantaneous mid-infrared absorption peak in the time domain up to 1 ps and a broad-band, long-lived absorption (maximum at $0.85\,\text{eV}$, width $\approx 0.5\,\text{eV}$), for t > 1 ps. The modelling succeeds by considering small $\text{Nb}_{\text{Nb}}^{4+}$ electron polaron formation along the sequence: (i) two-photon injection of hot electron-hole pairs at Nb-O-octahedra, (ii) dissociation and electron cooling by electron-phonon-scattering, and (iii) electron self-localization by strong electron-phonon-coupling.

5.2 Superposed picosecond luminescence kinetics in lithium niobate revealed by means of broadband fs-fluorescence upconversion spectroscopy

The author contributed to the paper *Superposed picosecond luminescence kinetics in lithium niobate revealed by means of broadband fs-fluorescence upconversion spectroscopy.* The abstract is printed with friendly permission of Springer Nature Limited. The complete manuscript can be found in the appendix A.5.

- Andreas Krampf, Simon Messerschmidt and Mirco Imlau
  Superposed picosecond luminescence kinetics in lithium niobate revealed by means of broadband fs-fluorescence upconversion spectroscopy
  Scientific Reports **10**, 11397 (2020)

  Abstract: Various manifestations of small polarons strongly affect the linear and nonlinear optical properties of the oxide crystal lithium niobate (LiNbO$_3$, LN). While related transient absorption phenomena in LN have been extensively studied in recent decades, a sound microscopic picture describing the blue-green (photo)luminescence of lithium niobate single crystals is still missing. In particular, almost nothing is known about: (i) the luminescence build-up and (ii) its room temperature decay. We present here the results of our systematic experimental study using nominally undoped and Mg-doped LN crystals with different Mg concentration. Picosecond luminescence was detected by means of femtosecond fluorescence upconversion spectroscopy (FLUPS) extended to the inspection of oxide crystals in reflection geometry. Two distinct luminescence decay components on the picosecond time scale are revealed. While a short exponential decay is present in each sample, a longer non-exponential decay clearly depends on the crystal composition. Since transient absorption spectroscopy excludes geminate small polaron annihilation as microscopic cause of the luminescence, both decay components are discussed in the context of self-trapped exciton (STE) transport and decay.

5.3 Rate equation analysis of ps-luminescence data

In section 5.2 the luminescence kinetic traces of lithium niobate samples with different stoichiometry and magnesium doping exhibited a pronounced peak around time zero. Whereas it could not be excluded that this observation is an artefact caused by pump light scattered from a degrading surface (as discussed in section 5.2) two alternative mechanisms, that may underlie the temporal maximum, are examined in this section. These are (i) an additional luminescence signal from directly recombining hot-electron hole pairs formed upon laser pulse excitation of the crystal and (ii) a delayed small polaron absorption quenching the luminescence.

As concluded in the last section, in both scenarios small polaron and self-trapped exciton formation are regarded as independent relaxation channels of the hot electron-hole pairs. The difference between both mechanisms is how the quasi-particles contribute to the observed luminescence signal. To describe the luminescence kinetics the time-dependent number densities of the various transients have to be determined first. These in turn are given by (coupled) rate equations. The starting point of both models is the generation of hot electron-hole pairs via two-photon absorption. These populate the

states of either small polarons or STEs by relaxation, so that their number density $N_{\text{h}}(t)$ is given by the rate equation

$$\frac{\mathrm{d}N_{\text{h}}}{\mathrm{d}t} = \epsilon_{\text{h}} I_{\text{p}}^2(t) - \left(\tau_{\text{h,r}}^{-1} + \tau_{\text{h,nr}}^{-1}\right) N_{\text{h}}$$
$$= \epsilon_{\text{h}} I_{\text{p}}^2(t) - \tau_{\text{f}}^{-1} N_{\text{h}}. \tag{5.1}$$

The hot states are directly populated via two-photon absorption of the Gaussian-shaped pump pulse I_{p} having a duration of 60 fs (FWHM). The efficiency to populate this state is ϵ_{h}. Since the theoretical kinetic trace is later compared with measurements of relative photon numbers and absorbance, an absolute value of this excitation efficiency can naturally not be deduced. Two decay channels, a radiative and a nonradiative one, described by the rates $\tau_{\text{h,r}}^{-1}$ and $\tau_{\text{h,nr}}^{-1}$ may be present. Both together determine the temporal behavior of the hot state population and cannot be separated. Instead, an effective decay rate $\tau_{\text{f}}^{-1} = \tau_{\text{h,r}}^{-1} + \tau_{\text{h,nr}}^{-1}$ is observed in the experiment. It should be noted that the relaxation time into self-trapped excitons and small polarons may be different. The rate equation of the hot state can be solved analytically. Considering the boundary condition $\lim_{t\to-\infty} N_{\text{h}}(t) \to 0$, the number density reads

$$N_{\text{h}}(t) \propto \exp\left(-\frac{t}{\tau_{\text{f}}}\right) \left[1 + \mathrm{erf}\left(\frac{t}{c} - \frac{c}{2\tau_{\text{f}}}\right)\right], \tag{5.2}$$

where $\mathrm{erf}(...)$ denotes the error function and c the standard deviation of the Gaussian shaped pump pulse.

In section 5.2 the two-component luminescence decay on the picosecond time scale is assumed to be caused by radiative recombination of two species of self-trapped excitons, i.e., singlet and triplet STEs. Their population $N(t)$ is here assumed to be filled by the decay of the hot states given by Eq. (5.2). Considering a single decay channel leads to the rate equation

$$\frac{\mathrm{d}N}{\mathrm{d}t} = \tau_{\text{f}}^{-1} N_{\text{h}} - \tau^{-1} N(t). \tag{5.3}$$

The decay rate $1/\tau$ is taken from the fit values in section 5.2. Subscripts indicating singlet and triplet STEs are omitted for better readability but will be added later.

5.3.1 Hot state luminescence

The first approach to model the luminescence peak around time zero includes luminescence of hot states, i.e., from recombination of hot electron-hole pairs. The rate equation (5.3) is solved numerically for two types of self-trapped excitons with different decay rates $\tau_{\text{s-STE}}$ and $\tau_{\text{t-STE}}$, where the number density of hot electron-hole pairs is given by Eq. (5.2). The theoretical luminescence kinetic trace is now the product of the number densities and the radiative decay rates

$$I(t) = \tau_{\text{h,r}}^{-1} N_{\text{h}}(t) + \tau_{\text{s-STE,r}}^{-1} N_{\text{s-STE}}(t) + \tau_{\text{t-STE,r}}^{-1} N_{\text{t-STE}}(t). \tag{5.4}$$

Since time-independent decay rates are assumed, the intensities of the luminescence emitted by the particles differ from their number densities only by a scaling factor, the radiative decay rate. As only relative photon numbers are measured, these scaling factors cannot be deduced and serve as fit parameters. Finally, for comparison with the experimental data the theoretical intensity trace (Eq. (5.4)) is convoluted with the temporal profile $g(t)$ of the Gaussian-shaped gate pulses ($\tau = 45\,\mathrm{fs}$)

$$I_{\mathrm{exp}}(t) = (I * g)(t). \tag{5.5}$$

The cross-correlation signal of scattered pump light and the gate pulses gives the apparatus response function. It reflects how a luminescence signal described by a delta pulse would appear in the measurement and is used to define time zero. It can be fitted by a Gaussian function with a FWHM of 160 fs (see grey area in Fig. 5.1 (a)).

The experimental data, with which the calculated kinetic trace is to be compared, is shown in Fig. 5.1 (a) as yellow dots. The relative photon number values are obtained exactly as in section 5.2, but now the extraordinarily polarized part of the fluorescence light of an Mg-doped congruent LN sample is detected. The measured fluorescence kinetic trace turns out to be independent of the polarization.

The input parameters are now varied to fit the model to the experimental data. The result of this procedure using $\tau_{\mathrm{f}} = 80\,\mathrm{fs}$, $\tau_{\text{s-STE}} = 1\,\mathrm{ps}$, and $\tau_{\text{t-STE}} = 200\,\mathrm{ps}$ is shown as a red line in Fig. 5.1 (a). The latter time constant is not a fitting value, but reflects the constant contribution of the triplet STEs on the short time scale considered (cf. section 5.2). It should be noted that the determined decay behavior of these long-living transients following a stretched-exponential behavior can be modeled with a rate equation as well. However, this approach leads to unphysical results as the luminescence signal would then tend to infinity for short times. Anyhow, Fig. 5.1 (a) shows that the assumed model reflects the local maximum near time zero quite well. The modeled curve thereby only corresponds to the luminescence build-up within the error limits.

The associated kinetics of the number densities is shown in Fig. 5.1 (b). Each of them is scaled to arbitrary values for better visibility. The grey area line now reflects the squared pump intensity according to the two-photon absorption process generating hot states (yellow). These decay either via emission of a photon or relaxation to singlet (blue) and triplet (green) STEs.

5.3.2 Luminescence quenching via small polaron absorption

As an alternative approach the maximum around time zero in the luminescence kinetic traces can be modeled taking small polaron absorption of the luminescence into account. For an interim maximum to occur as a result of polaronic absorption, the small polarons have to be formed with a time delay with respect to the luminescing self-trapped excitons. The formation time via hot electron-hole pair relaxation is therefore different for the two species. Again, the rate equations mentioned above are solved to obtain the number densities of the quasi-particles involved. The luminescence intensity, however,
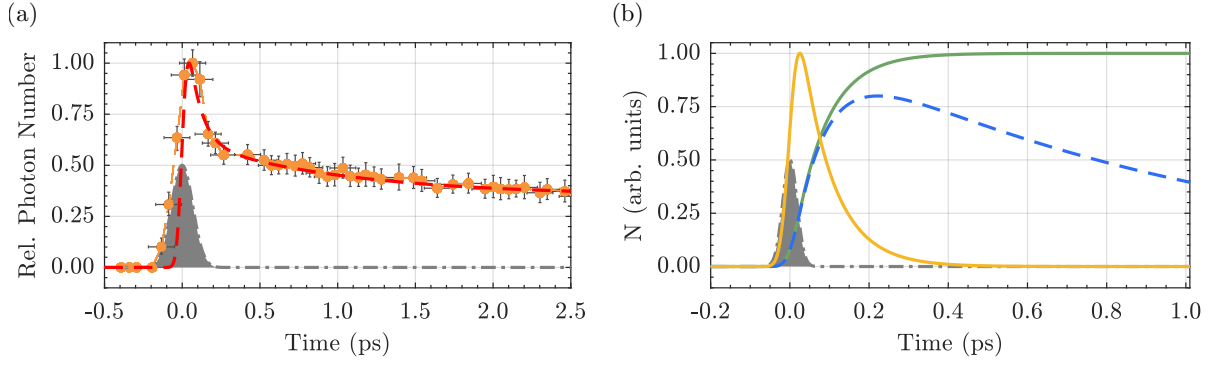
Figure 5.1 – **(a)** Normalized kinetic trace of the spectrally integrated luminescence of an Mg-doped $(6.5\,\mathrm{mol\%})$ congruently melting LN sample (yellow). In contrast to section 5.2 the extraordinarily polarized part of the fluorescence is detected. A fit according to Eq. (5.4) and the apparatus response function are depicted as dashed red line and grey area, respectively. **(b)** Kinetic traces of the number densities of optically generated transients. Hot states (yellow solid line) are directly formed upon irradiation by the Gaussian-shaped pump pulse via two-photon absorption (grey area) and subsequently decay into singlet (dashed blue line) and triplet STEs (green solid line).

is now given by the emission from the self-trapped excitons subtracted by small polaron absorption

$$I(t) = \tau_{\text{s-STE,r}}^{-1} N_{\text{s-STE}}(t) + \tau_{\text{t-STE,r}}^{-1} N_{\text{t-STE}}(t) - \sigma N_{\text{Pol}}, \qquad (5.6)$$

where σ is the small polaron absorption cross section.
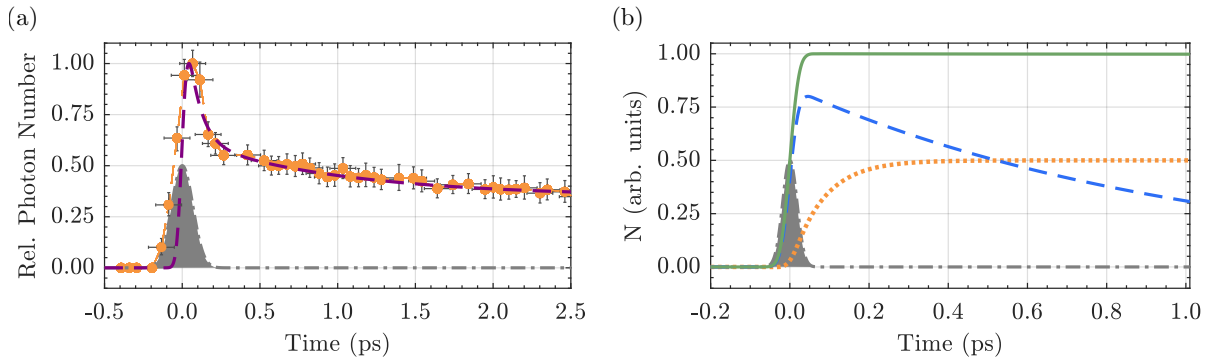
Figure 5.2 – **(a)** Normalized kinetic trace of the spectrally integrated luminescence of an Mg-doped $(6.5\,\mathrm{mol\%})$ congruently melting LN sample (yellow). In contrast to section 5.2 the extraordinarily polarized part of the fluorescence is detected. A fit according to Eq. (5.6) and the apparatus response function are depicted as dashed purple line and grey area, respectively. **(b)** Kinetic traces of the number densities of optically generated transients. Singlet (dashed blue line) and triplet (solid green line) STEs are quasi-instantaneously formed by the Gaussian-shaped pump pulse via two-photon absorption (grey area). Small polarons (dotted orange line) are formed after cooling of hot states.

Again the parameters are varied to fit the theoretical trace convoluted with the gate

pulses to the measured data. The result is depicted as purple line in Fig. 5.2 (a). A quasi-instantaneous formation of both self-trapped exciton species and a cooling time of hot electron-hole pairs relaxing to small polarons of 80 fs is used. The decay times of the self-trapped excitons are again taken from section 5.2. Since the small polaron population is constant on the time scale of a few ps (see section 5.1), no polaron decay is considered. Measuring relative photon numbers does not allow for an interpretation of the total amplitude, which would be given by the excitation efficiencies, the radiative decay times of the excitons, and the polaron absorption cross section σ. In our model approach the STEs are formed quasi-instantaneously by the pump event without any delay. Nevertheless, the rising edge of the luminescence signal is only reproduced within the error margin. The luminescence decay on the other hand is well reflected. Figure 5.2 (b) shows the number densities of the self-trapped excitons and small polarons. They are again scaled to arbitrary values. Since in this model the hot states only cause the delayed formation of small polarons, they are omitted in the figure for clarity. Their number density has the exact same kinetic trace as in Fig. 5.1 (b).

As already discussed in section 5.2, no temporal Stoke's shift could be detected for the photoluminescence of lithium niobate crystals at room temperature. Accordingly, the three observed decay components showed the same spectral fingerprint within the error of the experiment. Therefore, to account for the occurrence of the temporal luminescence maximum around time zero, the small polaron absorption has to be essentially flat in the relevant spectral range. This is checked by means of fs-pump-supercontinuum probe spectroscopy. The experimental setup is described in [141], the measurement has been conducted by Anton Pfannstiel. The result is shown in Fig. 5.3. It can be seen that the net absorption (yellow) of the transients excited via two photon absorption is indeed essentially flat in the spectral region of the observed luminescence (blue).
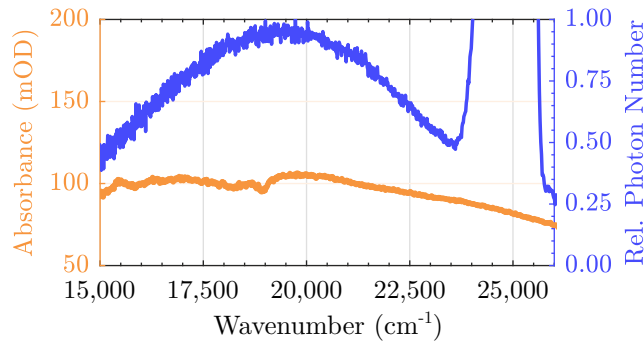

Figure 5.3 – Comparison of steady-state luminescence (blue) and transient absorption spectra (yellow) of a heavily Mg-doped congruent LN sample ($c_{Mg} = 6.5\,mol\%$) after excitation with fs laser pulses ($\tau = 60\,fs$, $\lambda = 400\,nm$).

5.3.3 Discussion

In chapter 4 and the previous sections it has already been shown that transient absorption assigned to small polaron formation and decay and luminescence occur on very different time scales. Even the room temperature kinetic traces give no indication of a relation between self-trapped exciton and small polaron dynamics. Thus, instead of a conversion of one species into another, they should be regarded as independent, competing species formed upon electron-hole generation.

However, the formation of small electron and hole polarons may explain the local maximum observed in the luminescence kinetic traces, which has not been assigned to a transient so far. Generally, it may be assumed that small polarons absorb some of the luminescence emitted by self-trapped exciton recombination. If small polaron formation, i.e., the presence of transient absorption centers, is delayed with respect to self-trapped exciton formation, a temporal maximum in the luminescence measurement could appear. In fact, two features of small polaron formation/absorption support this hypothesis. The first hint is the formation kinetic of small polarons. It does indeed appear delayed with respect to the pump event (see section 5.1 and Ref. [40]). The reason for this observation is assigned to the cooling time of hot electron hole pairs. Self-trapped excitons may form faster due to less lattice relaxation. As the relaxation is a dissipation of energy via emission of multiple phonons, a weaker relaxation may take less time. This would lead to a delay of small polaron formation not only with respect to the pump event, but also to STE formation. In contrast to the presented idea, STE formation is usually postponed with respect to small polaron formation. The reason is that unlike charge carriers excitons usually do not exhibit a considerable long-range interaction with the lattice, which lowers the energy barrier for self-trapping [73]. However, these studies are usually conducted at very low temperatures. Here, the formation times are observed at room temperature, where the thermal energy may be much higher than the energy barrier for self-trapping. Anyway, the decay time of the intermediate luminescence maximum equals the small polaron formation time extracted from separate transient absorption measurements. Both lie in the range of $\approx 100\,\text{fs}$.

The second argument is that this mechanism explains the unusual observation that there is no temporal Stoke's shift of the luminescence spectrum although clearly separable decays are revealed. The net absorption feature of free and hole polarons is more or less constant in the spectral range of the luminescence (see Fig. 5.3), which is in accordance with previous ns-pulse results [48]. Therefore, every spectral part of the luminescence would be equally quenched by polaronic absorption leading to the impression of a fast decay with the same spectral fingerprint as the longer one.

Alternatively, hot electron-hole pairs generated by band to band excitation could recombine radiatively leading to an additional luminescence signal for very short times. This decay would be a relaxation channel competing with small polaron and self-trapped exciton formation. Again the question arises how both decaying centers, i.e., self-trapped excitons and hot electron-hole pairs, can have the same spectral fingerprint. Normally, a considerable shift of the spectrum would be expected [76]. A simple explanation could

be that our experimental setup, as already discussed in section 5.2, has a limited access to the spectral shape of a very broad luminescence band.

5.4 Refined microscopic model for strong-coupling quasi-particle formation in magnesium-doped LN

Based on the observations and calculations presented in this and the last chapter, a revised microscopic model of light-induced transients in magnesium-doped lithium niobate can be proposed (cf. Fig. 5.4). The starting point is the generation of hot electron-hole pairs via absorption of super band gap photons (one or multiphoton absorption). In particular, an electron is transferred from an O^{2-} ion (valence band) to a Nb_{Nb}^{5+} ion (conduction band, 0). These hot states now have three relaxation channels: they may recombine directly (1), possibly via emission of radiation, or relax into polaronic states in the band gap. These are either self-trapped excitons located at the NbO_6 octahedra (2) or separated small electron and hole polarons (3). Either way, the investigations have shown that in the studied magnesium-doped samples, the net relaxation of the hot states occurs on the order of 100 fs. The self-trapped exciton and the small polaron pair formation appear to be independent, competing decay channels for the hot states. The self-trapped excitons can migrate through the crystal and get pinned on magnesium defects, where they form long-lived pinned excitonic states. It is also conceivable that these pinned STEs partly form directly from relaxing electron-hole pairs.
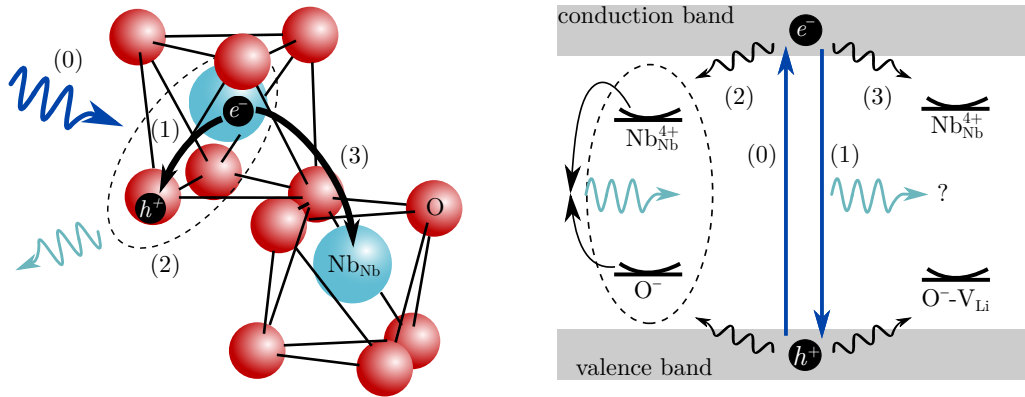
Figure 5.4 – Schematic representation of the formation of strong-coupling particles in magnesium-doped lithium niobate. Hot electron-hole pairs are formed upon super band gap photon absorption (0), i.e., via charge-transfer from O^{2-} (red) to Nb_{Nb}^{5+} ions (blue). The hot states may recombine directly (1), possibly via emission of radiation. Alternatively, they form self-trapped excitons (2) or separated small polaron pairs (3).

Depending on temperature, the relaxation of the hot and polaronic states, i.e., of electron-hole pairs, STEs, pinned STEs, and small polarons, takes place on very different time scales. Except for very low temperatures, a specific temporal order is found (Fig. 5.5): the fastest decay is ascribed to the hot electron-hole pairs occurring on the order

of 100 fs. The intrinsic, radiative decay of self-trapped excitons occurs within $\approx 200 \, \mu s$. This decay is observed for instance below $\approx 70 \, K$. For more elevated temperatures the STEs become increasingly mobile and get pinned on defect sites within $10 \, \mu s$ at $100 \, K$ or even tens of ps at room temperature. These pinned excitonic states survive for several seconds at room temperature and even thousands of seconds at $100 \, K$. In between these two time scales, small Nb_{Nb}^{4+} free polaron decay is observed. Whereas they decay within $\approx 1 \, \mu s$ at room temperature, the lifetimes are strongly increased to a few seconds when the temperature is reduced to $100 \, K$. From Fig. 5.5 it can be seen that the small polaron decay decelerates much faster than the pinned STEs decay. This is caused by their higher activation energy ($E_{A,pol} = (0.26 \pm 0.06) \, eV$ and $E_{A,p\text{-}STE} = 0.11 \, eV$ [56]). Accordingly, for temperatures much lower than $100 \, K$ the small polarons are the most durable quasi-particles.
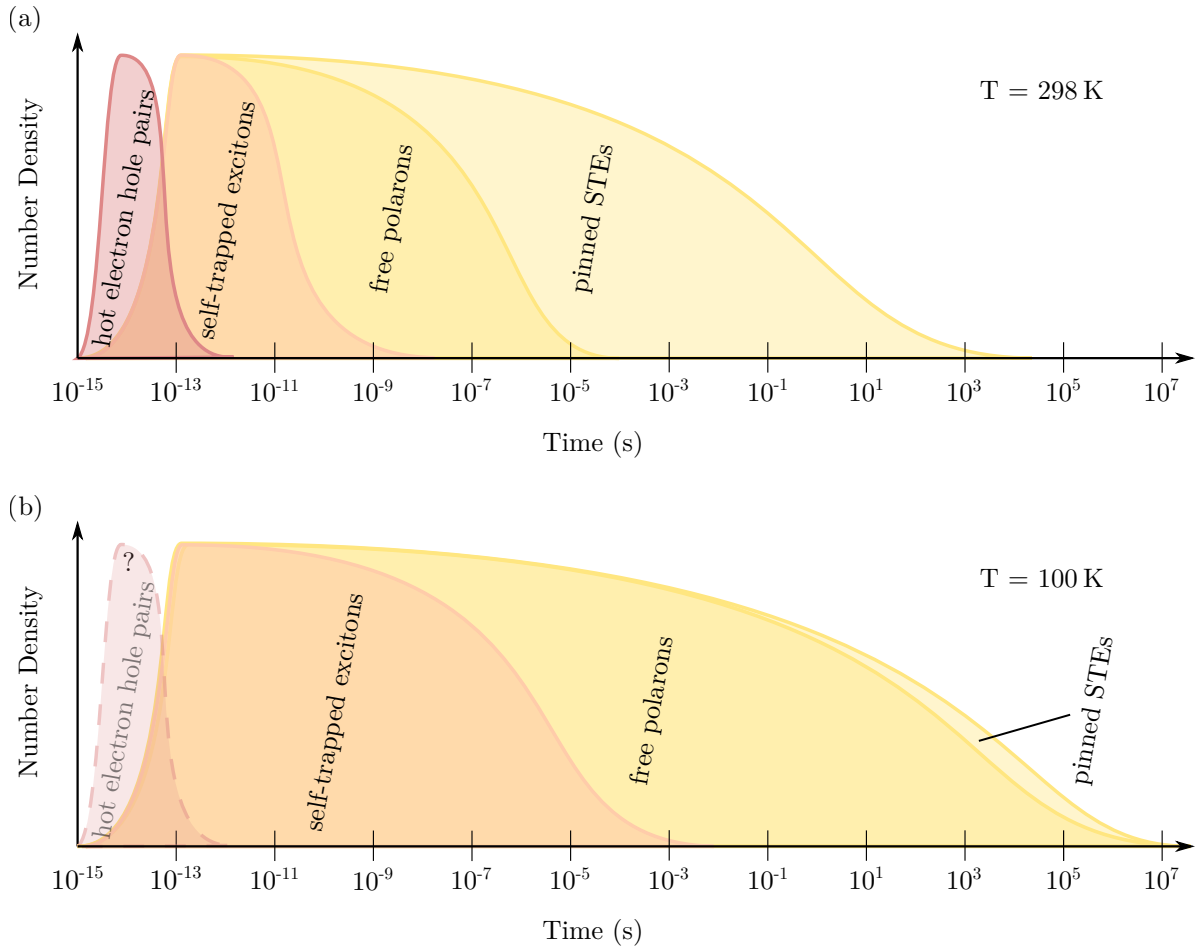

Figure 5.5 – Time scales of electron-hole pair and quasi-particle decay in magnesium-doped lithium niobate at **(a)** room temperature and **(b)** $T = 100 \, K$. In both cases hot electron-hole pairs are the fastest decaying states followed by self-trapped excitons, small polarons and STEs pinned on defects. The decay times are summarized in Table II of the publication A.3

.

6 Summary and Conclusion

In this work the transient non-instantaneous polarization, i.e., laser-pulse injected small polarons and self-trapped excitons, is studied in the perovskite-like ferroelectric lithium niobate. The investigations span a time scale from femtoseconds to several hours. It is shown that the established small polaron picture is not able to describe transient absorption and photoluminescence of lithium niobate consistently. Several strong indications are presented demonstrating that the photoluminescence cannot be caused by geminate small polaron annihilation.

Instead, the idea of radiatively decaying self-trapped excitons at the origin of the blue-green photoluminescence is revived. Excitons pinned on defect sites are proposed to lead to the already observed long-lived transient absorption in the blue spectral range in Mg- and Fe-doped crystals. Excitons pinned on iron-defects are studied in more detail. Their spectral fingerprint and absorption cross section is determined. Furthermore, it is shown that the occurrence of these pinned STEs can be tailored by chemical treatment of the samples and the experimental parameters such as the pump pulse intensity and photon energy. Based on the new experimental results and reviewing data published in literature, an atomistic picture of hopping and pinning of self-trapped excitons in lithium niobate is proposed.

The question is addressed whether small polarons and self-trapped excitons in lithium niobate are coupled species in the sense that oppositely-charged polarons may merge into self-trapped excitons or STEs break into small polaron pairs. Decay kinetics of transient absorption and luminescence assigned to free small polarons and STEs indicate that this is not the case. For a more complete picture the ultrafast time scale is investigated as well. The formation times of small polarons and STEs are determined, which both lie in the range of ≤ 200 fs. No indications are found on the (sub)picosecond time scale indicating a coupling of both quasi-particle species either.

In order to gain access to the formation of self-trapped excitons a custom-built femtosecond broadband fluorescence upconversion spectrometer is installed. Based on an already existing scheme, it is adapted to the inspection of weakly luminescent solid samples by changing to an all reflective geometry for luminescence collection. To avoid the necessity for an experimentally determined photometric correction of the used setup, an already established calculation method is extended considering the finite spectral bandwidth of the gate pulses.

The findings presented here are important not only as fundamental research, but also regarding the technical application of lithium niobate and other similar nonlinear optical crystals. The simultaneous occurrence of both small polarons and self-trapped

excitons is a rather rarely described phenomenon. Usually, the optical response of wide band gap oxide dielectrics is associated with only one of these quasi-particle species. This work may therefore be a stimulus to review the existing microscopic models for transient phenomena in other oxide dielectrics, which may help to improve their application in nonlinear optical and electro-optical devices. In this context the ultrafast transient photoluminescence spectroscopy established here for weakly luminescing solid samples may again provide valuable insight.

With respect to lithium niobate, the results do not only resolve inconsistencies between the microscopic pictures described in literature, but also provide information regarding the extends to which the propagation of ultrashort laser pulses may be affected by (pinned-)STE absorption. It is shown that tailoring of the long-lived absorption center in the blue spectral range is possible, which may be used to avoid optical damage when high repetition rates are applied.

It is important to emphasize that the microscopic model proposed in this work is mainly based on experimental indications. It is the task of further detailed theoretical investigations, e.g., via time-dependent density functional theory, to test whether the proposed model is justified. From an experimental perspective the important question remains whether (pinned-)STEs contribute to a photorefractive effect. In the experimentally easily accessible spectral range no absorption feature of mobile STEs is observed. As a complementary experimental technique, ultrafast holographic spectroscopy may reveal an excitonic contribution to photorefraction and provide further insight to STE transport and pinning phenomena.

Bibliography

[1] L. D. Landau. Über Die Bewegung der Elektronen in Kristallgitter. *Phys. Z. Sowjetunion* **3**, 644–645 (1933).

[2] W. Joosen, S. Guizard, P. Martin, G. Petite, P. Agostini, A. Dos Santos, G. Grillon, D. Hulin, A. Migus, A. Antonetti. Femtosecond multiphoton generation of the self-trapped exciton in α-SiO_2. *Appl. Phys. Lett.* **61**, 2260–2262 (1992).

[3] P. N. Saeta, B. I. Greene. Primary Relaxation Processes at the Band Edge of SiO_2. *Phys. Rev. Lett.* **70**, 3588–3591 (1993).

[4] S. Ismail-Beigi, S. G. Louie. Self-Trapped Excitons in Silicon Dioxide: Mechanism and Properties. *Phys. Rev. Lett.* **95**, 156401 (2005).

[5] H. Tang, H. Berger, P. E. Schmid, F. Lévi, G. Burri. Photoluminescence in TiO_2 anatase single crystals. *Solid State Commun.* **87**, 847–850 (1993).

[6] N. Hosaka, T. Sekiya, S. Kurita. Excitonic state in anatase TiO_2 single crystal. *J. Lumin.* **72–74**, 874–875 (1997).

[7] M. Wanatabe, S. Sasaki, T. Hayashi. Time-resolved study of photoluminescence in anatase TiO_2. *J. Lumin.* **87–89**, 1234–1236 (2000).

[8] A. Lushchik, M. Kirm, Ch. Lushchik, I. Martinson, G. Zimmerer. Luminescence of free and self-trapped excitons in wide-gap oxides. *J. Lumin.* **87–89**, 232–234 (2000).

[9] Y. Yamada, Y. Kanemitsu. Photoluminescence spectra of perovskite oxide semiconductors. *J. Lumin.* **133**, 30–34 (2013).

[10] M. Aguilar, F. Agulló López. X-ray induced processes in $SrTiO_3$. *J. Appl. Phys.* **53**, 9009–9014 (1982).

[11] D. Kéroack, Y. Lépine, J. L. Brebner. Drift mobility measurements of small-polaron transport in $SrTiO_3$. *J. Phys. C: Solid State Physics* **17**, 833–842 (1984).

[12] R. Leonelli, J. L. Brebner. Time-resolved spectroscopy of the visible emission band in strontium titanate. *Phys. Rev. B* **33**, 8649–8656 (1986).

[13] T. Hasegawa, M. Shirai, K. Tanaka. Localizing nature of photo-excited states in $SrTiO_3$. *J. Lumin.* **87–89**, 1217–1219 (2000).

[14] V. S. Vikhnin, H. Liu, W. Jia, S. Kapphan, R. Eglitis, D. Usvyat. Critical effects in optical response due to charge transfer vibronic excitons and their structure in perovskite-like systems. *J. Lumin.* **83–84**, 109–113 (1999).

[15] V. S. Vikhnin, R. I. Eglitis, S. E. Kapphan, E. A. Kotomin, G. Borstel. A new phase in ferroelectric oxides: The phase of charge transfer vibronic excitons. *EPL* **56**, 702–708 (2001).

[16] L. A. Kappers, K. L. Sweeney, L. E. Halliburton, J. H. W. Liaw. Oxygen vacancies in lithium tantalate. *Phys. Rew. B* **31**, 6792–6794 (1985).

[17] K. L. Sweeney, L. E. Halliburton, L. A. Kappers. Self-Trapped Electrons in Lithium Tantalate. *Phys. Lett. A* **116**, 81–84 (1986).

[18] G. K. Liu, V. S. Vikhnin, S. E. Kapphan. Anharmonic metastable charge transfer vibronic exciton in potassium tantalate. *Chem. Phys. Lett.* **420**, 401–404 (2006).

[19] L. Grigorjeva, D. Millers, A. I. Popov, E. A. Kotomin, E. S. Polzik. Luminescence properties of $KNbO_3$ crystals. *J. Lumin.* **72–74**, 672–674 (1997).

[20] E. A. Kotomin, R. I. Eglitis, G. Borstel. Quantum chemical modelling of electron polarons and excitons in ABO_3 perovskites. *J. Phys.: Condens. Matter* **12**, L557 (2000).

[21] Y. Qiu, K. B. Ucer, R. T. Williams, L. Grigorjeva, D. Millers, V. Pankratov. Transient absorption of polarons in $KNbO_3$. *Nucl. Instrum. Meth. B* **191**, 98–101 (2002).

[22] R. I. Eglitis, E. A. Kotomin, G. Borstel. Quantum chemical modelling of "green" luminescence in ABO_3 perovskites. *Eur. Phys. J. B* **27**, 483–486 (2002).

[23] S. Torbrügge, M. Imlau, B. Schoke, C. Merschjann, O. F. Schirmer, S. Vernay, A. Gross, V. Wesemann, D. Rytz. Optically generated small electron and hole polarons in nominally undoped and Fe-doped $KNbO_3$ investigated by transient absorption spectroscopy. *Phys. Rev. B* **78**, 125112 (2008).

[24] S. Zhu, Y. Zhu, N. Ming. Quasi-Phase-Matched Third-Harmonic Generation in a Quasi-Periodic Optical Superlattice. *Science* **278**, 843–846 (1997).

[25] J. Imbrock, D. Kip, E. Krätzig. Nonvolatile holographic storage in iron-doped lithium tantalate with continuous-wave laser light. *Opt. Lett.* **24**, 1302–1304 (1999).

[26] Y. Liu, K. Kitamura, S. Takekawa, M. Nakamura, Y. Furukawa, H. Hatano. Nonvolatile two-color holographic recording in nondoped near-stoichiometric lithium tantalate crystals with continuous-wave lasers. *Appl. Phys. Lett.* **82**, 4218–4220 (2003).

[27] K. Lengyel, Á. Péter, L. Kovács, G. Corradi, L. Pálfalvi, J. Hebling, M. Unferdorben, G. Dravecz, I. Hajdara, Zs. Szaller, K. Polgár. Growth, defect structure, and THz application of stoichiometric lithium niobate. *Appl. Phys. Rev.* **2**, 040601 (2015).

[28] J. He, C. Franchini, J. M. Rondinelli. Lithium Niobate-Type Oxides as Visible Light Photovoltaic Materials. *Chem. Mater.* **28**, 25–29 (2015).

[29] E. Bellingeri, L. Pellegrino, D. Marré, I. Pallecchi, A. S. Siri. All-SrTiO$_3$ field effect devices made by anodic oxidation of epitaxial semiconducting thin films . *J. Appl. Phys.* **94**, 5976 (2003).

[30] H. Takashima, K. Shimada, N. Miura, T. Katsumata, Y. Inaguma, K. Ueda, M. Itoh. Low-Driving-Voltage Electroluminescence in Perovskite Films. *Adv. Mater.* **21**, 3699–3702 (2009).

[31] R. S. Weis, T. K. Gaylord. Lithium niobate: Summary of physical properties and crystal structure. *Appl. Phys. A Solids and Surfaces* **37**, 191–203 (1985).

[32] M. Imlau, H. Badorreck, C. Merschjann. Optical nonlinearities of small polarons in lithium niobate. *Appl. Phys. Rev.* **2**, 040606 (2015).

[33] L. Arizmendi. Photonic applications of lithium niobate crystals. *Phys. Status Solidi (a)* **201**, 253–283 (2004).

[34] M. Bazzan, C. Sada. Optical waveguides in lithium niobate: Recent developments and applications. *Appl. Phys. Rev.* **2**, 040603 (2015).

[35] J. Li, J. Qiu, W. Guo, S. Wang, B. Ma, X. Mou, M. Tanes, H. Jiang, H. Liu. Cellular internalization of LiNbO$_3$ nanocrystals for second harmonic imaging and the effects on stem cell differentiation. *Nanoscale* **8**, 7416–7422 (2016).

[36] J. Koppitz, O. F. Schirmer, A. I. Kuznetsov. Thermal Dissociation of Bipolarons in Reduced Undoped LiNbO$_3$. *EPL* **4**, 1055–1059 (1987).

[37] B. Faust, H. Müller, O. F. Schirmer. Free small polarons in LiNbO$_3$. *Ferroelectrics* **153**, 297–302 (1994).

[38] F. Jermann, M. Simon, R. Bower, E. Krätzig, O. F. Schirmer. Light-induced absorption changes in reduced lithium niobate. *Ferroelectrics* **165**, 319–327 (1995).

[39] D. Berben, K. Buse, S. Wevering, P. Herth, M. Imlau, Th. Woike. Lifetime of small polarons in iron-doped lithium-niobate crystals. *J. Appl. Phys.* **87**, 1034–1041 (2000).

[40] Y. Qiu, K. B. Ucer, R. T. Williams. Formation time of a small electron polaron in LiNbO$_3$: measurements and interpretation. *Phys. Status Solidi (c)* **2**, 232–235 (2005).

[41] P. Herth, T. Granzow, D. Schaniel, Th. Woike, M. Imlau, E. Krätzig. Evidence for Light-Induced Hole Polarons in LiNbO$_3$. *Phys. Rev. Lett.* **95**, 067404 (2005).

[42] O. F. Schirmer. O$^-$ bound small polarons in oxide materials. *J. Phys.: Condens. Matter* **18**, R667–R704 (2006).

[43] O. F. Schirmer, M. Imlau, C. Merschjann, B. Schoke. Electron small polarons and bipolarons in LiNbO$_3$. *J. Phys.: Condens. Matter* **21**, 123201 (2009).

[44] O. Beyer, D. Maxein, Th. Woike, K. Buse. Generation of small bound polarons in lithium niobate crystals on the subpicosecond time scale. *Appl. Phys. B* **83**, 527–530 (2006).

[45] C. Merschjann, B. Schoke, D. Conradi, M. Imlau, G. Corradi, K. Polgár. Absorption cross sections and number densities of electron and hole polarons in congruently melting LiNbO$_3$. *J. Phys.: Condens. Matter* **21**, 015906 (2008).

[46] C. Merschjann, D. Berben, M. Imlau, M. Wöhlecke. Evidence for Two-Path Recombination of Photoinduced Small Polarons in Reduced LiNbO$_3$. *Phys. Rev. Lett.* **96**, 186404 (2006).

[47] C. Merschjann, B. Schoke, M. Imlau. Influence of chemical reduction on the particular number densities of light-induced small electron and hole polarons in nominally pure LiNbO$_3$. *Phys. Rev. B* **76**, 085114 (2007).

[48] D. Conradi, C. Merschjann, B. Schoke, M. Imlau, G. Corradi, K. Polgár. Influence of Mg doping on the behaviour of polaronic light-induced absorption in LiNbO$_3$. *Phys. Status Solidi (RRL)* **2**, 284–286 (2008).

[49] D. Maxein, S. Kratz, P. Reckenthaeler, J. Bückers, D. Haertle, T. Woike, K. Buse. Polarons in magnesium-doped lithium niobate crystals induced by femtosecond light pulses. *Appl. Phys. B* **92**, 543–547 (2008).

[50] H. Badorreck, S. Nolte, F. Freytag, P. Bäune, V. Dieckmann, M. Imlau. Scanning nonlinear absorption in lithium niobate over the time regime of small polaron formation. *Opt. Mater. Express* **5**, 2729–2741 (2015).

[51] S. Sasamoto, J. Hirohashi, S. Ashihara. Polaron dynamics in lithium niobate upon femtosecond pulse irradiation: Influence of magnesium doping and stoichiometry control. *J. Appl. Phys.* **105**, 083102 (2009).

[52] O. F. Schirmer, M. Imlau, C. Merschjann. Bulk photovoltaic effect of LiNbO$_3$:Fe and its small-polaron-based microscopic interpretation. *Phys. Rev. B* **83**, 165106 (2011).

[53] E. Krätzig, H. Kurz. Photorefractive and Photovoltaic Effects in Doped LiNbO$_3$. *Opt. Acta* **24**, 475–482 (1977).

[54] F. Jermann, M. Simon, E. Krätzig. Photorefractive properties of congruent and stoichiometric lithium niobate at high light intensities. *J. Opt. Soc. Am. B* **12**, 2066–2070 (1995).

[55] K. Buse, A. Adibi, D. Psaltis. Non-volatile holographic storage in doubly doped lithium niobate crystals. *Nature* **393**, 665–668 (1998).

[56] T. Kämpfe, A. Haußmann, L. M. Eng, P. Reichenbach, A. Thiessen, T. Woike, R. Steudtner. Time-resolved photoluminescence spectroscopy of Nb$_{Nb}^{4+}$ and O$^-$ polarons in LiNbO$_3$ single crystals. *Phys. Rev. B* **93**, 174116 (2016).

[57] P. Reichenbach, T. Kämpfe, A. Haußmann, A. Thiessen, T. Woike, R. Steudtner, L. Kocsor, Zs. Szaller, L. Kovács, L. M. Eng. Polaron-Mediated Luminescence in Lithium Niobate and Lithium Tantalate and Its Domain Contrast. *Crystals* **8**, 214 (2018).

[58] G. Blasse, A. Bril. The Influence of Crystal Structure on the Fluorescence of Oxidic Niobates and Related Compounds. *Z. Phys. Chem.* **57**, 187–202 (1968).

[59] D. M. Krol, G. Blasse, R. C. Powell. The influence of the Li/Nb ratio on the luminescence properties of LiNbO$_3$. *J. Chem. Phys.* **73**, 163–166 (1980).

[60] G. Blasse, L. G. J. De Haart. The nature of the luminescence of niobates MNbo3 (M = Li, Na, K). *Mater. Chem. Phys.* **14**, 481–484 (1986).

[61] M. H. J. Emond, M. Wiegel, G. Blasse, R. Feigelson. Luminescence of stoichiometric lithium niobate crystals. *Mat. Res. Bull.* **28**, 1025–1028 (1993).

[62] M. Wiegel, M. H. J. Emond, E. R. Stobbe, G. Blasse. Luminescence of alkali tantalates and niobates. *J. Phys. Chem. Solids* **55**, 773–778 (1994).

[63] H. Mahr, M. D. Hirsch. An optical up-conversion light gate with picosecond resolution. *Opt. Commun.* **13**, 96–99 (1975).

[64] L. Zhao, J. L. Pérez Lustres, V. Farztdinov, N. P. Ernsting. Femtosecond fluorescence spectroscopy by upconversion with tilted gate pulses. *Phys. Chem. Chem. Phys.* **7**, 1716–1725 (2005).

[65] X.-X. Zhang, C. Würth, L. Zhao, U. Resch-Genger, N. P. Ernsting, M. Sajadi. Femtosecond broadband fluorescence upconversion spectroscopy: Improved setup and photometric correction. *Rev. Sci. Instrum.* **82**, 063108 (2011).

[66] M. Sajadi, M. Quick, N. P. Ernsting. Femtosecond broadband fluorescence spectroscopy by down- and up-conversion in β-barium borate crystals. *Appl. Phys. Lett.* **103**, 173514 (2013).

[67] M. Gerecke, G. Bierhance, M. Gutmann, N. P. Ernsting, A. Rosspeintner. Femtosecond broadband fluorescence upconversion spectroscopy: Spectral coverage versus efficiency. *Rev. Sci. Instrum.* **87**, 053115 (2016).

[68] R. Boyd. *Nonlinear Optics.* Elsevir (2008).

[69] P. N. Butcher, D. Cotter. *The Elements of Nonlinear Optics.* Cambridge University Press (1990).

[70] F. Zernike, J. E. Midwinter. *Applied Nonlinear Optics.* John Wiley & Sons Inc. (1973).

[71] A. Yariv. *Quantum Electronics.* John Wiley & Sons, Inc. (1988).

[72] J.-C. Diels, W. Rudolph. *Ultrashort Laser Pulse Phenomena.* Elsevir (2006).

[73] D. Emin. *Polarons.* Cambridge University Press (2013).

[74] K. S. Song, R. T. Williams. *Self-Trapped Excitons.* Springer Series in Solid-State Sciences Springer-Verlag Berlin Heidelberg (1993).

[75] D. Emin. Small polarons. *Phys. Today* **35**, 34–40 (1982).

[76] Y. Toyozawa. *Optical Processes in Solids.* Cambridge University Press (2003).

[77] D. Emin, T. Holstein. Adiabatic Theory of an Electron in a Deformable Continuum. *Phys. Rev. Lett.* **36**, 323–326 (1976).

[78] E. Gorham-Bergeron, D. Emin. Phonon-assisted hopping due to interaction with both acoustical and optical phonons. *Phys. Rev. B* **15**, 3667–3680 (1977).

[79] T. Holstein. Studies of Polaron Motion: Part II. The "small" polaron. *Ann. Phys. (NY)* **8**, 343–389 (1959).

[80] Y. Toyozawa. Self-Trapping of an Electron by the Acoustical Mode of Lattice Vibration. I. *Prog. Theor. Phys.* **26**, 29–44 (1961).

[81] D. Emin. Formation and hopping motion of molecular polarons. *Phys. Rev. B* **61**, 14543–14553 (2000).

[82] N. F. Mott, A. M. Stoneham. The lifetime of electrons, holes and excitons before self-trapping. *J. Phys. C: Solid State Physics* **10**, 3391–3398 (1977).

[83] D. L. Dexter, C. C. Klick, G. A. Russel. Criterion for the Occurrence of Luminescence. *Phys. Rev.* **100**, 603–605 (1955).

[84] R. H. Bartram, A. M. Stoneham. On the luminescence and absence of luminescence of F centers. *Solid State Commun.* **17**, 1593–1598 (1975).

[85] I. Pelant, J. Valenta. *Luminescence Spectroscopy of Semiconductors*. OUP Oxford (2012).

[86] C. E. Tyner, W. D. Drotning, H. G. Drickamer. Asymmetric line shapes of localized optical excitations in condensed systems. *J. Appl. Phys.* **47**, 1044–1047 (1976).

[87] S. Suzuki, K. Tanimura, N. Itoh, K. S. Song. Shape of the π-Luminescence band in NaCl: Adiabatic potential surface at the lowest state of the self-trapped exciton. *J. Phys.: Condens. Matter* **1**, 6993–6999 (1989).

[88] D. Emin. Optical properties of large and small polarons and bipolarons. *Phys. Rev. B* **48**, 13691–13702 (1993).

[89] T. Holstein. Studies of Polaron Motion: Part I. The Molecular-Crystal Model. *Ann. Phys. (NY)* **8**, 325–342 (1959).

[90] D. Emin. Generalized Adiabatic Polaron Hopping: Meyer-Neldel Compensation and Poole-Frenkel Behavior. *Phys. Rev. Lett.* **100**, 166602 (2008).

[91] D. Emin. Correlated Small-Polaron Hopping Motion. *Phys. Rev. Lett.* **25**, 1751–1755 (1970).

[92] D. Emin. Lattice Relaxation and Small-Polaron Hopping Motion. *Phys. Rev. B* **4**, 3639–3651 (1971).

[93] D. Emin. Phonon-assisted transition rates I. Optical-phonon-assisted hopping in solids. *Adv. Phys.* **24**, 305–348 (1975).

[94] D. Emin. Semiclassical small-polaron hopping in a generalized molecular-crystal model. *Phys. Rev. B* **43**, 11720–11724 (1991).

[95] D. Emin. Barrier to recombination of oppositely charged large polarons. *J. Appl. Phys.* **123**, 055105 (2018).

[96] T. Volk, M. Wöhlecke. *Lithium Niobate*. Springer-Verlag Berlin Heidelberg (2008).

[97] D. E. Zelmon, D. L. Small, D. Jundt. Infrared corrected Sellmeier coefficients for congruently grown lithium niobate and 5 mol.% magnesium oxide-doped lithium niobate. *J. Opt. Soc. Am. B* **14**, 3319–3322 (1997).

[98] P. F. Bordui, R. G. Norwood, D. H. Jundt, M. M. Fejer. Preparation and characterization of off-congruent lithium niobate crystals. *J. Appl. Phys.* **71**, 875–879 (1992).

[99] K. Polgár, Á. Péter, L. Kovács, G. Corradi, Zs. Szaller. Growth of stoichiometric LiNbO₃ single crystals by top seeded solution growth method. *J. Cryst. Growth* **177**, 211–216 (1997).

[100] K. Kitamura, J. K. Yamamoto, N. Iyi, S. Kimura, T. Hayashi. Stoichiometric LiNbO₃ single crystal growth by double crucible Czochralski method using automatic powder supply system. *J. Cryst. Growth* **116**, 327–332 (1992).

[101] N . Iyi, K. Kitamura, F. Izumi, J. K. Yamamoto, T. Hayashi, H. Asano, S. Kimura. Comparative study of defect structures in lithium niobate with different compositions. *J. Solid State Chem.* **101**, 340–352 (1992).

[102] D. A. Bryan, R. Gerson, H. E. Tomaschke. Increased optical damage resistance in lithium niobate. *Appl. Phys. Lett.* **44**, 847–849 (1984).

[103] T. R. Volk, N. M. Rubinina, V. I. Pryalkin, V. V. Krasnikov, V. V. Volkov. Optical and non-linear optical investigations in LiNbO₃:Mg and LiNbO₃:Zn. *Ferroelectrics* **109**, 345–350 (1990).

[104] Y. Zhang, Y. H. Xu, M. H. Li, Y. Q. Zhao. Growth and properties of Zn doped lithium niobate crystal. *J. Cryst. Growth* **233**, 537–540 (2001).

[105] E. P. Kokanyan, L. Razzari, I. Christiani, V. Degiorgio, J. B. Gruber. Reduced photorefraction in hafnium-doped single-domain and periodically poled lithium niobate crystals. *Appl. Phys. Lett.* **84**, 1880–1882 (2004).

[106] L. Razzari, P. Minzioni, I. Christiani, V. Degiorgio, E. P. Kokanyan. Photorefractivity of Hafnium-doped congruent lithium-niobate crystals. *Appl. Phys. Lett.* **86**, 131914 (2005).

[107] N. Iyi, K. Kitamura, Y. Yajima, S. Kimura, Y. Furukawa, M. Sato. Defect Structure Model of MgO-Doped LiNbO₃. *J. Solid State Chem.* **118**, 148–152 (1995).

[108] Y. Furukawa, K. Kitamura, A. Alexandrovski, R. K. Route, M. M. Fejer, G. Foulon. Green-induced infrared absorption in MgO doped LiNbO₃. *Appl. Phys. Lett.* **78**, 1970–1972 (2001).

[109] J. Hirohashi, V. Pasiskevicius, S. Wang, F. Laurell. Picosecond blue-light-induced infrared absorption in single-domain and periodically poled ferroelectrics. *J. Appl. Phys.* **101**, 033105 (2007).

[110] F. Klose, M. Wöhlecke, S. Kapphan. Uv-excited luminescence of LiNbO₃ and LiNbO₃:Mg. *Ferroelectrics* **92**, 181–187 (1989).

[111] C. Fischer, M. Wöhlecke, T. Volk, N. Rubinina. Influence of the Damage Resistant Impurities Zn and Mg on the UV-Excited Luminescence in LiNbO₃. *Phys. Status Solidi (a)* **137**, 247–255 (1993).

[112] H. Lemmetyinen, N. V. Tkachenko, B. Valeur, J. Hotta, M. Ameloot, N. P. Ernsting, T. Gustavsson, N. Boens. Time-resolved fluorescence methods (IUPAC Technical Report). *Pure Appl. Chem.* **86**, 1969–1998 (2014).

[113] L. M. Bollinger, G. E. Thomas. Measurement of the Time Dependence of Scintillation Intensity by a Delayed-Coincidence Method. *Rev. Sci. Instrum.* **32**, 1044–1050 (1961).

[114] D. Phillips, R. C. Drake, D. V. O'Connor, R. L. Christensen. Time Correlated Single-Photon Counting (Tcspc) Using Laser Excitation. *Instrum. Sci. Technol.* **14**, 267–292 (1985).

[115] W. Becker. *Advanced Time-Correlated Single Photon Counting Techniques.* Springer Verlag Berlin Heidelberg (2005).

[116] I. Eom, T. Joo. Polar solvation dynamics of coumarin 153 by ultrafast time-resolved fluorescence. *J. Chem. Phys.* **131**, 244507 (2009).

[117] M. A. Kahlow, W. Jarzeba, T. P. DuBruil, P. F. Barbara. Ultrafast emission spectroscopy in the ultraviolet by time-gated upconversion. *Rev. Sci. Instrum.* **59**, 1098–1109 (1988).

[118] K. Kash, J. Shah. Carrier energy relaxation in $In_{0.53}Ga_{0.47}As$ determined from picosecond luminescence studies. *Appl. Phys. Lett.* **45**, 401–403 (1984).

[119] K. Kash, J. Shah, D. Block, A. C. Gossard, W. Wiegmann. Picosecond luminescence measurements of hot carrier relaxation in III-V semiconductors using sum frequency generation. *Physica* **134B**, 189–198 (1985).

[120] J. Shah, B. Deveaud, T. C. Damen, W. T. Tsang, A. C. Gossard, P. Lugli. Determination of Intervalley Scattering Rates in GaAs by Subpicosecond Luminescence Spectroscopy. *Phys. Rev. Lett.* **59**, 2222–2225 (1987).

[121] D. Block, J. Shah, A. C. Gossard. Femtosecond luminescence measurements in GaAs. *Solid State Commun.* **59**, 527–531 (1986).

[122] J. Shah, T. C. Damen, B. Deveaud, D. Block. Subpicosecond luminescence spectroscopy using sum frequency generation. *Appl. Phys. Lett.* **50**, 1307–1309 (1987).

[123] T. C. Damen, J. Shah. Femtosecond luminescence spectroscopy with 60 fs compressed pulses. *Appl. Phys. Lett.* **52**, 1291–1293 (1988).

[124] A. Mokhtari, J. Chesnoy, A. Laubereau. Femtosecond time- and frequency-resolved fluorescence spectroscopy of a dye molecule. *Chem. Phys. Lett.* **155**, 593–598 (1989).

[125] T. Gustavsson, G. Baldacchino, J.-C. Mialocq, S. Pommeret. A femtosecond fluorescence up-conversion study of the dynamic Stokes shift of the DCM dye molecule in polar and non polar solvents. *Chem. Phys. Lett.* **236**, 587–594 (1995).

[126] E. W. Castner, M. Maroncelli, G. R. Fleming. Subpicosecond resolution studies of solvation dynamics in polar aprotic and alcohol solvents. *J. Chem. Phys.* **86**, 1090–1097 (1987).

[127] P. Hébert, G. Baldacchino, T. Gustavsson, J.-C. Mialocq. Sub-picosecond fluorescence study of the LDS 751 dye molecule in ethanol. *Chem. Phys. Lett.* **213**, 345–350 (1993).

[128] S. Haacke, R. A. Taylor, I. Bar-Joseph, M. J. S. P. Brasil, M. Hartig, B. Deveaud. Improving the signal-to-noise ratio of femtosecond luminescence upconversion by multichannel detection. *J. Opt. Soc. Am. B* **15**, 1410–1417 (1998).

[129] G. Zgrablić, K. Voitchovsky, M. Kindermann, S. Haacke, M. Chergui. Ultrafast Excited State Dynamics of the Protonated Schiff Base of All-trans Retinal in Solvents. *Biophys. J.* **88**, 2779–2788 (2005).

[130] G. Zgrablić, S. Haacke, M. Chergui. Heterogeneity and Relaxation Dynamics of the Photoexcited Retinal Schiff Base Cation in Solution. *J. Phys. Chem. B* **113**, 4384–4393 (2009).

[131] A. Cannizzo, O. Bräm, G. Zgrablic, A. Tortschanoff, A. Ajdarzadeh Oskouei, F. van Mourik, M. Chergui. Femtosecond fluorescence upconversion setup with broadband detection in the ultraviolet. *Opt. Lett.* **32**, 3555–3557 (2007).

[132] C. Bonati, M. B. Mohamed, D. Tonti, G. Zgrablic, S. Haacke, F. van Mourik, M. Chergui. Spectral and dynamical characterization of multiexcitons in colloidal CdSe semiconductor quantum dots. *Phys. Rev. B* **71**, 205317 (2005).

[133] M. Gerecke, C. Richter, M. Quick, I. N. Ioffe, R. Mahrwald, S. A. Kovalenko, N. P. Ernsting. Effect of a Tertiary Butyl Group on Polar Solvation Dynamics in Aqueous Solution: Femtosecond Fluorescence Spectroscopy. *J. Phys. Chem. B* **121**, 9631–9638 (2017).

[134] H. Rhee, T. Joo. Noncollinear phase matching in fluorescence upconversion. *Opt. Lett.* **30**, 96–98 (2005).

[135] R. C. Miller. Optical second harmonic generation in piezoelectric crystals. *Appl. Phys. Lett.* **5**, 17–19 (1964).

[136] T. Honma, Y. Benino, T. Fujiwara, T. Komatsu, R. Sato. Technique for writing of nonlinear optical single-crystal lines in glass. *Appl. Phys. Lett.* **83**, 2796–2798 (2003).

[137] I. H. Malitson. Interspecimen Comparison of the Refractive Index of Fused Silica. *J. Opt. Soc. Am.* **55**, 1205–1209 (1965).

[138] B. Sturman, E. Podivilov, M. Gorkunov. Origin of Stretched Exponential Relaxation for Hopping-Transport Models. *Phys. Rev. Lett.* **91**, 176602 (2003).

[139] C. Merschjann, M. Imlau, H. Brüning, B. Schoke, S. Torbrügge. Nonexponential relaxation dynamics of localized carrier densities in oxide crystals without structural or energetic disorder. *Phys. Rev. B* **84**, 052302 (2011).

[140] M. Yan, L. J. Rothberg, F. Papadimitrakopoulos, M. E. Galvin, T. M. Miller. Defect Quenching of Conjugated Polymer Luminescence. *Phys. Rev. Lett.* **73**, 744–747 (1994).

[141] S. Nolte. *Mutual interactions of femtosecond pulses and transient gratings in nonlinear optical spectroscopy.* Dissertation, Osnabrück University, 2018.

A Publications

A.1 The role of self-trapped excitons in polaronic recombination processes in lithium niobate

- Simon Messerschmidt, Andreas Krampf, Felix Freytag, Mirco Imlau, Laura Vittadello, Marco Bazzan, and Gábor Corradi
  The role of self-trapped excitons in polaronic recombination processes in lithium niobate
  J. Phys.: Condens. Matter **31** (2019); doi: 10.1088/1361-648X/aaf4df

The role of self-trapped excitons in polaronic recombination processes in lithium niobate

S Messerschmidt[1], A Krampf[1], F Freytag[1], M Imlau[1], L Vittadello[2], M Bazzan[2] and G Corradi[3]

[1] School of Physics, Osnabrueck University, Barbarastraße 7, 49076 Osnabrueck, Germany
[2] Dipartimento di Fisica e Astronomia, Università di Padova, Via Marzolo 8, 35131 Padova, Italy
[3] Wigner Research Centre for Physics, Institute for Solid State Physics and Optics, Hungarian Academy of Sciences, Konkoly-Thege u. 29-33, 1121 Budapest, Hungary

E-mail: mirco.imlau@uni-osnabrueck.de

CrossMark

Abstract

Transient absorption and photoluminescence are experimentally investigated in the polaronic reference system lithium niobate, $LiNbO_3$ (LN), with the aim to refine the microscopic model of small polaron dynamics in materials with strong electron–phonon coupling. As a unique feature, our study is performed by using two different spectroscopic methods, in crystals with dopants enhancing photorefraction or damage resistance, and over a broad temperature range from 15–400 K. Although being self-consistent for particular experimental conditions, the hitherto used microscopic polaronic models reveal inconsistencies when applied to this larger data set. We show that comprehensive modeling is unlocked by the inclusion of an additional type of polaronic state with the following characteristics: (i) strongly temperature- and dopant-dependent relaxation times, (ii) an absorption feature in the blue-green spectral range, and (iii) a Kohlrausch–Williams–Watts decay shape with a temperature-dependent stretching factor $\beta(T)$ showing a behavior contrary to that of small, strong-coupling polarons. The hypothesis of self-trapped excitons (STEs, i.e. bound electron–hole pairs strongly coupled to Nb^{5+} and O^{2-} within a niobium-oxygen octahedron) and their pinning on defects as the microscopic origin of these characteristics is supported by a spectroscopic linkage of photoluminescence at low (15 K) and elevated (300 K) temperatures and explains the long-lifetime components in transient absorption as due to pinned STEs.

(Some figures may appear in colour only in the online journal)

1. Introduction

The study of charge carrier dynamics with strong-coupling to the lattice, e.g. small polarons and self-trapped excitons (STEs) in lithium niobate, $LiNbO_3$ (LN), triggered widespread attention even in nanosciences since the verification of their decisive role in the microscopic mechanisms of ferroelectric photovoltaics [1, 2], of THz wave damping [3] and laser-induced bulk damage mechanisms [4, 5], but also of photocatalysis in other oxide dielectrics like TiO_2, MgO, or ZnO [6–10]. LN is a ferroelectric oxide with excellent photoelectrical and (nonlinear) optical features, exhibits pronounced electron-/hole-phonon coupling, and hosts four different kinds of intrinsic small polarons [1, 4, 11, 12]:

the free polaron Nb_{Nb}^{4+}, the bound polaron Nb_{Li}^{4+}, the bipolaron $Nb_{Li}^{4+}:Nb_{Nb}^{4+}$, and the hole polaron $O^- - V_{Li}$. It should be noted that electrons bound to Fe_{Li}^{3+} [1, 13] or $Ti_{Li/Nb}^{4+}$ [14, 15] may also be described in the framework of the strong-coupling-polaron picture. Luminescent STEs in LN are bound electron–hole pairs with strong coupling to Nb^{5+} and O^{2-} within a single niobium-oxygen octahedron and reveal different optical properties depending whether the STEs form in stoichiometric materials or in niobium-oxygen octahedra near defect sites [16, 17]. Small polarons can be accessed by transient absorption spectroscopy (TAS) due to their characteristic, broad-band absorption features (for a rough overview of the absorption cross sections of the different polaron species see [18]), whereas time-resolved photoluminescence (TRPL) is applied for STEs, showing broad-band luminescence in the blue-green spectral range (see [11, 16, 19–23]).

To this date, carrier self-trapping and recombination in LN, i.e. polaron formation and decay, is described by microscopic models restricted to certain temperature ranges, stoichiometries and dopings of the particular study [16, 24–27], and appear consistent on their own, i.e. within the framework of given experimental boundary conditions and/or within the focus of a specific physical question. The restrictions of these models naturally contradict to the demand of a comprehensive microscopic model for pulse-induced transient absorption (TA) and luminescence in LN as reflected in detail by the following striking examples of our previous studies: (i) room temperature (RT) TA measurements of Conradi *et al* [24] in LN doped with Mg above the optical damage resistance threshold (ODRT) showed that neither a slow decay component at $\lambda = 488$ nm nor the spectral form of the TA-signal can be explained by absorption features of hole and free polarons alone. (ii) Comparing the results of Herth *et al* [25] and Berben *et al* [26] who investigated the TA in Fe:LN in the blue-green spectral range and at $\lambda = 785$ nm, respectively, several inconsistencies regarding the stretching-factor β obtained by fitting a Kohlrausch–Williams–Watts function (KWW) to the data can be found. For Fe_{Li}^{2+} polarons absorbing in the blue-green, Herth *et al* reveal β values between $0.55 - 1$, depending on the wavelength whereas Berben *et al* published $\beta \approx 0.35$ at 785 nm for the decay of bound polarons under similar experimental conditions. This is in contrast with the claim of Herth *et al*, according to which the decrease of the near-infrared signal is due to a direct transition from Nb_{Li}^{4+} bound polarons to Fe_{Li}^{3+}. In this case, the increasing numbers of Fe_{Li}^{2+} polarons should be described by the same τ and β values as obtained from the bound polaron decay function.

Studies of STEs in LN, generated also by band-to-band excitation, refer to (TR)PL measurements [19, 21, 22], usually carried out at temperatures below 100 K. At elevated temperatures, in particular at RT, the luminescence signal becomes weak so that STEs have been disregarded in small polaron dynamics, so far. Using intense laser pulses and considering the complex formation paths in the temporal regime from electron–hole-pair generation up to small polaron formation [4], a considerable number density of STEs and their contribution to the transients can per se not be neglected. Only

recently, Reichenbach *et al* showed that photoluminescence (PL) of unknown microscopic origin can be raised in LN by femtosecond pulse illumination at RT [28, 29].

Thus—despite the presence of a sound knowledge on the formation, transport and recombination of small polarons as well as on the luminescence properties of STEs—we need to accept that nearly nothing is known about the possible interplay of STEs with small polarons in LN in different temperature ranges. This interplay may occur at different stages during the various lifetimes of the individual quasi-particles. For instance small polaron and STE formation may be highly competitive in the ultrafast time range upon hot carrier excitation. On longer timescales, transformations of small polaron pairs to STEs may be discussed and may be decisive to explain the variety of optical phenomena being unexplained in TA experiments, so far.

The intention of this work is to fill this gap in knowledge by inspection of the possible role of self-trapped excitons in the polaronic recombination processes in LN in its very details. This topic inherently comprises a large degree of complexity: two different experimental techniques (TAS and PL) have to be applied, and the studies need to be performed with LN crystals with different doping below and above the photorefractive concentration threshold, over a large temperature range from about 15 K up to RT and on timescales up to minutes upon an incident pump event. Furthermore, it is challenging to uncover an appropriate experimental fingerprint to identify STEs within the polaronic recombination process. We address this complex task by stepwise answering the most obvious and driving questions, at first: (i) *are STEs at the origin of PL in LN up to room temperature?*, (ii) *is there a justified need for a revision of the microscopic polaronic recombination processes?*, and (iii) *is there any experimental fingerprint pointing to a role of STEs in the polaronic recombination process?* After (positively) answering these questions, we become able to focus our discussion on the development of a comprehensive picture for polaronic recombination including STEs and, finally, to tackle the revision of the existing microscopic model.

The paper is organized according to this concept: we first present steady state PL data over a large temperature range uncovering STEs as the microscopic origin of PL at RT (see question (i)). Then, TA data of Fe- and Mg-doped lithium niobate samples, again obtained over a large temperature and an extended wavelength range, indicate, beyond experimental incertitude, that the dynamics of TA in the red/near-infrared ($\lambda = 633$ nm or 1310 nm, $\lambda = 785$ nm), and the blue ($\lambda = 445$ nm, $\lambda = 488$ nm) spectral range cannot be correlated with each other for a number of experimental conditions in the framework of the current model proposed by Herth *et al* (see question (ii)). Finally TRPL and TA data in Mg:LN are presented and compared over a large temperature range demonstrating some distinct properties of the stretching factor β of STEs deviating from the ones of small polarons, which is used to identify STE-related phenomena in the transient blue absorption in Fe:LN (see question (iii)). Based on these results, we discuss that STEs, and mainly *pinned* STEs (STEs bound to a defect), shall be considered in polaronic recombination.

S Messerschmidt *et al*

We present a revised comprehensive microscopic model, being an extension of the original Herth model [25]. It is capable to explain all inconsistencies in TA and TRPL measurements discussed, so far.

2. Experimental methods

Three experimental techniques were used in this study.

(i) PL: Photoluminescence spectra under fs-exposure (regeneratively amplified Ti:Sapphire laser, $\tau_{FWHM} = 35$ fs, repetition rate 1 kHz; Coherent Inc., type *Astrella*) were obtained using a spectrograph with an air-cooled back-illuminated CCD-camera (Roper Scientific, type *Isoplane* and *PIXIS-UV*). The frequency doubled pump beam ($\lambda = 400$ nm) with an energy of 40 μJ per pulse was slightly focused into the sample and the luminescent emission was collected over the duration of a whole second (averaging over 1000 pump events).

(ii) TAS: Transient absorption spectroscopy using a Q-switched, frequency doubled Nd:YAG pulse laser (Innolas, type *Spitlight 600*) at a center wavelength of $\lambda = 532$ nm (ordinary light polarization) with a pulse duration of $\tau_{FWHM} = 8$ ns and a maximum pulse energy of $E_{max} \approx 290$ mJ. Pulse-induced changes of the absorption were detected by the dynamic transmission loss of continuous-wave probe lasers at wavelengths: $\lambda = 445$ nm, 488 nm, 785 nm, and 633 nm or 1310 nm (ordinary light polarization) via Si-PIN photodiodes and a fast digital storage oscilloscope (LeCroy, type *Waverunner LT584*). The recording took place in a time range from 30 ns after excitation up to the complete recovery of the sample (up to several tens of seconds). As shown by comparisons with as-grown crystals, effects of permanent photorefractive damage can be neglected for the given pulse parameters.

(iii) TRPL: Time-resolved photoluminescence measurements were performed utilizing the above mentioned ns-pulse laser, but now in the frequency tripled configuration with a center wavelength of $\lambda = 355$ nm ($E_{max} \approx 120$ mJ, extraordinary polarization). A combination of a monochromator and a photon counter with a time resolution of 250 ns was used to detect the emitted luminescence in a direction perpendicularly to the pump pulse propagation. In both setups, the measurement was triggered by a diode detecting the scattered pump light and in the case of TRPL the signal to noise ratio was improved by averaging over a total of 1000 shots.

In all setups, the sample temperature could be tuned in the range from 15 K to 400 K using a closed-cycle cryostat with optical windows.

Samples: Polished plates of thickness 1 mm of congruent lithium niobate, with the *c*-axis in the plane, with dopant concentrations of 0.1 mol% Fe or 6.5 mol% Mg in the melt were prepared by Czochralski growth at the University of Padova, and the WIGNER Research Centre for Physics Budapest by the high-temperature top-seeded solution growth method, respectively.

3. Are STE's at the origin of photoluminescence in LN up to room temperature?

The first question to be experimentally answered is whether STEs can be identified unambiguously at the origin of PL up to RT. The anchor for addressing this question is the low temperature luminescence spectrum that already has been attributed to the radiative decay of STEs, i.e. of electron–hole-pairs localized in a Nb–O-octahedron. By temperature-dependent measurements of the steady state PL signal in the temperature range from 15–300 K, we intend to gradually track the evolution of peak position and width of emission as the temperature changes. The results then allow for a clear assignment of the emission to STEs in the entire range. We note that the measurement series is performed with over-threshold Mg:LN (6.5 mol% Mg in the melt) where luminescence can be observed also at elevated temperatures.

Figure 1(a) shows the spectral fingerprints of the PL of Mg:LN in the temperature range from 15 K to 300 K for the particular case of an exposure to a train of fs-laser pulses with a center wavelength of 400 nm. The spectra, all normalized to their respective peak maxima, feature at 15 K a spectral width of $\approx$0.6 eV (FWHM) at a peak position of 2.82 eV. For the first time, clear evidence for a red-shift of the peak maximum by a total of about 0.2 eV upon heating to RT (see figure 1(b)), together with a spectral broadening to a bandwidth of $\approx$0.95 eV (see figure 1(c)), is found. It should be noted that the total PL intensity decreases by several orders of magnitude at elevated temperatures.

The data are in good agreement with low temperature data published in the literature [16, 19–21], where the PL signal was mostly assigned to the recombination of STEs, and additionally confirm the results of Reichenbach *et al* [28, 29] about RT emission in Mg:LN. Up to $T \approx 200$ K the gradual shift of the luminescence peak maximum corresponds to the Varshni equation [30] expected for luminescence also in semiconductors [31], and can be understood, together with the observed broadening as the impact of phonon coupling on the electron–hole pairs bound in the STE [32]. At higher temperatures the flattening of the peak maximum's temperature dependence, accompanied by a decreased broadening rate, may indicate the gradual appearance of a second, weak, slightly blue-shifted luminescence signal reported by Kämpfe *et al* [19]. The authors attributed it to a recombination process similar to the one at low temperatures, only involving trapping centers at larger distances with respect to the formation area.

It is thus very reasonable to conclude, that (i) up to RT the PL signal must be assigned to the radiative decay of optically generated STEs, and (ii) STEs have to be present within the entire temperature range. The assignment of the luminescence to STEs generated at early stages of pumping is strongly supported by TAS results indicating much slower transport
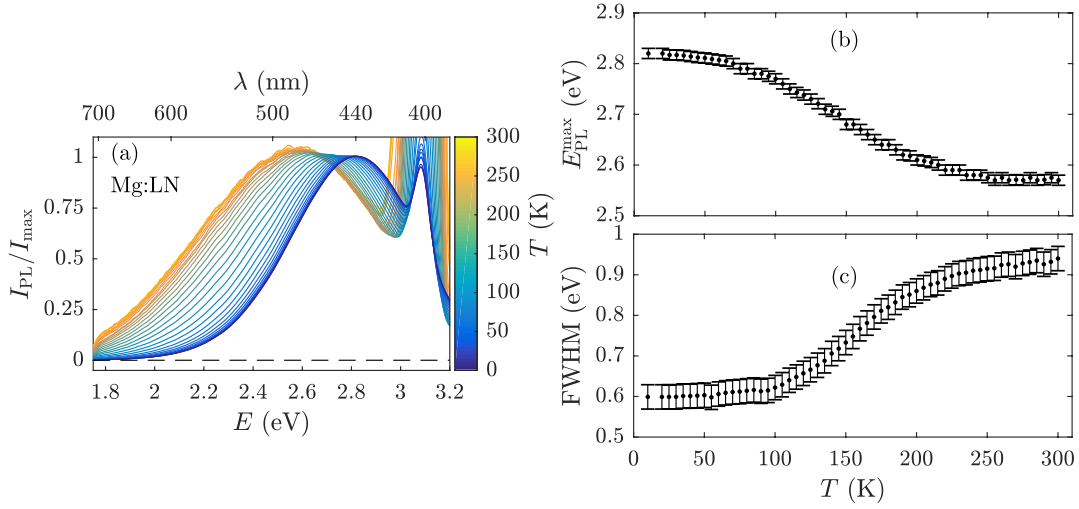
Figure 1. (a) Normalized temperature-dependent emission spectra of Mg:LN following exposure to a fs pump pulse at 400 nm. (b) Emission maximum and (c) full width at half maximum (FWHM) of the emitted luminescence as a function of temperature. A red-shift and a spectral broadening with increasing temperature can be observed.

processes for charged electron polarons (up to minutes), compared to PL dynamics, both to be presented and discussed in the forthcoming sections.

4. Is there a justified need for a revision of the microscopic polaronic recombination processes?

Previous experimental studies on polaronic recombination by means of TA already revealed a few inconsistencies in the microscopic models for polaronic recombination that could not be resolved satisfactorily, so far. In particular, inconsistencies were uncovered if the experimental boundary conditions, such as doping concentration or wavelength of inspection were changed significantly (examples are given in the introduction). We here address the question, whether it is possible to clearly demonstrate the failure of the established models under certain experimental conditions. For this purpose, we use the temperature as main tuning parameter, but also extend the spectral range of optical inspection to the ultraviolet-blue spectral range. A particular feature of the previous microscopic models, a relaxation of electrons from Nb_{Li}^{4+} to Fe_{Li}^{3+}, can specifically be inspected in the ultraviolet spectral range. Our results are finally capable to highlight the model failure by severe differences in the relaxation and rise times of the number densities of Nb_{Li}^{4+} and Fe_{Li}^{3+}, respectively, at temperatures below RT. The studies are performed (a) with Fe:LN (0.1 mol% Fe in the melt) in order to connect and compare our findings with the literature data, and (b) with over-threshold Mg:LN in order to foster the presence of STEs, but also to exclude that our findings may mainly be related to the presence of Fe_{Li}.

4.1. Transient absorption experiments in Fe-doped lithium niobate

In figure 2(a), measurements of the transient absorption on the Fe:LN sample are shown at $T = 293$ K at the probing wavelengths 445 nm, 488 nm, 633 nm, and 785 nm. The first two are monitoring the nearly coinciding Fe_{Li}^{2+} and trapped hole absorption bands and the last one roughly corresponding to the maximum of the Nb_{Li}^{4+} band, all being strongly overlapping broad asymmetric features characteristic for polarons [18]. Following the incident pump pulse at $t = 0$ s, a transient absorption appears in the near-infrared spectral range and vanishes almost completely in the microsecond range at RT. In the blue spectral range (445 nm and 488 nm), the transient absorption increases on a time scale up to several microseconds and vanishes to zero only after a few seconds.

In comparison, at $T = 198$ K (figure 2(b)), the TA signals show clearly decelerated decay dynamics affecting much stronger the blue than the red spectral range, the maximum for 445 nm and 488 nm being preceded by an almost flat stage up to the millisecond time regime. The blue absorption signal vanishes to zero only after a duration of tens of seconds. This behavior suggests a pronounced time delay between the decaying red and increasing blue transients and can, in fact, be observed for various reduction and oxidation pre-treatments, i.e. for differently adjusted $[Fe^{2+}]/[Fe^{3+}]$ ratios between 0.01 and 0.19.

Previously, Berben *et al* [26] and Herth *et al* [25] reported that a sum of stretched-exponential functions (Kohlrausch–Williams–Watts function, KWW)

$$\alpha_{li}(t,\lambda,T) = \sum_{i=1}^{N} \alpha_{li,i}^{0}(\lambda,T) \cdot \exp\left[-\left(\frac{t}{\tau_i(\lambda,T)}\right)^{\beta_i(\lambda,T)}\right], \tag{1}$$
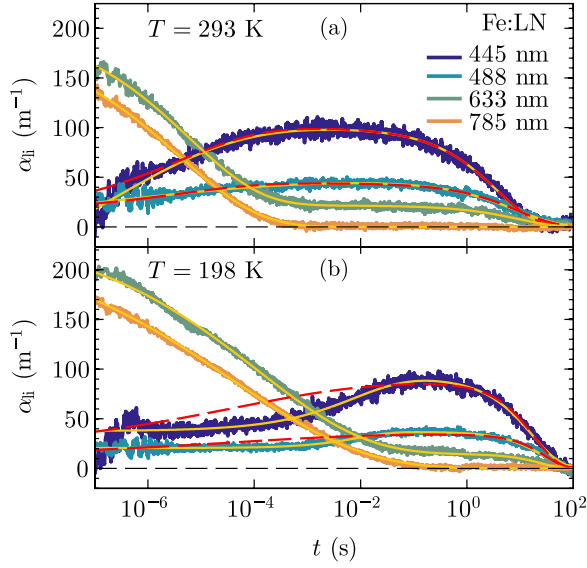
Figure 2. Temporal development of the transient absorption in Fe:LN at (a) $T = 293$ K and (b) 198 K ($I_P \approx 133$ MW cm^{-2}). The continuous yellow and dashed red lines represent fits of equation (1) to the data set. A two-term KWW-function ($N = 2$) was used at wavelengths 445 nm, 488 nm, and 633 nm, whereas a one-term function ($N = 1$) for $\lambda = 785$ nm. In the case of the continuous lines $\alpha_{li,i}^0(\lambda, T)$, $\tau_i(\lambda, T)$, and $\beta_i(\lambda, T)$ were chosen as free parameters in the fitting procedure, whereas in the case of the dashed red lines the fixed values $\tau_1(785 \text{ nm}, T)$ and $\beta_1(785 \text{ nm}, T)$ obtained in the red region were also used in the blue spectral range. The results are summarized in table 1.

is a reasonable ansatz for the description of the temporal behavior of the transient absorption in Fe:LN. Accordingly, equation (1) has been fitted to the entire experimental data set as represented in figure 2 by the continuous yellow lines. For the absorption at 785 nm a single KWW-function is used to describe the data ($N = 1$), while $N = 2$ is chosen for all other wavelengths. The obtained values of the fitting parameters providing a fair description of the results are presented in table 1 for both temperatures and all four probe wavelengths. The mean relaxation and build-up times for the various components defined by

$$\langle \tau_i(\lambda, T) \rangle = \int_0^\infty \exp\left[-(t/\tau_i(\lambda, T))^{\beta_i(\lambda, T)}\right] \mathrm{d}t$$
$$= \tau_i(\lambda, T)\Gamma\left(\frac{1}{\beta_i(\lambda, T)} + 1\right) \quad (2)$$

are also included in table 1. Here, Γ denotes the gamma function. It should be noted that the error intervals for $\langle \tau_i(\lambda, T) \rangle$ can be close to the order of the calculated value itself due to the combined error of β and τ. Still, the activation energies given in section 5 can be estimated very well, as we deal with different orders of magnitude of the decay time $\langle \tau_i(\lambda, T) \rangle$ at different temperatures. Furthermore, a large number of separate measurements over a broad temperature range is available.

At RT, all transients seem to be in accordance with the model proposed by Herth *et al* [25]. In the red spectral range,

the initial absorption change α_{li}^0 is attributed to the formation of Nb_{Li}^{4+} bound electron polarons excited either from the valence band or Fe_{Li}^{2+} to the conduction band by a two-photon or one-photon process, respectively. The initial absorption change in the blue spectral range can be assumed to originate from various sources. There is a negative contribution, i.e. induced transparency due to the transformation of the Fe_{Li}^{2+} (part or all) into non-absorbing Fe_{Li}^{3+} centers [1, 18]. A positive contribution comes from valence band holes trapped next to Li vacancies as $O^- - V_{Li}$ hole polarons together with a much smaller positive contribution coming from the overlapping absorption tail of the Nb_{Li}^{4+} bound electron polarons formed during the parallel electron trapping event.

According to the Herth model, the hopping motion of electron polarons may lead to the formation of stable or intermediate Fe_{Li}^{2+} centers, resulting in the decrease of red absorption and to the simultaneous appearance of the rising component in the blue on the microsecond timescale, which is in agreement with the coincidence of the values τ_1, β_1 and $\langle \tau_1 \rangle$ measured at RT for different wavelengths simultaneously. Some of the Fe_{Li}^{2+} centers might be metastable (e.g. due to their specific charge compensation), whereby electron trapping and release at such iron centers could occur repeatedly while electrons recombine with all available pump-induced trapped-hole centers; this process could lead to a decrease of the blue absorption of both trapped holes and metastable Fe_{Li}^{2+} centers, contributing to some (rather) long TA component. This model neglects the formation of Nb_{Li}^{4+} electron polarons between possible repeated trapping events on iron which can be justified by Nb_{Li}^{4+} lifetimes shorter by several orders of magnitude than those of metastable Fe_{Li}^{2+} centers (a similar argument explains the neglect of Nb_{Nb}^{4+} free polarons compared to Nb_{Li}^{4+} bound ones at faster stages).

In contrast, cooling the sample by $\approx$100 K (figure 2(b)) results in clear changes that are no longer consistent with Herth's model assuming the same τ_1 and β_1 for all probe wavelengths. In particular significant deviations appear in the first few milliseconds in this low temperature regime (dashed red lines in figure 2). The non-zero blue absorption remains remarkably constant during most of the Nb_{Li}^{4+} decay, prior to its rise to an interim maximum value. Adopting for $\tau_1(445/488 \text{ nm}, 198 \text{ K})$ and $\beta_1(445/488 \text{ nm}, 198 \text{ K})$ the values $\tau_1(785 \text{ nm}, 198 \text{ K})$ and $\beta_1(785 \text{ nm}, 198 \text{ K})$ obtained at 785 nm as fixed parameters, i.e. applying the Herth model, the data set cannot be reconstructed by a converging fit. The only way to reach a very good fit quality is by treating the τ_1 and β_1 parameters at various wavelengths as independent free parameters in the fitting procedures (see yellow lines in figure 2). The decay time in the near-infrared and the rise time in the blue deviate by a factor of 100 and only the mean relaxation/build-up times $\langle \tau_1(\lambda, 198 \text{ K}) \rangle$ have approximately the same values. The bound polarons thus seem to disappear without having recombined simultaneously with holes or having promptly filled $Fe_{Li}^{3+/2+}$ traps, and reappear only later as Fe_{Li}^{2+}

Table 1. Parameters of the KWW-function used to describe the TA of the 0.1 mol% Fe:LN sample at $T = 293$ K and 198 K exemplarily for the data set depicted in figure 2.

	293 K			
	445 nm	488 nm	633 nm	785 nm
$\alpha_{li,1}^0$ (m^{-1})	-72 ± 10	-25 ± 5	184 ± 10	191 ± 10
τ_1 (μs)	5 ± 3	2 ± 1	6 ± 2	4 ± 2
β_1	0.39 ± 0.04	0.30 ± 0.03	0.32 ± 0.03	0.29 ± 0.03
$\langle \tau_1 \rangle$ (μs)	18 ± 16	19 ± 17	42 ± 30	43 ± 42
$\alpha_{li,2}^0$ (m^{-1})	99 ± 10	41 ± 5	21 ± 5	—
τ_2 (s)	4 ± 2	7 ± 4	9 ± 4	—
β_2	0.61 ± 0.06	0.64 ± 0.06	0.62 ± 0.06	—
$\langle \tau_2 \rangle$ (s)	5.9 ± 3.0	9.7 ± 6.0	13 ± 6.5	—
	198 K			
	445 nm	488 nm	633 nm	785 nm
$\alpha_{li,1}^0$ (m^{-1})	-41 ± 10	-16 ± 5	227 ± 10	238 ± 10
τ_1 (μs)	$(20 \pm 10) \cdot 10^3$	$(9 \pm 4) \cdot 10^3$	121 ± 30	40 ± 10
β_1	0.52 ± 0.05	0.69 ± 0.07	0.22 ± 0.02	0.18 ± 0.01
$\langle \tau_1 \rangle$ (μs)	$(37 \pm 3) \cdot 10^3$	$(12 \pm 6) \cdot 10^3$	$(68 \pm 62) \cdot 10^3$	$(13 \pm 10) \cdot 10^3$
$\alpha_{li,2}^0$ (m^{-1})	82 ± 10	37 ± 5	14 ± 5	—
τ_2 (s)	20 ± 10	26 ± 10	25 ± 10	—
β_2	0.9 ± 0.1	0.9 ± 0.1	0.8 ± 0.08	—
$\langle \tau_2 \rangle$ (s)	21 ± 11	27 ± 11	28 ± 15	—

centers. This trend is already indicated for temperatures below $\approx$250 K.

The considerable displacement of the TA signal towards longer times and its changed shape at low temperatures have to be described by strongly increased τ_1 and β_1 values in the blue ($\lambda = 445/488$ nm) compared to a moderately rising τ_1 and decreasing β_1 in the red region. The increased stretching factor $\beta_1(488$ nm, 198 K$) = 0.69$ in the blue has to be contrasted with its decreased value $\beta_1(785$ nm, 198 K$) = 0.18$ in the red (table 1). The slow decreasing component shows an even larger β value in the blue: $\beta_2(445/488$ nm,198 K$) = 0.9$. The weakly defined mean values $\langle \tau \rangle$ show much less variation which is also due to the fact that different combinations of τ and β can, by coincidence, lead to the same value of $\langle \tau \rangle$.

Taking into account the widely accepted interpretation of β [33–35] including the attempt of Merschjann *et al* [36] to relate τ and β directly to characteristic parameters of the hopping transport (time of a single hopping event, number of hopping events, etc), means that the blue transients have a much weaker dependence on hopping history before annihilation than the respective transients in the red. While the electron polaron decay for lower temperatures is increasingly characterized by slow hopping, the blue transients become nearly mono-exponential.

These data point to a clear failure of the Herth model and support the previous reports on inconsistencies in Fe:LN crystals under rather different conditions. In particular at low temperatures and with probing wavelengths in the blue and near-infrared spectrum, we are faced by two striking experimental observations: (i) the decay of bound polaron absorption in the near-infrared is not correlated with the increase of
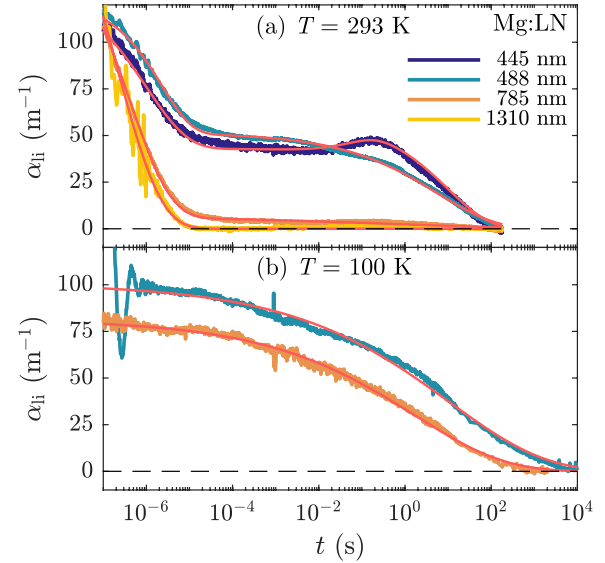

Figure 3. Temporal development of the light-induced absorption in Mg:LN at (a) $T = 293$ K and (b) $T = 100$ K for a pump pulse intensity of $I_P \approx 130$ MW cm^{-2}. The red lines represent fits of equation (1) to the experimental data. Fitting results are summarized in table 2.

the Fe$_{Li}^{2+}$ absorption anymore, and (ii) there is a strong discrepancy of the determined β value with the state-of-the-art knowledge for small, strong-coupling polaron dynamics in LN [26, 35, 37] to be further discussed in section 5. At the same time, these data are not sufficient to conclude a general failure of the Herth model, i.e. that Herths' model also fails for

Table 2. Parameters of the KWW-function used to describe the TA of the 6.5 mol% Mg:LN sample at $T = 293$ K and $T = 100$ K (figure 3).

	293 K				100 K	
	445 nm	488 nm	785 nm	1310 nm	488 nm	785 nm
$\alpha^0_{\text{li,1a}}$ (m^{-1})	90 ± 10	71 ± 10	177 ± 10	248 ± 20	100 ± 5	81 ± 10
τ_{1a} (μs)	1.0 ± 0.2	2.3 ± 0.5	0.4 ± 0.1	0.2 ± 0.1	$(10 \pm 5) \cdot 10^6$	$(1.7 \pm 1) \cdot 10^6$
β_{1a}	0.45 ± 0.1	0.62 ± 0.1	0.44 ± 0.1	0.45 ± 0.1	0.19 ± 0.01	0.19 ± 0.01
$\langle \tau_{\text{1a}} \rangle$ (μs)	2.5 ± 1.5	3.3 ± 1.1	1.0 ± 0.6	0.5 ± 0.3	$(1890 \pm 1200) \cdot 10^6$	$(321 \pm 200) \cdot 10^6$
$\alpha^0_{\text{li,1b}}$ (m^{-1})	-15 ± 5	—	—	—	—	—
τ_{1b} (ms)	70 ± 20	—	—	—	—	—
β_{1b}	0.8 ± 0.2	—	—	—	—	—
$\langle \tau_{\text{1b}} \rangle$ (ms)	79 ± 40	—	—	—	—	—
$\alpha^0_{\text{li,2}}$ (m^{-1})	58 ± 10	51 ± 5	6 ± 2	—	—	—
τ_2 (s)	10 ± 3	6 ± 2	5 ± 3	—	—	—
β_2	0.45 ± 0.05	0.32 ± 0.04	0.25 ± 0.1	—	—	—
$\langle \tau_2 \rangle$ (s)	25 ± 10	42 ± 24	120 ± 110	—	—	—

the description of TA in LN crystals of different stoichiometry and/or with/without different dopants (including non-photore-fractive defect centers). In what follows, we intend to exclude that the failure is solely related to the dominating existence of $Fe_{\text{Li}}^{2+/3+}$ by means of equivalent TAS studies with over-threshold Mg:LN.

4.2. Transient absorption experiments in Mg-doped lithium niobate

The dynamics of the transient absorption in Mg:LN at 445 nm, 488 nm, 785 nm, and 1310 nm at RT (the latter approximately centered on the broad absorption band of Nb_{Nb}^{4+} free polarons) is depicted in figure 3, showing, in addition to a fast decreasing transient on the same time scale for all wavelengths, a long-lived transient blue absorption as previously reported by Conradi *et al* [24]. However, in comparison to former studies a new probe at 445 nm was applied and we were able to observe an unexpected feature, i.e. a clear increase in the absorption at surprisingly long timescales. The newly measured transient local maximum for 445 nm is observed after a significant period (few milliseconds) of constant absorption that resembles the dominant feature of the low-temperature TA dynamics of Fe:LN. This corresponds to a small rising component (denoted by the index 1b) with a time constant $\tau_{\text{1b}}(445 \text{ nm}, 293 \text{ K}) = (70 \pm 20)$ ms. The fitting parameters derived for all KWW components in Mg:LN are summarized in table 2, essentially coinciding at RT with those reported in [24]. The fast component on the microsecond timescale (denoted by the index 1a) is decreasing in the blue region at variance from the case of Fe:LN. The slow component extends to hundreds of seconds in the visible and is absent in the infrared as in Fe:LN.

The dynamics in Mg:LN at RT should be compared to scenarios in Fe:LN taking into account the changed defect structure of Mg:LN: (i) Nb_{Li} antisites and most Fe_{Li} centers are missing as indicated by the vanishing photorefractive effect

in over-threshold crystals [38], (ii) a portion of Mg^{2+} dopant ions and some of the background Fe impurities on the ppm level are incorporated on Nb sites [39, 40], where their charge state remains fixed.

The lack of Nb_{Li} antisites results in an increase of the electron polaron hopping frequency, now occurring in the regular Nb sublattice, leading to a shortening of τ_{I} by nearly an order of magnitude, compared to Fe:LN, so that $\tau_{\text{I}}(785/1310 \text{ nm},$ RT$) \approx 0.3$ μs. Accordingly, there are even longer delays (compared to Fe:LN) between this fast decay of free polarons and the slower components in the blue. Due to the small number of Fe_{Li}^{2+} centers, a significant influence on the TA can be excluded as supported also by the monotonous decrease of the 488 nm TA signal in the entire observed temporal region. Only the small rising component τ_{1b} at 445 nm extending into the 70 ms range has to be attributed to background Fe impurities, based on the analogy with component τ_{I} in Fe:LN. The fast blue TA component in Mg:LN, temporarily locked with polaron decay monitored in the near-infrared, can be attributed to a direct process of polaron recombination with trapped-hole centers. For $T < 100$ K, TA signals in Mg:LN extend to several minutes both in the near-infrared and the blue region due to the slow hopping of polarons and delays in the recombination processes. Therefore, the three KWW-components in the blue spectral range cannot be satisfactorily distinguished anymore due to similar decay times of several overlapping TA components. A single-component fit at $T = 100$ K and $\lambda = 488$ nm yields $\tau \approx 10$ s and $\beta \approx 0.19$, and therefore $\langle \tau \rangle \approx 1.9 \cdot 10^3$ s. The latter is much longer in comparison to the value determined in the near-infrared, thus indicating the presence of the RT processes at low temperatures, as well. The values obtained for 785 nm and 488 nm are summarized in table 2.

Apart from the latter process, the RT TA-data in Mg:LN thus clearly resemble the findings in Fe:LN, and further stress the failure of the original microscopic model for polaronic recombination. Similarly to the case of Fe:LN the model cannot be
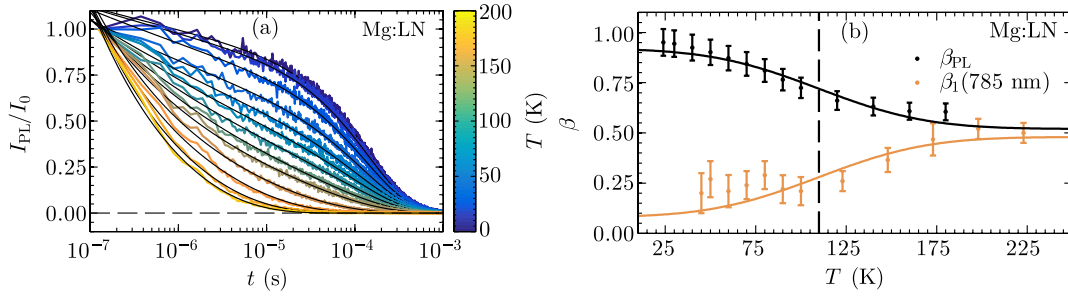
Figure 4. (a) Temporal decay of the PL intensity at 460 nm Mg:LN following exposure to a single ns laser pulse for temperatures given by the color code. The signal is normalized to the value determined at $t = 10^{-7}$ s; the black lines represent fits to the experimental data using equation (3). (b) Temperature dependence of the stretching-factors: β_{PL} (black) obtained from fitting equation (3) to the luminescence decay data and β_1(785 nm) (orange) obtained from fitting equation (1) to TA results in Mg:LN. The solid lines are phenomenological descriptions of the $\beta(T)$ behavior with an error-function. The dashed line represents a common inflection point at $T_\beta^{Mg} = (110 \pm 10)$ K.

corrected by simply considering some process of more complex type but involving only single-electron transfers. Instead, a more complex electronic center, the STE, having clear fingerprints for its identification, will be discussed in more detail below.

5. Is there any experimental fingerprint pointing to a role of STE's in the polaronic recombination process?

The PL spectra presented in section 3 clearly indicate the presence of STEs over the temperature range 15–300 K suggesting that STEs should not be neglected in non-radiative recombination processes either. In order to find the various transient manifestations of STEs, in this section temperature-dependent TRPL measurements are presented and combined with corresponding TA results. The temperature dependence of the stretching coefficient $\beta(T)$ will be shown to be an unambiguous fingerprint for a clear separation between STE-related phenomena on the one hand and processes determined by the hopping of electron polarons on the other hand. This distinction is also supported by the different Arrhenius-type activation energies obtained from the respective time constants. First we use Mg:LN in order to benefit from the comparison with the characteristic blue PL feature, then turn to the peculiarities offered by Fe:LN.

5.1. Stretching-factors and activation energies in the photoluminescence and transient absorption of Mg:LN

Figure 4(a) shows the TRPL of Mg:LN upon ns-pulse exposure at 355 nm ($I_P \approx 100$ GW m^{-2}, extraordinary polarization) for the emission wavelength of 460 nm for a series of temperatures in the broad range from 15 K to 200 K in a semi-logarithmic plot. For comparison, all data have been normalized to the maximum luminescence signal at $t = 10^{-7}$ s. With increasing temperature the luminescence decay time is found to decrease from the milli- to the microsecond time range as expected from the studies of Powell and Freed, and Fischer *et al* [21, 23]. For a quantitative analysis, and according to Zatryb *et al* [41], the evolution rate of excited emitters has to be considered, so that the first time derivative

of the stretched-exponential KWW function is used for the fitting procedure:

$$I(t, T) = I_0(T) \cdot t^{(\beta_{PL}(T)-1)} \cdot \exp\left[-\left(\frac{t}{\tau_{PL}(T)}\right)^{\beta_{PL}(T)}\right].$$
(3)

As shown by the black lines in figure 4(a), very good correspondence could be achieved between equation (3) and the experimental data using only a single KWW component with two independent fitting parameters, the stretching coefficient $\beta_{PL}(T)$ and the decay time $\tau_{PL}(T)$, giving further support to the unambiguous (STE-related) origin of the PL observed. The dependence $\beta_{PL}(T)$ depicted in figure 4(b) is in full accordance with a trend recently recognized in a smaller temperature interval by Kämpfe *et al* [19]. The change of $\beta_{PL}(T)$ is very significant and represents a transition from unity for a mono-exponential function at $T \approx 25$ K to the stretched case $\beta_{PL} \approx 0.6$ at $T \approx 180$ K (see figure 4(b)). The decay time $\tau_{PL}(T)$ remains nearly constant for temperatures below 100 K with a value of $\tau \approx 10^{-4}$ s whereas an Arrhenius-like behavior with an activation energy $E_A \approx 0.09$ eV is found for $T \gg 100$ K.

We interpret both findings by assuming that at low T the decay time of the luminescence is defined by a localized process where hopping is suppressed leading to a single exponential decay ($\beta_{PL} = 1$). As the temperature is increased above 100 K, the steep decrease of both τ and the stretching exponent β suggests that a hopping process becomes dominant. To explain the extremely low activation energy for luminescence decay, we assume that hopping of the STE as a whole is involved. In comparison, for free polaron hopping a clearly larger activation energy $E_A \approx 0.26$ eV can be derived from the observed temperature dependence of the mean relaxation time $\langle\tau_1(785 \text{ nm}, T)\rangle$ which also follows an Arrhenius behavior for $T > 100$ K in our Mg:LN sample; practically the same value has been estimated earlier as one fourth of the optical excitation energy ≈ 1 eV of Nb$_{Nb}^{4+}$ [12, 42]. Accordingly the temperature dependence of β_{PL} has to be attributed to the hopping of STEs and their subsequent localized recombination.

Comparing $\beta_{PL}(T)$ with TA measurements of β_1(785 nm, T) on Mg:LN displaying the behavior expected for polaron hopping (see figure 4(b)), it is immediately clear
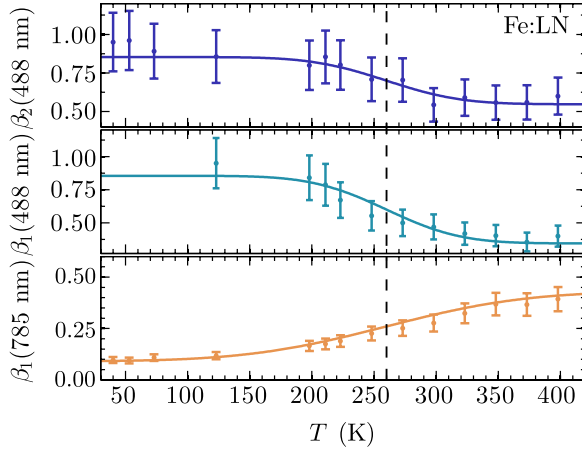
Figure 5. Temperature dependence of the stretching-factors $\beta_1(785\ \text{nm}, T)$, $\beta_1(488\ \text{nm}, T)$, and $\beta_2(488\ \text{nm}, T)$ in Fe:LN. The solid lines are qualitative descriptions of the $\beta(T)$ behavior with an error-function. The dashed line represents a common inflection point at $T_\beta^{\text{Fe}} = (260 \pm 10)$ K.

that $\beta_{\text{PL}}(T)$ exhibits a reversed temperature dependence. We chose $\lambda = 785$ nm as a probe wavelength where the largest contribution, in the absence of antisites, can be attributed to $\text{Nb}_{\text{Nb}}^{4+}$ free polarons. Both types (TRPL and TA) of temperature behavior in figure 4(b) can be described phenomenologically, e.g. by an error-function with a common inflection point at $T_\beta^{\text{Mg}} = (110 \pm 10)$ K indicating the temperature where the processes due to hopping become dominant. Thus, the given reverse type of $\beta_{\text{PL}}(T)$ dependence, can be regarded as a fingerprint of STEs, in contrast to the $\beta(T)$ behavior observed for small electron polarons; this is supported by the fact that the activation energies obtained for luminescence and red/near-infrared absorption decay are different requiring a second hopping entity, STEs. Note, that even though the transients in luminescence and absorption are on different timescales, a comparison between the $\beta(T)$ behaviors may be justified as the stretching-factor is a good indicator for the type of transport and annihilation processes involved.

5.2. Stretching-factors and activation energies in the transient absorption of Fe:LN

In this section detailed temperature-dependent measurements of the red and blue TA on Fe:LN are presented with the goal to uncover similar fingerprints. The obtained behavior of the various stretching-factors $\beta_i(\lambda, T)$ is shown in figure 5. Results in the red and blue spectral range differ in two major points: (i) with decreasing temperatures $\beta_1(T)$ is observed to decrease in the red spectral range, compared to the opposite behavior of both $\beta_1(T)$ and $\beta_2(T)$ in the blue (see figure 5, but also table 1). Both types of temperature behavior in figure 5, again, can be described by an error-function (orange and blue lines in figure 5) where $T_\beta^{\text{Fe}} = (260 \pm 10)$ K is discovered as a common inflection point. (ii) At higher temperatures, the mean decay

times $\langle \tau_i(\lambda, T) \rangle$ follow an Arrhenius behavior, however, for temperatures $T < T_\beta^{\text{Fe}}$ the mean decay times in the blue range become nearly temperature-independent. The obtained activation energy $E_A^1(785\ \text{nm}) \approx 0.37$ eV apparently corresponds to polaron hopping in the presence of antisites (to be compared to one fourth of the optical excitation energy ≈ 1.6 eV of $\text{Nb}_{\text{Li}}^{4+}$ [12]). It should be added that the most recent value of the polaron stabilization energy was determined to ≈ 0.75 eV [37]. The activation energies derived for the blue region, $E_A^1(488\ \text{nm}) \approx 0.71$ eV and $E_A^2(488\ \text{nm}) \approx 0.78$ eV are correspondingly higher and will be discussed in section 6.

The temperature dependence of the stretching exponents $\beta_1(T)$ and $\beta_2(T)$ in the blue of the TA of Fe:LN (figure 5) qualitatively shows the same fingerprint behavior as $\beta_{\text{PL}}(T)$ obtained from time-resolved luminescence measurements on Mg:LN (figure 4(b)). The similar dynamics of the considered blue transients in emission and absorption strongly suggests their common origin, namely STEs. In Mg:LN the temperature $T_\beta^{\text{Mg}} \approx 110$ K equally characterizes the onset of polaronic and excitonic hopping processes observed in transient absorption and luminescence decay, respectively. In Fe:LN, the $T_\beta^{\text{Fe}} \approx 260$ K value reflects the smaller mobility of the polarons and a parallel change in electron–phonon coupling due to the presence of antisite Nb defects, as compared to Mg:LN where antisites are absent. These findings will be used in the following section to reconsider the microscopic polaronic recombination model in LN.

6. Extension of the microscopic model by STE's and pinned STE's

So far, our analysis was able to answer the most striking questions related to the role of STEs in the polaronic recombination processes in LN. First, it is clearly demonstrated, that the observed, pulse-induced blue-green luminescence in LN can be attributed to the decay of STEs up to RT. Second, the failure of the microscopic model comprising solely small electron and hole polarons is highlighted and evident as soon as the temperature is reduced or the doping is changed. Third, the stretching factors and activation energies are recognized to yield sensitive information on the dynamics of both PL and TA indicating the presence of STEs.

As a result, it becomes necessary to extend the microscopic picture by including the additional electronic states of STEs and STEs pinned on defects, as schematically depicted in figure 6. As a matter of fact, such pinned STEs (i) may be long-lived, (ii) should absorb in the blue spectral range, and (iii) decay preferably non-radiatively and, thus, considerably contribute to the blue TA in LN crystals. We like to note that the alternative consideration of an interim formation of bipolarons, that are strongly absorbing in the blue region (see e.g. [11, 18]), would not explain the delayed appearance of the blue component in Fe:LN. The same holds for Mg:LN due to the lack of antisites. We will thus disregard the presence of bipolarons in our model approach, though it may be included if thermally reduced LN is considered.
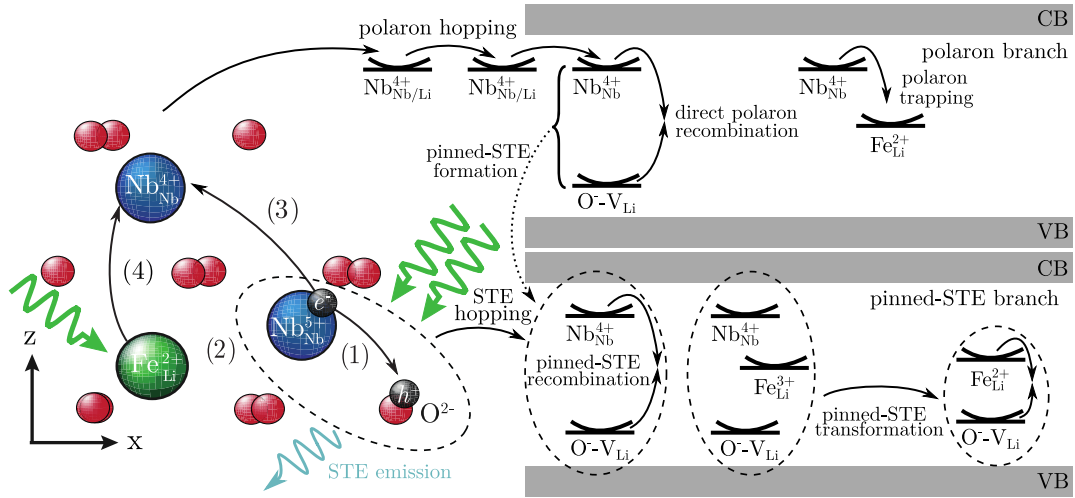
Figure 6. Excitation and recombination model after pulse exposure (green thick arrows) in LN. Hot electron–hole pairs created by the pump pulse in a two-photon process either recombine directly (1), form STEs within NbO_6 octahedra (2), or dissociate to form separate oppositely charged small polarons (3), as a further option, electrons from Fe_{Li}^{2+} may be excited to form additional small polarons leaving back Fe_{Li}^{3+} (4). The recombination paths are divided into a polaron and an exciton branch, for more detail see text.

As seen on the left-hand side of figure 6, the starting situation can be summarized as follows: immediately (on the ps scale) after the pump pulse, a given concentration of free or bound electron polarons and holes is created, together with a certain amount of emptied Fe_{Li}^{3+} traps [4, 42]. Small electron polarons forming the polaron branch (upper right-hand part of figure 6) move through the lattice by thermally activated hopping [43, 44] which terminates in deep traps like Fe_{Li}^{3+} converting to Fe_{Li}^{2+} or they annihilate with trapped holes. However, depending on conditions of temperature and composition, a considerable concentration of STEs, disregarded in earlier TA studies, may be present as well, as indicated by luminescence. Since this radiative recombination is observed to be orders of magnitude faster than the small polaron decay time measured by TA (see our measurements), we can assume that it stems from STEs formed directly after light exposure forming a second relaxation channel parallel to the polaron recombination. Besides the possibility to recombine radiatively, the STE is the starting point of a pinned-STE branch (lower right-hand part of figure 6) which will be described in more detail in the following.

6.1. (Pinned) STEs in LN

STEs may be assumed to have a significant hopping mobility as confirmed by the presence of a thermally activated process ($E_A \approx 0.09$ eV) of the luminescence decay. At higher temperatures and in defective materials, STEs formed at early stages of pumping are expected to get pinned on defects, similarly to the formation and trapping of single-site small polarons. Resonant excitonic/energy transfer can be discarded due to the large Stokes shifts. In particular, STEs may be captured, among others, by the same defects as free holes (e.g. by lithium vacancies or Mg_{Nb}^{2+} defects). The final recombination site should

play a decisive role, especially at lower temperatures, when localization sets in and τ gets nearly temperature-independent. The exact optical properties depend on the presence and type of defects adjacent to the niobium-oxygen octahedron containing the STE as shown by luminescence studies in LN with various stoichiometric compositions [16] including also crystals with ilmenite type cationic stacking order [17]. While the presence of Mg up to the $\approx$5 mol% threshold, i.e. the elimination of antisites, leads to increased emission [21], Fe doping seems to lead to luminescence quenching comparable to the case of Cr doping [23], indicating that both intrinsic defects and Fe form pinning centers for STEs where luminescence is suppressed. Non-radiative decay should be strongly preferred for STEs pinned on defects with high pinning/stabilizing energies leading to the longer absorption decay times and higher activation energies as observed for TA in the blue. In this case, the decreasing $\beta_{PL}(T)$ function characterizes the temperature dependent pinning history of the STE influencing its decay. The existence of a second, slow component, with activation energies slightly larger than in our case (0.14 eV and 0.11 eV) valid above somewhat higher temperatures 140 K and 160 K for the respective luminescence components, obtained in 7.5 mol% Mg-doped samples by Kämpfe *et al* [19], may then be attributed to minor deviations from the crystal structure optimal for luminescence. It should be noted that pinned STEs might also be formed as interim states during the recombination of electron polarons with trapped-hole centers.

6.2. Absorption properties of (pinned) STEs

STEs, which have been established in various materials, e.g. alkali halides, beside their capability to decay radiatively, have absorption bands similar to those of small polarons as demonstrated by Williams *et al* [5, 45]. As pointed out by these authors, the hole and electron, which a STE consists

of, can be excited optically and show a near ultraviolet and a near-infrared absorption, respectively, corresponding to optically triggered jumps of the respective constituent to equivalent neighboring sites. In LN, due to the transfer of the hole constituent to an equivalent or non-equivalent neighboring oxygen site, STEs are also expected to have an absorption in the blue/near-ultraviolet region. However, a separate contribution of the radiatively decaying STEs to the TA at the measured wavelengths was not observed even in Mg:LN at low temperatures although the luminescence and TA decay times deviate by a factor of at least 1000 from each other and a TA of such STEs—if present—should have been clearly visible. Furthermore, to the best of our knowledge, evidence for the presence of excitonic infrared/ultraviolet absorption in LN is not reported in literature, so far.

Concerning the absorption properties of pinned STEs, we have no experimental indication for the presence of a near-infrared absorption. The 'quenching' of infrared-absorption may be understood by taking into account proposed dynamic or static models of trapped hole O^- centers containing a unique Nb neighbor in a strongly preferred position for electron trapping [46, 47]. In such cases electron hopping may be hampered or requires much higher energy. The blue/ultraviolet absorption of pinned STEs, though present, might be nearly indistinguishable from the absorption of an O^- trapped hole.

6.3. Two-step recombination model of STEs pinned on Fe^{3+} centers

STEs should also be capable to get pinned on iron centers. Most Fe_{Li}^{3+} centers in LN may be assumed to have a nearest neighbor charge-compensating lithium vacancy (V_{Li}) suggesting the following scenario: the constituents of a nearby STE are attracted by the constituents of the $Fe_{Li}^{3+} - V_{Li}$ dipole leading to an STE pinned on $Fe_{Li}^{3+} - V_{Li}$ with the Nb^{4+} and O^- sites at nearest neighbor positions of the Fe_{Li}^{3+} and V_{Li} sites, respectively. A single jump of the electron from Nb_{Nb}^{4+} to the Fe site (along the *c* axis) transfers the complex into a new state, which is a coupled $Fe_{Li}^{2+} - O(V_{Li})^-$ defect. Both Fe_{Li}^{2+} and the hole constituent absorb in the blue, their aggregate causing a net increase of the total blue TA with respect to the pinned STE absorption, thus providing a rising TA component. However, this new defect state again has a metastable excitonic character and tends to recombine, restoring the original $Fe_{Li}^{3+} - V_{Li}$ defect having no absorption at all. Thus we consider a strongly localized two-step STE recombination process where the electron constituent, starting from a Nb_{Nb}^{4+} state, proceeds to a lower Fe_{Li}^{2+} level before rejoining its O^- partner. Since both the pinned STE and the intermediary $Fe_{Li}^{2+} - O(V_{Li})^-$ complex can be assumed to have metastable ground states with differently relaxed lattice environments, both jumps have to be phonon-induced/assisted, and may involve significant, separate temperature dependent time delays. This two-step STE recombination path, leading to an interim TA maximum with a subsequent steep decay clearly

explains the most conspicuous features of the TA at 445 nm, while it seems to be much less pronounced at 488 nm. As the second jump seems to take significantly longer than the first, a description in terms of two separate KWW-functions has to be a good approximation.

The derived activation energies support the two-step relaxation model of the STE pinned on $Fe_{Li}^{3+} - V_{Li}$ yielding $E_A^1 \approx 0.71$ eV for the first and a larger $E_A^2 \approx 0.78$ eV for the second step, the latter corresponding to the decay of the strongly distorted $Fe_{Li}^{2+} - O(V_{Li})^-$- state, and roughly equaling one fourth of the strong absorption measured at 445 nm (2.79 eV). A similar ratio may hold for the STE pinned on $Fe_{Li}^{3+} - V_{Li}$ in the first step as well, confirming $\propto E_{opt}/4$ as the activation energy characterizing the hopping of a polaron from a given site to an adjacent one [12]. Negligible differences between 488 nm and 445 nm data (τ, β) in Fe:LN indicate small superpositions from other recombination centers not containing Fe.

At low temperatures the proposed two-step relaxation of the STE pinned on $Fe_{Li}^{3+} - V_{Li}$ clearly dominates the 445 nm TA spectrum in Fe:LN for $t > 10$ ms (see figure 2(b)). While these two steps seem to explain both the rising and decreasing 445 nm components in Fe:LN, an important contribution to the long decreasing component in Mg:LN may come from STEs pinned on hole-trap defects like (V_{Li})-pinned STEs. Contributions from such pinned STEs correspond to centers with observed lifetimes in the minute range and have been attributed to O^--type centers in 5 mol% Mg-doped LN by Xin *et al* [40]. In fact, our probe wavelengths are in the central part of the O^- and on the very wing of a TA band attributed to $O^- (Mg_{Nb}^{2+})$ centers in [40].

Accordingly the first-step lifetime of the ($Fe_{Li}^{3+} - V_{Li}$)-pinned STE state recombination may correspond to the lifetimes of the rising components τ_1 and τ_{1b} observed at 445 nm in Fe:LN at low temperatures and in Mg:LN at RT, respectively. In contrast, much longer second-step lifetime may correspond to τ_2 of the long decreasing component at 445 nm in Fe:LN. The separation of time domains of polaron and pinned-STE decay is rather large in Mg:LN (figure 3). However, there may be a considerable overlap in Fe:LN at RT which resulted in the earlier misinterpretation of the blue TA components discussed above.

7. Summary and conclusion

In this paper the question is answered whether STEs play a role in polaronic recombination processes in LN. In a first step it was shown that STEs can be optically generated in Mg:LN in the whole temperature range from 15–300 K. In particular, our data, collected for the first time continuously up to 300 K, demonstrate that the PL signal can clearly be assigned to similar STEs in the entire temperature range.

In the next step shortcomings of earlier microscopic polaronic recombination models were demonstrated. Transient absorption measurements in an extended temperature and spectral range on Fe:LN and Mg:LN reveal

S Messerschmidt *et al*

inconsistencies when Herth's model is applied on these new data sets: (i) the decay of bound polarons absorbing in the near-infrared is not correlated with the increase of blue absorption, (ii) the fact that the β coefficient in the blue spectral range is larger for lower temperatures is in contrast to the state-of-the-art knowledge for small, strong-coupling polaron dynamics in LN.

Third, the temperature-dependent TA was compared with the corresponding TRPL data to check whether features in TA could also be attributed to STEs. The striking increase of the stretching factor β with decreasing temperature attributed to STEs in TRPL, but present also in TA in the blue spectral range, was found to be such a fingerprint. In fact, this is in contrast to the usual $\beta(T)$ behavior which is expected for small polarons in LN.

Based on these results, we propose and discuss for the first time an excitation and recombination model by including a STE branch in addition to the established polaron recombination branch. Both together are capable to describe in a comprehensive model TA and PL over a broad temperature-range. Here, STEs and pinned STEs formed during or immediately after pumping were found to be important transporters of negative charges towards deep Fe^{3+} traps. The presence of long-lived perturbed O^- centers containing an adjacent lithium vacancy in their clusters have to be assumed in both LN systems, while a second distinct group of STE hosts can be attributed to doping (Mg_{Nb} or Fe_{Li}). The varying accessibility of these centers and/or the different stability of the corresponding pinned STEs can be ascribed to different clustering with intrinsic and extrinsic defects, taking into account that clustering not only results in various levels of charge compensation but may also result in different restrictions for polaron and exciton hopping. However, further investigations are required regarding the absorption of the emitting STEs on even shorter timescales and the type of centers at which pinned STEs are formed. We further assume that the concept of both the polaron and (pinned) STE branch in LN could also be transferred to other materials with perovskite structure such as $KNbO_3$, $LiTaO_3$, etc, since all these materials may host similar kinds of defects. Furthermore, we expect that our approach may also serve as a basis for new models and insights to describe related phenomena such as photocatalysis in TiO_2, MgO and/or ZnO.

Acknowledgments

ORCID iDs

S Messerschmidt ● https://orcid.org/0000-0001-6193-7487
M Bazzan ● https://orcid.org/0000-0002-1451-1368

References

[1] Schirmer O F, Imlau M and Merschjann C 2011 *Phys. Rev.* B **83** 165106
[2] He J, Franchini C and Rondinelli J M 2016 *Chem. Mater.* **28** 25
[3] Lengyel K *et al* 2015 *Appl. Phys. Rev.* **2** 040601
[4] Imlau M, Badorreck H and Merschjann C 2015 *Appl. Phys. Rev.* **2** 040606
[5] Williams R T and Song K S 1990 *J. Phys. Chem. Solids* **51** 679
[6] Nolan M 2012 *ACS Appl. Mater. Interfaces* **4** 5863
[7] Migani A and Blancafort L 2016 *J. Am. Chem. Soc.* **138** 16165
[8] Sezen H *et al* 2015 *Nat. Commun.* **6** 6901
[9] Liu Z, Yin Z, Cox C, Bosman M, Qian X, Li N, Zhao H, Du Y, Li J and Nocera D G 2016 *Sci. Adv.* **2** e1501425
[10] Hamid S B A, Teh S J and Lai C W 2017 *Catalysts* **7** 93
[11] Schirmer O F, Thiemann O and Wöhlecke M 1991 *J. Phys. Chem. Solids* **52** 185
[12] Schirmer O F, Imlau M, Merschjann C and Schoke B 2009 *J. Phys.: Condens. Matter* **21** 123201
[13] Sanson A, Zaltron A, Argiolas N, Sada C, Bazzan M, Schmidt W G and Sanna S 2015 *Phys. Rev.* B **91** 094109
[14] Juppe S and Schirmer O F 1986 *Phys. Lett.* A **117** 150
[15] Corradi G, Zaritskii I M, Hofstaetter A, Polgár K and Rakitina L G 1998 *Phys. Rev.* B **58** 8329
[16] Krol D M, Blasse G and Powell R C 1980 *J. Chem. Phys.* **73** 163
[17] Wiegel M, Blasse G, Navrotsky A, Mehta A, Kumada N and Kinomura N 1994 *J. Solid State Chem.* **109** 413
[18] Merschjann C, Schoke B, Conradi D, Imlau M, Corradi G and Polgár K 2008 *J. Phys.: Condens. Matter* **21** 015906
[19] Kämpfe T, Haußmann A, Eng L M, Reichenbach P, Thiessen A, Woike T and Steudtner R 2016 *Phys. Rev.* B **93** 174116
[20] Blasse G 1968 *J. Chem. Phys.* **48** 3108
[21] Fischer C, Wöhlecke M, Volk T and Rubinina N 1993 *Phys. Status Solidi* a **137** 247
[22] Klose F, Wöhlecke M and Kapphan S 1989 *Ferroelectrics* **92** 181
[23] Powell R C and Freed E E 1979 *J. Chem. Phys.* **70** 4681
[24] Conradi D, Merschjann C, Schoke B, Imlau M, Corradi G and Polgár K 2008 *Phys. Status Solidi RRL* **2** 284
[25] Herth P, Granzow T, Schaniel D, Woike T, Imlau M and Krätzig E 2005 *Phys. Rev. Lett.* **95** 067404
[26] Berben D, Buse K, Wevering S, Herth P, Imlau M and Woike T 2000 *J. Appl. Phys.* **87** 1034
[27] Herth P, Schaniel D, Woike T, Granzow T, Imlau M and Krätzig E 2005 *Phys. Rev.* B **71** 125128
[28] Reichenbach P, Kämpfe T, Thiessen A, Haußmann A, Woike T and Eng L M 2014 *Appl. Phys. Lett.* **105** 122906
[29] Reichenbach P, Kämpfe T, Thiessen A, Schröder M, Haußmann A, Woike T and Eng L M 2014 *J. Appl. Phys.* **115** 213509
[30] Varshni Y 1967 *Physica* **34** 149
[31] Botha J and Leitch A W R 2000 *J. Electron. Mater.* **29** 1362
[32] Toyozawa Y 2003 *Optical Processes in Solids* (Cambridge: Cambridge University Press)

[33] Klafter J and Shlesinger M F 1986 *Proc. Natl Acad. Sci.* **83** 848

[34] Sturman B, Podivilov E and Gorkunov M 2003 *Phys. Rev. Lett.* **91** 176602

[35] Mhaouech I and Guilbert L 2016 *Solid State Sci.* **60** 28

[36] Merschjann C, Imlau M, Brüning H, Schoke B and Torbrügge S 2011 *Phys. Rev.* B **84** 052302

[37] Guilbert L, Vittadello L, Bazzan M, Mhaouech I, Messerschmidt S and Imlau M 2018 *J. Phys.: Condens. Matter* **30** 125701

[38] Volk T and Wöhlecke M 2010 *Lithium Niobate* (New York: Springer)

[39] Malovichko G I, Grachov V G and Kokanyan E P 1992 *Ferroelectrics* **125** 289

[40] Xin F, Zhai Z, Wang X, Kong Y, Xu J and Zhang G 2012 *Phys. Rev.* B **86** 165132

[41] Zatryb G, Podhorodecki A, Misiewicz J, Cardin J and Gourbilleau F 2011 *Nanoscale Res. Lett.* **6** 106

[42] Freytag F, Booker P, Corradi G, Messerschmidt S, Krampf A and Imlau M 2018 *Opt. Mater. Express* **8** 1505

[43] Emin D 1975 *Adv. Phys.* **24** 305

[44] Emin D 2012 *Polarons* (Cambridge: Cambridge University Press)

[45] Song K S and Williams R T 1993 *Self-Trapped Excitons* (Berlin: Springer)

[46] Miki T, Hantehzadeh M R and Halliburton L E 1989 *J. Phys. Chem. Solids* **50** 1003

[47] Zaritskii I M, Rakitina L G, Corradi G, Polgar K and Bugai A A 1991 *J. Phys.: Condens. Matter* **3** 8457

A.2 Pulse-induced transient blue absorption related with long-lived excitonic states in iron-doped lithium niobate

- Simon Messerschmidt, Bjoern Bourdon, David Brinkmann, Andreas Krampf, Laura Vittadello, and Mirco Imlau
  Pulse-induced transient blue absorption related with long-lived excitonic states in iron-doped lithium niobate
  Opt. Mater. Express **9**, 2748-2760 (2019); doi: 10.1364/OME.9.002748

Pulse-induced transient blue absorption related with long-lived excitonic states in iron-doped lithium niobate

SIMON MESSERSCHMIDT, BJOERN BOURDON, DAVID BRINKMANN, ANDREAS KRAMPF, LAURA VITTADELLO, AND MIRCO IMLAU[*]

School of Physics, Osnabrueck University, Barbarastraße 7, 49076 Osnabrueck, Germany
[*]*mirco.imlau@uni-osnabrueck.de*

Abstract: Transient absorption is studied in Fe-doped lithium niobate single crystals with the goal to control and probe a blue absorption feature related with excitonic states bound to Fe_{Li} defect centers. The exciton absorption is deduced from the comparison of ns-pump, supercontinuum-probe spectra obtained in crystals with different Fe-concentration and $Fe_{Li}^{2+/3+}$-ratio, at different pulse peak and photon energies as well as by signal separation taking well-known small polaron absorption bands into account. As a result, a broad-band absorption feature is deduced being characterized by an absorption cross-section of up to $\sigma^{max}(2.85\,eV) = (4 \pm 2) \cdot 10^{-22}\,m^2$. The band peaks at about $2.85\,eV$ and can be reconstructed by the sum of two Gaussians centered at $2.2\,eV$ (width $\approx 0.5\,eV$) and $2.9\,eV$ (width $\approx 0.4\,eV$), respectively. The appropriate build-up and decay properties strongly depend on the crystals' composition as well as the incident pulse parameters. All findings are comprehensively analyzed and discussed within the model of $Fe_{Li}^{2+} - O^- - V_{Li}$ excitonic states.

1. Introduction

The microscopic understanding of pulse-induced transient absorption phenomena, such as green-induced infrared absorption (GRIIRA) [1] or blue-induced infrared absorption (BLIIRA) [2], is mandatory for the control of laser-induced damage mechanisms in lithium niobate ($LiNbO_3$, LN) and, thus, for applications of LN in nonlinear photonics [3]. From the beginning, the appearance of transient infrared absorption was successfully explained by the coupling of optically generated electrons with phonons, i.e., by the formation of $Nb_{Nb/Li}^{4+}$ small, strong-coupling electron polarons [4]. In contrast, the microscopic origin of transient blue-absorption remains fairly unexplained since advanced information about its respective features is still unsettled. In detail, neither the involved localized carrier states, nor their exact peak position, the shape, the band-width, and the absorption cross-section are known for the most of them. Furthermore, important knowledge to control the appearance of blue absorption by adjustment of, e.g., Fe-concentration, of the $Fe_{Li}^{2+/3+}$-ratio, and/or by means of pulse peak energy and/or photon energies is missing in literature completely, so far.

The presence of transient absorption in the blue-green spectral range in LN was discovered in 2005 by Herth *et al.* in Fe-doped LN using single probe-laser lines [5] and – as a first attempt – has been attributed to the coupling of optically generated holes with the lattice in direct vicinity of V_{Li} lithium vacancies. The formation of O^--hole polarons with strong coupling is in full accordance with the original expectations formulated by Schirmer *et al.* for nearly all polar oxide crystals [6]. Later on, investigations with continuous wave [7] and pulsed laser light [8,9], however, revealed several discrepancies to the hole polaron model. The results of Waasem *et al.* [7] demanded for the existence of further electronic states within the band-gap, being handled

109

as *X*-center of unknown microscopic nature. Quite recently, Messerschmidt *et al.* discussed excitonic states at the origin of long-lived transient blue absorption [9].

Self-trapped electron-hole-pairs at Nb-O-octahedra, commonly called *self-trapped excitons* (STEs) were widely investigated by Blasse *et al.* in nominally pure and doped LN by means of photoluminescence at temperatures below $100\,\mathrm{K}$ [10–12]. Similar luminescence phenomena were observed at room temperature using fs-NIR-pulse trains in Mg-doped LN [13] and have been assigned to the recombination of electron and hole polarons [14]. The goal of the work of Messerschmidt *et al.* [9] was to re-address charge-transport phenomena in LN by considering excitonic states as intermediate steps in addition. The authors succeeded to show, that the temperature dependence of transient absorption in LN crystals with Fe (and Mg) doping can be explained comprehensively by considering the presence of further (pinned) excitonic states, e.g., $\mathrm{Fe_{Li}^{2+} - O^- - V_{Li}}$. It is noteworthy, that a main conclusion of this model approach is, that (pinned) STEs cause a pronounced long-lived blue absorption in Fe-doped LN (Fe:LN). We use the expression "pinned" in the context of this paper, if lattice defects or doping atoms hamper the movement and recombination of an STE in the regular lattice. In some cases, the pinned STE can be transformed into a self-trapped excitonic state in which at least one constituent is bound to the defect, e.g., the $\mathrm{Fe_{Li}^{2+} - O^- - V_{Li}}$ STE.

In this paper, we address the open question about peak position, shape, bandwidth and absorption cross-section of the long-lived transient blue absorption under the assumption of self-trapped excitonic states as microscopic origin, i.e., following the general model approach of Ref. [9]. The study is performed using Fe-doped LN crystals according to previously reported pronounced transient blue absorption observed in these crystals. For the first time, ns-pump, supercontinuum-probe spectroscopy is applied in order to get a direct experimental access to the spectral shape of the optically induced excitonic blue absorption bands. At the same time, the determination of the temporal evolution of the absorption over a broad spectral range is mandatory for our analysis since it enables the spectral separation from further bound electronic states, such as, e.g., $\mathrm{Nb_{Li}^{4+/5+}}$ or $\mathrm{Fe_{Li}^{2+/3+}}$. These centers additionally show individual broad-band ($\approx 1.0\,\mathrm{eV}$) transient absorption [15] and, therefore, strongly overlap with the expected excitonic optical fingerprints. Quite recently, Schirmer *et al.* [16] and Sanson *et al.* [17] showed that the $\mathrm{Fe_{Li}^{2+/3+}}$ center can be described in the small polaron model as well.

The experimental study is performed with LN crystals of various doping concentrations and $\mathrm{Fe_{Li}^{2+/3+}}$-ratio in order to account for three of the most common optical excitation paths in Fe:LN [18–20]:

- Iron D-band excitation, $E_{\mathrm{abs}}^{\mathrm{max}} = 2.6\,\mathrm{eV}$: A charge transfer from iron to the conduction band: $\mathrm{Fe_{Li}^{2+} \rightarrow Nb_{Nb}^{5+}}$

- Iron C-band excitation, $E_{\mathrm{abs}} > 3.1\,\mathrm{eV}$: A charge transfer from the valence band to iron: $\mathrm{O^{2-} \rightarrow Fe_{Li}^{3+}}$

- Interband excitation, $E_{\mathrm{abs}} > (3.8 - 4.1)\,\mathrm{eV}$: A charge transfer from the valence to the conduction band: $\mathrm{O^{2-} \rightarrow Nb_{Nb}^{5+}}$

Accordingly, photon energies at $2.33\,\mathrm{eV}$ ($532\,\mathrm{nm}$) and $3.49\,\mathrm{eV}$ ($355\,\mathrm{nm}$) are used to pump the transients.

The individual spectra reveal that any spectral and temporal feature of the $(E - t)$-plots can be modeled straightforwardly considering the additional presence of (pinned) excitonic states at iron. This knowledge is the anchor for the assignment of the excitonic absorption fingerprint from spectra obtained under rather different conditions. Finally, it is possible to analyze the main features (peak position, width) of the absorption band and, particularly to determine the respective absorption cross-section. For this purpose, the saturation of the $\mathrm{Fe_{Li}^{2+} - O^- - V_{Li}}$ STE population is estimated by a pump intensity dependent measurement series. An instruction

for the control of the transient blue absorption can be clearly deduced for Fe-doped LN. At the same time, the reconstruction of the excitonic absorption feature with probably two individual absorption bands demands for further investigations, in particular of the electronic transition mechanisms of excitonic states in LN.

2. Experimental methods

Our experimental series is performed by means of ns-pump, supercontinuum-probe absorption spectroscopy. Electronic detection at room temperature using continuous-wave, single line probe lasers at 2.54 eV (488 nm) and 1.58 eV (785 nm) are additionally applied as described in previous studies (cf. e.g. [9]). The combined setup is schematically depicted in Fig. 1. The supercontinuum setup obtains an accessible time range of 100 ns up to 100 s and is capable to detect carrier-lattice phenomena with strong coupling, whereas formation dynamics and intermediate trapping states, such as the intermediate trapping of small, free Nb_{Nb}^{4+} electron polarons, remain hidden.
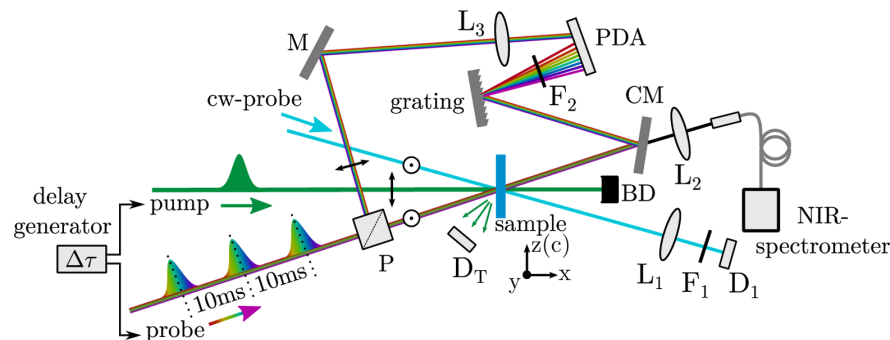

Fig. 1. Sketch of the ns-pump, supercontinuum-probe spectrometer applied in this study. The sample is pumped by a single pulse of a ns-pump pulse laser. Detection of the transient absorption is performed (i) using a diode (D_1) for the detection of the dynamic transmission change of a continuous wave probe laser transmitted through the sample (for a better visibility, only one cw-probe beam is shown) or (ii) by means of a supercontinuum. Here, the ns-pump pulse can be delayed for a certain time by a delay generator with respect to the supercontinuum probe pulse. The transmission change per wavelength is detected with two different spectrometers, one for the near-infrared part and one for the visible part of the supercontinuum pulse. $L_{1,2,3}$: lenses, $F_{1,2}$: optical filters, M: mirror, CM: cold mirror, P: polarizing beamsplitter cube, D_T: trigger diode for setup (i), BD: beam dump, PDA: photodiode array. The reader is referred to the text for further details.

A frequency-doubled and -tripled Nd:YAG pulse laser (Innolas Inc., *Spitlight*) and a broad-bandwidth light of a supercontinuum ns-pulse laser (LEUKOS, *STM-1-UV*) serve as pump ($\tau_{FWHM} = 8$ ns, extraordinarily polarized, $\lambda = 532$ nm (2.33 eV) or $\lambda = 355$ nm (3.49 eV), respectively) and probe sources ($\tau_{FWHM} < 1$ ns, unpolarized, $\lambda = (350 - 1800)$ nm $\equiv E = (3.54 - 0.69)$ eV, total average pulse energy of 35 μJ). The probe pulse is split by a broadband polarizing beamsplitter cube into two parts with perpendicular polarization states, i.e., ordinary (transmitted) and extraordinary (reflected) with respect to the crystal's c-axis. The latter is used as a reference signal whereas the ordinary polarized part is adjusted to an optimum overlap with the pump within the sample's volume. After the sample, the probe light is split in a near-infrared (NIR) and visible (VIS) spectral region by a longpass dichroic mirror ($\lambda_{cut} = 950$ nm). A fiber-spectrometer (OceanOptics *NIRQuest 512*) and a discrete photodiode

array (PDA, *Hamamatsu-S3902-512Q, TEC5*) are used simultaneously for the detection of the NIR and VIS signal fractions. A time resolution of up to 100 ns is achieved using an electronic delay of the pump. The time delay $\Delta\tau$ between pump and probe pulse is exponentially increased for $t = 100\,\text{ns} - 10\,\text{ms}$ so that the data points are equidistant on a logarithmic time axis. Data points for $t > 10\,\text{ms}$ are obtained by measuring the subsequent pulses of the supercontinuum laser taking advantage of its repetition rate of 100 Hz. The signal-to-noise ratio is increased by signal averaging over 20 individual measurements. The transient absorption is calculated from the transmitted intensities via $\alpha_{\text{li}}(E,t) = -(1/d)\cdot\ln[I(E,t)/I(E,t \leq 0)]$, where $I(E,t)$ and $I(E,t \leq 0)$ are the transmitted probe light intensities after and before the pump pulse, respectively.

Our setup obeys minor limitations with respect to the spectral detection window, most of them being irrelevant for the purpose of our study: A lack of detection at 1.17 eV (1064 nm) and 2.33 eV (532 nm) due to a residual pump signal within the supercontinuum light and the SHG of the Nd:YAG pulse laser; one between 1.3 eV and 1.4 eV due to a low intensity of the supercontinuum laser and a weak sensitivity of the detectors; one above ≈ 3 eV due to a low intensity of the supercontinuum laser and a high intrinsic Fe_{Li}^{2+} steady-state absorption of Fe-doped LN (particularly visible in the data of section 3.1).

Four LN crystals of the congruently melting composition [21,22] with different Fe dopant concentrations in the melt were used as depicted in Table 1. All samples were cut in a manner that the crystallographic c-axis is parallel to the polished surface and the y-axis along one edge. The Fe_{Li}^{2+}-concentration ($c_{Fe^{2+}}$) in the samples, obtained from MolTech GmbH (Fe:LN_1) and the University of Padova (Fe:LN_2, Fe:LN_3, and Fe:LN_4), was estimated by optical absorption measurements [23,24].

Table 1. Fe-doped LN crystals used in this study as obtained from MolTech GmbH (Fe:LN_1) and the University of Padova (Fe:LN_2, Fe:LN_3, and Fe:LN_4). The Fe_{Li}^{2+}-concentrations were determined by optical absorption measurements [23,24]. *d* is denoting the thickness of the sample and α(2.6 eV) the steady-state absorption at 2.6 eV.

Sample	d (mm)	α (2.6 eV) (m^{-1})	$c_{Fe_{\text{Li}}}$ (mol %)	$c_{Fe_{\text{Li}}^{2+}}$ (10^{17}cm^{-3})	$c_{Fe_{\text{Li}}^{2+}}/c_{Fe_{\text{Li}}^{3+}}$
Fe:LN_1	2.0	468	0.185	10.4	0.029
Fe:LN_2	0.8	230	0.100	5.1	0.028
Fe:LN_3	2.0	45	0.020	1.0	0.027
Fe:LN_4	1.0	14	0.005	0.3	0.033

3. Experimental results

3.1. Excitation via the iron D-band

Figure 2 (left) shows the experimentally determined transient absorption for the case of optical excitation via the iron D-band, i.e., by means of a one-photon absorption process from Fe_{Li}^{2+} to Nb_{Nb}^{5+} (schematically sketched in Fig. 2 (right)).

The study is performed with sample Fe:LN_1 that obeys a high Fe_{Li}^{2+}-concentration. Furthermore, we have chosen a photon energy of 2.33 eV for the pump pulse that is close to resonant excitation (Fe_{Li}^{2+} peaks at 2.6 eV). The transients can be detected with sufficient signal-to-noise ratio in the spectral range of 0.7 eV to ≈ 3 eV and are exemplarily shown for a weak pulse peak intensity of $I_P \approx 30\,\text{MW/cm}^2$. The $(E-t)$-color plots are composed of two data sets that have been determined simultaneously with the VIS and NIR detector systems. The change of the light-induced absorption α_{li} is visualized by blue-yellow color coding as shown by the legend. Here, blue areas denote spectral regions with no change of the absorption upon the pump event, i.e., $\alpha_{\text{li}} \approx 0\,\text{m}^{-1}$ and yellow regions mark noticeable changes with amplitudes up to $\alpha_{\text{li}} = 75\,\text{m}^{-1}$. Black lines indicate a contour plot in steps of $\Delta\alpha_{\text{li}} = 15\,\text{m}^{-1}$. Boxed white

areas refer to the regions where spectral detection is not possible due to the above mentioned experimental limitations.
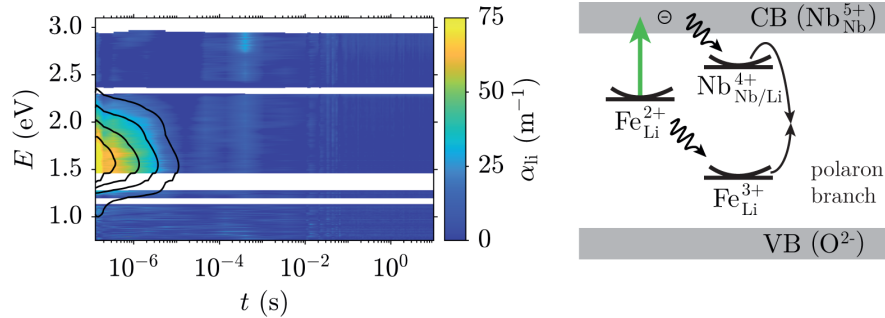

Fig. 2. Left: Transient absorption after an incident ns-pulse ($E = 2.33\,\text{eV}$, $I_P \approx 30\,\text{MW/cm}^2$) in the sample Fe:LN_1. The color coding of the light-induced absorption change is given in the legend on the right. Black lines indicate contour lines for steps of $\Delta\alpha_{li} = 15\,\text{m}^{-1}$. Boxed white areas refer to the regions where spectral detection is not possible. **Right:** Excitation and recombination scheme for the case of optical excitation via the iron D-band. For details see text.

This plot shows that a single, broad-band light-induced absorption feature is induced in the near-infrared immediately after the incident pump pulse. In more detail, it appears in the spectral window of $E = (0.7 - 2.5)\,\text{eV}$ with a peak at about $1.6\,\text{eV}$ and shows a noticeable signal on the timescale up to $10\,\mu\text{s}$. Within the experimental errors no change of the absorption shape during the decay can be observed. Further analysis of the spectra measured at $t = 100\,\text{ns}$ reveals a maximum value of $\alpha_{li}^{max} \approx 75\,\text{m}^{-1}$ with a full width at half maximum of $\approx 0.9\,\text{eV}$. In addition, the dynamic trace measured with a cw-laser at $1.58\,\text{eV}$ can be reconstructed by means of a single stretched-exponential function [24] with a lifetime $\tau_{KWW}(1.58\,\text{eV}) = 10\,\mu\text{s}$ and stretching factor $\beta(1.58\,\text{eV}) = 0.4$.

3.2.　Excitation via the iron D-band + C-band

Figure 3 (left) shows the experimentally obtained spectrum using conditions that additionally account for optical excitation via the C-band, i.e., via one-photon absorption from the O^{2-} valence band to Fe_{Li}^{3+} (cf. Fig. 3 (right)).

For this purpose, the sample Fe:LN_2 is used that was grown with a lower concentration of Fe in the melt. In addition, a photon energy of $3.49\,\text{eV}$ of the pump pulse is used. Again, a moderate pump pulse intensity of $I_P \approx 27\,\text{MW/cm}^2$ is chosen. The plot shows a considerable change of the transient absorption in comparison with the data of Fig. 2: a broad-band absorption feature appears immediately upon the incident pulse; it covers the total spectral range from the near-infrared to the blue, i.e., from $1.0\,\text{eV}$ to $3.1\,\text{eV}$. A maximum of the light-induced absorption with values up to $\alpha_{li}^{max} \approx 350\,\text{m}^{-1}$ is determined. Along the time axis, a disappearance of the NIR signal within a few microseconds is obvious ($\tau_{KWW}(1.58\,\text{eV}) = 2\,\mu\text{s}$ and stretching factor $\beta(1.58\,\text{eV}) = 0.3$). In contrast, the long-lived blue absorption is nearly constant over tenth of milliseconds and develops a significant peak around $2.85\,\text{eV}$. It follows as well a single stretched-exponential function with $\tau_{KWW}(2.54\,\text{eV}) = 2\,\text{s}$ and $\beta(2.54\,\text{eV}) = 0.7$.
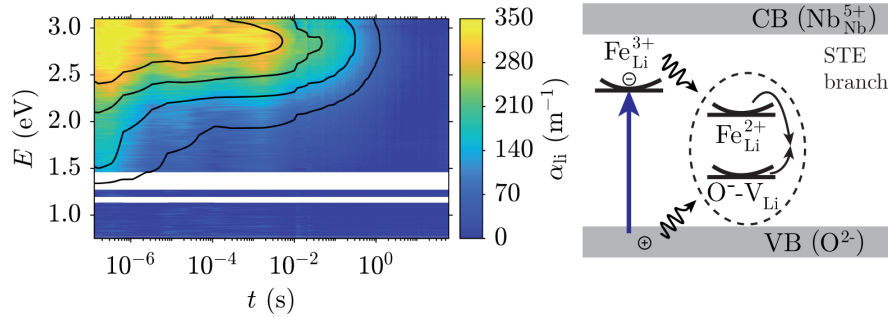
113

Fig. 3. Left: Transient absorption after an incident ns-pump pulse ($E = 3.49$ eV, $I_P \approx 27$ MW/cm^2) in the sample Fe:LN_2. Color coding according to the legend on the right. The contour plot marks steps of $\Delta\alpha_{li} = 70$ m^{-1}. Boxed white areas refer to the regions where spectral detection is not possible. **Right:** Excitation and recombination scheme for optical excitation via the iron C-band. For details see text.

3.3. *Excitation via the iron D-band + C-band + TPA*

Figure 4 (left) shows the results of our study using the sample Fe:LN_3, that features again a lower iron concentration in order to foster optical interband excitation, i.e., from the O^{2-} valence band to the Nb_{Nb}^{5+} conduction band (cf. Fig. 4 (right)).
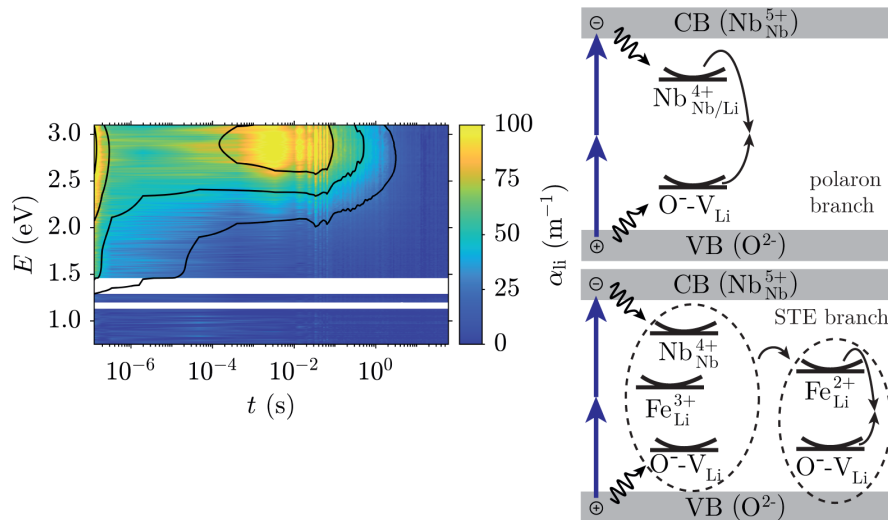

Fig. 4. Left: Supercontinuum transient absorption after 3.49 eV pulse exposure ($I_P \approx 12$ MW/cm^2) in the sample Fe:LN_3 for the case of optical excitation via the D-band, C-Band and two-photon absorption. See legend on the right for color coding. The contour lines indicate steps of $\Delta\alpha_{li} = 25$ m^{-1}. Boxed white areas refer to the regions where spectral detection is not possible. **Right:** Excitation and recombination scheme after excitation via a two-photon-absorption. For details see text.

Again, a photon energy of 3.49 eV is chosen for the pump pulse with a comparably weak pulse peak intensity of $I_P \approx 12$ MW/cm^2. These experimental conditions result in the most complex dynamics of the transient absorption in Fe-doped LN: immediately upon the pump pulse, a broad-band absorption feature is detected with characteristics very similar to the situation in section 3.2, but with reduced maximum amplitude of the light-induced absorption with values up to $\alpha_{li}^{max} \approx 100$ m^{-1}. It is very remarkable that this initial absorption shows a fast decay all over the blue and NIR spectral range with nearly the same temporal behavior. It results in a complete decay of the signal in the NIR with $\tau_{KWW}(1.58$ eV$) = 10$ μs and $\beta(1.58$ eV$) = 0.3$. In contrast, a temporally constant transient absorption value ($\alpha_{li} > 0$ m^{-1}) can be detected in the blue that remains over a duration of hundreds of microseconds. Subsequently, in the time range of milliseconds, the appearance of a delayed maximum with values up to $\alpha_{li}^{max} \approx 100$ m^{-1} is detected. Similar to the findings in section 3.2, it peaks around 2.85 eV and the long decay can be described with the parameters $\tau_{KWW}(2.54$ eV$) = 2$ s and $\beta(2.54$ eV$) = 0.6$.

3.4. Absorption spectra and saturation of the long-lived blue absorption

Figure 5 shows the direct comparison of the long-lived transient blue absorption features as obtained from a more detailed analysis of the spectra depicted in Figs. 3 and 4.

The spectra were deduced by normalizing the data points at every delay position to the respective spectral maximum of the light-induced absorption and subsequently averaging the data set over the time interval from $t > 1 \cdot 10^{-3}$ s to 10 s. Obviously, both spectra reveal a comparable shape with respect to the peak position of $E_{peak} = (2.85 \pm 0.05)$ eV and full width at half maximum of FWHM$= (1.00 \pm 0.25)$ eV.
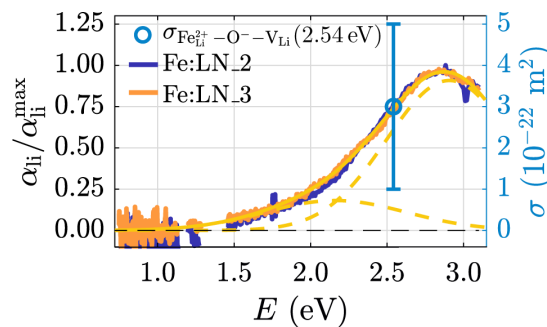

Fig. 5. Spectra of the long-lived blue absorption as deduced from the data in Fig. 3 and Fig. 4 by normalizing the data points at every delay position to the spectral maximum of the light-induced absorption and averaging the data set over the time interval from $t > 1 \cdot 10^{-3}$ s to 10 s. The yellow line represents a converging result of fitting Eq. (1) to the data. The dashed yellow lines refer to the individual Gaussians as given in Table 2. The blue data point is an experimentally determined value of the absorption cross-section at 2.54 eV and serves as scaling factor for the *y*-axis on the right.

Table 2. Parameters obtained from fitting the sum of two Gaussian functions (Eq. (1)) to the experimental data set for the case of two distinct absorption bands as sketched in Fig. 5. The fitting procedure reveals two solutions with a root mean square error of RMSE = 0.0387.

fit	a_1	a_2	b_1 (eV)	b_2 (eV)	c_1 (eV)	c_2 (eV)
1	0.91 ± 0.18	0.18 ± 0.17	2.91 ± 0.07	2.16 ± 0.50	0.41 ± 0.06	0.46 ± 0.17
2	0.37 ± 0.08	0.60 ± 0.40	2.88 ± 0.15	2.88 ± 0.34	0.31 ± 0.04	0.64 ± 0.03

It is possible to reconstruct the absorption shape by the sum of two Gaussians via:

$$\frac{\alpha_{li}(E)}{\alpha_{li}^{max}} = a_1 \cdot \exp\left[-\frac{(E-b_1)^2}{2c_1^2}\right] + a_2 \cdot \exp\left[-\frac{(E-b_2)^2}{2c_2^2}\right], \tag{1}$$

where $a_{1,2}$, $b_{1,2}$ and $c_{1,2}$ represent the amplitude, peak position and standard deviation of the individual Gaussian functions. As a result of the fitting procedure, two converging solutions are found. One, with two distinct absorption bands, is shown in Fig. 5. The associated fitting parameters are given in Table 2. A second converging solution of the fitting procedure results in two absorption bands peaking at the same photon energy of $E_{peak} \approx 2.88$ eV, but with rather different amplitudes and FWHM values.

In order to check whether the long-lived blue absorption shows a saturation value at high intensities, we have performed appropriate measurements using our standard pump-probe experiment due to the higher signal-to-noise ratio and signal stability along with the use of a 2.54 eV continuous-wave laser system. Figure 6 shows the maximum amplitude $\alpha_{li}^{max}(2.54\,\text{eV})$ measured for various pump intensities at $E_P = 3.49$ eV in the sample Fe:LN_4 which contains the lowest iron concentration in this study. The maximum amplitude follows at low pump intensities a quadratic behavior with increasing intensities. However, above $I_P \approx 50$ MW/cm^2 the amplitudes start to saturate. The data can be described with the following function:

$$\alpha_{li}^{max}(E, I) = \alpha_{li}^{max}(E, I \to \infty) \cdot \left[1 - \exp\left(-\frac{I^2}{I_\alpha^2}\right)\right], \tag{2}$$

where $\alpha_{li}^{max}(E, I \to \infty)$ is the saturation value and I_α is the characteristic intensity. A fit of Eq. (2) to the data reveals $\alpha_{li}^{max}(2.54\,\text{eV}, I \to \infty) = (276 \pm 25)\,\text{m}^{-1}$ and $I_\alpha = (50 \pm 5)\,\text{MW/cm}^2$.
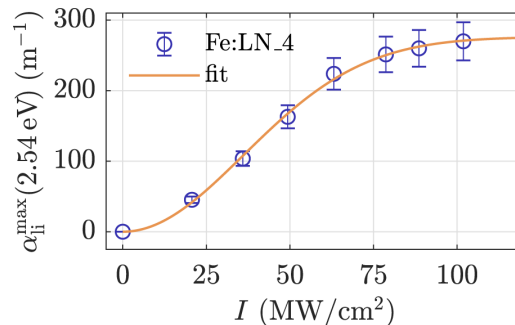

Fig. 6. Maximum amplitude of the long-lived blue absorption probed at 2.54 eV after pulse exposure at 3.49 eV for various intensities in the sample Fe:LN_4. The orange line is a fit of Eq. (2) to the data.

4. Discussion

Our experimental study reveals that ns-pump, supercontinuum-probe spectroscopy is successfully applied for the detection of transient absorption in Fe-doped lithium niobate. New insight to the temporal and, particularly, spectral evolution of pulse-induced absorption phenomena is obtained in the time interval from nanoseconds up to a few seconds and (nearly) without a gap from the blue to the near infrared spectral range. At a glance, the obtained $(E - t)$-plots demonstrate (i) the variety of transient absorption phenomena that appear in Fe-doped LN upon a single laser pulse, (ii) their complexity with respect to the spectral overlap of different absorption

features as well as to a time-delayed build-up and (iii) their dependence on the experimental boundary conditions. The signal-to-noise-ratio is sufficient to resolve intensity changes in the order of $\delta I/I_0 \approx 0.5\,\%$. In this respect, the experimental detection by means of single-line continuous-wave laser beams remains as a mandatory tool for the detection of very weak signals and/or for the detailed inspection of the temporal shapes of the absorption features. The presented experimental combination brings together the advantage of both techniques and enables the comprehensive analysis of transient absorption in LN without any constraint.

In what follows, we will first discuss the individual data sets in more detail according to the state-of-the-art knowledge of small polarons with strong coupling and considering the model of (pinned) excitonic states, i.e., according to the previously reported model approach by Messerschmidt *et al.* [9]. Then, we focus on the absorption features of the $Fe_{Li}^{2+} - O^- - V_{Li}$ excitonic state and will deduce the respective absorption cross-section, peak position and bandwidth. It should be noted that we neglect the inclusion of the intrinsic luminescent $Nb_{Nb}^{4+} - O^-$ STE in all excitation/recombination schemes. It is because such centers are expected to appear predominantly in stoichiometric or Mg-doped LN in a time range much shorter than the used pulse duration, i.e., not accessible with our experimental setup (at room temperature) [9,25].

4.1. Excitation via the iron D-band

The experimental conditions resulting in the data presented in Fig. 2 (left) were prepared in a manner that a one-photon excitation via the iron D-band is highly preferred (high Fe_{Li}^{2+}-concentration, pump wavelength near the maximum of the Fe_{Li}^{2+} absorption band). We therefore analyze the transients by considering optical excitation/subsequent relaxation from/back to $Fe_{Li}^{2+/3+}$ and the interim formation of small $Nb_{Li/Nb}^{4+}$ polarons (c.f. Fig. 2 (right)). In particular, we expect that the pulse-induced absorption over the entire spectral range results from the interplay of a light-induced transparency due to less Fe_{Li}^{2+} (ground-state bleach) and an increased absorption due to the formation of small bound polarons, i.e., $\alpha_{li}(E) = \Delta N_{Nb_{Li}^{4+}} \cdot \sigma_{Nb_{Li}^{4+}}(E) + \Delta N_{Fe_{Li}^{2+}} \cdot \sigma_{Fe_{Li}^{2+}}(E)$. Here, $\Delta N_{Nb_{Li}^{4+}} = -\Delta N_{Fe_{Li}^{2+}}$ where ΔN is the change of concentration induced by the pump pulse. Considering the dispersion features of the two absorption species with well separated peak positions (1.6 eV and 2.6 eV) [15], a pronounced NIR absorption change shall remain that is mainly attributed to Nb_{Li}^{4+}. At the same time, no changes are expected for the blue-green spectral range since the absorption cross sections of Nb_{Li}^{4+} and Fe_{Li}^{2+} strongly overlap in this region and are nearly identical: $\sigma_{Fe_{Li}^{2+}}(\text{blue}) \approx \sigma_{Nb_{Li}^{4+}}(\text{blue})$ [15]. Our experimental findings in Fig. 2 are in full agreement with both expectations: a broad-band NIR absorption is clearly visible with nearly no absorption change in the blue-green spectral range (within the noise of our experiment). Moreover, three significant polaron fingerprints can be verified, particularly considering Nb_{Li}^{4+}: a lifetime in the sub-ms-time range, a NIR absorption feature with a peak at about 1.6 eV and a stretched-exponential decay behavior with a β-value below 1/2. We need to note, that in this discussion, we neglect the interim formation of Nb_{Nb}^{4+} free polarons due to experimental constraints: the free polaron lifetime is much shorter than the temporal resolution of our experiment [8]. A transient signal at the the peak maximum of small free polarons of about 1.0 eV [15] was therefore not observed. All these findings and interpretations are in full agreement with the state-of-the-art knowledge of the interaction of continuous-wave and pulsed laser light with Fe-doped LN at moderate average power [24,26].

4.2. Excitation via the iron D-band + C-band

The second measurement was performed with an iron-doped LN sample containing a lower Fe-concentration and with a pump wavelength in the UV. This fosters the optical excitation via the iron C-band, though an excitation via the D-band cannot be excluded. We additionally need to consider that the cross-sections of these two excitation paths are very similar at 355 nm [27],

i.e, a contribution of both paths to the transient spectrum is to be expected. In this sense, and in direct comparison with the discussion of the previous section, it is likely to assume that the observed NIR absorption feature with fast decay in the spectra of Fig. 3 originates from the mechanisms associated with the D-band excitation (see section 4.1). All deduced experimental features (peak position, lifetime, stretching factor) support this assumption. Accordingly, the UV-induced long-lived blue absorption in Fig. 3 is assigned to the second excitation path via the iron C-band. To the best of our knowledge, the latter has not been investigated in the context of either small polarons or STEs in lithium niobate, so far. At a first glance, a relation to the formation of small $O^- - V_{Li}$ hole and Fe_{Li}^{2+} polarons may be assumed considering the charge-transfer from O^{2-} to Fe_{Li}^{3+} [18] (c.f. Fig. 3 (right)). However, in this case, the blue absorption must feature a broad-band absorption centered in the range of $2.5 - 2.6$ eV [6,15], that does not correspond with the experimentally determined peak position of about 2.85 eV in our spectra (see Fig. 5 and discussion below). An alternative microscopic approach is to consider $Fe_{Li}^{2+} - O^- - V_{Li}$ STEs as proposed by Messerschmidt *et al.* [9]. Such states are reported to form after pinning and subsequent transformation of an intrinsic STE at an iron center within a few hundred microseconds. They show absorption in the blue-green spectral range and their decay dynamics feature a stretching factor $\beta > 2/3$. According to the characteristics of the induced blue absorption deduced from the data in Fig. 2 (absorption feature with a peak at about 2.85 eV, an increased stretching factor of $\beta \approx 0.7$), it is reasonable to assume the presence of such states in our case, as well. A remarkable consequence of this approach is that the direct STE formation via the C-band is discovered for the first time. This finding is of particular importance of applications with doped LN and ultraviolet laser pulses, e.g., UV photorefraction.

4.3.   *Excitation via the iron D-band + C-band + TPA*

The third measurement in this study was performed with a sample containing a lower Fe_{Li}^{2+}- and Fe_{Li}^{3+}-concentration and, thus, also obeys the one-photon excitation and the subsequent recombination paths via the iron C- and D-band as discussed in the two previous sections 4.1 and 4.2. In addition, the low Fe-concentration increases the probability for excitation via two-photon absorption (TPA). It is because the negligible fundamental absorption conserves the peak intensity of the incident laser pulse. The influence of the electron-hole-pairs generated via TPA on the decay dynamics can be deduced by comparing the results in the two previous sections 4.1 and 4.2 with the data in section 3.3 (c.f. Fig. 4). The main differences are (i) an additional fast decay and (ii) a delayed increase in the blue spectral range. Both phenomena can be explained as follows: the generation of electron-hole pairs in the LN-host lattice results in the formation of $O^- - V_{Li}$ hole and Nb_{Li}^{4+} bound polarons as well as STEs which can be pinned next to Fe_{Li}^{3+} (c.f. Fig. 4 (right)). The formed polarons/STEs contribute to the transient spectra with absorption features in the blue and near-infrared spectral range. The decay of the initial transient signals in the blue and NIR spectral range is a characteristic fingerprint for the recombination of hole polarons with bound polarons known from undoped lithium niobate samples [3,15]. However, in contrast to an undoped sample, the initial temporal decay in the blue spectral range is superimposed by the transformation of pinned STEs at Fe_{Li}^{3+} into $Fe_{Li}^{2+} - O^- - V_{Li}$ inducing a strong blue absorption in the time range of milliseconds [9]. The observed complex behavior in the blue spectral range then is due to the different decay dynamics of the hole/bound polaron recombination on the one hand and the transformation of pinned STEs on the other hand.

4.4.   *Determination of the shape and absorption cross-section of the long-lived blue absorption*

The discussion of the previous sections points to a dominant role of $Fe_{Li}^{2+} - O^- - V_{Li}$ STEs at the origin of the long-lived blue absorption in Fe-doped LN which is in accordance with Ref. [9]. Following this microscopic approach, the spectra of Fig. 3 and Fig. 4 will both be related with

this excitonic state. Figure 5 compares the spectral shapes of the long-lived blue absorption as obtained from a further analysis of these data sets. Obviously, both spectra are characterized by a comparable shape, peak position and bandwidth and are nearly indistinguishable from each other. This result is very remarkable since the data sets were obtained in two completely different Fe-doped LN crystals and by using different pulse intensities for excitation. Moreover, it supports the finding that $Fe_{Li}^{2+} - O^- - V_{Li}$ STEs can be formed directly after the pump pulse via the iron C-band.

Let us now further analyze the absorption spectrum depicted in Fig. 5 in the microscopic model of $Fe_{Li}^{2+} - O^- - V_{Li}$ STEs. First, we discuss the shape of the STE absorption feature. Figure 5 shows that the pulse-induced absorption appears with a large amplitude over the entire VIS-NIR spectral region that is experimentally accessible with our setup. It can be expected that the band extends even far into the ultraviolet region and, that it overlaps with the interband absorption (starting at about 3.8 eV). Fitting the spectrum in the accessible region reveals that at least the sum of two Gaussian functions (c.f. Eq. (1)) with six free fitting parameters is required for its description. Exemplarily, one of the converging solutions is depicted in Fig. 5 with different peak positions (2.2 eV and 2.8 eV, respectively) but comparable FWHMs of the constituents (c.f. Table 2). We note that it is alternatively possible to perform the fitting procedure with two Gaussians at the same peak position (of about 2.9 eV), but with different FWHM values.

Taking these findings into account, we refer to the state-of-the-art knowledge of STE absorption bands and find that they typically resemble the interplay of at least two spectrally separated single bands in a first approximation [28–30]: a straightforward explanation is that the two bands originate from an optical excitation of both the electron and the hole to higher states, respectively. Or, the two bands refer to the photo-ionization process of STEs. Against this background, it is reasonable to expect two absorption bands for STEs in LN as well, one associated with the electron excitation from Fe_{Li}^{2+} and the other one from the $O^- - V_{Li}$-center. Peak position, bandwidth and the relative fraction of the total absorption amplitude (c.f. Table 2) then reflect the individual absorption features and absorption cross-sections of the two constituents involved. In particular, the effective absorption coefficient of the STE then is given by $\alpha_{eff}(E) = \alpha_1(E) + \alpha_2(E)$ in this case.

Second, we intend to estimate the effective absorption cross-section of the $Fe_{Li}^{2+} - O^- - V_{Li}$ STE. For this purpose, following the discussion of the previous paragraph, it is assumed that the absorption feature originates from a single absorption center of number density N, i.e., $\alpha_{eff}(E) = \sigma_{eff}(E) \cdot N$. In our case, the number density N can be determined experimentally by intensity dependent measurements of $\alpha_{li}(I)$ as depicted in Fig. 6. It is because $N(I)$ saturates due to a limited Fe_{Li}^{3+}-concentration such that $\alpha_{li}(I)$ saturates, too. The experimentally determined saturation value $\alpha_{li}^{max}(E, I \rightarrow \infty)$ then enables the calculation of the effective cross-section via $\sigma_{eff}(E) = \alpha_{li}^{max}(E, I \rightarrow \infty)/c_{Fe_{Li}^{3+}}$. This study has been performed at a minimum total iron concentration to (i) ensure that a saturation value can be achieved with our experimental conditions and (ii) enable the utilization of low pump intensities to avoid laser induced damages. With the data deduced from Fig. 6 we obtain $\sigma_{eff}(2.54 \, eV) = (3 \pm 2) \cdot 10^{-22} \, m^2$. This value serves for scaling the right y-axis in Fig. 5 which leads to a maximum effective cross-section of $\sigma_{eff}^{max}(2.85 \, eV) = (4 \pm 2) \cdot 10^{-22} \, m^2$. The large error of these values is a combination of both, the precision of our measurement and the determination of the iron concentration. We would also like to mention that the estimated values are only a lower bound because the calculation is based on the assumption that all Fe_{Li}^{3+}-centers are occupied in the saturation state. If this assumption is inapplicable, the number density of STEs is reduced which will result in a larger value of the absorption cross-section. In comparison to small polarons in lithium niobate [15], the absorption cross-section of the STE is in the same order of magnitude. Assuming that (pinned) STEs formed under similar conditions, e.g., in Mg-doped LN, exhibit similar absorption bands and

cross-sections, they have to play an important role in the blue absorption and might be responsible for a damping of frequency conversion and laser induced damages in this spectral range.

5. Conclusion

This study reveals the striking impact of ns-pump, supercontinuum-probe spectroscopy for the microscopic understanding of strongly localized electronic states in oxide crystals with lithium niobate as an example. The spectra allow to distinguish the temporal and spectral action of individual optically generated species under rather different experimental conditions and their formation/transport/recombination/relaxation description within a quite complex band model scheme. As a result it is possible to discover new properties of the interaction of light pulses with a strong polar crystal, e.g., the possibility to optically generate $Fe_{Li}^{2+} - O^- - V_{Li}$ STEs directly by a charge transfer via the iron C-band. Furthermore, the STE absorption cross-section obeys similar values as reported for small polarons. Another impressive result of this study is that the combination of transient spectroscopy and the polaron/exciton model in LN enables the precise prediction of the complex dynamics of transient absorption over a large spectral and temporal range. At the same time, it supports the validity of the model of (pinned) STEs for lithium niobate, which have been disregarded in the mechanisms of light-induced transport, so far. Our findings are of particular importance for the field of photorefraction since the formation of STEs will not result in the optically induced separation of charges that is mandatory for the photorefractive effect. The possibility to solely generate excitonic states by means of optical adjustment of pulse parameters (photon energy, pulse peak energy) and/or material adjustment ($Fe^{2+/3+}$-ratio) enables, e.g., the efficient suppression of optical damage in LN-based frequency converters. In the same manner, it is possible to determine temporal regimes that allow for photorefractive recording at elevated efficiencies, such as, e.g., the sub-millisecond time range for recording with a single, intense laser pulse.

Funding

Acknowledgements

References

1. R. Batchko, G. Miller, A. Alexandrovski, M. Fejer, and R. Byer, "Limitations of high-power visible wavelength periodically poled lithium niobate devices due to green-induced infrared absorption and thermal lensing," Tech. Dig. Summ. Pap. Present. at Conf. on Lasers Electro-Optics. Conf. Ed. 1998 Tech. Dig. Series, Vol. 6 (IEEE Cat. No.98CH36178) (1998).
2. H. M. Yochum, K. B. Üçer, R. T. Williams, L. Grigorjeva, D. Millers, and G. Corradi, "Subpicosecond Laser Spectroscopy of Blue-Light-Induced Absorption in $KNbO_3$ and $LiNbO_3$," Defects Surface-Induced Eff. Adv. Perovskites pp. 125–138 (2000).
3. M. Imlau, H. Badorreck, and C. Merschjann, "Optical nonlinearities of small polarons in lithium niobate," Appl. Phys. Rev. **2**(4), 040606 (2015).
4. Y. Furukawa, K. Kitamura, A. Alexandrovski, R. K. Route, M. M. Fejer, and G. Foulon, "Green-induced infrared absorption in MgO doped $LiNbO_3$," Appl. Phys. Lett. **78**(14), 1970–1972 (2001).
5. P. Herth, T. Granzow, D. Schaniel, T. Woike, M. Imlau, and E. Krätzig, "Evidence for Light-Induced Hole Polarons in $LiNbO_3$," Phys. Rev. Lett. **95**(6), 067404 (2005).
6. O. F. Schirmer, "O^- bound small polarons in oxide materials," J. Phys.: Condens. Matter **18**(43), R667–R704 (2006).
7. N. Waasem, A. Markosyan, M. M. Fejer, and K. Buse, "Green-induced blue absorption in MgO-doped lithium niobate crystals," Opt. Lett. **38**(16), 2953 (2013).

8. D. Conradi, C. Merschjann, B. Schoke, M. Imlau, G. Corradi, and K. Polgár, "Influence of Mg doping on the behaviour of polaronic light-induced absorption in LiNbO₃," Phys. Status Solidi RRL **2**(6), 284–286 (2008).

9. S. Messerschmidt, A. Krampf, F. Freytag, M. Imlau, L. Vittadello, M. Bazzan, and G. Corradi, "The role of self-trapped excitons in polaronic recombination processes in lithium niobate," J. Phys.: Condens. Matter **31**(6), 065701 (2019).

10. D. M. Krol, G. Blasse, and R. C. Powell, "The influence of the Li/Nb ratio on the luminescence properties of LiNbO₃," J. Chem. Phys. **73**(1), 163–166 (1980).

11. M. Wiegel, M. Emond, E. Stobbe, and G. Blasse, "Luminescence of alkali tantalates and niobates," J. Phys. Chem. Solids **55**(8), 773–778 (1994).

12. M. Wiegel, G. Blasse, A. Navrotsky, A. Mehta, N. Kumada, and N. Kinomura, "Luminescence of the Ilmenite Phase of LiNbO₃," J. Solid State Chem. **109**(2), 413–415 (1994).

13. P. Reichenbach, T. Kämpfe, A. Haußmann, A. Thiessen, T. Woike, R. Steudtner, L. Kocsor, Z. Szaller, L. Kovács, and L. Eng, "Polaron-Mediated Luminescence in Lithium Niobate and Lithium Tantalate and Its Domain Contrast," Crystals **8**(5), 214 (2018).

14. T. Kämpfe, A. Haußmann, L. M. Eng, P. Reichenbach, A. Thiessen, T. Woike, and R. Steudtner, "Time-resolved photoluminescence spectroscopy of Nb_{Nb}^{4+} and O^- polarons in LiNbO₃ single crystals," Phys. Rev. B **93**(17), 174116 (2016).

15. C. Merschjann, B. Schoke, D. Conradi, M. Imlau, G. Corradi, and K. Polgár, "Absorption cross sections and number densities of electron and hole polarons in congruently melting LiNbO₃," J. Phys.: Condens. Matter **21**(1), 015906 (2009).

16. O. F. Schirmer, M. Imlau, and C. Merschjann, "Bulk photovoltaic effect of LiNbO₃:Fe and its small-polaron-based microscopic interpretation," Phys. Rev. B **83**(16), 165106 (2011).

17. A. Sanson, A. Zaltron, N. Argiolas, C. Sada, M. Bazzan, W. G. Schmidt, and S. Sanna, "Polaronic deformation at the $Fe^{2+/3+}$ impurity site in Fe:LiNbO₃ crystals," Phys. Rev. B **91**(9), 094109 (2015).

18. M. G. Clark, F. J. DiSalvo, A. M. Glass, and G. E. Peterson, "Electronic structure and optical index damage of iron-doped lithium niobate," J. Chem. Phys. **59**(12), 6209–6219 (1973).

19. B. Dischler, J. Herrington, A. Räuber, and H. Kurz, "Correlation of the photorefractive sensitivity in doped LiNbO₃ with chemically induced changes in the optical absorption spectra," Solid State Commun. **14**(11), 1233–1236 (1974).

20. L. Kovács, G. Ruschhaupt, K. Polgár, G. Corradi, and M. Wöhlecke, "Composition dependence of the ultraviolet absorption edge in lithium niobate," Appl. Phys. Lett. **70**(21), 2801–2803 (1997).

21. J. R. Carruthers, G. E. Peterson, M. Grasso, and P. M. Bridenbaugh, "Nonstoichiometry and Crystal Growth of Lithium Niobate," J. Appl. Phys. **42**(5), 1846–1851 (1971).

22. T. Volk and M. Wöhlecke, *Lithium Niobate: Defects, Photorefraction and Ferroelectric Switching*, Springer Series in Materials Science (Springer Berlin Heidelberg, 2008).

23. H. Kurz, E. Krätzig, W. Keune, H. Engelmann, U. Gonser, B. Dischler, and A. Räuber, "Photorefractive centers in LiNbO₃, studied by optical-, Mössbauer- and EPR-methods," Appl. Phys. **12**(4), 355–368 (1977).

24. D. Berben, K. Buse, S. Wevering, P. Herth, M. Imlau, and T. Woike, "Lifetime of small polarons in iron-doped lithium–niobate crystals," J. Appl. Phys. **87**(3), 1034–1041 (2000).

25. F. Klose, M. Wöhlecke, and S. Kapphan, "UV-excited luminescence of LiNbO₃ and LiNbO₃:Mg," Ferroelectrics **92**(1), 181–187 (1989).

26. P. Herth, D. Schaniel, T. Woike, T. Granzow, M. Imlau, and E. Krätzig, "Polarons generated by laser pulses in doped LiNbO₃," Phys. Rev. B **71**(12), 125128 (2005).

27. M. V. Ciampolillo, A. Zaltron, M. Bazzan, N. Argiolas, and C. Sada, "Quantification of Iron (Fe) in Lithium Niobate by Optical Absorption," Appl. Spectrosc. **65**(2), 216–220 (2011).

28. R. T. Williams and M. N. Kabler, "Excited-state absorption spectroscopy of self-trapped excitons in alkali halides," Phys. Rev. B **9**(4), 1897–1907 (1974).

29. R. Williams and K. Song, "The self-trapped exciton," J. Phys. Chem. Solids **51**(7), 679–716 (1990).

30. P. Li, S. Gridin, K. B. Ucer, R. T. Williams, and P. R. Menge, "Picosecond absorption spectroscopy of self-trapped excitons and transient Ce states in LaBr₃ and LaBr₃:Ce," Phys. Rev. B **97**(14), 144303 (2018).

A.3 Excitonic hopping-pinning scenarios in lithium niobate based on atomistic models: different kinds of stretched exponential kinetics in the same system

- Gábor Corradi, Andreas Krampf, Simon Messerschmidt, Laura Vittadello and Mirco Imlau
  Excitonic hopping-pinning scenarios in lithium niobate based on atomistic models: different kinds of stretched exponential kinetics in the same system
  J. Phys.: Condens. Matter **32**, 413005 (2020); doi: 10.1088/1361-648X/ab9c5b

Excitonic hopping-pinning scenarios in lithium niobate based on atomistic models: different kinds of stretched exponential kinetics in the same system

G Corradi[1,2], A Krampf[1], S Messerschmidt[1], L Vittadello[1], M Imlau[1]

[1]*Osnabrück University, Barbarastraße 7, D-49076 Osnabrück, Germany and*
[2]*Wigner Research Center for Physics, Konkoly-Thege M. út 29-33, H-1121 Budapest, Hungary*

(Dated: March 16, 2020)

Based on a model of coupled processes with differently time-dependent decay kinetics we present a critical review on photoluminescence (PL) and transient absorption (TA) experiments in undoped and Mg or Fe-doped LiNbO$_3$, together with a comprehensive interpretation of visible radiative and parallel non-radiative decay processes on timescales ranging from 50 ns up to minutes. Analogies and peculiarities of the kinetics of mobile self-trapped and pinned excitons are investigated and compared with those of hopping polarons in the same system. Exciton hopping with an activation energy of $\approx$0.18 eV is shown to govern the lifetime and quenching of the short PL component above 100 K. Strong interaction between excitons and dipolar pinning defects explains the exorbitant lifetimes and large depinning energies characterizing delayed TA components in doped LiNbO$_3$, while restricted hopping of the pinned excitons is proposed to play a role in strongly delayed PL in LiNbO$_3$:Mg exhibiting a narrowed emission band due to locally reduced electron-phonon coupling. Atomistic models of pinned excitons are proposed corresponding to charge-compensated dipolar defects predicted by theories of dopant incorporation in LiNbO$_3$ and are systematically assigned to absorption bands observed near the UV edge. Excitation in these bands is shown to lead directly to pinned exciton states confirming also the previously proposed two-step exciton-decay scenario in LiNbO$_3$:Fe. Weak intrinsic sub-80 ns luminescence in congruent LiNbO$_3$ is explained as an opposite effect of enhanced electron-phonon coupling for excitons pinned on Nb$_{\text{Li}}$ antisite defects. The comparison of the different observed stretching behaviors in the paradigmatic system LiNbO$_3$ provides an intuitive picture of the underlying physical processes. The findings are relevant not only for holographic and non-linear optical applications of LiNbO$_3$ but are of general interest also for the treatment of stretched exponential or other time-dependent kinetics in complex condensed systems ranging from nanocrystals and polymers to liquids and biophysical systems.

I. INTRODUCTION

Beyond the multifarious applications of LiNbO$_3$ (LN) coupling mechanical, optical, electrical and thermal properties, this paradigmatic ferroelectric material continues exhibiting unexpected phenomena of general interest [1–3]. A recent example in LN:Mg, doped above the photorefractive threshold concentration (c$_{\text{Mg}} \approx$ 5 mol%) eliminating Nb$_{\text{Li}}$ antisites, is the long-lived blue photoluminescence (PL) component with a lifetime of several seconds at low temperatures reported by Kämpfe *et al.* [4], accompanied by a large long component in transient absorption (TA) near 488 nm having a $\approx$1 minute lifetime at RT (Conradi *et al.* [5]). Xin *et al.* [6] discerned two long TA components in the blue/near UV range. However, the proposed standard descriptions [7] in terms of electron small polarons and their capture by O$^-$ trapped holes absorbing in the blue range cannot explain the strongly delayed recombination processes. Indeed, the electron polaron, characterized in LN:Mg by EPR and optical absorption at $\approx$1 eV as a Nb$_{\text{Nb}}^{4+}$ center on an essentially undisturbed Nb site [8, 9], becomes mobile already at low temperatures and decays on a much shorter, microsecond timescale at RT; this is represented by a single absorption transient observed in the near infrared (IR) [5]. The standard description therefore explains the time-locked short blue absorption component, but fails for the long blue components observed in Refs. [5, 6]. Similar discrepancies were also observed in LN

doped with 0.1 mol% Fe between the fast absorption decay ($\tau \approx$ 10 μs at RT) of Nb$_{\text{Li}}^{4+}$ antisite-bound polarons monitored at 785 nm [10] and the slow decay ($\tau \approx$ 1s at RT) of the blue absorption [11] observed by Herth *et al.* At RT this was attributed to interim capturing of the polarons by Fe$^{3+/2+}$ traps yielding a large *rising* absorption component with a similarly short characteristic time $\tau \approx$ 10 μs; the latter was observed in the blue region where Fe^{2+} centers have an absorption band overlapping that of O$^-$ centers. Thereby thermal detrapping of electrons from the deep Fe^{2+} center was assumed by implication to occur on the 1 second scale, which is much shorter than hologram dark decay times, clearly attributed to an analogous charge redistribution in similar crystals even without thermal fixing [12, 13]. The crudeness of this model was also indicated by inconsistent values of the stretching factors β obtained for the various components [10, 11, 14].

Stretched exponentials of the form

$$N(t) = N_0 \exp\left[-(t/\tau)^\beta\right] \tag{1}$$

have been found to describe decay or build-up kinetics remarkably well in LN and a large variety of complex systems [15–22], where $N(t)$ is the number density or concentration, τ the characteristic time, and β the stretching factor for the entity in question. Equation (1) is a phenomenological approximation accounting for a distribution of decay rates and may, e.g., correspond to various distances between i) the recombining partners or ii) the

recombination center and the surrounding lattice defects. While the absorption coefficient α characterizing a given species is expected to be directly proportional to the population of the species ($\alpha \propto N$), the time-resolved luminescence intensity in descriptions neglecting non-radiative decay was assumed to be proportional to the first time derivative of equation (1):

$$I_{\mathrm{lum}}(t) \propto -\frac{dN(t)}{dt} = \beta\tau^{-\beta}t^{\beta-1}N(t). \qquad (2)$$

However, in the presence of a parallel non-radiative channel, in particular one having an independently distributed decay probability, this approximation leads to incorrect results [23]. For $\beta \leq 1$ an average decay time

$$\langle\tau\rangle = (1/N_0)\int_0^\infty N(t)dt = \tau\Gamma(1 + 1/\beta) \qquad (3)$$

has been defined; $\langle\tau\rangle$ equals τ for the mono-exponential case $\beta = 1$, but has strongly increased values for decreasing β, e.g., for $\beta = 1/n$ with integer n, one has $\langle\tau\rangle = n!\tau$ as required for the gamma-function $\Gamma(x)$.

Our recent ns-pulse-induced investigations of the optical transients in Mg and Fe-doped $LiNbO_3$ [24] revealed qualitatively differing temperature dependences of the lifetimes and stretching factors for the various transients making them incompatible within the same polaronic scenario. To explain the long-lived optical transients the presence of hopping excitons capable to get pinned on lattice defects was suggested, whereby the hopping of excitons was also proposed to govern the temperature dependence of fast PL. However, the simultaneous presence of parallel radiative and non-radiative decay channels was given insufficient consideration in Refs. [4, 24] despite previous reports about the temperature quenching of luminescence [25–27]. While the analysis of carrier trapping in Ref. [4] was restricted to polarons and their spatial distribution, in Ref. [24] an attempt to identify pinning defects for excitons was undertaken, though the classes of defects capable to the unprecedented prolongation of exciton lifetimes have not been discerned.

In this work we critically summarize and partially reinterpret existing experimental results on UV-excited luminescence, time-resolved PL and TA in undoped and Mg or Fe-doped $LiNbO_3$ crystals taking into account also recent crucial data of Messerschmidt *et al.* [28] on the selective excitation of long TA. We also present better resolved, fs-pulse-induced PL results, together with detailed temperature dependences of the reinterpreted parameters. Relying on the experimentally observed clear separation of the timescales of the various components corresponding to different recombination centers, we start with a new systematic treatment of the PL components. In each case we distinguish parallel radiative and non-radiative channels using two alternatives: for mobile self-trapped excitons we consider local decay channels, which are essentially of mono-exponential and radiative type, together with substantially stretched non-radiative transformation channel(s), while for already

pinned excitons we assume similarly stretched channels of both radiative and non-radiative kinds taking into account the effect of further nearby defects. The proposed treatment within the excitonic scenarios leads to a description accounting for all observed properties of the reported PL and long TA components. Similar arguments can also be applied to polaronic processes to interpret properties observed for short TA transients. This gives a basis for a straightforward classification and description of defects involved in the different scenarios and timescales. Moreover, comparison of the different temperature dependences of the respective β factors yields insight into the different causes of the given behaviors, thus helping to clarify the physical meaning of stretched exponential decay in general. The proposed treatment can be applied for coupled decay channels exhibiting stretched-exponential or other non-trivial kinetics in any condensed system.

This work is restricted to excitations in the visible or UV range and to timescales above 50 ns, much longer than defect generation, luminescence build-up or lattice relaxation times [29, 30]. More energetic irradiation in LN was reported to result in additional faster transients and further thermostimulated luminescence (TSL) peaks [31, 32], while specific lower energy excitations were found to lead to dopant/impurity luminescence, e.g., of Cr centers, a case first clarified by Macfarlane *et al.* [33]. As nearly all experimental details have already been described in Ref. [24], the paper is organized in sections modeling coupled processes with time-dependent decay rates (S. II), followed by a critical discussion of earlier and recent results on blue PL (S. III) and TA spectra (S. IV), subsequent sections interpreting fast PL decay (S. V) and long components in TA (S. VI) and PL (S. VII). In the Conclusion we give a tabular overview of the derived parameters and mechanisms for the various transients and summarize the trends revealed. In all discussed processes the excitons are more or less strongly coupled to the LN lattice maintaining their small-polaronic character with local lattice distortion and broad optical bands, often described in the literature by the term 'self-trapped exciton'. However, as we are concerned in LN with dipolar, mobile, hopping or pinned excitons, for simplicity we will often omit the adjective 'self-trapped'; for excitons pinned on dipolar defects this term even becomes irrelevant. The kinetic model, on the other hand, has no restriction concerning the type of the exciton, moreover, it can in principle be applied also for other types of energy carriers.

II. MODELS OF COUPLED PROCESSES WITH DISTRIBUTED DECAY PROBABILITIES

The first ingredient required for a comprehensive description of the observed light-induced optical transients in LN or any other complex condensed system is the clarification and modeling of the decay kinetics of the gener-

ated energy carriers, which may, e.g., be arbitrary types of excitons or polarons. We start with the first-order rate equation

$$dN/dt = -\gamma(t)N, \tag{4}$$

where $N(t)$ is the number density (or concentration) of a carrier of a fixed type and $\gamma(t)$ its time-dependent decay rate, the source of the time dependence being the different surroundings of the carriers or any other changing outside influence. The function

$$g(t) = \gamma(t)N(t)/N_0 \tag{5}$$

with $N_0 = N(0)$ can be interpreted as a normalized probability density function (see, e.g., [23]) characterizing the disappearance of a carrier at time t. The average of $\gamma(t)$ over $N(t)$ can be defined as

$$\langle\gamma\rangle = \int_0^\infty \gamma(t)N(t)dt / \int_0^\infty N(t)dt$$
$$= N_0 / \int_0^\infty N(t)dt \equiv \langle\tau\rangle^{-1}, \tag{6}$$

meaning that $\langle\tau\rangle$ defined in equation (3) retains its elegant physical significance as an average decay time but instead of multiplication of τ by a gamma function, in the general case it has to be taken from experiment or the numerical integration of the fit of $N(t)/N_0$. An equivalent definition of $\langle\tau\rangle$ is the first moment of the density function $g(t)$, (see, e.g., [23]). The temperature dependence of $\langle\tau\rangle$ serves as a basis for the definition of an activation energy; this is meaningful in a temperature region where a given decay channel dominates.

To consider radiative and non-radiative channels, $\gamma(t)$ and $N(t)$ have to be split up

$$\gamma(t) = \gamma_r(t) + \gamma_{nr}(t), \qquad N(t) = N_r(t) + N_{nr}(t), \tag{7}$$

where the indices r and nr stand for the respective channels. The population, e.g., in the radiative channel is defined via integration of the term in equation (4) corresponding only to $\gamma_r(t)$:

$$N_r(t) = \int_t^\infty \gamma_r(t')N(t')dt'. \tag{8}$$

This corresponds to the number density (or concentration) of carriers expected to decay between time t and infinity due to the radiative channel. The relative weight of this population is given by $N_r(t)/N(t)$, which may change with time; for $t = \infty$ it is usually called emission branching ratio.

The general solution of equation (4) has the form

$$N(t) = N_0 e^{-q(t)} \tag{9a}$$

$$q(t) = \int_0^t \gamma(t)dt. \tag{9b}$$

However, at the present experimental level achieved in LiNbO$_3$ we only consider time-independent or Kohlrausch-type time-dependent decay rates for the various channels and proceed with three special cases.

A. Time-independent radiative and stretched non-radiative channel, $\beta_{nr} < \beta_r \approx 1$

As a first case we consider a constant radiative ($\beta_r \approx 1$) and a Kohlrausch-type non-radiative channel using the notation

$$\gamma_r = \tau_r^{-1} \tag{10a}$$

$$\gamma_{nr}(t) = \beta t^{\beta-1}\tau_{nr}^{-\beta} \tag{10b}$$

the latter obtained from equation (1) by inverting equation (9b) according to the original reasoning of Kohlrausch [15, 22]. The choice in equation (4) of a constant γ_r corresponds to the classical local decay and that of γ_{nr}, e.g., to the pinning scenario of excitons provided that exciton formation is assumed to be much faster compared to its full hopping lifetime. For the specific choices in equations (10a),(10b) the solution of the rate equation has the simple form

$$N(t) = N_0 \exp\left[-(t/\tau_r) - (t/\tau_{nr})^\beta\right] \tag{11}$$

and the observed transient luminescence intensity corresponds to the radiative parts on both sides of equation (4)

$$I_{lum}(t) \propto -dN_r/dt = \gamma_r N(t)$$
$$= \tau_r^{-1} N_0 \exp\left[-(t/\tau_r) - (t/\tau_{nr})^\beta\right], \tag{12}$$

which clearly differs from equation (2). We will see in S. III.A that both equations still may yield rather similar decay curves for appropriate choices of the parameters whose number increased from two in equation (2) to three in equation (12) apart from the unknown proportionality factor in the measured $I_{lum}(t)$ function. The number density of centers expected to decay radiatively between time t and infinity equals

$$N_r(t) = \tau_r^{-1} N_0 \int_t^\infty \exp\left[-(t'/\tau_r) - (t'/\tau_{nr})^\beta\right] dt' \tag{13a}$$

$$N_{r0} \equiv N_r(0) = N_0 \langle\tau\rangle/\tau_r. \tag{13b}$$

This means that from a time-resolved luminescence experiment, in addition to the various time constants, information on the time-dependent branching ratio N_r/N and its starting value N_{r0}/N_0 can also be derived. It should be noted that equation (13b) remains unchanged for a general, non-Kohlrausch type $\gamma_{nr}(t)$ as well.

B. Radiative and non-radiative channels with coinciding stretching factors $\beta_r = \beta_{nr}$

A second special case worth considering is the one where the radiative and non-radiative channels are of similar types in the sense that $\gamma_r(t)/\gamma_{nr}(t)$ remains constant in time due, e.g., to a common physical reason.

For Kohlrausch-type functions this means identical $\beta_{\mathrm{r}} = \beta_{\mathrm{nr}} = \beta$ parameters:

$$\gamma_{\mathrm{r}}(t) = \beta t^{\beta-1} \tau_{\mathrm{r}}^{-\beta} \tag{14a}$$

$$\gamma_{\mathrm{nr}}(t) = \beta t^{\beta-1} \tau_{\mathrm{nr}}^{-\beta} \tag{14b}$$

where, apart from limiting cases, the time constants τ_{r} and τ_{nr} of the respective channels cannot be observed directly in PL (or TA). However, their combination τ defined via the relation

$$\tau^{-\beta} = \tau_{\mathrm{r}}^{-\beta} + \tau_{\mathrm{nr}}^{-\beta} \tag{15}$$

can be considered as a single observable time constant together with equation (1) in a description of the resulting decay of the species in question. An example for this case are excitons formed upon the encounter of an electron and a hole polaron but needing a slow hopping diffusion (of at least one of the partners, i.e., the electron polaron in LiNbO$_3$) for the encounter, followed by much faster annihilation via local radiative and non-radiative processes of any type. This model may be a good approximation also for already pinned excitons to be discussed later. The transient luminescence intensity again corresponds to the radiative part of equation (4):

$$I_{\mathrm{lum}}(t) \propto \gamma_{\mathrm{r}}(t) N(t) = (\tau/\tau_{\mathrm{r}})^{\beta} \gamma(t) N(t)$$
$$= \beta \tau_{\mathrm{r}}^{-\beta} t^{\beta-1} N_0 \exp\left[-(t/\tau)^{\beta}\right], \tag{16}$$

which restores for this case the previously assumed proportionality equation (2). The number density $N_{\mathrm{r}}(t)$ is again given by integration of $I_{\mathrm{lum}}(t)$

$$N_{\mathrm{r}}(t) = (\tau/\tau_{\mathrm{r}})^{\beta} \int_t^{\infty} \gamma(t') N(t') dt' = (\tau/\tau_{\mathrm{r}})^{\beta} N(t) \tag{17a}$$

$$N_{\mathrm{r}0} = N_0 (\tau/\tau_{\mathrm{r}})^{\beta} \tag{17b}$$

directly yielding a time-independent branching ratio. The 'effective' radiative decay rate averaged over $N(t)$ equals

$$\langle \gamma_{\mathrm{r}} \rangle \equiv \int_0^{\infty} \gamma_{\mathrm{r}}(t) N(t) dt / \int_0^{\infty} N(t) dt = (\tau/\tau_{\mathrm{r}})^{\beta} \langle \tau \rangle^{-1}$$
$$= (\tau^{\beta-1}/\tau_{\mathrm{r}}^{\beta}) / \Gamma(1 + 1/\beta) \tag{18}$$

playing the role of a time-independent radiative decay constant. Relations like equations (17a), (17b) and (18) also hold for the non-radiative channel. In the given special case, as indicated by equation (17a), the various number densities $N(t)$, $N_{\mathrm{r}}(t)$ and $N_{\mathrm{nr}}(t)$ differ only by their amplitudes and obey the same Kohlrausch-type time dependence given by equation (1). Equations (15), (17a) and (17b) are generalizations for $\beta < 1$ of more familiar formulas for $\beta = 1$ (see, e.g., [34]). This justifies the formal use of the proportionality equation (2) for fitting the PL intensity even in the presence of a parallel non-radiative channel if both channels have the same stretching behavior due to the common physical origin of stretching. Formulae similar to equations (15)-(18) can be obtained for non-Kohlrausch-type decay rates with constant $\gamma_{\mathrm{r}}(t)/\gamma_{\mathrm{nr}}(t)$ ratio as well.

C. General case of Kohlrausch type

As a third case we consider radiative and non-radiative channels having different Kohlrausch-type time dependences with independent stretching parameters leading to the formulas

$$N(t) = N_0 \exp\left[-(t/\tau_{\mathrm{r}})^{\beta_{\mathrm{r}}} - (t/\tau_{\mathrm{nr}})^{\beta_{\mathrm{nr}}}\right] \tag{19a}$$

$$I_{\mathrm{lum}}(t) \propto \beta_{\mathrm{r}} t^{\beta_{\mathrm{r}}-1} \tau_{\mathrm{r}}^{-\beta_{\mathrm{r}}} N(t), \tag{19b}$$

whereby branching information can be derived from integration of the latter formula. However, even a larger number (> 2) of independent decay channels with different stretching behavior may be considered at the price of a further increasing number of independent parameters. This still leads to an analytical solution of the rate equation (4) leading to formulas reminding equations (19a) and (19b) apart from the increased number of terms in the exponent.

In some systems, instead of the radiative/non-radiative distinction specified up to now, some other classification, e.g., partition according to local/hopping type may be more important. The chosen formalism offers a uniform treatment for all temperatures and times, and provides, especially via integration over time, a description for the ratio of number densities decaying in any of the considered channels (see equations (13a), (13b), (17a) and (17b) for special cases). In the following the various cases will be applied to PL and TA processes observed in LN systems and attributed to clearly identifiable energy carriers.

III. DISCUSSION OF BLUE PHOTOLUMINESCENCE IN UNDOPED LN AND LN:MG

A. Antisite-related and regular fast luminescence due to NbO$_6$ octahedra

The fastest UV-excited decaying emission reported to our knowledge in undoped LN systems at low temperatures is the rather weak PL in congruent LN single crystals or Li-deficient LN powder, that can also be called 0th PL component, having a lifetime of ≤ 80 ns at 5 K [25, 26] and only ≈ 50 ns at T = 70 K [27]. Its emission band at ≈ 520 nm with a full width at half maximum (FWHM) of ≈ 0.67 eV corresponds to an excitation band near ≈ 305 nm under the UV absorption edge [25, 26] and was attributed to excitons annihilating in Nb$_{\mathrm{Li}}$O$_6$ octahedra containing an antisite Nb$_{\mathrm{Li}}$ atom (for simplicity most linewidth data in eV units cited in this paper are differences of simply converted wavelength values at half-maximum, which is an acceptable approximation of the true energy-scale linewidths [35] for such broad bands). This 'fastest' decay can be explained by the reduced Nb$_{\mathrm{Li}}-$O distances for three oxygens in such octahedra. The strong quenching of this component can

be attributed to the softness of the Nb_{Li} sites having much larger thermal radial r.m.s. displacements (17 pm) than Nb_{Nb} (6 pm) [36].

Li-enriched LN powder, where antisites are eliminated, provides at 5 K an intense PL with a lifetime ≈ 130 μs, FWHM linewidth ≈ 0.59 eV and blueshifted emission and excitation spectra peaking near 440 nm and 260 nm, respectively. This 'fast' PL was attributed to self-trapped excitons recombining in undisturbed NbO_6 octahedra of the regular LN lattice [25]. Closely stoichiometric LN crystals show very similar PL spectra but with a tendency for energy transfer from the regular to the remaining antisite-centered octahedra [37]. It should be noted that no hints for a TA component on the timescale corresponding to that of the fast PL have been observed in the $455-1310$ nm region [24] indicating that the excitons in regular NbO_6 groups have no or very weak absorption in this region. Similarly to the effect of improved stoichiometry, Mg doping near the photorefractive threshold also tends to suppress antisite-type PL [26, 27] in accordance with the elimination of antisites, while for specific values of c_{Mg} the appearance of a much slower PL component [4], to be discussed in the next subsection, was also observed.

The temperature dependence of the fast PL decay near 460 nm, induced by nanosecond laser pulses with (total) photon energy above the band gap at 4.66 eV or 7 eV via one- or two-photon absorption, was reported in Refs. [4] and [24] in LN:Mg doped by 7% and 6.5% Mg, respectively. Though its decay could be described at each temperature by a fast stretched exponential component of the type given by equation (2) (with a lifetime $\tau_{lum,1}$ in the time domain $1-150$ μs for temperatures between 200 K and 20 K [4, 24]), this approach is problematic due to the neglect of the parallel non-radiative decay channel. The existence of the latter is clearly required by the observed temperature quenching of the PL.

We reproduced the raw data by repeating the measurements in the same LN:Mg(6.5%) sample for $\lambda_{em} = 440$ nm where overlap with any rests of antisite-type PL is negligible using the same setup but with single fs pulses of a frequency-doubled Ti:Sapphire laser with a double-photon energy of 6.2 eV yielding better signal to noise ratio than the previously used ns laser; the setup and both lasers have been described in Ref. [24]. In this time domain a possible quasi-constant contribution of the long PL in the 6.5% Mg-doped sample was within the experimental error. For selected temperatures the decay data are shown in figure 1 and are very similar to those reported in Ref. [24]. For modeling the decay we used the $\beta_{nr} < \beta_r = 1$ approximation given by equation (12) (continuous red lines), and for comparison also the $\beta_r = \beta_{nr} = \beta$ fit (equation (16), dashed black lines). The quality of both fits was rather comparable but still with an advantage for the first one at longest times and in the $r \approx 0$ region where the constraint of divergence inherent in equations (2) or (16) was removed. Fitting the data with the general Kohlrausch-type model given by
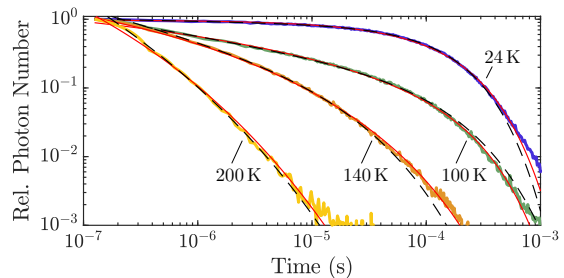

Figure 1. Fast PL decay in LN:Mg(6.5 mol%) for selected temperatures and comparison of the fits using the $\beta_{nr} < \beta_r = 1$ (continuous red lines, equation (12)) and $\beta_r = \beta_{nr}$ (dashed black lines, (equation 16)) models. The fit parameters for the first model are plotted in figure 2. Experimental points are given for $\lambda_{em} = 440$ nm and excitation by single pulses of a Ti:Sapphire laser at $\lambda_{exc} = 400$ nm, FWHM pulse duration $\tau_{FWHM} = 60$ fs, pulse energy of 8 μJ, and a power density 14 GW/cm^2. The data for temperatures above 50 K are taken from [30].

equations (19a) and (19b) was also attempted but gave unstable results. This indicates that even the given improved data set is insufficient to identify any deviations from the $\beta_{nr} < \beta_r = 1$ special case. The temperature dependences of τ_r, $\langle \tau \rangle$, $\beta_{nr} = \beta$, in the $\beta_r \approx 1$ model and the time-integrated PL intensity N_{r0} calculated from equation (13b), are shown as Arrhenius plots in figures 2(a-c). The total number of the generated mobile excitons $N_{0,1}$ is plotted in figure 2(d) and can be assumed as directly proportional to the efficiency of the generation of excitons ϵ^{exc}.

At low temperatures the radiative term dominates, with a temperature independent decay time $\tau = \tau_r = \tau_{10K} \approx 220$ μs (see figure 2(a), experimental points in blue), which is slightly larger than the $\tau_r \approx 100$ μs value obtained in [24]. The independence of τ_r from temperature indicates that no phonon-assisted processes like hopping are involved in the radiative decay of frozen-in or mobile unpinned excitons, while the assumption $\beta_r \approx 1$ corresponds to the expectation that their emission rate is essentially independent from perturbations by defects. The $\beta_{nr} < \beta_r = 1$ model thus provides an adequate picture for fast PL by consequently describing the nearly mono-exponential character of the decay at low temperatures, without putting constraint on the non-radiative channel. The values of β_{nr} are now in the range $0.1-0.23$, much smaller than those obtained earlier at low temperatures assuming a single stretched channel. There is also a slightly increasing tendency for $\beta_{nr}(T)$ with temperature, in sharp contrast to the steep reversed temperature dependence of β found earlier [4, 24]. The β values derived previously in the single channel model can be considered as some weighted mean of the large $\beta_r \approx 1$ and the new small β_{nr} values, both contributing to the stretched char-

acter of the overall decay. There are some changes also for the average decay time $\langle\tau\rangle$ and its temperature dependence. In the $140 - 200$ K region where $\tau_{nr} \ll \tau_r$ holds and the average decay rate can be approximated as $\langle\tau\rangle^{-1} = \nu_0 \exp(-E^{\langle\tau\rangle}/k_B T)$, we obtained the fitting values $\nu_0 = 3.5 \cdot 10^{12\pm1}$ Hz and $E^{\langle\tau\rangle}_{lum,1} = (0.18 \pm 0.05)$ eV for the attempt frequency and the thermal activation energy, respectively. The interpretation of the activation energy $E^{\langle\tau\rangle}_{lum,1}$ and the $\beta(T)$ function will be given in S. V.

B. Properties of the long extrinsic luminescence component in LN:Mg

In 7 mol% Mg-doped LN the existence of a second, slow emission component with a time constant $\tau_{lum,2} = 0.2-2$ s between 200 K and 100 K has been reported [4]. The authors fitted the measured luminescence intensity by the sum of two derivative stretched exponential functions of the type given in equation (2). Given the huge timescale difference between the terms, the obtained separation of the luminescence components is genuine, and is independent of the details of the description of each component by itself; even if the processes were physically coupled, their independent modeling is a good approximation. However, to assess the relative amplitudes of the two components and their channels, the non-radiative decay channels in both components have to be taken into account, which is model dependent. The interplay of the channels in the long PL component must have a different character than that in the fast PL discussed in the previous subsection, given their qualitatively different stretching behavior found in our analysis (see below), but present as a quantitative difference also in the description of Ref. [4]; the different timescales also suggest different mechanisms. Assuming for the short component the $\beta_{nr} < \beta_r \approx 1$ type model found adequate for 6.5% Mg doping and for the long component descriptions by the three models in Sections II A-II C in turn, we used the fit parameters of Ref. [4] to reconstruct the relative number densities involved in the various components and their channels. This could be done in two steps: first we added the non-radiative channels on a $\beta_{nr} = \beta_r = \beta$ level by simply replacing equation (2) by equation (16) meaning a reinterpretation of the fitting constants by accepting for $\tau_{r,i}$ a value of $\tau_i(T)$ extrapolated to low temperature. In the second step, carried out successfully for the fast PL component, we then recalculated the parameters by essentially repeating the fitting procedure within the $\beta_{nr} < \beta_r \approx 1$ model. Such a recalculation, while it was quite satisfactory for fast PL, was impossible for long PL due to poor fits. Attempts to use the general Kohlrausch-type model again yielded unstable fits, so for the long PL we had to accept $\beta_r \approx \beta_{nr}$ as a reasonable approximation. Details of the reconstruction are given in the supplementary information, the results are presented in Table I. An approximate 'activation energy' $E_{lum,2} \approx 0.11$ eV for the

slow PL component, derived from the temperature dependence of τ_2 in the narrow region $160 - 200$ K, was accompanied by a $\beta_2(T)$ function decreasing from 0.8 to 0.5 between 100 K and 200 K [4]. Further properties of the slow component are its slightly blueshifted emission band maximum and smaller bandwidths (FWHM bandwidth (0.56 ± 0.06) eV at 150 K) as compared to the fast component [4]. Its strong dependence on doping and defects clearly supports its extrinsic character (see [7] and references therein). The same references also report reduced luminescence sums for domains inverted at RT by high voltage, which could be nearly returned to their original level in the virgin sample by RT repoling or thermal annealing.

In our near-threshold single-domain 6.5% Mg doped samples poled at temperatures close to the melting point, no long component could be separated by single-ns-pulse experiments [24]. Preliminary fs multi-pulsed experiments, however, show the presence of a long PL component with similar spectral properties (band maximum at ≈ 438 nm and a small FWHM bandwidth (0.58 ± 0.02) eV at 60 K). In 5% Mg doped congruent samples Reichenbach et al. [7] recently observed the presence of a long PL component, however, the derived shorter τ_2 values, together with those of β_2 close to unity, suffered from great uncertainties. Similar was reported in the same Ref. for stoichiometric LN doped by Mg in the range $1\% - 5\%$, i.e., far above the photorefractive threshold for this Li/Nb composition ratio. For 3% Mg doped congruent LN the presence of a rather weak slow PL component was detected [4], with a less long lifetime $\tau_2 = 10$ ms at 150 K where the $N_{0,2}/N_{0,1}$ ratio was larger compared to the 7% Mg case but only due to the suppression of the fast component caused by the presence of Nb_{Li} antisites.

C. Comparison with thermostimulated and x-ray luminescence

An interesting additional result disregarded in later studies, is the absence of TSL in undoped LN, both congruent and stoichiometric, irradiated at 15 K, while a single intense TSL peak at ≈ 70 K with spectral properties (peak at 430 nm, FWHM of ≈ 0.5 eV) similar to those of the long PL transient component can be observed in similarly irradiated congruent LN:Mg(5%) and nearly stoichiometric LN:Mg(3%). This was shown by careful measurements of Sweeney et al. [38] using, beside a low irradiation temperature, also a slow heating rate of 2 K/min, while others [31, 39] used i) higher irradiation temperatures of ≈ 80 K resulting in TSL peaks near 90 K both in undoped and Mg-doped LN, and ii) much faster heating rates causing spectral broadening. This was an early indication that durable charge separation and the separate trapping of electron and hole polarons at 15 K was possible only in the presence of Mg, thus the TSL emission seen at 70 K in LN:Mg must have an extrinsic origin. Similar spectral properties (peak at ≈ 440
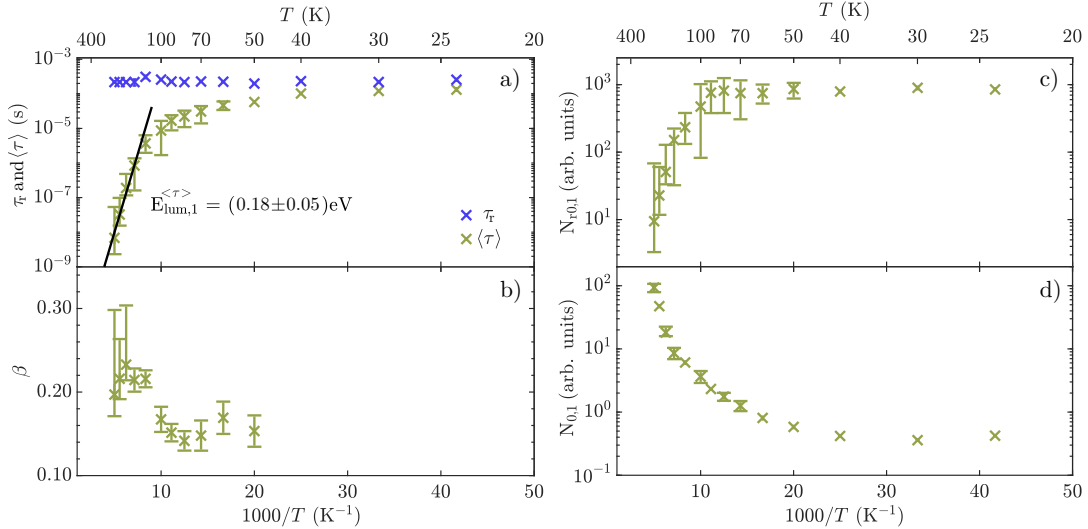
Figure 2. Fast PL in LN:Mg(6.5 mol%): temperature dependence of the temporal decay parameters τ_r (blue symbols) and $\langle\tau\rangle$ (green symbols) (a), stretching factor β (b), temporally integrated luminescence intensity $N_{r0,1}$ (c), and $N_{0,1}$ (d) derived from measurement and fit of the fast luminescence decay component using the $\beta_{nr} < \beta_r = 1$ model at $\lambda_{em} = 440$ nm. The activation energy derived for the non-radiative component is attributed to exciton hopping. For excitation data see caption of figure 1. Data for temperatures above 50 K are taken from [30].

nm, FWHM 0.55 eV) are observed also in x-ray luminescence at 80 K in over-threshold LN:Mg, compared to much weaker, redshifted and broadened XL (≈ 470 nm, FWHM 0.65 eV) in undoped LN [40, 41]. This again supports the dominantly extrinsic character of the various steady-state blue emissions in over-threshold LN:Mg, a character also reflected by the similar spectral properties of the long component of the transient PL. Before proceeding to interpretations of the mechanisms underlying the various excitonic transients first a comparison with the stretched exponential decay of polarons in the same system seems to be appropriate.

IV. DISCUSSION OF TRANSIENT ABSORPTION IN UNDOPED AND MG OR FE-DOPED LN

Transient absorption experiments do not discern radiatively and non-radiatively decaying centers. For convenience the decay of the TA induced by two-photon band-to band excitation is summarized in figure 3 for congruent LN crystals doped by 6.5 mol% Mg or 0.1% Fe for selected temperatures [24]. The detection wavelengths 1310 nm, 785 nm, 488 nm and 445 nm approximately correspond to the peaks of the broad, partly overlapping absorption bands of Nb_{Nb}^{4+} free polarons, Nb_{Li}^{4+} polarons bound on antisites, O^- hole polarons trapped, e.g., by lithium vacancies V_{Li}, and electrons deeply trapped as Fe_{Li}^{2+} centers, respectively [42, 43]. The fast, single decaying TA component in the near IR or red region is

clearly separated, spectrally and mostly also temporarily from all components in the blue, and has been unambiguously ascribed to the hopping of free or temporarily bound polarons prevailing in the absence or presence of antisites in LN:Mg(6.5%) [5] and undoped/Fe-doped LN [10, 11, 14, 44], respectively. The fitted amplitude $\alpha_{li,0}$ of the light-induced absorption of centers involved in this component, which can be assumed as directly proportional to the efficiency of the generation of polarons ϵ^{pol}, was found to be practically independent of temperature up to RT in LN:Mg(6.5%) and to have a moderate $\approx 35\%$ decrease for heating from ≈ 70 K to 400 K in LN:Fe(0.1%). This should be contrasted to the previously discussed larger increase of $\epsilon^{exc} \propto N_{0,1}$ in LN:Mg(6.5%) (see figure 2(d)). The disappearance of the electron polarons was attributed to their capture by O^- trapped holes or Fe^{3+} centers [5, 10, 11, 14, 44]. In undoped LN and LN:Mg, indeed, a fast TA component in the blue can be seen with corresponding $\tau(T)$, $\beta(T)$ dependences, i.e., time-locked with the polaron decay at all investigated temperatures (figure 3(a,b)), and has to correspond to the simultaneous decay of trapped O^- holes. In undoped LN these may be mainly holes trapped at essentially isolated V_{Li}'s while the association with protons trapped as OH^- centers near similar vacancies is also possible but represents a small effect of a few percent [45]. The absence of a comparable or longer luminescence process [25–27] indicates that any Nb^{4+}-O^- recombination centers formed near isolated V_{Li} defects decay non-radiatively. In LN:Fe, where apart from isolated V_{Li}'s, also Fe^{3+} centers have to be present, a similar

Table I. Temperature dependence of parameters and number density ratios for excitons decaying via different components and channels in LN:Mg(7mol%), reconstructed from data in Ref. [4] using the $\beta_r = 1$ and the $\beta_r = \beta_{nr}$ model for the fast and slow component, respectively (see Sections II, III B, and supplementary information). Indices 1 and 2 refer to unpinned and pinned excitons (see Sections V, and VII), r and nr to radiative and non-radiative channels, respectively, while 0 means starting amplitudes of the number densities. For the radiative decay time constants $\tau_{r,iK}$ of the components we assumed values of τ_i extrapolated to low temperature, $\tau_{r,1} = 220$ μs and $\tau_{r,2} = 3$ s.

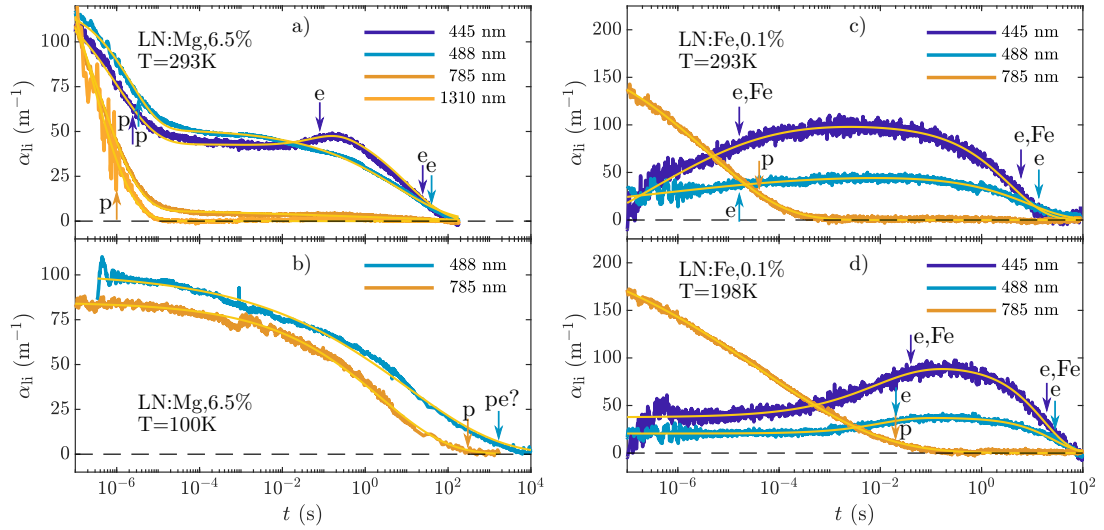| T (K)	$\tau_{r,1}$ μs	$\langle\tau_1\rangle$ (s)	$\beta_{nr,1}$	$N_{0,2}/N_{0,1}$	$N_{r0,1}/N_{0,1}$	$N_{r0,2}/N_{0,2}$	$N_{r0,2}/N_{t00,1}$	$N_{0,2}/N_{nr0,1}$
100	171	16.9	0.19	0.12	0.099	0.72	0.84	0.13
120	199	3.59	0.19	0.084	0.018	0.61	2.8	0.086
140	430	0.784	0.19	0.01	0.0018	0.58	3.2	0.01
160	308	0.121	0.18	0.013	0.0004	0.53	18	0.013

Figure 3. Transient absorption detected in LN:Mg(6.5 mol%) at RT (a) and 100 K (b) and in LN:Fe(0.1 mol%) at RT (c) and 198 K (d) arranged using plots from Ref. [24]. The probe wavelengths indicated in the legends preferentially characterize free Nb_{Nb}^{4+} (1310 nm) and antisite-bound Nb_{Li}^{4+} (785 nm) polarons, O^--V_{Li} trapped-hole polarons (488 nm), and electrons trapped as Fe^{2+} centers (445 nm). Polarons and excitons were generated in two-photon absorption processes by 8 ns pulses at $\lambda = 532$ nm with pulse energies of 290 mJ. The continuous lines correspond to fits using sums of independent stretched exponential functions, the letters p and e indicate polaronic and excitonic transients, respectively. The positions of the arrows correspond to the respective average time $\langle\tau\rangle$ constant for each component, taking into account the horizontal scale, with the exception of the unresolved components in (b) where pe is used for marking the overlapping components of both types. Reproduced and modified from Messerschmidt *et al.* Journal of Physics: Condensed Matter, Volume 31, Number 6, 065701, 2019; licensed under a Creative Commons Attribution 3.0 (CC-BY) license.

decreasing O^- band *and* a *rising* Fe^{2+} band on a similar (or slightly differing) timescale, partly compensating each other in blue TA, has to be expected in the polaronic scenario. At low temperatures, in fact, the blue absorption remains flat in this range (see figure 3(d)), and a large rising component only occurs at times longer by several orders of magnitude. A coincidence of both ranges takes place only near RT (see figure 3(c)) and can be considered as accidental, taking into account the purely excitonic explanation of the delayed rising component (see S. VI A).

The temperature dependence of the $\langle\tau\rangle$ and β parameters of the single polaronic TA component in the red/near IR region is given for both dopants as Arrhenius plots in figure 4 using the data of Ref. [24]. Hopping activation energies for free Nb_{Nb}^{4+} (FP) and antisite-bound Nb_{Li}^{4+} polarons (AP) could be derived, $E_{FP}^{\langle\tau\rangle} = (0.26 \pm 0.04)$ eV above ≈ 100 K for LN:Mg(6.5%) and $E_{AP}^{\langle\tau\rangle} = (0.37\pm0.04)$ eV above ≈ 200 K for LN:Fe(0.1%) [24], in satisfactory agreement with an $E^{\langle\tau\rangle} = (0.39 \pm 0.03)$ eV parameter derived for temperatures above RT from the temperature dependence of the time constant τ in similar
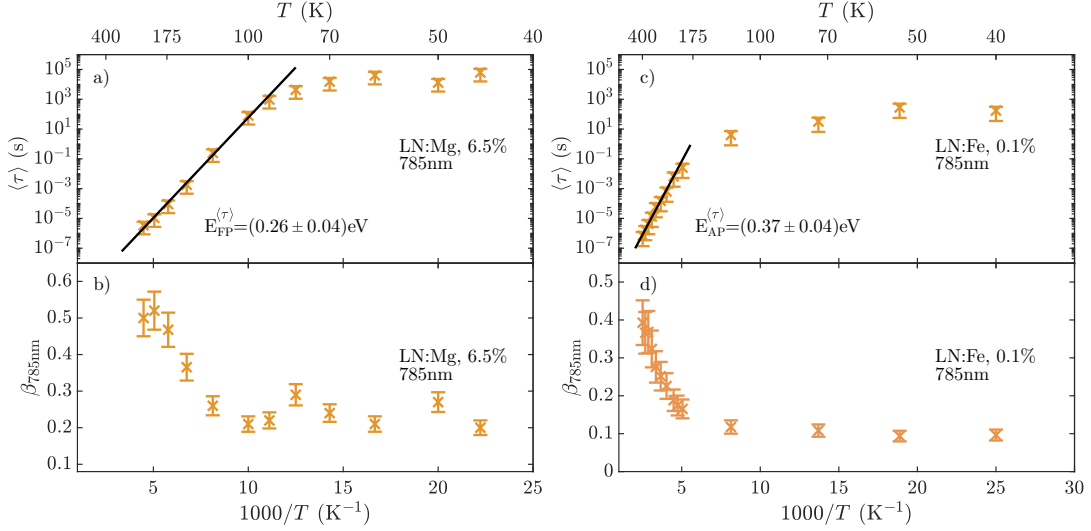
Figure 4. Temperature dependence of the fitted average lifetime $\langle\tau\rangle$ (a, c) and stretching factor β (b, d) for the single, polaronic component of the absorption decay at $\lambda_{\text{probe}} = 785$ nm, $\lambda_{\text{pump}} = 532$ nm in LN:Mg(6.5 mol%) (a, b) and LN:Fe(0.1 mol%) (c, d) using detailed data summarized in Ref. [24]. $E_{\text{FP}}^{\langle\tau\rangle}$ and $E_{\text{AP}}^{\langle\tau\rangle}$ the derived activation energies for free and antisite-bound polarons, respectively.

LN:Fe(0.1%) crystals by Herth *et al.* [10]. The corresponding attempt frequencies are $\nu_0^{\text{FP}} = 5 \cdot 10^{11\pm2}$ Hz and $\nu_0^{\text{AP}} = 5 \cdot 10^{10\pm2}$ Hz for free and antisite-bound polarons, respectively. The obtained values of the hopping activation energy approximately equal one fourth of the optical absorption energy for the same type (free or bound) of polarons: $E_{\text{hop}} \approx 1/4 E_{\text{opt}}$, in good agreement with Emin's theory [46] and Schirmer's analysis [9]. The temperature dependence of polaron hopping has been described in Refs. [46, 47] and has been modeled by Monte-Carlo simulations [17, 48, 49].

The $\beta_{\text{pol}}(T)$ function is *increasing* in the corresponding temperature ranges from small values of ≈ 0.2 at low temperatures to ≈ 0.5 at 200 K in LN:Mg(6.5%) while in LN:Fe(0.1%) it changes in the $0.1 - 0.4$ range in a temperature range shifted to higher temperatures. Above RT and for large, near-saturation values of the pump intensity, the increase of the $\beta_{\text{pol}}(T)$ function was found to continue up to ≈ 0.6 in LN:Fe [14]. The temperatures where thermally activated polaron decay starts correspond to the decay temperatures of their fingerprints in EPR and optical absorption, found at ≈ 70 K and ≈ 150 K for $\text{Nb}_{\text{Nb}}^{4+}$ free and $\text{Nb}_{\text{Li}}^{4+}$ antisite-bound polarons, respectively [38, 42].

The picture formed on the basis of earlier and recent results on polarons in LN can be summarized in the following way: The distribution of electron polarons produced by the laser pulse with respect to the trapping centers is mostly defined by the temperature independent light-induced hopping processes following their generation, provided the pulse duration exceeds the 100 fs timescale [29] of generation processes. For shorter pulses,

especially at lower temperatures, the weight of geminate pairs with small electron-hole distances generated in the same elementary process may be larger in the distance distribution, leading to smaller β. Even for longer pulses the distribution of polarons at the end of the pulse is to some extent influenced by the presence of traps. The distribution of traps, on the other hand, is even less random as it is the frozen-in result of the overall defect structure comprising charged aggregates. Again, with increasing temperature these interaction effects become negligible. The increasing $\beta_{\text{pol}}(T)$ function observed in the experiments may also come from the influence of defect-related energy level shifts, modifying the jump rate of the polaron while moving in the imperfect lattice as suggested by Sturman et al. [17]. This effect may result in less stretching at higher temperatures even for unchanged starting polaron distribution. The largest polaronic β values observed at high temperature correspond to a random walk random trap distribution situation. The remaining time dependence in this case is due to the limited number of trapped holes and is called the trap saturation effect. For an equal number of polarons and traps this corresponds to the fixed value $\beta = 3/5$ derived for the classical diffusion case for small trap densities and non-interacting particles (see [17, 20] and references therein). Accordingly, in the absence of strongly unbalanced quantities of electrons and traps, β values near unity are unrealistic for the polaron hopping scenario. Similarly, decreasing $\beta(T)$ functions, as derived, e.g., for long PL in LN:Mg, and the long TA components in LN:Fe, cannot be attributed to polarons either. Also, two distinct decay components with widely different τ, β pairs cannot

be explained by a continuous distance distribution of polarons. For alternative interpretations we consider in the following sections the peculiarities of decay processes of mobile and variously pinned excitons.

V. INTERPRETATION OF ANTISITE-TYPE AND REGULAR FAST LUMINESCENCE

Due to the marked differences between the τ, β parameter sets obtained for the fast PL and the polaronic TA component in LN:Mg (see figures 2(a,b) and 3(a,b), respectively), polaron hopping has been excluded as a possible mechanism leading to this PL component [24]. To explain the small $E_{\text{lum},1}^{\langle\tau\rangle} \approx 0.18$ eV activation energy observed for over-threshold LN:Mg, the scenario involving exciton hopping in essentially undisturbed parts of the LN lattice can be proposed confirming [24]. This value corresponds to the estimated activation energies in the range of $0.15 - 0.21$ eV for the hopping of (self-trapped) excitons in NaCl [50]. The exciton hopping activation energy is apparently larger than any energy barrier involved in the original localization of free excitons leading to their self-trapping. For the original self-trapping of holes in AgCl an energy barrier of only 1.7 meV was estimated by Kobayasi et al. [51]. A similar thermalization process of hot electrons in LN was found at RT to occur on the 100 femtosecond scale [29, 52]; as highest phonon frequencies in LN are in the 20 THz range [3, 53], this excludes thermalization barriers larger than a few tens of meV. Energy transfer to dopant centers has often been described in terms of exciton migration, e.g., in CaWO$_4$ [54], YVO$_4$ [55], Bi$_4$Ge$_3$O$_{12}$ [56], TiO$_2$-anatase [57], and ZnO [58] but a similar attempt in Eu and Cr co-doped LiNbO$_3$ [59] was later revoked [25]; the reason for the failure may have been the presence of efficient Nb$_{\text{Li}}$ antisite sinks for excitons in the congruent samples used.

Hopping of the self-trapped exciton should be feasible in the LN lattice characterized by outstandingly strong electron-phonon coupling, similarly to polaron hopping. Both phenomena are sketched in figure 5 showing two nearest-neighbor regular Nb atoms and their oxygen octahedra sharing a single O atom. Electron hopping between Nb's is governed by the lattice geometry (Nb$-$Nb distance 3.6 Å, Nb$-$O$-$Nb angle $\approx 140°$) and the 4d(3z^2-r^2)-type electron orbitals of the polaron on each Nb^{4+} atom oriented along the C$_3$ crystal symmetry axis, while it is also influenced by lattice relaxation and the phonon coupling. Hole hopping can be assumed to be much faster than electron hopping due to the smaller O$-$O distances and the large overlap of the 2p functions involved. Therefore exciton hopping can be assumed to differ from polaron hopping only by the presence of the hole on the shared oxygen atom. The net positive charge of this hole reduces the Coulomb barrier between the Nb^{4+} sites and tilts their 4d(3z^2-r^2) orbitals towards the shared oxygen atom, thereby increasing their overlap. Moreover, relaxation around the exciton is smaller than around the po-

laron due to partially cancelling contributions of single charges leaving only contributions of dipolar character; this reduces the energy shift between the initial and final state caused by the Franck-Condon principle. For these reasons exciton hopping can be assumed to require somewhat smaller or comparable activation energy than polaron hopping, in accordance with our interpretation of the observed data.

However, the hopping of self-trapped excitons may also lead to their pinning on defects, abruptly changing their decay behavior [24]. Due to their sizable dipole moment excitons are preferably attracted by common dipolar defects. An evident example are Nb$_{\text{Li}}$O$_6$ antisite complexes in Li-deficient LN, charge-compensated by a number of lithium vacancies: exciton pinning on these complexes results in antisite-type recombination centers leading to the fastest PL component dominating in undoped congruent LN and under-threshold LN:Mg, with a parallel non-radiative channel apparently causing substantial quenching. Extrinsic dipolar defects like charge-compensated Mg$_{\text{Li}}^{2+}$-V$_{\text{Li}}$ and Fe$_{\text{Li}}^{3+}$-V$_{\text{Li}}$ complexes lead to an opposite effect (long components) to be discussed in Sections VI and VII. Polarons, on the other hand, are preferably interacting with defects carrying net charges like weakly charge-compensated Fe$_{\text{Li}}^{3+}$ or trapped holes.

While both free polarons and mobile self-trapped excitons are generated with a more or less random spatial distribution in the crystal, and both can be captured by defects leading to their disappearance or transformation, the cases of these carriers differ in two important aspects:

i) for polarons hopping is indispensable for recombination, while self-trapped excitons have additional on-site radiative and possibly also local non-radiative decay channels, moreover, further, presumably weaker, purely hopping-related 'hot' channels are also thinkable (see figure 6).

ii) the density of intrinsic or extrinsic pinning defects may be very different from that of excitons, while the numbers of polarons and trapped holes coincide in the absence of extrinsic traps.

According to item i) the mono-exponential radiative decay of excitons dominates for fast PL at low temperatures, taking into account that excitons at low T are immobile and do not reach any pinning defects before radiative recombination. While the temperature dependence of the β parameter for fast PL (figure 2(b)) is similar to the case of fast TA (see figure 5(b) in Ref. [24]), the β values for fast PL are smaller roughly by a factor of 2. This can be attributed to the much higher concentration of dopant pinning centers compared to that of excitons; for the latter an upper limit of the order of 0.01 mol% can be estimated from the pulse energy by assuming full energy conversion (this estimate holds also for trapped hole and polaron concentrations). This is in line with the observed essentially linear dependence of the fast PL intensity on the average UV-pump intensity; neither saturation effects nor significant changes of the corresponding decay parameters could be found up to 4
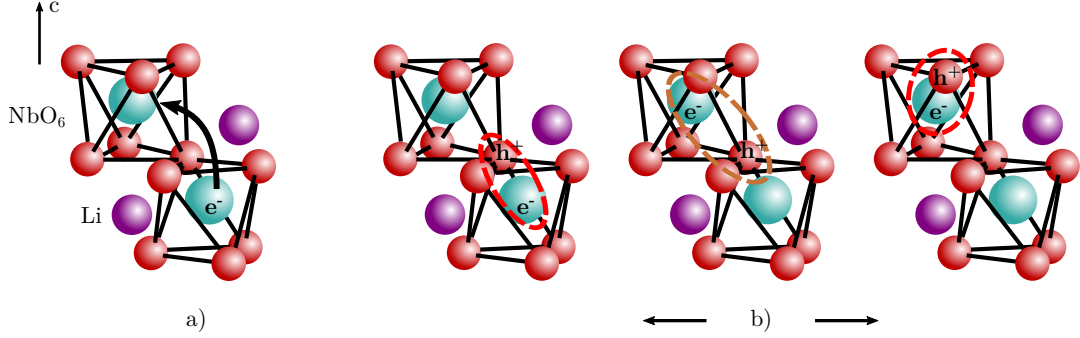
Figure 5. Hopping of polarons (a) and self-trapped excitons (b) in LiNbO$_3$. The presence of a hole on the oxygen shared by the involved octahedra reduces the Coulomb barrier, increases the overlap and decreases the energy difference between the initial and final state of the hopping electron. Hole hopping, required by the ferroelectric displacement of Nb atoms making the involved oxygen atoms inequivalent, is shown as a separate step but can be assumed to be instantaneous due to small O−O distances.
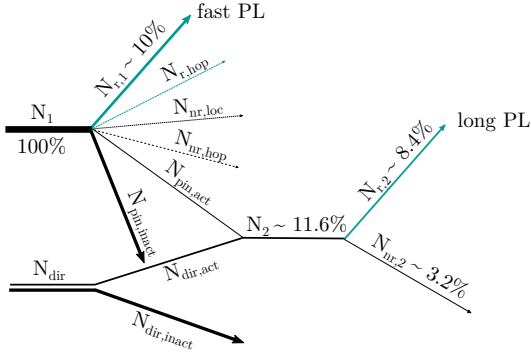

Figure 6. Channel chart of exciton decay in LN:Mg(7mol%). Mobile self-trapped excitons (N_1) get pinned or decay locally by radiative (r) or non-radiative (nr) channels, while hopping induced processes cannot be excluded either. Out of the pinned excitons generated either via hopping (N_{pin}) or by direct generation (N_{dir}), only a fraction $N_{pin,act}$ and $N_{dir,act}$, respectively, possibly those with higher C_3 symmetry, have an additional radiative decay channel contributing to long PL. The estimated starting percentages for PL components and their channels are given for 100 K (see Table I and Ref. [4]) and are also reflected by line thickness. The extra percentage of N_{dir} depends on the excitation photon energy.

MW/cm^2 [4] (see also [60]). Using fs pulses with a much higher peak intensity of 14 GW/cm^2 we have seen no changes either.

Any further channels are not expected to provide the observed extremely small β values of fast PL. Hopping channels could be due to thermally excited transient states occupied only during a hopping step, however, the practically constant $\tau_r \approx 220$ μs value in the whole assessed temperature range (see figure 2(a)) indicates that the radiative decay itself is not due to exciton hopping directly, the latter only leading to its quenching. As demonstrated in the next sections, pinning on dipolar

defects may considerably increase the lifetime of self-trapped excitons, in fact leading to the appearance of slower components in TA and also in PL.

VI. INTERPRETATION OF LONG TA PROCESSES AND THEIR SELECTIVE EXCITATION

The extrinsic nature of the rising and long decreasing TA components in the blue region is strongly supported by their absence in undoped congruent LiNbO$_3$. Excitons pinned on extrinsic defects are expected to have absorption in the blue region and should play an important role in TA. This can be rationalized by the comparison of their structure with that of trapped-hole O$^-$ centers. The hole in the O$^-$ center is strongly localized by an intrinsic defect like a lithium vacancy, while in the self-trapped exciton it is only fixed by the mobile electron constituent, however, both parts are additionally stabilized if pinned on a dipolar defect. Similarly to the O$^-$ center, the pinned exciton should also have absorption corresponding to hole transfer as a first step towards dissociation. The required energy should be larger than or comparable to ≈ 2.6 eV required by the O$^-$-V$_{Li}$ center for a similar excitation, but evidently clearly smaller than the bandgap ≈ 4 eV.

A. LN:Fe

The analysis of the temperature dependences of the parameters of long TA components in the blue region indeed supports the assumption about their pinned-excitonic origin. The temperature dependence of the average decay time $\langle \tau_{abs} \rangle$ for the rising and long decreasing components at 488 nm is reproduced for LN:Fe(0.1%) in figure 7 as an Arrhenius plot, together with the corresponding $\beta_{abs}(T)$
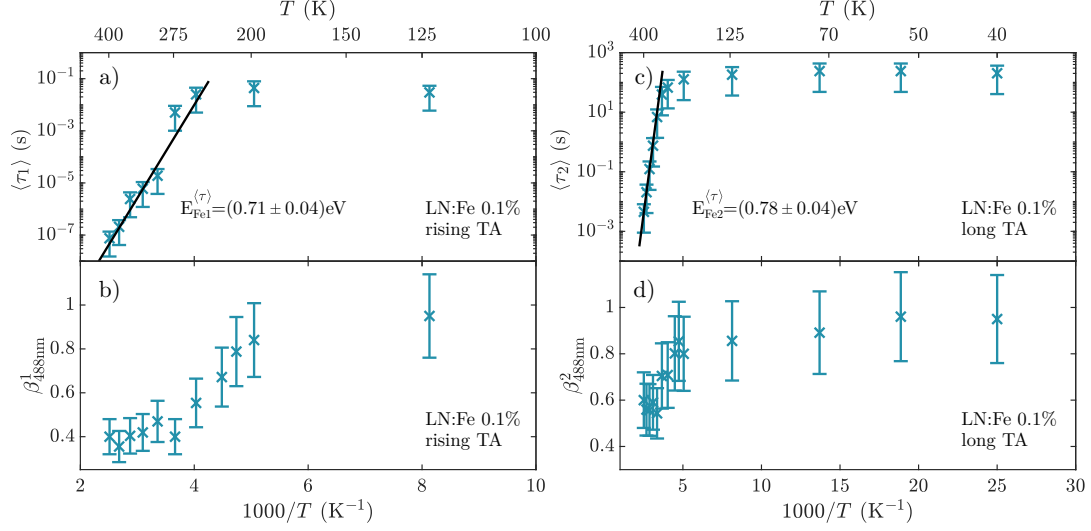
Figure 7. Temperature dependences of the fitted average lifetimes $\langle\tau_i\rangle$ (a, c) and stretching factors β_i (b, d) for the rising (a, b) and the delayed decreasing (c, d) components of the transient absorption at $\lambda = 480$ nm induced by ≈ 8 ns laser pulses with $\lambda_{pump} = 532$ nm in LN:Fe(0.1mol%) using detailed data summarized in [24]. $E_{Fe1}^{\langle\tau\rangle}$ and $E_{Fe2}^{\langle\tau\rangle}$ are the derived activation energies required for the formation and final decay of the deep excitonic state at a vacancy assisted Fe center, respectively.

functions [24]. The large activation energies $E_{Fe,1}^{\langle\tau\rangle} = 0.71$ eV and $E_{Fe,2}^{\langle\tau\rangle} = 0.78$ eV obtained for the rising and delayed decaying components above 250 K, respectively, are of the order of $E_{Fe,i} \approx 1/4 E_{opt}$ where $E_{opt} \approx 2.85$ eV is the absorbed energy quantum in the predicted range corresponding to the wavelength of the probe at $\lambda = 435$ nm where the transients can be best observed, as confirmed at RT experimentally by Messerschmidt et al. [28]. The corresponding attempt frequencies are $\nu_0^{Fe,1} = 1 \cdot 10^{15\pm2}$ Hz and $\nu_0^{Fe,2} = 2 \cdot 10^{12\pm2}$ Hz. These values may indicate the existence of optical local modes above/near the phonon spectrum edge. As shown in figure 7(b), the decreasing functions $\beta_1(T)$ and $\beta_2(T)$ remain larger than 0.8 up to ≈ 200 K, which indicates that local recombination rather than hopping processes are involved.

These observations in LN:Fe have been explained by exciton pinning on the dominant Fe^{3+}-related defect in the crystal [24]. This is the dipolar Fe_{Li}^{3+}-V_{Li} defect shown in figure 8(a) where the Fe dopant on Li site has (at least) one charge-compensating vacancy at another nearest-neighbor Li site. In the Fe^{3+} valence state this defect has no absorption in the visible range. The optimally pinned state of the exciton (figure 8(b)) is characterized by the nearest-neighbor position of the electron constituent with respect to Fe_{Li}^{3+} while the optimal site for the hole is the oxygen atom next to both Nb_{Nb}^{4+} and the lithium vacancy V_{Li} but avoiding the proximity of Fe_{Li}^{3+}. In this position the exciton is 'torn apart' by Fe_{Li}^{3+} and V_{Li} pulling the electron and the hole in different directions. This stretching distortion strongly increases the pinned exciton's lifetime: instead of direct annihilation

the electron rather gives way to the attraction of Fe^{3+} leading to the formation of a Fe_{Li}^{2+}-O^--V_{Li} more deeply trapped exciton (figure 8(c)). This is still a metastable cluster of unusually charged partners temporarily stabilized by V_{Li}, which finally recombine restoring the initial dipolar defect. The proposed scenario is a two-step recombination process of the pinned exciton via a deep gap level involving Fe_{Li}^{2+}, while the adjacent V_{Li} decisively prolongs lifetime in both stages. While the pinned exciton is expected to have some blue absorption, the Fe_{Li}^{2+}-O^--V_{Li} cluster has an increased number of excited configurations corresponding to blue absorption of the Fe_{Li}^{2+} *and* O^--V_{Li} parts taken together. This provides the huge blue rising transient while the subsequent final recombination explains the blue decay component in the minute range (see figures 3(c,d) and 7(a,c)). The energy barriers encountered by a self-trapped exciton in LN:Fe, compared to those for a polaron, are sketched in figure 9.

Stable near-UV-edge absorption, called iron C-band and starting already near 400 nm (≈ 3.1 eV), has been detected in as-grown LN:Fe [61, 62] and should accordingly have an explanation in terms of Fe_{Li}^{3+}-V_{Li} dipoles directly transformed into Fe_{Li}^{2+}-O^--V_{Li} trapped-exciton states. In other words, excitation in this wavelength range may directly lead to the described trapped-excitonic state even without excitonic hopping. Unless directly excited in this band, the ratio of direct generation against hopping-induced formation for trapped excitons can be roughly estimated from the molar concentration ≈ 0.1 mol% of pinning defects to be up to a few times of this concentration, taking into account also the
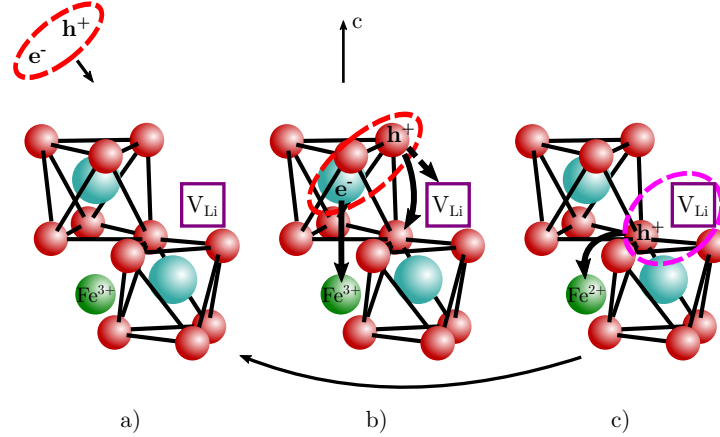
Figure 8. Exciton pinning and two-step decay in LN:Fe. A dipolar Fe_{Li}-V_{Li} defect (a) attracts an exciton, the pinned exciton (b) is 'torn apart' by Fe_{Li}^{3+} and V_{Li}, leading to prolonged lifetime, and transforms into a still metastable Fe_{Li}^{2+}-O^--V_{Li} cluster (c), until final recombination restores the dipolar defect.
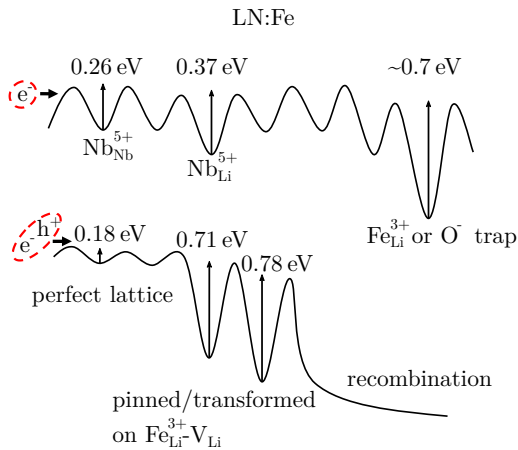

Figure 9. Energy barriers encountered upon hopping by the polaron and the self-trapped exciton in LN:Fe. The trap depth ≈ 0.7 eV for polarons is estimated as one fourth of the energy E_{opt} corresponding to the nearly coinciding absorption maxima of Fe_{Li}^{2+} and O^- centers.

attractive double surplus charge on Fe_{Li}^{3+} as compared to Li^+. In fact, each Fe_{Li}^{3+}-V_{Li} dipole has a single optimal geometry for the pinned exciton with a few other Nb^{4+}-O^- configurations from where the optimal one can be reached by a single hop. The trapped exciton is an improved assignation of the iron C-band compared to the earlier one in terms of a direct charge transfer from O^{2-} to Fe^{3+} [61], which neglected the fact that the dominant Fe_{Li}^{3+} defect should be at least partially charge compensated. The results of such TA experiments at RT, using the same sample, equipment and similar parameters as described in [24] with the difference that a UV pulse at

355 nm instead of 532 nm was used for selective pumping, are shown in figure 10. The data can be fitted *without* an interim rising component, just by the sum of two decaying stretched exponentials with parameters coinciding for $\lambda_{probe} = 785$ nm and $\lambda_{probe} = 488$ nm: $\tau_1 = (4 \pm 2)$ μs, $\beta_1 = 0.3 \pm 0.1$ for the fast component and $\tau_2 = (2 \pm 1)$ s, $\beta_2 = 0.7 \pm 0.05$ for the slow one. There is a strong dominance for the fast one in the red and for the slow one in the blue region; the parameters of the respective weaker components, possibly due to the overlap of the absorption bands monitored, have larger error intervals. Moreover, these data essentially coincide with the data sets previously obtained under 532 nm pulse exposure(see [24] and figure 3(c)). Recent TA measurements using various excitation sources and Fe concentrations [28] confirm the presence of two different broad absorption bands near 435 nm corresponding to different excited configurations of the pinned exciton. These data also confirm the predicted assignation and two-step scenario: pumping at 355 nm in fact results in the long decreasing TA component in the blue region without a preceding rising component, which means that for this low excitation energy the Fe_{Li}^{2+}-O^--V_{Li} state is directly formed without the interim pinned state.

The $\beta_i(T)$ functions observed for the slow components can then be attributed to local disorder, e.g., due to an additional charge compensator in the vicinity of the discussed metastable defects. The small differences between $\beta_1(T)$ and $\beta_2(T)$ seem to obey the tendency: the more localized and deeper the defect the smaller its susceptibility for perturbations. While the discussed dipolar Fe^{3+}-V_{Li} defects may also attract electrons, their hole trapping (at the vacancy end) is rather unlikely due to the surplus double charge of Fe^{3+} on Li^+ site. This is an argument against sequential trapping (capture of a free hole followed by that of a much less mobile electron) as an
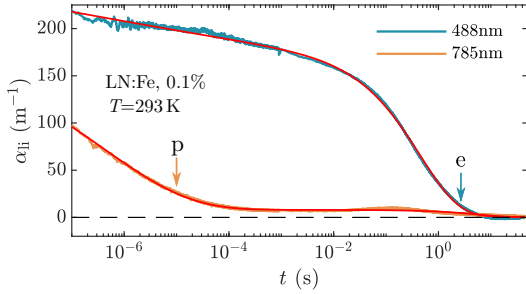
Figure 10. Long-lived transient absorption decay selectively excited in LN:Fe(0.1 mol%) at 355 nm using ≈ 8 ns UV pulses with a pump intensity $I_P = 27$ MW/cm^2. The data at the probe wavelengths 785 nm and 488 nm are fitted with sums of two stretched exponentials (shown in red) without an interim rising component. The fast and long decay, attributed to polarons and trapped excitons, respectively, can be described within error by the same pairs of τ and β values as the respective components in the same sample but under 532 nm pulse exposure (see [28]). The positions of the arrows correspond to the average time constants $\langle \tau \rangle$ of the respective dominant components of polaronic (p) or excitonic (e) origin.

Figure 11. Excitons pinned near Mg_{Nb}-clusters with C_3 symmetry containing one or two on-axis (a) or three off-axis (b) Mg_{Li} charge-compensators. The excitons may have a thermally activated restricted hopping motion between three equivalent positions around the symmetry axis. Small admixtures of the excitonic state extending to oxygen atoms also in the upper oxygen plane above Mg_{Nb}, especially in the case of cluster (b), are also possible.

alternative process for exciton pinning on these defects.

B.   LN:Mg

In LN:Mg(6.5%) a similar two-step process due to background Fe may have resulted in the small bump in the ms - s region (see figure 3(a)). However, unlike to Fe$^{3+/2+}$, the Mg^{2+} defects cannot be recharged, so we have no rising transient due to Mg and the large slow decaying blue component in LN:Mg has to be mainly attributed to the decay of excitons pinned on dipolar Mg^{2+} defects. These long-lived states can be formed by exciton hopping leading to pinning on the dipolar defect or by their local generation on the defect. Taking into account only processes in the undisturbed lattice, the ratio of direct generation against hopping-induced formation should have an upper limit of the order of the molar Mg concentration. In principle, sequential trapping of a hole and an electron cannot be excluded either. Even in the latter case the total lifetime would be defined by the longer lifetime of the pinned excitonic state, and not by a possible polaronic prehistory as discussed in Ref. [4]. This is at variance from the case of the fast intrinsic polaronic TA component where interim excitonic states near an isolated lithium vacancy, if formed at all, are apparently of a different structure resulting in negligible nonradiative lifetimes compared to polaronic hopping times. As suggested by defect models of the LN:Mg system (for a summary see [1]), dipolar Mg_{Li}^{2+}-V_{Li} defects are present for all doping levels while variously charge-compensated Mg_{Nb}^{2+} defects should be increasingly formed above the 5 mol% threshold. Defects of the latter type were found
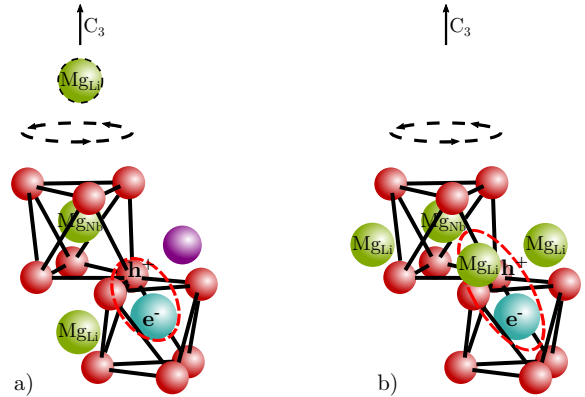
by EPR to be the dominating hole-trapping centers for $c_{Mg} \approx 8$ mol% [63]. Accordingly we attribute the long absorption components to dipolar Mg_{Li}^{2+}-V_{Li} and/or charge-compensated Mg_{Nb}^{2+} compound defects, for which exciton pinning geometries very similar to that shown for Fe defects in figure 8(b) but without further transformation as in figure 8(c), can be proposed. Configurations for Mg_{Nb}^{2+}-Mg_{Li}^{2+}-type defects with C_3 symmetry are shown in figure 11, but additional configurations containing other combinations of charge-compensators and looser aggregates of Mg^{2+} and V_{Li} defects are also possible. All these pinning defects may host differently outstretched excitons leading to a broad distribution of pinned-excitonic decay times, overlapping even that of polarons at low temperatures where only crude approximations of the blue TA with a single component (see figure 3(b)) having a small effective β value are feasible [24].

In conventional absorption measurements of the UV edge in LN:Mg(6.5%) Xin et al. [6] discerned two bands at 3.83 eV and 4.03 eV, which could be separated from the Urbach-type UV absorption edge with FWHM bandwidths of ≈ 1.2 eV and ≈ 0.56 eV, respectively; the width data were derived only from the observed low energy sides of the overlapping bands. Using UV excitation at 3.81 eV near to the maxima of these bands, two distinct light-induced TA components with $\tau_1 \approx 13$ s and $\tau_2 \approx 112$ s at RT could also be measured, having similarly broadened spectra peaking at 2.64 eV and 3.45 eV and approximate activation energies $E_1^{(\tau)} = 0.55$ eV and $E_2^{(\tau)} = 0.82$ eV, respectively; the latter derived from temperature dependent measurements between RT and ≈ 380 K. Our TA data for $c_{Mg} \approx 6.5\%$ (see figure 3(b)) do not contradict to the existence of one or more weak unresolved tran-

sients within the $10 - 100$ s range, however, as discussed above, their interpretation should be given in the excitonic scenario instead of the polaronic one. The results of Xin et al. [6] thus indicate that long TA components in LN:Mg can be selectively excited near the absorption edge and can be assigned to the local generation of excitons directly at the various dipolar complexes of Mg_{Li}^{2+}-V_{Li} and Mg_{Nb}^{2+}-Mg_{Li}^{2+} types, similarly to the case of the iron C-band. The presence of a broad absorption band near 3.88 eV was also reported by [39] in stoichiometric LN doped by an over-threshold amount of 1% Mg, but was attributed to trace amounts of background Fe^{3+} ions despite its significant intensity and blueshifted position compared to the iron C band.

Apparently the light-induced absorption bands at 2.64 and 3.45 eV also observed in Ref. [6] should be attributed to the (further) excitation of these long-lived pinned excitons and not to short-lived trapped holes. On the other hand, due to the broadened near-UV bands of the dipolar complexes both in their stable ground and light-induced pinned-excitonic state, intense excitation in this region may lead to the eventual dissociation of the pinned exciton involved. This explains the generation of electron-hole pairs by below-band-gap excitations observed even at 3.5 eV, e.g., in Ref. [39]. Similar applies also for the case of LN:Fe excited via the iron C-band. The absorption shoulder near 3.7 eV observed near the UV edge in over-threshold LN:Zn [27] may also have a similar explanation.

Even in undoped congruent LN an absorption band at 3.83 eV could be separated from the UV absorption edge [6], but with an FWHM halfwidth of only ≈ 0.27 eV, which is two times smaller than found for the corresponding 3.83 eV band in LN:Mg(6.5%). Apart from dipolar defects due to background impurities this may correspond to the absorption of intrinsic dipolar defects, similar to those playing a role in fast antisite-type luminescence. While in undoped congruent $LiNbO_3$ there are no long TA components [11], under-threshold LN:Mg(4.2%) represents an intermediary case with a relatively weak and less long TA component in the blue region [5]. This may be attributed to excitons pinned on Mg_{Li}^{2+}-V_{Li} defects and/or their looser variants, with the simultaneous suppression of fast PL as reported for LN:Mg(3%) [4] due to the presence of Nb_{Li} antisites.

VII. INTERPRETATION OF THE LONG LUMINESCENCE DECAY IN LN:MG

The long component in PL dominating in over-threshold LN:Mg(7%) with time constants between $\tau_{lum,2} = 0.2 - 2$ s for temperatures between 200 and 100 K [4], occupies an intermediary time domain between those of the polaronic short (6 μs $- 1$ s) and the longest excitonic TA components ($10 - 100$ s) in the same temperature range [24]. As recombination centers playing a role in long PL are also expected to contribute to TA,

they have to be a small minority not identical with those playing the leading role in long TA. Still there may be little doubt about their extrinsic nature as indicated by their dependence on Mg concentration and suggested also by their spectral properties (see Sections III B and III C). Accordingly, the long PL transient, similarly to long TA, may essentially originate from excitons got pinned on or directly generated at dipolar defects, but PL-active defects must be of special type(s) resulting in a somewhat less long pinned-excitonic lifetime. The fact that these pinned excitons must have, in addition to a possibly persisting non-radiative decay channel, also a radiative channel, may contribute to the shortening of $\tau_{lum,2}$. Both channels are influenced by randomly distributed further defects in the vicinity of the pinned exciton causing non-exponential decay, however, differences in the stretching of the channels could not be derived and may be assumed to be small especially at lower temperatures. It cannot be excluded that isolated lithium vacancies can also trap mobile excitons but these should have a similar history as short-lived excitonic states formed upon sequential trapping of hole and electron polarons on V_{Li} and observed only in the short TA of polarons.

For LN:Mg(7%) the relative weights of the various PL components and channels are visualized in figure 6 and can be discussed using the estimated number density ratios shown in Table I. The last column compares the total density $N_{0,2}$ of pinned excitons available for long PL with the number $N_{nr0,1}$ of mobile excitons not decayed radiatively in the local process described by the fast PL component. The ratio $N_{0,2}/N_{nr0,1}$ is definitely smaller than 1 and decreases in the $100 - 160$ K region from $\approx 13\%$ to $\approx 1.3\%$ indicating that most of the mobile excitons 'get lost' with increasing temperature and do not participate in the long PL component. This may be due to the non-radiative channels for mobile exciton decay shown in figure 6. Out of these the formation of PL-inactive pinned excitons has to play the main role, while local and hot channels may have a much smaller contribution. As already discussed in S. V, the local or single-hop non-radiative channels are not expected to provide the observed extremely small β_{nr} values involved in the fast PL component, while hot radiative channels, if fast enough, might influence the temperature dependence of τ_r for this PL component, which is not observed in the assessed temperature region. As shown by the large amplitudes of the fast luminescence at the lowest temperatures, even channels due to hopping-induced pinning become insignificant at those temperatures.

Similarly to the case of long TA, the percentage due to direct generation among PL-active pinned excitons should also depend on the pump photon energy. In Ref. [4] single photon excitation with 4.66 eV was used; this corresponds to the wing of the 3.83 eV and 4.03 eV absorption bands reported by Xin et al. [6] having FWHM bandwidths of ≈ 1.2 eV and ≈ 0.56 eV, respectively. Accordingly in this case enhanced direct generation of pinned excitons of at least two types may be expected.

This may provide, apart from TA, a considerable part of the long PL observed in [4], taken into account that our similar ns-pulsed measurements in LN:Mg(6.5%) with a higher two-photon energy 7 eV practically showed no long PL component [24]. Our recent fs-pulse experiments with two-photon energy 6.2 eV also showed moderate intensities of long PL insufficient for their detailed characterization.

As discussed above,the number density of PL-active pinned excitons compared to that of the PL-inactive ones must be substantially smaller; on the other hand, the small $N_{\text{act}}/N_{\text{inact}}$ ratio can be assumed to be identical for directly generated and hopping-induced pinned excitons. However, the $N_{\text{act}}/N_{\text{inact}}$ ratio must depend on the Mg concentration and the crystal composition, as indicated by the varying intensities and decay parameters reported by Reichenbach et al. [7] for long PL in different LN:Mg systems. Different concentration dependences for various types of Mg complexes are in fact predicted by defect incorporation theories. Reduced luminescence sums observed after high-voltage-enforced domain inversion at RT, reported in Ref. [7], can also be understood taking into account the increased internal fields in the inverted domains acting near unchanged non-centrosymmetric Mg complexes. The mechanism leading to less emission in these frustrated domains (and thereby to domain contrast) may be facilitated pinning of the excitons and the increased weight of the non-radiative decay channels.

The observed narrowing of the emission band of the long component may be ascribed to reduced phonon coupling near the involved Mg defects [6, 9, 64]. The thermally induced process determining the activation energy $E_{\text{lum},2}^{\langle \tau \rangle} < E_{\text{lum},2}^{(\tau)} = 0.11$ eV between 160 K and 200 K [4], may be restricted hopping around the defect without depinning (see figure (11)) leading to parallel decay channels with moderate $\beta > 0.5$ values due , e.g., to further random defects nearby. Depinning characterized by higher activation energy and resulting in fast quenching might be possible at higher temperature. It should be noted that restricted hopping or low temperature tunneling restoring C_3 symmetry has been proposed for an important minority of O^- trapped-hole centers near an isolated cation vacancy, based on EPR spectra exhibiting hyperfine interaction with three equivalent Nb nuclei [65]. Dynamic processes of this kind are well known for O^- centers in a number of oxides [64]. Therefore a similar merry-go-round type process may be assumed to take place for excitonic states pinned on defects with axial symmetry as well.

A tempting assignation for defects dominating in long PL are therefore compound pinning defects with C_3 symmetry, like Mg_{Nb}^{2+} with one or two further on-axis or three off-axis Mg_{Li}^{2+} charge compensators conserving this symmetry (figure 11). Such a correspondence is suggested by the symmetries of the other discussed recombination sites with known preference for radiative/non-radiative decay: intrinsic fast or antisite-type PL occurs at clusters with full C_3 symmetry like regular NbO_6 octahedra or those $Nb_{\text{Li}}O_6$ groups, which are charge-compensated by arrays of three Li vacancies conserving C_3 symmetry. Non-radiative slow decay, on the other hand, can be assumed to be preferred by excitons pinned on compound defects with reduced, C_1 symmetry, like dipolar Fe_{Li}-V_{Li} and Mg_{Li}-V_{Li} defects or Mg_{Nb}^{2+} defects with randomly associated Mg_{Li}^{2+} charge-compensators reducing symmetry. The relative concentration of pinning defects with C_3 symmetry is expected to be maximal for Mg concentrations moderately exceeding the photorefractive threshold value, in accordance with the clear-cut results obtained for the long PL for 7% Mg in congruent LN compared to the elusive long PL at higher or lower dopant levels.

VIII. CONCLUSION

The decaying optical transients identified in various $LiNbO_3$ systems are summarized in Table SI in the supplementary information. At variance from earlier descriptions fixed on point-like polarons and charged traps, we developed an interpretation demonstrating the role of mobile self-trapped excitons and dipolar intrinsic and extrinsic pinning defects. The proposed quantitative description of the decay kinetics and its temperature dependence, based on parallel constant or weakly time-dependent radiative and clearly time-dependent non-radiative decay rates, accounts for mono-exponential and stretched exponential processes observed at low and higher temperatures, respectively. Specialized cases of the coupled kinetic model have been used for the derivation of radiative/non-radiative branching ratios and temperature dependences of the stretching factors from experiment, giving a genuine description also for the non-radiative channels in $LiNbO_3$ at variance from earlier treatments.

In doped $LiNbO_3$ PL processes in three different time domains could be identified corresponding to various excitonic species, i) mobile or frozen-in self-trapped excitons emitting on the micro-to-millisecond scale, ii) excitons trapped on essentially charge-compensated complexes of Nb_{Li} antisites and decaying on the nanosecond scale, and iii) excitons pinned on charge-compensated dipolar complexes formed by Mg dopants yielding long PL on the second scale. The three levels correspond to strong electron-phonon coupling normal in stoichiometric $LiNbO_3$ and to its further enhanced and moderated variants near intrinsic and extrinsic defects, respectively, governed by different levels of Mg doping. The average excitonic lifetime is thus found to be anti-correlated with electron-phonon coupling while being directly correlated with the dipole moment of the exciton.

Processes involving exciton pinning and polaron trapping have been compared, clearly identifying the differences in the relative concentrations of the mobile and fixed partners. The additional decay channels available only for excitons contribute to their faster decay while hopping. The important role of direct pinned-exciton

generation as compared to thermally induced exciton hopping/pinning has been clarified for excitation near the UV absorption edge. The elusive absorption bands observed earlier in the UV-edge region in doped and undoped LiNbO$_3$ can accordingly be assigned to excitonic excitations of dipolar pinning defects.

In addition to slow PL, similar or longer processes in TA have also been attributed to pinned excitons absorbing in the blue range. Exorbitant lifetimes have again been traced back to the outstretched structure of pinned excitons demonstrated on the two-step recombination model of excitons pinned on Fe^{3+}-Li-vacancy complexes. Selective excitation at below-band-gap energy, directly resulting in the intermediate state, provides decisive proof for both the two-step model in the case of the Fe dopant and the existence in LiNbO$_3$ of pinned-exciton type excitations in general.

Polaronic and excitonic scenarios together allow for a coherent explanation of the available experimental results in the given field with relevance for a large class of complex systems. The reason why LiNbO$_3$ may play a paradigmatic role for the analysis of complex kinetic processes are the clearly discernable properties and decay times of the different unrelaxed, polaronic, and mobile excitonic carriers and their variously trapped/pinned counterparts.

[1] Lengyel K et al. 2015 Growth, defect structure, and THz application of stoichiometric lithium niobate *Appl. Phys. Rev.* **2** 040601

[2] Imlau M, Badorreck H and Merschjann C 2015 Optical nonlinearities of small polarons in lithium niobate *Appl. Phys. Rev.* **2** 040606

[3] Fontana M D and Bourson P 2015 Microstructure and defects probed by Raman spectroscopy in lithium niobate crystals and devices *Appl. Phys. Rev.* **2** 040602

[4] Kämpfe T, Haußmann A, Eng L M, Reichenbach P, Thiessen A, Woike Th and Steudtner R 2016 Time-resolved photoluminescence spectroscopy of Nb$_{Nb}^{4+}$ and O$^-$ polarons in LiNbO$_3$ single crystals *Phys. Rev. B* **93** 174116

[5] Conradi D, Merschjann C, Schoke B, Imlau M, Corradi G and Polgár K 2008 Influence of Mg doping on the behaviour of polaronic light-induced absorption in LiNbO$_3$ *phys. stat. sol. (RRL)* **2** 284

[6] Xin F, Zhai Z, Wang X, Kong Y, Xu J and Zhang G 2012 Threshold behavior of the Einstein oscillator, electron-phonon interaction, band-edge absorption, and small hole polarons in LiNbO$_3$:Mg crystals *Phys. Rev. B* **86** 165132

[7] Reichenbach P, Kämpfe T, Haußmann A, Thiessen A, Woike Th, Steudtner R, Kocsor L, Szaller Z, Kovács L and Eng L M 2018 Polaron-Mediated Luminescence in Lithium Niobate and Lithium Tantalate and Its Domain Contrast *Crystals* **8** 214

[8] Faust B and Schirmer O F 1994 Free small polarons in LiNbO$_3$ *Ferroelectrics* **153** 297

[9] Schirmer O F, Imlau M, Merschjann C and Schoke B 2009 Electron small polarons and bipolarons in LiNbO$_3$ *J. Phys. Condens. Matter* **21** 123201

[10] Herth P, Schaniel D, Woike Th, Granzow T, Imlau M and Krätzig E 2005 Polarons generated by laser pulses in doped LiNbO$_3$ *Phys. Rev. B* **71** 125128

[11] Herth P, Granzow T, Schaniel D, Woike Th, Imlau M and Krätzig E 2005 Evidence for Light-Induced Hole Polarons in LiNbO$_3$ *Phys. Rev. Lett.* **95** 067404

[12] Staebler D L and Amodei J J 1972 Thermally fixed holograms in LiNbO$_3$ *Ferroelectrics* **3** 107

[13] Yariv A, Orlov S S and Rakuljic G A 1996 Holographic storage dynamics in lithium niobate: theory and experiment *J. Opt. Soc. Am. B* **13** 2513

[14] Berben D, Buse K, Wevering S, Herth P, Imlau M and Woike T 2000 Lifetime of small polarons in iron-doped lithium-niobate crystals *J. Appl. Phys.* **87** 1034

[15] Kohlrausch R 1854 Theorie des elektrischen Rückstandes in der Leidener Flasche *Ann. Phys.* **167** 179

[16] Phillips J C 1996 Stretched exponential relaxation in molecular and electronic glasses *Rep. Prog. Phys.* **59** 1133

[17] Sturman B, Podivilov E and Gorkunov M 2003 Origin of Stretched Exponential Relaxation for Hopping-Transport Models *Phys. Rev. Lett.* **91** 176602

[18] Berberan-Santos M N, Bodunov E N and Valeur B 2005 Mathematical functions for the analysis of luminescence decays with underlying distributions 1. Kohlrausch decay function (stretched exponential) *Chem. Phys.* **315** 171

[19] Berberan-Santos M, Bodunov E N and Valeur B 2008 History of the Kohlrausch (stretched exponential) function: Focus on uncited pioneering work in luminescence, *Ann. Phys.* **17** 460

[20] Merschjann C, Imlau M, Brüning H, Schoke B and Torbrügge S 2011 Nonexponential relaxation dynamics of localized carrier densities in oxide crystals without structural or energetic disorder *Phys. Rev. B* **84** 052302/1

[21] Elton D C 2017 The origin of the Debye relaxation in liquid water and fitting the high frequency excess response *Phys. Chem. Chem. Phys.* **19** 18739

[22] Elton D C 2018 Stretched Exponential Relaxation https://arxiv.org/pdf/1808.00881[cond-mat.dis-nn]

[23] van Driel A F, Nikolaev I S, Vergeer P, Lodahl P, Vanmaekelbergh D and Vos W L 2007 Statistical analysis of time-resolved emission from ensembles of semiconductor quantum dots: Interpretation of experimental decay models *Phys. Rev. B* **75** 035329/1

[24] Messerschmidt S, Krampf A, Freytag F, Imlau M, Vit-

tadello L, Bazzan M and Corradi G 2019 The role of self-trapped excitons in polaronic recombination processes in lithium niobate *J. Phys. Condens. Matter* **31** 065701

[25] Krol D M, Blasse G and Powell R C 1980 The influence of the Li/Nb ratio on the luminescence properties of LiNbO$_3$ *J. Chem. Phys.* **73** 163

[26] Klose F, Wöhlecke M and Kapphan S 1989 Uv-excited luminescence of LiNbO$_3$ and LiNbO$_3$:Mg *Ferroelectrics* **92** 181

[27] Fischer C, Wöhlecke M, Volk T and Rubinina N 1993 Influence of the Damage Resistant Impurities Zn and Mg on the UV-Excited Luminescence in LiNbO$_3$ *Phys. Status Solidi (a)* **137** 247

[28] Messerschmidt S, Bourdon B, Brinkmann D, Krampf A, Vittadello L and Imlau M 2019, Pulse-induced transient blue absorption related with long-lived excitonic states in iron-doped lithium niobate *Opt. Mater. Express* **9** 2748

[29] Freytag F, Booker P, Corradi G, Messerschmidt S, Krampf A and Imlau M 2018 Picosecond near-to-mid-infrared absorption of pulse-injected small polarons in magnesium doped lithium niobate *Opt. Mater. Express* **8** 1505

[30] Krampf A, Messerschmidt S and Imlau M 2019 Superposed picosecond luminescence kinetics in lithium niobate revealed by means of broadband fs-fluorescence up-conversion spectroscopy *Sci. Rep.* submitted

[31] Pankratov V, Grigorjeva L, Millers D, Corradi G and Polgár K 2000 Luminescence of ferroelectric crystals: LiNbO$_3$ and KNbO$_3$ *Ferroelectrics* **239** 241

[32] Grigorjeva L, Pankratov V, Millers D, Corradi G and Polgár K 2001 Relaxation of electronic excitations in LiNbO$_3$ crystals *Ferroelectrics* **257** 281

[33] Macfarlane P I, Holliday K, Nicholls J F H and Henderson B 1995 Characterization of Cr^{3+} centres in LiNbO$_3$ using fluorescence line narrowing *J. Phys. Condens. Matter* **7** 9643

[34] Pooley D and Runciman W A 1970 Recombination luminescence in alkali halides *J. Phys. C: Solid State Physics* **3** 1815

[35] Wang Y and Townsend P D 2012 Common mistakes in luminescence analysis *J. Phys. Conf. Ser.* **398** 012003

[36] Abrahams S C and Marsh P 1986 Defect Structure Dependence on Composition in Lithium Niobate *Acta Cryst. B* **42** 61

[37] Emond M H J, Wiegel M, Blasse G and Feigelson R 1993 Luminescence of stoichiometric lithium niobate crystals *Mater. Res.* **28** 1025

[38] Sweeney K L, Halliburton L E, Bryan D A, Rice R R, Gerson R and Tomaschke H E 1985 Point defects in Mg-doped lithium niobate *J. Appl. Phys.* **57** 1036

[39] Chirila M M, Garces N Y and Halliburton L E 2002 Thermoluminescence study of stoichiometric LiNbO$_3$ crystals *J. Appl. Phys.* **92** 1221

[40] Koppitz J, Schirmer O F, Wöhlecke M, Kuznetsov A I and Grabmaier B C 1989 Threshold effects in LiNbO$_3$:Mg caused by change of electron-lattice coupling *Ferroelectrics* **92** 233

[41] Arizmendi L, Cabrera J M and Agulló-López F 1981, X-ray induced luminescence of LiNbO$_3$ *Solid State Commun.* **40** 583

[42] Schirmer O F, Thiemann O and Wöhlecke M 1991 Defects in LiNbO$_3$ - I. experimental aspects *J. Phys. Chem. Solids* **52** 185

[43] Merschjann C, Schoke B, Conradi D, Imlau M, Corradi G and Polgár K 2009 Absorption cross sections and number densities of electron and hole polarons in congruently melting LiNbO$_3$ *J. Phys. Condens. Matter* **21** 015906

[44] Grigorjeva L, Millers D, Corradi G, Polgár K and Pankratov V 1999 Induced optical absorption and ITS relaxation in LiNbO$_3$ *Radiat. Eff. Defect. S.* **150** 193

[45] Freytag F, Corradi G and Imlau M 2016 Atomic insight to lattice distortions caused by carrier self-trapping in oxide materials *Sci. Rep.* **6** 36929

[46] Emin D 2012 *Polarons* (Cambridge: Cambridge University Press)

[47] Emin D 1975 Phonon-assisted transition rates I. Optical-phonon-assisted hopping in solids *Adv. Phys.* **24** 305

[48] Mhaouech I and Guilbert L 2016 Temperature dependence of small polaron population decays in iron-doped lithium niobate by Monte Carlo simulations *Solid State Sci.* **60** 28

[49] Carnicero J, Carrascosa M, García G and Agulló-López F 2005 Site correlation effects in the dynamics of iron impurities Fe^{2+}/Fe^{3+} and antisite defects Nb$_{Li}^{4+}$/Nb$_{Li}^{5+}$ after a short-pulse excitation in LiNbO$_3$ *Phys. Rev. B* **72** 245108

[50] Williams R T and Song K S 1990 The self-trapped exciton *J. Phys. Chem. Solids* **51** 679

[51] Kobayasi M, Matsushima Y, Nishi O, Mizuno K and Matsui A H 1995 Indirect free-exciton luminescence in AgCl *Proc. SPIE Vol. 2362, Excitonic Processes in Condensed Matter* 225

[52] Qiu Y, Ucer K B and Williams R T 2005 Formation time of a small electron polaron in LiNbO$_3$: measurements and interpretation *phys. status solidi C* **2** 232

[53] Chowdhury M R, Peckham G E and Saunderson D H 1978 A neutron inelastic scattering study of LiNbO$_3$, *J. Phys. C: Solid State Physics* **11** 1671

[54] Treadaway M J and Powell R C 1975 Energy transfer in samarium-doped calcium tungstate crystals *Phys. Rev. B* **11** 862

[55] Venikouas G E and Powell R C 1978 Laser time-resolved spectroscopy: Investigations of energy transfer in Eu^{3+} and Er^{3+} doped YVO$_4$ *J. Lumin.* **16** 29

[56] Neikirk D P and Powell R C 1979 Laser time-resolved spectroscopy studies of host-sensitized energy transfer in Bi$_4$Ge$_3$O$_{12}$: Er^{3+} crystals *J. Lumin.* **20** 261

[57] Tang H, Berger H, Schmid P E, Lévy F and Burri G 1993 Photoluminescence in TiO$_2$ anatase single crystals *Solid State Commun.* **87** 847

[58] Makino T, Tamura K, Chia C H, Segawa Y, Kawasaki M, Ohtomo A and Koinuma H 2003 Temperature quenching of exciton luminescence intensity in ZnO/(Mg,Zn)O multiple quantum wells *J. Appl. Phys.* **93** 5929

[59] Powell R C and Freed E E 1979 Laser time-resolved studies of exciton migration in doped lithium niobate *J. Chem. Phys.* **70** 4681

[60] Yamada Y and Kanemitsu Y 2013 Photoluminescence spectra of perovskite oxide semiconductors *J. Lumin.* **133** 30

[61] Clark M G, DiSalvo F J, Glass A M and Peterson G E 1973 Electronic structure and optical index damage of iron-doped lithium niobate *J. Chem. Phys.* **59** 6209

[62] Ciampolillo M V, Zaltron A, Bazzan M, Argiolas N and Sada C 2011 Quantification of Iron (Fe) in Lithium Niobate by Optical Absorption *Appl. Spectrosc.* **65** 216

[63] Zaritskii I M, Rakitina L G, Corradi G, Polgar K and Bugai A A 1991 A new trapped-hole radiation defect in heavily Mg-doped LiNbO$_3$ *J. Phys. Condens. Matter* **3**

8457

[64] Schirmer O F 2006 O$^-$ bound small polarons in oxide materials *J. Phys. Condens. Matter* **18** R667

[65] Miki T, Hantehzadeh M R and Halliburton L E 1989 A new trapped-hole center in irradiated LiNbO$_3$ *J. Phys. Chem. Solids* **50** 1003

Excitonic hopping-pinning scenarios in lithium niobate based on atomistic models: different kinds of stretched exponential kinetics in the same system - Supplementary Information -

G Corradi[1,2], A Krampf[1], S Messerschmidt[1], L Vittadello[1], M Imlau[1]

Osnabrück University, Barbarastraße 7, D-49076 Osnabrück, Germany and
Wigner Research Center for Physics, Konkoly-Thege M. út 29-33, H-1121 Budapest, Hungary

(Dated: March 16, 2020)

Appendix A: Relative number densities for decay channels involved in short and long PL

Despite the single-channel model used in Ref. [1] its data for LN:Mg(7%) can be used to reconstruct the number density ratio $N_{r0,2}/N_{r0,1}$ of centers involved in the slow and fast PL decay components, and also the radiative/non-radiative branching ratios within each component.

As a first step the parameters τ and β derived in Ref. [1] are reinterpreted as results obtained within the $\beta_{nr} = \beta_r = \beta$ approach described in S. 2B by choosing for τ_r an extrapolated low temperature limit value of $\tau(T)$, while considering τ as the observed effective characteristic time of both channels combined, defined as $\tau^{-\beta} = \tau_r^{-\beta} + \tau_{nr}^{-\beta}$, where τ_{nr} turns out to be a thermally activated parameter. In this approach the branching information is given by $N_{r0} = N_0(\tau/\tau_r)^{\beta}$. This seems to be a reasonable approximation for the long component.

For the case of the fast PL, however, the $\beta_{nr} < \beta_r \approx 1$ model has to be preferred both for microscopic reasons and better fit. To obtain the new parameter values τ_r, τ_{nr} and β according to S. 2A we used as raw data the excellent fit functions of Ref. [1] given by its earlier fit parameters. The reinterpretation changes the assessment of the total number density of excitons $N_{0,1}$ involved in the fast PL while $N_{r0,1}$ measured as the luminescence sum has to remain the same, independent of the interpretation given. The same luminescence sum can be calculated in both approaches from Eqs. (17b) and (13b), respectively, leading to the equation

$$N_{0,1}\langle\tau_1\rangle/\tau_{r,1} = N_{0,1K}(\tau_{1K}/\tau_{r,1K})^{\beta_{1K}} \quad \text{(A1)}$$

for the fast component, while we accept $N_{0,2} \approx N_{0,2K}$ for the long one (here we used indices 1 and 2 to discern the fast and slow component, respectively, and an additional index K to discern the parameters defined and determined in [1]).

To connect the two components we use the I_{2K}/I_{1K} ratios determined in [1], where the parameter I was defined as a time-independent pre-factor $I_K = N_{0K}\beta_K\tau_K^{-\beta_K}$ for each component (see also Eq. (2)) and obtain

$$N_{0,2K}/N_{0,1K} = (\beta_{1K}/\beta_{2K})\left(\tau_{2K}^{\beta_{2K}}/\tau_{1K}^{\beta_{1K}}\right)(I_{2K}/I_{1K}) \quad \text{(A2)}$$

For the similar ratio in the reinterpreted case we have,

using the above equations and approximations,

$$N_{0,2}/N_{0,1} \approx (\langle\tau_1\rangle/\tau_{r,1})(\tau_{r,1K}/\tau_{1K})^{\beta_{1K}}$$
$$\times (\beta_{1K}/\beta_{2K})\left(\tau_{2K}^{\beta_{2K}}/\tau_{1K}^{\beta_{1K}}\right)(I_{2K}/I_{1K}) \quad \text{(A3)}$$

This modified component-branching ratio was calculated for selected temperatures between 100 and 200 K together with the relative weights of the radiative channels within each component

$$N_{r0,1}/N_{0,1} = \langle\tau_1\rangle/\tau_{r,1} \quad \text{(A4a)}$$

$$N_{r0,2}/N_{0,2} \approx (\tau_{2K}/\tau_{r,2K})^{\beta_{2K}} \quad \text{(A4b)}$$

and the ratio of the amplitudes of the radiative channels

$$N_{r0,2}/N_{r0,1} = (\beta_{1k}/\beta_{2k})\left(\tau_{2K}^{\beta_{2K}}/\tau_{1K}^{\beta_{1K}}\right)^2$$
$$\times \left(\tau_{r,1K}^{\beta_{1K}}/\tau_{r,2K}^{\beta_{2K}}\right)(I_{2K}/I_{1K}). \quad \text{(A5)}$$

The results are summarized in Table I in the manuscript. It should be noted that the ratios calculated using Eqs. (A4b) and (A5) only depend on the excellent fit parameters determined in [1], and are independent of our model choice. Though $\tau_{r,2}$ may be even slightly temperature dependent, its exact choice together with that of $\tau_{r,1}$ is not crucial for the interpretation; changes by a factor of 2 in $\tau_{r,iK}$ result in changes by smaller factors of the various ratios without appreciably modifying the character of their temperature dependence. Similar applies to uncertainties due to experimental or fitting errors.

For LN:Mg(3%) only the $N_{0,2K}/N_{0,1K}$ value at 150 K can be reconstructed from [1], and is increased by 3 orders of magnitude compared to the 7% Mg case. This leads to a clearly increased $N_{r0,2K}/N_{r0,1K}$ value as well, though the larger quenching of the first component has a compensating effect.

Table S I. Summary of transients in absorption and photoluminescence of LiNbO$_3$ systems. Approximate ranges of the stretching factors β are given for the temperature range between 50 K and 200 K unless indicated in brackets. Information on the non-radiative decay mechanisms *local*, *hopping* (leading to trapping or pinning) or *restricted hopping*, is given in the column of the activation energy $E^{\langle\tau\rangle}$; the mechanism of the fast radiative channel is of local character.

Transient	Spectral range	Sample	Carrier	$\tau_r = \langle\tau\rangle$ $T=24K$	τ $T\approx100K$	$\langle\tau\rangle$ $T\approx100K$	τ RT	$\langle\tau\rangle$ RT	$\beta_r(T)$	$\beta_{nr}(T)$ 50→200K	$E^{\langle\tau\rangle}$	Ref.
?			free/hot hole									
TA	near-mid IR	near-st. LN:Mg 1%	unrelaxed electron					≈100 fs				[7]
Antisite PL	520nm	congr. LN undoped	exciton at Nb$_{Li}$-O$_6$		≈50 ns (70K)							[5]
Fast PL	440nm	LN:Mg 6.5%	self-trapped exciton	220μs	≈70ns^a	≈10μs		≈85ps	≈1	0.15→0.22	≈0.18eV hopping	Figs. 2(a,b) [8]
TA	785nm 1310nm	LN:Mg 6.5%	free polaron		≈1s	≈80s	≈0.4μs	≈1μs ≈1μs		0.2→0.5	≈0.26eV hopping	[4], Figs. 4(a,b) [2]
TA	785nm	LN:Fe 0.1%	antisite polaron		≈40μs	≈20s	≈4μs ≈4μs	≈43μs ≈37μs		0.1→0.3	≈0.37eV hopping	[4] Figs. 4(c,d),10
Rising TA	488nm	LN:Fe 0.1%	exciton pinned on Fe^{3+}-V$_{Li}$		≈28ms (125K)	≈30ms (125K)	≈3μs	≈19μs		0.9→0.4 (125K→RT)	≈0.71eV local	[4], Figs. 7(a,b)
Long PL	438nm	LN:Mg 7%	C$_3$ exciton? pinned on Mg$_{Nb}$ cluster		≈2s	≈2.2s			0.8→0.5 (100→200K)	0.8→0.5 (100→200K)	≈0.11eV restricted hopping?	[1]
Long TA	488nm	LN:Fe 0.1%	exciton pinned as Fe^{2+}-O$^-$-V$_{Li}$		≈190s	≈200s	≈7s	≈10s		0.9→0.6 (125K→RT)	≈0.78eV local	[4], Figs. 7(c,d) Fig. 10, [6]
Long TA	488nm	LN:Mg 6.5%	exciton pinned on Mg cluster		≈10s	≈0.5hour	≈6s	≈40s		0.32 (RT)	local 0.55-0.82eV	[4] [3]

^{a} Instead of τ, undefined for fast PL, the value of τ_{nr} is given(see Eq. 12), taken into account that the non-radiative channel is already dominating at 100K.

[1] Kämpfe T, Haußmann A, Eng L M, Reichenbach P, Thiessen A, Woike Th and Steudtner R 2016 Time-resolved photoluminescence spectroscopy of Nb_{Nb}^{4+} and O^- polarons in $LiNbO_3$ single crystals *Phys. Rev. B* **93** 174116

[2] Conradi D, Merschjann C, Schoke B, Imlau M, Corradi G and Polgár K 2008 Influence of Mg doping on the behaviour of polaronic light-induced absorption in $LiNbO_3$ *phys. stat. sol. (RRL)* **2** 284

[3] Xin F, Zhai Z, Wang X, Kong Y, Xu J and Zhang G 2012 Threshold behavior of the Einstein oscillator, electron-phonon interaction, band-edge absorption, and small hole polarons in $LiNbO_3$:Mg crystals *Phys. Rev. B* **86** 165132

[4] Messerschmidt S, Krampf A, Freytag F, Imlau M, Vittadello L, Bazzan M and Corradi G 2019 The role of self-trapped excitons in polaronic recombination processes in lithium niobate *J. Phys. Condens. Matter* **31** 065701

[5] Fischer C, Wöhlecke M, Volk T and Rubinina N 1993 Influence of the Damage Resistant Impurities Zn and Mg on the UV-Excited Luminescence in $LiNbO_3$ *Phys. Status Solidi (a)* **137** 247

[6] Messerschmidt S, Bourdon B, Brinkmann D, Krampf A, Vittadello L and Imlau M 2019, Pulse-induced transient blue absorption related with long-lived excitonic states in iron-doped lithium niobate *Opt. Mater. Express* **9** 2748

[7] Freytag F, Booker P, Corradi G, Messerschmidt S, Krampf A and Imlau M 2018 Picosecond near-to-mid-infrared absorption of pulse-injected small polarons in magnesium doped lithium niobate *Opt. Mater. Express* **8** 1505

[8] Krampf A, Messerschmidt S and Imlau M 2019 Superposed picosecond luminescence kinetics in lithium niobate revealed by means of broadband fs-fluorescence upconversion spectroscopy *Sci. Rep.* submitted

A.4 Picosecond near-to-mid-infrared absorption of pulse-injected small polarons in magnesium doped lithium niobate

- Felix Freytag, Phillip Booker, Gábor Corradi, Simon Messerschmidt, Andreas Krampf, and Mirco Imlau
  Picosecond near-to-mid-infrared absorption of pulse-injected small polarons in magnesium doped lithium niobate
  Opt. Mater. Express **8**, 1505-1514 (2018); doi: 10.1364/OME.8.001505

Picosecond near-to-mid-infrared absorption of pulse-injected small polarons in magnesium doped lithium niobate

Felix Freytag,[1] **Phillip Booker,**[2] **Gábor Corradi,**[3] **Simon Messerschmidt,**[1] **Andreas Krampf,**[1] **and Mirco Imlau**[1,*]

[1]*School of Physics, Osnabrueck University, Barbarastrasse 7, 49076 Osnabrueck, Germany*
[2]*Laser Zentrum Hannover e.V., Hollerithallee 8, 30419 Hannover, Germany*
[3]*Wigner Research Centre for Physics, Institute for Solid State Physics and Optics, Hungarian Academy of Sciences, Konkoly-Thege u. 29-33, 1121 Budapest, Hungary*
[*]*mimlau@uos.de*

Abstract: Femtosecond-pulse-induced ($E_{pump} = 2.5\,\text{eV}$) picosecond infrared absorption is studied in the spectral region between $0.30\,\text{eV}$ and $1.05\,\text{eV}$ in $LiNbO_3$:Mg. We find a non-instantaneous mid-infrared absorption peak in the time domain up to 1 ps and a broad-band, long-lived absorption (maximum at $0.85\,\text{eV}$, width $\approx 0.5\,\text{eV}$), for $t > 1\,\text{ps}$. The modelling succeeds by considering small Nb_{Nb}^{4+} electron polaron formation along the sequence: (i) two-photon injection of hot electron-hole pairs at Nb-O-octahedra, (ii) dissociation and electron cooling by electron-phonon-scattering, and (iii) electron self-localization by strong electron-phonon-coupling.

References and links

1. Y. Furukawa, K. Kitamura, A. Alexandrovski, R. K. Route, M. M. Fejer, and G. Foulon, "Green-induced infrared absorption in MgO doped LiNbO$_3$," Appl. Phys. Lett. **78**, 1970–1972 (2001).
2. J. Hirohashi, V. Pasiskevicius, S. Wang, and F. Laurell, "Picosecond blue-light-induced infrared absorption in single-domain and periodically poled ferroelectrics," J. Appl. Phys. **101**, 033105 (2007).
3. S. Favre, T. Sidler, and R.-P. Salathe, "High-power long-pulse second harmonic generation and optical damage with free-running Nd: YAG laser," IEEE J. Quantum Electron. **39**, 733–740 (2003).
4. R. M. Wood, *Laser-Induced Damage of Optical Materials (Series in Optics and Optoelectronics)* (CRC Press, 2003).
5. G. Li and X. Xu, "Thermally induced dephasing of high power second harmonic generation in MgO:LiNbO$_3$ waveguides," Chin. Opt. Lett. **9**, 121901–121904 (2011).
6. O. F. Schirmer, "O$^-$ bound small polarons in oxide materials," J. Phys. Conden. Matter **18**, R667–R704 (2006).
7. O. F. Schirmer, M. Imlau, C. Merschjann, and B. Schoke, "Electron small polarons and bipolarons in LiNbO$_3$," J. Phys. Conden. Matter **21**, 123201 (2009).
8. D. Emin, "Optical properties of large and small polarons and bipolarons," Phys. Rev. B **48**, 13691–13702 (1993).
9. Y. Qiu, K. B. Ucer, and R. T. Williams, "Formation time of a small electron polaron in LiNbO$_3$: Measurements and interpretation," Phys. Status Solidi C **2**, 232–235 (2005).
10. T. Holstein, "Studies of polaron motion," Annals Phys. **8**, 343–389 (1959).
11. D. Berben, K. Buse, S. Wevering, P. Herth, M. Imlau, and T. Woike, "Lifetime of small polarons in iron-doped lithium–niobate crystals," J. Appl. Phys. **87**, 1034–1041 (2000).
12. O. Beyer, D. Maxein, T. Woike, and K. Buse, "Generation of small bound polarons in lithium niobate crystals on the subpicosecond time scale," Appl. Phys. B **83**, 527–530 (2006).
13. D. A. Bryan, R. Gerson, and H. E. Tomaschke, "Increased optical damage resistance in lithium niobate," Appl. Phys. Lett. **44**, 847 (1984).
14. D. Conradi, C. Merschjann, B. Schoke, M. Imlau, G. Corradi, and K. Polgár, "Influence of Mg doping on the behaviour of polaronic light-induced absorption in LiNbO$_3$," Phys. Status Solidi RRL **2**, 284–286 (2008).
15. S. Sasamoto, J. Hirohashi, and S. Ashihara, "Polaron Dynamics in Lithium Niobate upon Femtosecond Pulse Irradiation: Influence of Magnesium Doping and Stoichiometry Control," J. Appl. Phys. **105**, 083102 (2009).
16. S. Enomoto and S. Ashihara, "Comparative study on light-induced absorption between MgO:LiNbO3 and MgO:LiTaO3," J. Appl. Phys. **110**, 063111 (2011).

146

17. G. M. Greetham, P. Burgos, Q. Cao, I. P. Clark, P. S. Codd, R. C. Farrow, M. W. George, M. Kogimtzis, P. Matousek, A. W. Parker, M. R. Pollard, D. A. Robinson, Z. Xin, and M. Towrie, "Ultra: A unique instrument for time-resolved spectroscopy," Appl. Spectrosc. **64**, 1311–1319 (2010).
18. F. Xin, Z. Zhai, X. Wang, Y. Kong, J. Xu, and G. Zhang, "Threshold behavior of the einstein oscillator, electron-phonon interaction, band-edge absorption, and small hole polarons in linbo$_3$:mg crystals," Phys. Rev. B **86**, 165132 (2012).
19. O. Beyer, D. Maxein, K. Buse, B. Sturman, H. T. Hsieh, and D. Psaltis, "Investigation of nonlinear absorption processes with femtosecond light pulses in lithium niobate crystals," Phys. Rev. E **71** (2005).
20. D. Maxein, S. Kratz, P. Reckenthaeler, J. Bückers, D. Haertle, T. Woike, and K. Buse, "Polarons in magnesium-doped lithium niobate crystals induced by femtosecond light pulses," Appl. Phys. B **92**, 543–547 (2008).
21. X. Yang, G. Xu, H. Li, J. Zhu, and X. Wang, "Optical absorption edge of Mg + Zn: LiNbO$_3$," Cryst. Res. Technol. **31**, 521–527 (1996).
22. T. Roth and R. Laenen, "Absorption of free carriers in diamond determined from the visible to the mid-infrared by femtosecond two-photon absorption spectroscopy," Opt. Commun. **189**, 289–296 (2001).
23. R. Williams and K. Song, "The self-trapped exciton," J. Phys. Chem. Solids **51**, 679–716 (1990).
24. M. D. Fontana and P. Bourson, "Microstructure and defects probed by raman spectroscopy in lithium niobate crystals and devices," Appl. Phys. Rev. **2**, 040602 (2015).
25. G. Blasse, "Fluorescence of niobium-activated antimonates and an empirical criterion for the occurrence of luminescence," J. Chem. Phys. **48**, 3108–3114 (1968).
26. C. Fischer, M. Wöhlecke, T. Volk, and N. Rubinina, "Influence of the damage resistant impurities Zn and Mg on the UV-excited luminescence in LiNbO$_3$," Phys. Status Solidi (a) **137**, 247–255 (1993).
27. D. Emin, "Dynamics of the optically induced properties of a small-polaronic glass," J. Non-Cryst. Solids **35-36**, 969–973 (1980).
28. D. Emin, *Polarons* (Cambridge University Press, 2013).
29. H. Badorreck, S. Nolte, F. Freytag, P. Bäune, V. Dieckmann, and M. Imlau, "Scanning nonlinear absorption in lithium niobate over the time regime of small polaron formation," Opt. Mater. Express **5**, 2729 (2015).
30. M. Imlau, H. Badorreck, and C. Merschjann, "Optical nonlinearities of small polarons in lithium niobate," Appl. Phys. Rev. **2**, 040606 (2015).
31. B. Faust, H. Müller, and O. F. Schirmer, "Free small polarons in LiNbO$_3$," Ferroelectrics **153**, 297–302 (1994).
32. G. Kitaeva, K. Kuznetsov, V. Morozova, I. Naumova, A. Penin, A. Shepelev, A. Viskovatich, and D. Zhigunov, "Reduction-induced polarons and optical response of Mg-doped LiNbO$_3$ crystals," Appl. Phys. B **78**, 759–764 (2004).

1. Introduction

Pulse-induced transient absorption (TA) is a widely accepted nonlinear optical phenomenon in lithium niobate, LiNbO$_3$ (LN), prominently observed as green- or blue-induced infrared absorption (GRIIRA and BLIIRA) with a relaxation time of several seconds [1, 2]. Due to a long-lived transient absorption, propagating laser pulses in lithium niobate foster to a great extent the appearance of laser-induced bulk- and surface damages, and limits the conversion efficiency mainly by damping [3, 4]. It may also cause phase-detuning via localized crystal heating and the thermo-optical effect [5]. In LN, pulse-induced TA is closely connected with the optical generation of small polarons of the hole and electron type, trapped at O^{2-} and $Nb^{5+}_{Nb/Li}$ sites and absorbing in the blue and near-IR region, respectively [6, 7]. Consequently, the amplitude of the absorption maximum is expected to become proportional to the small polaron number density and the TA spectrum should be determined by the broad-bandwidth optical absorption features of small polarons [8]. The temporal evolution of TA is expected to reflect the complex path of carrier cooling and self-localization via phonon-scattering and -coupling [9], subsequent small polaron transport via thermally activated hopping [10] and its termination, e.g., via electron-hole recombination [11]. As a result, TA in LN ranges over 15 decades of time from sub-picoseconds up to seconds [12] and is best studied by a combination of ultrafast pump-probe spectroscopy (fs - ns) and conventional spectrophotometric techniques (ns - D.C.).

The effects of GRIIRA/BLIIRA can almost completely be suppressed by doping LN with Mg, Zn, etc. over their respective threshold concentrations [1]. The doping has the effect to eliminate Nb^{5+}_{Li} antisite defects in LN and, thus, suppresses the formation of Nb^{4+}_{Li} electron and Nb^{4+}_{Li}:Nb^{4+}_{Nb} (bi-)polarons. Although the optical damage resistance is fairly increased in the visible range [13] a significant TA in the visible as well as in the infrared spectral region at timescales $< 10^{-5}$ s becomes more dominant in Mg-doped LN [14]. Despite the broad knowledge on the

147

dependence of GRIIRA/BLIIRA on the crystal composition only little is known about the spectral and temporal properties of TA. In particular, nearly nothing is known about the TA in the mid-IR (MIR) on the ultrafast time scale which is mandatory for the further improvement of high-power mid-infrared optical parametric oscillators (OPOs).

This contribution focuses on the spectral detection of picosecond MIR-TA in LN:Mg related to small Nb_{Nb}^{4+} free polaron (FP) formation in the range between 0.30 eV and 1.05 eV that is difficult to access from the experimental point of view. Our study uncovers that free polaron TA is overlaid by a non-instantaneous, broad-band MIR absorption peak on timescales up to ≈ 1 ps that cannot be attributed to multi-photon absorption processes. Under the assumption of pulse-injection of hot-electron-hole pairs, electron-phonon-scattering and -coupling, both TA contributions can well be separated on the temporal axis. An undisturbed, broad-band small polaron absorption spectrum emerges at a temporal delay of 2 ps after the pump pulse. The obtained data set can be quantitatively modelled on the basis of theoretical expectations for the formation and absorption of small, free Nb_{Nb}^{4+} polarons tested earlier using steady-state spectrophotometric techniques in thermally pre-treated Mg-doped LN and TA-measurements limited to near-IR frequencies [9, 15, 16].

2. Experiment

2.1. VIS-pump-MIR-probe spectrometer

The ps-MIR TA studies were performed by a home-made VIS-pump-MIR-probe spectrometer (schematically sketched in the insert of Fig. 1, for a typical setup see [17]) with a temporal resolution $\Delta t \approx 200$ fs, beam diameters of $d_{pump} = (500 \pm 50)\,\mu m$, $d_{probe} = (400 \pm 50)\,\mu m$ and an intersection angle of $\alpha = (8 \pm 1)°$. The pump (2.5 eV; $\tau_{pump} = (100 \pm 10)$ fs; I_{pump}^0 up to 2.5 PW $\cdot$ m^{-2}; $f_{pump} = 500$ Hz) and the probe (0.30 eV - 1.05 eV; $\tau_{probe} \approx 170$ fs; $I_{probe}^0 < 0.03$ PW $\cdot$ m^{-2}, $f_{probe} = 1$ kHz) pulses are polarized along the c-axis and within the plane of the incident pulses. The infrared signal was detected with a spectral resolution of $\Delta\omega/\omega < 10^{-3}$ and a sensitivity $\Delta\alpha/\alpha \approx 2 \cdot 10^{-2}$ (exemplarily at 0.6 eV) using a combination of a Czerny-Turner spectrograph and a mercury-cadmium-telluride-detector pixel array (32-elements). To improve the signal to noise ratio, every data point is averaged over 2000 sequential pump-probe events. A single crystal (dimensions 6×7 mm^2; thickness $(200 \pm 10)\,\mu m$) of near-stoichiometric LiNbO$_3$:Mg (Mg concentration in the melt 1.0 mol, residual iron content below 5 ppm, estimated molar Li/Nb ratio in the crystal 0.985), grown at the *WIGNER Research Centre for Physics*, Budapest, Hungary is used with a fundamental absorption in the near- to mid-infrared spectral range not exceeding $\alpha_0 = 100$ m^{-1} over the spectral range under investigation (0.30 eV$-$1.05 eV), apart from absorption due to OH$^-$-stretching vibrations in the spectral window $E = (0.424 - 0.443)$ eV [13]. The exact time of maximum overlap between pump and probe pulses was determined using the signal generated via difference frequency generation (DFG) in the LN sample under study (photon energy at about 2 eV). The DFG process was enabled by a weak phase-matching condition using a very thin sample as well as a slightly non-collinear geometry (outer angle $\alpha = (8 \pm 1)°$ between the incident pulses). The DFG pulse energy was measured by a standard Si-detector in transmission geometry. The temporal profile of the DFG signal was measured individually for each probe photon energy. Slight differences in the tails of the qualitatively similar profiles were observed and attributed to differences in the probe pulse durations. The two-photon absorption coefficient is determined to $\beta = (7.9 \pm 0.3)$ mm $\cdot$ GW^{-1} at 2.5 eV. Laser-induced damages of surface and bulk as well as cumulative effects of the MIR-TA between two sequential pump events were carefully checked, but not observed for $I_{pump}^0 = 1.4$ PW $\cdot$ m^{-2}.

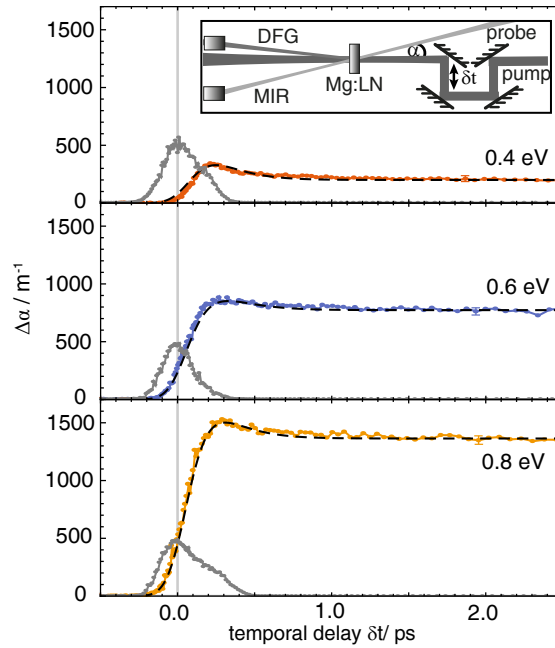Fig. 1. Transient absorption in the ps range for a 2.5 eV pump pulse (I_{pump}^{0} = $(1.4 \pm 0.2)\,\mathrm{PW/m^2}$) and probe photon energies E_{probe} = 0.40 eV (3000 nm), 0.60 eV (2066 nm), 0.80 eV (1550 nm). The transient absorption is defined as $\Delta\alpha(E_{\mathrm{probe}}, \delta t) = \alpha(E_{\mathrm{probe}}, \delta t)_{\mathrm{pumped}} - \alpha(E_{\mathrm{probe}}, \delta t)_{\mathrm{unpumped}}$. The depicted values represent the average over 2000 pump-probe events and the error margin is given by the standard deviation. The gray data points are the corresponding DFG correlation signal between pump and probe pulse (schematic setup shown in the insert) and the dotted black lines correspond to the numerical fits (see chapter 3.2).

2.2. Transient absorption of LN:Mg in the infrared spectral range

Figure 1 shows the transient absorption $\Delta\alpha(\delta t)$ of LN:Mg for three probe photon energies (E_{probe} = 0.4 eV, 0.6 eV, and 0.8 eV) as examples. The vertical gray line (cf. Fig. 1) marks the zero point $\delta t = 0$ defined as the maximum of DFG between pump and probe pulses (type-II eoe phasematching). The cross-correlation signal (dark gray dots in Fig. 1) has a Full-Width-Half-Maximum (FWHM) of (200 ± 10) fs.

All transients of Fig. 1 show qualitatively similar TA dynamics: A moderate non-instantaneous absorption peak dominates the time domain up to 1 ps after the pump pulse. Its maximum shows a marked dependence on the photon energy of the probe pulse and increases from $\Delta\alpha^{\mathrm{max}} \approx 340\,\mathrm{m^{-1}}$ (0.4 eV) up to $\Delta\alpha^{\mathrm{max}} \approx 1520\,\mathrm{m^{-1}}$ (0.8 eV). It is important to note that this absorption peak has a remarkable temporal shift of $\Delta t^{\mathrm{peak}} \approx (270 \pm 30)$ fs (0.6 eV) compared to the pump pulse. In the time domain $t > 1$ ps, a plateau absorption materializes with an amplitude that also depends on the photon energy. The values, e.g., at $\delta t = 2.5$ ps, rise from $\Delta\alpha(2.5\,\mathrm{ps}) = (200 \pm 10)\,\mathrm{m^{-1}}$ (0.4 eV) up to $\Delta\alpha(2.5\,\mathrm{ps}) = (1350 \pm 20)\,\mathrm{m^{-1}}$ (0.8 eV) and remain constant all over the sub-ns time domain. Similar data sets were obtained for all probe photon energies in the investigated range between 0.30 eV and 1.05 eV. For photon energies below 0.4 eV as well as those above

0.8 eV, the MIR-TA shows a clear tendency to smaller values of $\Delta\alpha^{max}$ and $\Delta\alpha(2.5\,ps)$. All transients were investigated as a function of pump peak energy in the range from $0.03\,PW/m^2$ to $2.50\,PW/m^2$ and for different polarizations, as well. Qualitatively, the transients show a similar behavior, but the overall absorption change rises with increasing peak energy. In particular, a quadratic dependence of non-instantaneous peak maximum and plateau absorption is found. The polarization of the beams was chosen to optimize the absorption signal (in accordance with Ref. [15]).

Similar transients were obtained for different crystals of the same boule. We have limited our study to a Mg concentration in the melt of 1.0 mol% in order to suppress the impact of either Nb_{Li}^{4+} formation (for lower Mg concentrations) and of the incorporation of Mg on Nb sites (larger Mg concentrations) [18]. Furthermore, only slight differences in the observed time constants and absolute values of the absorption signals are to be expected (cf. Ref. [15]).

3. Discussion

3.1. Carrier-formation path

These data cannot be explained straightforwardly with the state-of-the-art knowledge of picosecond TA in LN and provide further insights into the optical formation of small Nb_{Nb}^{4+} electron polarons. In particular, to our knowledge, there are no reports on a temporal shift of the absorption peak of the TA with respect to the incident pump pulse in LN for any probe energy. This observation most likely remained inaccessible since the zero point $\delta t = 0$ has been assigned to the time of the maximum value of the absorption peak in recent studies. Consequently, the absorption peak itself was attributed to a *quasi-instantaneous* non-linearity, i.e., non-degenerate two- or multi-photon absorption in Refs. [15, 19, 20] using probe energies E_{probe}=1.55 eV in nominally undoped LN and LN:Mg. For the given fs-pump-probe technique some delay between the pump and a non-degenerate Two-Photon-Absorption (TPA) peak might indeed be expected due to the different group velocities of the probe and pump pulse, as it has been discussed comprehensively by Beyer et al. [19]. According to our experimental approach, we here need to consider the GVD difference between the probe and the DFG pulses. For this case, our calculations reveal temporal corrections of up to $\delta t = (50 \pm 10)\,fs$ depending on the probe photon energy. These values are below our temporal resolution ($\approx 200\,fs$) and below the discovered temporal offset between DFG maximum and non-instantaneous absorption peak. The temporal offset can therefore not be attributed to the effect of GVD, only. Furthermore, the probe photon energies between 0.30 eV and 1.05 eV of our experiment are insufficient to enable non-degenerate two-photon absorption with a pump photon energy of 2.5 eV at a band gap energy of LN of $\approx 3.92\,eV$ [21]. Three-photon interaction of two VIS and one MIR photons may be assumed, instead, but this does not comply with the considerable TA signal amplitudes of our study. However a similar shift of the peak-absorption, dependent on the photon energy, has been reported for diamond [22]. The authors attribute this phenomenon to the long-lasting presence of electrons within the conduction band.

In what follows, we attribute our findings to small Nb_{Nb}^{4+} electron polaron formation according to the process schematically depicted in Fig. 2.

It is reasonable to expect the excitation of hot electron-hole pairs (hot excitons) to occur in a process localized within a Nb-O-octahedron of the LN structure. Such e^--h^+-pairs may recombine immediately (1) or may become self-trapped as self-trapped excitons (STE) [23] by strong coupling to the lattice (2). According to the phonon frequencies in LN up to the 10 THz range [24], the latter process will be delayed by a few hundreds of femtoseconds. It is noteworthy that the STE decay is closely connected with the emission of light in the blue-green spectrum in Mg-doped LN crystals [25, 26] as used in our present study. Path (3) marks the possibility of phonon-assisted small polaron formation from an essentially unrelaxed e^--h^+-pair [27] by transfer of the electron to a next-neighboring Nb_{Nb}^{5+} ion (analogously, a transfer of a hole to a next
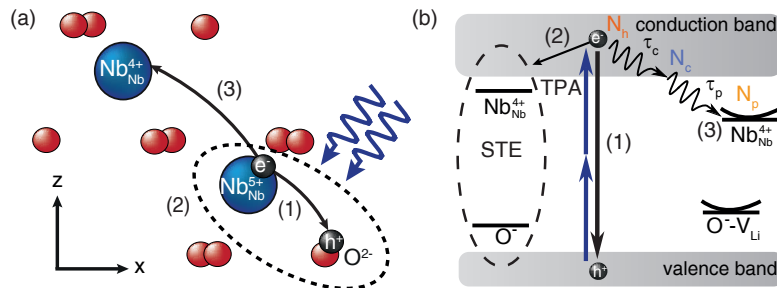
Fig. 2. Recombination paths of fs-pulse generated hot electrons and holes in LN:Mg displayed (a) in a model of the atomic structure and (b) in an energy level diagram. Three recombination paths are considered: (1) the direct recombination of electrons and holes, (2) the formation of self-trapped excitons within a Nb-O-octahedron, and (3) the phonon-assisted formation of small polarons. Our modelling of Eqs. 1-3 is based on relaxation path (3), i.e., paths (1) and (2) are disregarded in our model. This assumption accords with our experimental setup and crystal choice being tailored for small free polaron detection. Furthermore, it considers the comparably low probability for paths (1) and (2).

neighboring O^{2-} also resulting in the dissociation of the e^--h^+-pair may also be considered). This electron will be cooled by means of electron-phonon scattering prior to self-localization via electron-phonon coupling. From the perspective of our experiment, we will be able to detect the MIR absorption features of cooled electrons and Nb_{Nb}^{4+} electron polarons. In contrast, hot exciton states, that most probably show a UV/blue absorption feature, may not be accessible within the spectral region of our probe pulse. As a result, the transients in the MIR should reflect at least two main characteristic time constants: τ_c that takes into account the phonon-assisted processes of e^--h^+ dissociation and hot-electron cooling and τ_p that is determined by the response time of the lattice.

A very similar understanding of TA related to small free Nb_{Nb}^{4+} polaron formation in MgO-doped LN was presented by Qiu et al. [9]. Although a non-instantaneous absorption peak of TPA was not observed, after a delay of the order of 1 ps a long-lived absorption plateau with rise time of about 200 fs at room temperature was clearly discovered and attributed to the formation of Nb_{Nb}^{4+} polarons. The delay was assigned to phonon-assisted cooling of optically excited hot carriers and the time required for carrier localization by electron-phonon coupling. We here note, that paths (1-3) represent three different options for the initially generated electron hole pair. According to D. Emin [28] a sequence of paths (2) → (3) may occur, i.e., the transformation of a STE into a Nb_{Nb}^{4+} electron and O^- hole polaron. In our modelling, however, we disregard paths (1) and (2) as well as a sequential formation process due to a low probability for these processes. In agreement with a theoretical estimate, a delay time of about 80 fs [9] was deduced for the cooling process. In a recent work of Badorreck et al. [29], we were able to verify this delay-time experimentally in nominally undoped, congruent LN with a value of $\tau_c \approx 80$ fs for a TPA excitation process at 2.5 eV, i.e., equivalent to this work.

The characteristics of the absorption plateau remain in full accordance with the state-of-the-art knowledge on TA in the near-infrared spectral range. Its interpretation via small, strong-coupling Nb_{Nb}^{4+} electron polarons is verified by a temperature dependent formation time of a few hundred femtoseconds [9, 15, 19, 20]. The respective decay process obeys a stretched-exponential behavior with a decay time in the regime of a few hundred nanoseconds (over-threshold LN:Mg) [14, 15, 20]. This is short enough to avoid cumulative effects upon repetitive polaron formation at frequencies of 1 kHz.

3.2. Modelling

Based on these considerations, we will now turn to the numerical analysis of our data applying the following set of rate equations:

$$\frac{\partial N_h(L,t)}{\partial t} = \frac{\beta I^2(L,t)}{2\hbar\omega} - \frac{N_h(L,t)}{\tau_c} \tag{1}$$

$$\frac{\partial N_c(L,t)}{\partial t} = \frac{N_h(L,t)}{\tau_c} - \frac{N_c(L,t)}{\tau_p} \tag{2}$$

$$\frac{\partial N_p(L,t)}{\partial t} = \frac{N_c(L,t)}{\tau_p}, \tag{3}$$

where L is a coordinate along the light propagation direction in the crystal, β the TPA-coefficient at the photon energy of the pump pulse $\hbar\omega$, $N_{h,c,p}$ the number densities of injected hot electrons, cold electrons, and polarons, respectively and $I(L,t)$ is the pump light intensity inside the crystal for a gaussian shaped pulse influenced by two-photon absorption based on the considerations from Beyer et al. [19]:

$$I(t,L) = \frac{2 \cdot \exp[-4\log(2)(\frac{t}{\tau_{pump}})^2]}{\beta L\sqrt{\pi}} \int_0^\infty \ln[1 + \beta I_{pump}^0 L \cdot \exp(-s^2)]\,\mathrm{ds}. \tag{4}$$

The calculated transient absorption signal α_{calc} is given by the mean value over the sample length d of the sum of three individual number densities multiplied by their respective absorption cross sections:

$$\alpha_{calc}(t) = \frac{1}{d}\int_0^d [\sigma_p \cdot N_p(L,t) + \sigma_h \cdot N_h(L,t) + \sigma_c \cdot N_c(L,t)]\,\mathrm{dL}. \tag{5}$$

For comparison with the experimentally determined transient absorption α_{exp} the calculated absorption α_{calc} has to be convolved with the gaussian temporal envelope of the probe pulse:

$$\alpha_{exp}(\Delta t) = 2\sqrt{\frac{\log(2)}{\pi\tau_{probe}^2}} \int_{-\infty}^\infty \alpha_{calc}(t) \cdot \exp\left[-4\log(2)\left(\frac{t-\Delta t}{\tau_{probe}}\right)^2\right]\,\mathrm{dt} \tag{6}$$

This interplay of three types of carriers (see Eq. 5) is the key for a successful modelling of the determined characteristics of the MIR-TA. The numerical solution of equations (1)-(6) with the simultaneous fitting of the parameters $\tau_{c,p}$ and $\sigma_{h,c,p}$ could only be performed with the following restrictions: (i) at $t = -300\,\mathrm{fs}$ the number densities of all carriers are assumed to be zero, (ii) according to the sequence of carriers in our approach the number densities initially have to fulfill the relation $N_h^{total} \geq N_c^{total} \geq N_p^{total}$, (iii) the absorption cross section of hot electrons in the MIR is neglected: $\sigma_h \approx 0$, and (iv) electronic cooling stages are faster than lattice relaxation (both on the sub-ps scale): $\tau_c < \tau_p \ll 1\,\mathrm{ps}$. Again, we note that losses of the probe pulse by three-photon absorption including the pump pulse are not considered.

Figure 3 compares the spatially integrated, convolved outcome of fitting equation (6) (green line) to the experimental data set (green dots), exemplarily for $E_{probe} = 0.6\,\mathrm{eV}$.

The temporal evolution of the individual number densities $N_h(t)$, $N_c(t)$ and $N_p(t)$ at $L = 200\,\mu\mathrm{m}$ are depicted as determined from the solution of the rate equations (1)-(3). Fitting was performed for all spectra with a very high quality according to the fitting results depicted as dotted lines in Fig. 1 (normalized root-mean-square deviation (NRMSD) values of (7.1% (0.4 eV), 3.0%
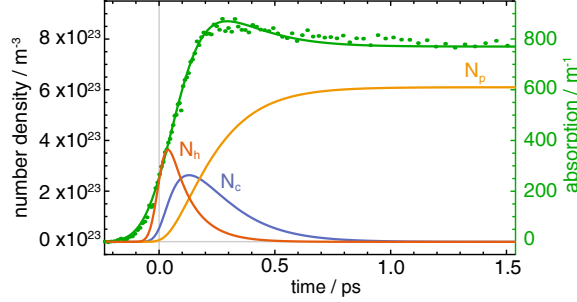
Fig. 3. Numerical fit of the transient absorption (green line) and the data set (green dots) at 0.6 eV. Fitting parameters: τ_c = 100 fs and τ_p = 150 fs. The dynamics of the individual number densities are calculated assuming full conversion of pump photons to hot electrons and are plotted as orange (N_h), blue (N_c) and yellow (N_p) lines. Note that N_h does not contribute to the MIR absorption as σ_h = 0, but is still fully defined due to the nonlinear term in Eq. 1.

(0.6 eV), 2.3% (0.8 eV)). We note that the fitting procedure was performed iteratively for all photon energies using the same set of free fitting parameters τ_c = 100 fs, τ_p = 150 fs.

All fitting parameters agree very well with previously reported values of the generation time of free ($\approx$ 100 fs in [15]) and bound polarons (< 400 fs in [12], [30]) and the free electron cooling time (cf. $\tau_c \approx$ 80 fs in [9, 29]), confirming our assumptions. We note, that the sum of τ_c and τ_p may be interpreted as polaron formation time with respect to the incident pump pulse.

In the time range of -0.2 ps$< t <$ 1 ps, we find that only the number densities of cold electrons and polarons contribute to the overall TA signal. For $t >$ 1 ps, on the other hand, TA is solely determined by the absorption of small, strong-coupling polarons. At the same time, our fit reveals a non-zero population of hot carriers at the maximum of the incident pulse. This feature can be attributed to the temporal width of the incident pulse peak with a pulse duration of $\approx$ 100 fs at peak maximum $t = 0$ fs. Therefore, it must be considered that the pump pulse intensity already rises considerably at $t \approx -50$ fs that results in a non-zero population of hot carriers at $t = 0$ fs.

3.3. Small polaron fingerprint

Based on these findings, it is possible to deduce the absorption fingerprint of Nb_{Nb}^{4+} electron polarons by plotting the spectral dependence of the TA signal at a fixed delay time of $t = 2$ ps as displayed in Fig. 4.

The data reveal a broad spectral distribution with a maximum at $E(h\nu)_{peak} \approx 0.80$ eV that can be applied for an estimate of the small-polaron stabilization energy E_p due to the induced lattice distortion: $E_p = (1/2)E(h\nu)_{peak} \approx 0.40$ eV. A more precise approach with respect to the asymmetric shape of the spectral distribution is given by Emin's theory of small free polarons at elevated temperatures [8]:

$$\Delta\alpha(\hbar\omega) \propto \frac{1}{\hbar\omega} \exp[-(2E_p - \hbar\omega)^2/(8E_p k_B T)], \tag{7}$$

describing the lineshape in excellent agreement with experimental data (cf. solid line in Fig. 4), with k_B being the Boltzmann constant. The fit yields the free polaron binding energy $E_p = (0.44 \pm 0.02)$ eV, a peak maximum at $E(h\nu)_{peak} = (0.83 \pm 0.04)$ eV and a half width at half maximum of $W = (0.26 \pm 0.01)$ eV at room temperature and $t = 2$ ps. A comparison of the values obtained in this study with previous investigations using thermally stabilized small polarons
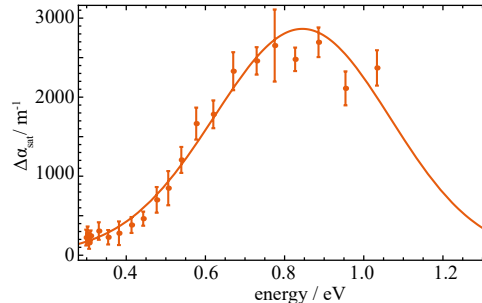
Fig. 4. Absorption fingerprint of fs-pulse induced free polarons at a fixed time delay of $t = 2\,\mathrm{ps}$ ($I_{\mathrm{pump}}^0 = (2.5 \pm 0.2)\,\mathrm{PW/m}^2$). The continuous line fits Eq. 7 to the experimental data set. The error margin is given by the standard deviation and the error made by determining the light intensity.

is given in Tab. 1. The peak position is in agreement with previous studies, whereas slight differences can be seen in the case of the spectral width.

The discovered differences can be attributed to (i) the use of an asymmetric fitting function and (ii) the impact of a non-equilibrium electronic state that has to be expected on the picosecond time scale after exposure to an intense fs-laser pulse. Driving evidence for the latter conclusion is the short lifetime of a few μs of the transient absorption with a complete recovery of the involved electronic state.

Table 1. Polaron stabilization energy E_p and half width at half maximum W of the MIR absorption feature in comparison.

E_p(eV)	W(eV)	T(K)	Reference
0.44± 0.02	0.26 ± 0.01	295	this study
0.48	≈ 0.23	295	[31]
0.54	≈ 0.40	6	[31]
0.54	0.37	295	[7]
0.47	≈0.25	295	[32]

4.   Conclusion & novelty

In conclusion, our analysis clarifies the picosecond transient absorption of femtosecond-pulse injected carriers during their relaxation to small free $\mathrm{Nb}_{\mathrm{Nb}}^{4+}$ electron polarons in the spectral range of 0.30 eV up to 1.05 eV. It extends the knowledge about the optical properties of small electron polarons to the ultrafast time regime that also comprises small polaron formation.

From a fundamental viewpoint, our findings demonstrate that the theoretical concepts about the optical properties of small, strong-coupling polarons (Holstein-Emin approach) can be transferred to the field of nonlinear optics and femtophysics in general, i.e., to the non-equilibrium state, which is indicated by a fair agreement of the spectral parameters of the TA plateau with 'steady-state' values for free polarons.

A specific result of our study is the interpretation of the TA maximum as a non-instantaneous absorption peak due to an intermediary (unrelaxed cold) electron state that cannot be attributed to the action of multiphoton absorption. This was obtained using a methodical peculiarity of fs-VIS-pump-MIR-probe spectroscopy in nonlinear optical LN that makes use of the difference frequency generation signal between pump and probe to define the exact time of maximal overlap.

By comprehensive modelling of the multi-step flow of electronic energy induced by two-photon absorption, that was missing in the literature so far, existing models for small polaron formation are supported, confirming also predictions for the lifetimes of early stages despite the negligible mid-IR absorption of hot electrons. The ps-MIR TA may be considered for fs-pulse-exposed frequency converters based on lithium niobate crystals and for the further development and engineering of demanding high-power MIR fs-laser sources using polar representatives of niobates and of the borate class (LBO, BBO, etc.).

This study may also serve as a hint for the need of a further subdivision of the small polaron formation process and will push forward studies on the appearance and transport of hot excitons by probing the UV/VIS spectral range.

A.5 Superposed picosecond luminescence kinetics in lithium niobate revealed by means of broadband fs-fluorescence upconversion spectroscopy

- Andreas Krampf, Simon Messerschmidt and Mirco Imlau
  Superposed picosecond luminescence kinetics in lithium niobate revealed by means of broadband fs-fluorescence upconversion spectroscopy
  Scientific Reports **10**, 11397 (2020); doi: 10.1038/s41598-020-68376-6

SCIENTIFIC REPORTS

natureresearch

Check for updates

OPEN

Superposed picosecond luminescence kinetics in lithium niobate revealed by means of broadband fs-fluorescence upconversion spectroscopy

A. Krampf, S. Messerschmidt & M. Imlau✉

Various manifestations of small polarons strongly affect the linear and nonlinear optical properties of the oxide crystal lithium niobate (LiNbO₃, LN). While related transient absorption phenomena in LN have been extensively studied in recent decades, a sound microscopic picture describing the blue-green (photo)luminescence of lithium niobate single crystals is still missing. In particular, almost nothing is known about: (i) the luminescence build-up and (ii) its room temperature decay. We present here the results of our systematic experimental study using nominally undoped and Mg-doped LN crystals with different Mg concentration. Picosecond luminescence was detected by means of femtosecond fluorescence upconversion spectroscopy (FLUPS) extended to the inspection of oxide crystals in reflection geometry. Two distinct luminescence decay components on the picosecond time scale are revealed. While a short exponential decay is present in each sample, a longer non-exponential decay clearly depends on the crystal composition. Since transient absorption spectroscopy excludes geminate small polaron annihilation as microscopic cause of the luminescence, both decay components are discussed in the context of self-trapped exciton (STE) transport and decay.

ABO_3 perovskite-like ferroelectrics exhibiting unique electronic properties[1] are important materials for optical frequency converters[2], THz pulse generation[3] or promise advances in the fields of photovoltaics[4], oxide electronics[5] and electroluminescent devices[6]. In these materials, strong charge carrier-phonon coupling often lead to pronounced photo-induced polaronic effects manifesting in, e.g., laser-induced bulk damage[7,8], and broad photoluminescence bands emitted from BO_6 octahedra[9–11].

Lithium niobate is a frequently studied example of ferroelectric perovskite-like oxides, known for its rich defect structure leading to a conglomeration of intrinsic and extrinsic small polarons[7]. Whereas light-induced phenomena in LN, such as transient absorption, have been extensively studied in recent decades relating them with formation and transport of small polarons[12–23], a sound microscopic picture describing the blue-green (photo)luminescence of lithium niobate single crystals is still missing.

While recently geminate small polaron annihilation has been proposed to lead to a two component luminescence decay in Mg-doped lithium niobate at low temperatures[24], Messerschmidt et al. showed that low temperature luminescence and absorption decay on very different time scales[25]. They revived the idea of radiatively decaying self-trapped excitons located at niobium-oxygen octahedra, which has been introduced over thirty years ago in the pioneering work of Blasse et al.[9,26–29]. They concluded that an effect of STE formation on the light-matter interaction at elevated temperatures could per se no longer be neglected. In fact, no absorption feature of intrinsic self-trapped excitons has been reported so far, while Messerschmidt et al. related long-lived STEs pinned on extrinsic defects with a transient absorption in the blue-green spectral range[25]. These transients, which can last from seconds to hours, should naturally have a major influence on light-induced damage of the crystals, especially when illuminated with continuous wave lasers or short laser pulses at high repetition rates.

School of Physics, Osnabrueck University, Barbarastrasse 7, 49076 Osnabrueck, Germany. ✉email: mirco.imlau@uni-osnabrueck.de

1

In their revised excitation and relaxation model, different excitation paths entailing pinned-STE formation are proposed, which have recently been confirmed experimentally for Fe-doped crystals[30]. One of these paths is the band-to-band generation of electron-hole-pairs subsequently forming self-trapped excitons, which in turn migrate through the crystal until they are pinned on a defect. Therefore, the STE formation and decay times are important characteristics regarding the extend to which the propagation of ultrashort laser pulses is affected by the (pinned-)STE absorption features, especially at elevated temperatures where STE migration and pinning could play a dominant role. The authors showed that the temperature-dependent luminescence peak position deviates from the Varshni behavior for temperatures above $\approx$ 200 K[25]. Room temperature luminescence kinetics might therefore not be assessable from low temperature data via extrapolation.

For a comprehensive understanding of fs-laser pulse propagation in the presence of STEs and moreover of photo-excited charge carrier kinetics in lithium niobate in general, two important aspects have not yet been (sufficiently) investigated due to lack of temporal resolution[24–26,31–34]: (i) luminescence build-up and (ii) room temperature decay. The second point is particularly important with regard to applications. The self-trapped exciton formation time, on the other hand, helps to clarify whether small polarons and self-trapped excitons in lithium niobate are correlated species. Previous studies have already shown that a merging of small electron and hole polarons into self-trapped excitons is unlikely[25]. In contrast, the question of whether STEs break up into pairs of oppositely-charged small polarons on a short time scale is still completely unsolved.

To address these points, an experimental approach with maximum temporal resolution has to be used. We therefore apply broadband femtosecond fluorescence upconversion spectroscopy, which provides luminescence spectra at fixed time delays with femtosecond temporal resolution[35]. For this purpose a very thin nonlinear optical crystal and a fixed non-collinear geometry is used for frequency mixing. Compared to the conventional upconversion scheme, where luminescence spectra are reconstructed from kinetic traces at single wavelengths, such an approach benefits from a faster measurement routine, a reduced background signal and a robust photometric correction procedure (see[35–37] and this manuscript).

As an experimental novelty we adapt the existing scheme designed to measure molecules solved in liquids to solid samples. In detail, we combine a reflection geometry to collect luminescence known from the conventional upconversion scheme[38] with the broadband non-collinear sum frequency mixing. This avoids deterioration of the temporal resolution introduced by the relatively large group velocity dispersion in lithium niobate. The apparatus response function has a full width at half maximum of < 160 fs offering a temporal resolution much better than state of the art streak cameras[39]. The experimental setup is tested by measuring the reference system Coumarin 153 solved in dimethyl-sulfoxide (DMSO). The theoretical photometric correction procedure again proves to be very rigid[35] and is further improved by additional consideration of the finite spectral bandwidth of the gate pulses. Both can be found in the supplementary information.

Samples with different stoichiometry and magnesium doping concentration are examined. First, it is demonstrated that it is possible to adapt such an experimental approach to the relatively weak room temperature luminescence of ABO_3 perovskite-like ferroelectrics such as lithium niobate. Since the broadband scheme naturally suffers from low conversion efficiencies, it is not clear a priori whether the luminescence intensity is sufficiently high for a detectable sum frequency signal. In a second step, the room temperature luminescence kinetics of a heavily Mg-doped LN crystal is compared with data at low temperature (50–200 K) measured with a photomultiplier and a gated photon counter. A combination of both experimental techniques extends the observed temperature range from 50 K to 300 K resulting in a much more reliable activation energy of the decay process compared to previous studies. Moreover, we are able to estimate an upper time limit for the ultrafast luminescence build-up and measure the luminescence decay of congruently melting lithium niobate. As these crystals exhibit the fastest and weakest luminescence decay of the LN compositions under study, the room temperature luminescence decay of samples with very different stoichiometries can be compared for the first time. Both luminescence formation and decay show a rather complicated temporal behavior, while no spectral change with time is observed. Whereas a second long, stretched-exponential decay component is clearly dependent on the defect structure, a fast exponential component with approximately 1 ps decay constant is present in each sample.

Since light-induced phenomena in LN are often related to the formation and transport of small polarons, which is usually studied by transient absorption spectroscopy, we additionally present fs-transient absorption data showing that luminescence and transient absorption decay times differ by an order of magnitude, which is in full agreement with Ref.[25]. The luminescence decay is largely independent of the small polaron absorption. Based on these findings, a microscopic picture is discussed that consistently describes the luminescence decay of the different samples. As microscopic origin self-trapped exciton decay and/or migration is suggested. Having shown elsewhere that it is unlikely that oppositely-charged small polarons merge into STEs[25], our results indicate that the opposite case, i.e., STEs breaking into small polarons, does not occur either. It must therefore be concluded that self-trapped excitons and small polarons in lithium niobate are independent species.

Results

Transient luminescence of cLN:Mg (6.5 mol%).   Figure 1a shows the upconverted luminescence build-up of a congruently melting LN crystal with 6.5 mol% Mg in the melt. As the relative photon number decreases, the color coding changes linearly from blue to yellow. The upconverted spectra appear over a spectral range from 26, 000 to 30, 000 cm^{-1}. A long pass filter in the optical path and a white glass filter in front of the optical fiber quench (upconverted) scattered pump light. Intensities above the maximum luminescence signal are cut off for better contrast. Therefore, the upconverted pump scatter appears as blue region without intensity information in the spectral range 30,000–32, 000 cm^{-1} around time zero. A temporal change of the spectral shape and/or peak position cannot be deduced at a first glance. The small temporal delay between the luminescence maxima at
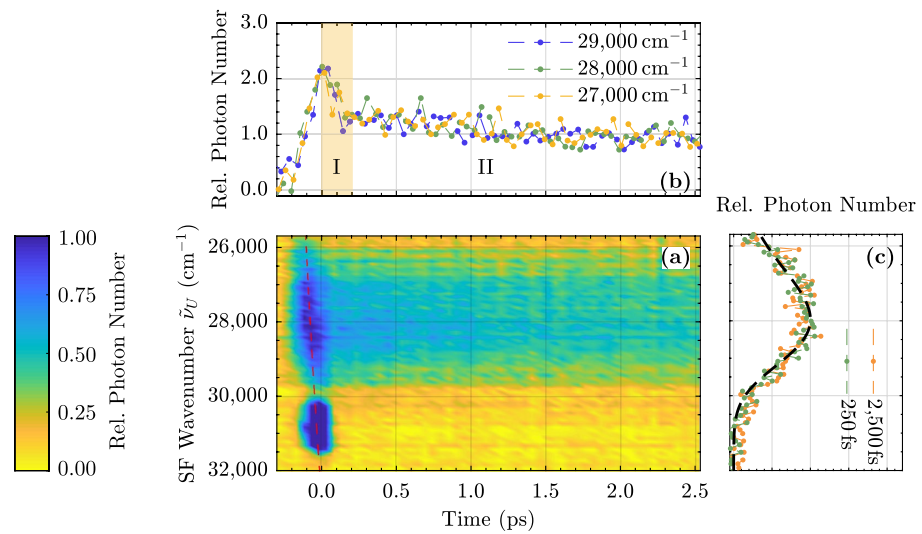
Figure 1. (**a**) Upconverted luminescence spectra of 6.5 mol% Mg-doped LN as a function of time up to 2.5 ps. The red dashed line illustrates the temporal delay between the luminescence kinetic traces at different wavenumbers introduced by their different group velocities in the long pass filter. (**b**) Normalized kinetic trace for three selected wavenumbers. (**c**) Detailed view of the spectra normalized to their maximum value for two fixed delay times (250 and 2,500 fs). The black dashed line is the steady state spectrum upconverted in silico (cf. blue curve in Fig. 5a).

different wavenumbers is due to different group velocities in the 1 mm thick fused silica long pass filter F_1 (red dashed line) and is easily corrected for further analysis in Fig. 1b.

Here, kinetic traces at different wavenumbers normalized to their value at 2.5 ps are shown for comparison. For each spectral component, a rapidly increasing photon number is observed on a 100 fs time scale, resulting in a luminescence peak near time zero, followed by a very fast and a slower decay component. The fast one, hereinafter referred to as decay I, is clearly visible within the first 200 fs, while the longer one (referred to as II) corresponds to the one shown in Fig. 2. Within the experimental error, the different traces exhibit identical temporal behavior, indicating that no temporal Stokes' shift or broadening occurs within the first 2.5 ps.

A more detailed view of the upconverted spectra for different times is given in Fig. 1c. Obviously the spectral shape of the upconverted light does not change with time within the first 2.5 ps. For comparison, the steady state spectrum (see blue curve in Fig. 5a) is upconverted in silico to the expected distribution of UV photons and depicted in Fig. 1c as a dashed black line. The spectra agree almost perfectly.

The upconverted luminescence decay is shown in Fig. 2a. Now the white glass filter is removed, since the scattered pump light is not observed for later times. Accordingly, the upconverted spectra extend to higher wavenumbers. At first glance, no spectral change with time is observed here either. A detailed look at the decay kinetics of different detected wavenumbers supports this impression. All spectral components show the same non-exponential decay behavior (see Fig. 2b). Accordingly, the upconverted spectra do not change over time as shown in Fig. 2c up to 50 ps. Again, the steady state spectrum upconverted in silico is consistent with the measured data for all times (black dashed line).

Since no spectral change is observed over time, further analysis is limited to the temporal evolution of the luminescence intensity. The spectra are spectrally integrated for each point in time to increase the signal-to-noise ratio. For this purpose, Gaussian functions are fitted to the distributions of UV photons and integrated over equally spaced wavenumber intervals. This suppresses the influence of pump scatter at short times on the total photon count. The result is shown in Fig. 3 as blue dots. The luminescence decays non-exponentially on the time scale of a few hundred picoseconds. For comparison, a fit of a single exponential function is shown as turquoise dashed line. A better fit to the data (dashed black line) is achieved applying a recently proposed microscopic model. There the temperature-dependent luminescence decay in lithium niobate is described by the local, radiative decay of self-trapped excitons and/or their migration and subsequent pinning at defect sites[25]. From this qualitative model we obtain, as explained in more detail in the discussion, a rate equation for the number density of transients $N(t)$

$$\frac{\partial N}{\partial t} = -\left(\tau_\mathrm{r}(T)^{-1} + \beta(T)\, t^{\beta(T)-1}\, \tau_\mathrm{nr}(T)^{-\beta(T)} \right) N(t, T), \tag{1}$$

where τ_r describes the local, radiative decay channel and $\beta\, t^{\beta-1}\, \tau_\mathrm{nr}^{-\beta}$ describes a stretched-exponential, non-radiative recombination path with the stretching factor β. This leads to the expression
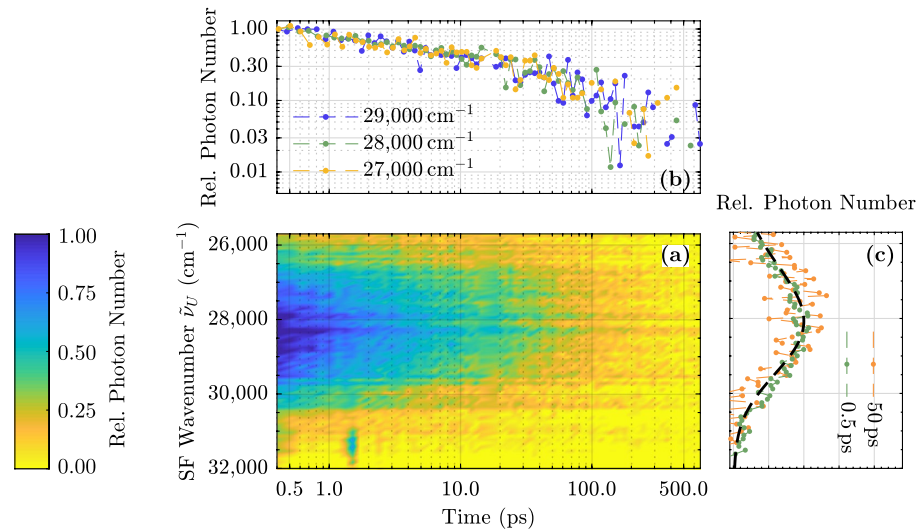
Figure 2. (**a**) Upconverted luminescence spectra of 6.5 mol% Mg-doped LN as a function of time up to 500 ps. (**b**) Normalized kinetic trace for three selected wavenumbers. (**c**) Detailed view of the spectra normalized to their maximum value for two fixed delay times (0.5 and 50 ps). The black dashed line is the steady state spectrum upconverted in silico (cf. blue curve in Fig. 5a).
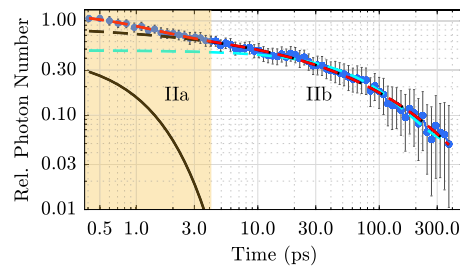

Figure 3. Normalized kinetic trace of the spectrally integrated luminescence of an Mg-doped (6.5 mol%) congruently melting sample. The turquoise dashed line is a fit of an exponential function to the data. The red dashed line is the sum of an exponential function (black straight line) and a Kohlrausch-Williams-Watts function (black dashed line) fitted to the data.

$$N(t, T) = N_0(T) \exp\left[-\frac{t}{\tau_\mathrm{r}(T)} - \left(\frac{t}{\tau_\mathrm{nr}(T)} \right)^{\beta(T)} \right] \tag{2}$$

for the number density of transients as a function of time. The luminescence signal would then be

$$I(t, T) = p_\mathrm{r}(T)\, N(t, T) = N_0(T)\, \tau_\mathrm{r}(T)^{-1} \exp\left[-\frac{t}{\tau_\mathrm{r}(T)} - \left(\frac{t}{\tau_\mathrm{nr}(T)} \right)^{\beta(T)} \right]. \tag{3}$$

A special case of this function, i.e., with $\beta = 1/3$, has already been used to describe 1D diffusion of polaronic excitons to quenching centers in emissive conjugated polymers[40]. For elevated temperatures, at which the non-radiative decay channel dominates the relaxation process, equation (3) can be approximated by a simple Kohlrausch-Williams-Watts function ($\propto \exp(-(t/\tau)^{\beta})$). The region IIb in Fig. 3 can be fitted with such a function with a non-radiative decay time $\tau_\mathrm{nr} = (31 \pm 13)$ ps and a stretching factor $\beta = 0.43 \pm 0.06$ (black dashed line). For an overall fit of the decay kinetics (red dashed line), an additional exponential component (straight black line) is required to reflect the deviation between the data and the fit function equation (3) in region IIa. Its decay time is 1 ps. Based on the microscopic model used, we therefore obtain two decay components in the temporal region II. Together with the ultrafast decay I a three-component decay is observed.
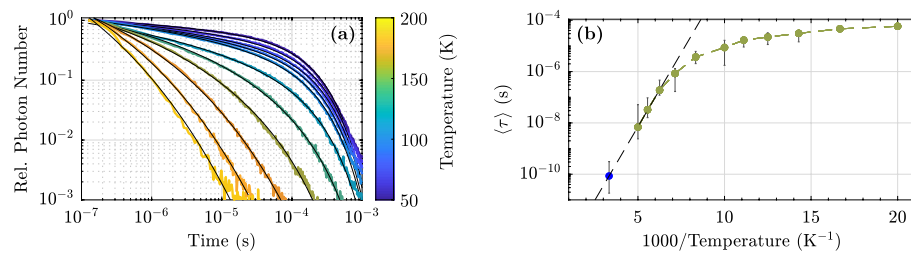
Figure 4. (**a**) Luminescence decay of a heavily Mg-doped LN crystal (6.5 mol% Mg) for different temperatures between 50 and 200 K, obtained with a photomultiplier and a gated photon counter at an emission wavelength of 440 nm. The kinetic traces are fitted with equation (3) (black lines). (**b**) Luminescence mean decay time calculated via equation (4) as a function of temperature. The green dots are calculated from fits of the left part of this figure. The blue dot is the mean decay time (IIb) obtained via upconversion spectroscopy. The black dashed line is an Arrhenius fit.

For comparison, the luminescence decay at low temperatures at a single wavelength of 440 nm is measured with a photomultiplier and a gated photon counter. Again fs-laser pulses at 400 nm are used to excite the sample. The experimental setup, but using ns-pump pulses, has already been described in Ref.[25]. The luminescence decay kinetics for temperatures between 50 K and 200 K are fitted with equation (3) and depicted in Fig. 4a. The radiative decay time can be determined for temperatures up to 120 K and has a value independent of temperature of $\approx 220\,\mu$s. Above this temperature $\tau_{nr} \ll \tau_r$ and τ_r can be neglected. The mean decay time $\langle \tau \rangle$ is calculated for every temperature via

$$\langle \tau \rangle(T) = \frac{1}{N_0(T)} \int_0^\infty N(t,T)\mathrm{dt} \tag{4}$$

and is depicted in Fig. 4b, where the mean decay time (IIb) at room temperature is depicted as a blue dot. For temperatures $\geq 160\,$K an Arrhenius function is fitted to the data (black dashed line). The resulting activation energy is $E_a = (0.23 \pm 0.04)\,$eV.

Composition-dependent kinetics.   Similar investigations at room temperature were performed for samples with different stoichiometries/Mg-dopings. The results are presented in the Supplementary Information. All of them have in common that no spectral change is observed over time. Further analysis is therefore again limited to the luminescence intensity. The result is shown in Fig. 5, in which the luminescence build-up and decay of congruently melting samples (left column, (c)/(e)) and near-stoichiometric samples (right column, (d)/(f)) with different Mg-doping concentrations are compared. All samples show the before-mentioned intensity peak around time zero. Various measurements indicate that this peak is related to surface degradation, as it seems to become more pronounced the longer a sample is illuminated.

However, the luminescence kinetics of the different samples reveal a further correlation. Each luminescence signal again consists of two components, a short exponential decay IIa with a decay time of $\tau = (1 \pm 0.5)$ ps and a longer non-exponential decay IIb with a stoichiometry-dependent decay time.

While in the congruent sample (yellow dots) the exponential decay dominates the overall signal, successive Mg-doping (green and blue dots) lead to an increased contribution of the longer non-exponential component. The change from congruently melting compositions to near-stoichiometric samples shows, that this long component is also present without any Mg-doping (dark yellow dots). A magnesium-doping above the optical damage resistance threshold (1 mol% Mg in the melt) of such samples prolongs the luminescence decay only slightly (dark blue dots). Sorting the samples by the length of the longer decay and the ratio of the amplitude of the short and long decay leads to the same order.

Transient absorption.   As a complementary experimental technique, transient absorption spectroscopy is performed to probe the light-induced transients. Again, the intense laser pulses at 400 nm are used as pump source. Probe pulses with wavelengths of 910 nm and 460 nm are provided by the optical parametric amplifier used in the upconversion setup. Both pulses are focused on the samples with concave mirrors (f = 500 mm) at a small angle of $\approx 6°$. The probe light is ordinarily polarized with respect to the optical axes of the lithium niobate samples. The pump pulses are blocked, while the probe pulses are focused on the entrance of the optical fiber connected to the same spectrograph as in the fluorescence upconversion setup. Spectral integration of the probe pulses for each time step $I(t)$ is used to calculate the absorbance

$$A(t) = -\log_{10}\left(\frac{I(t)}{I(t \ll 0)}\right), \tag{5}$$

where $I(t \ll 0)$ is the spectrally integrated pulse signal for time delays, where the probe pulse arrives at the samples before the pump pulse. The apparatus response function has a full width at half maximum of 130 fs.
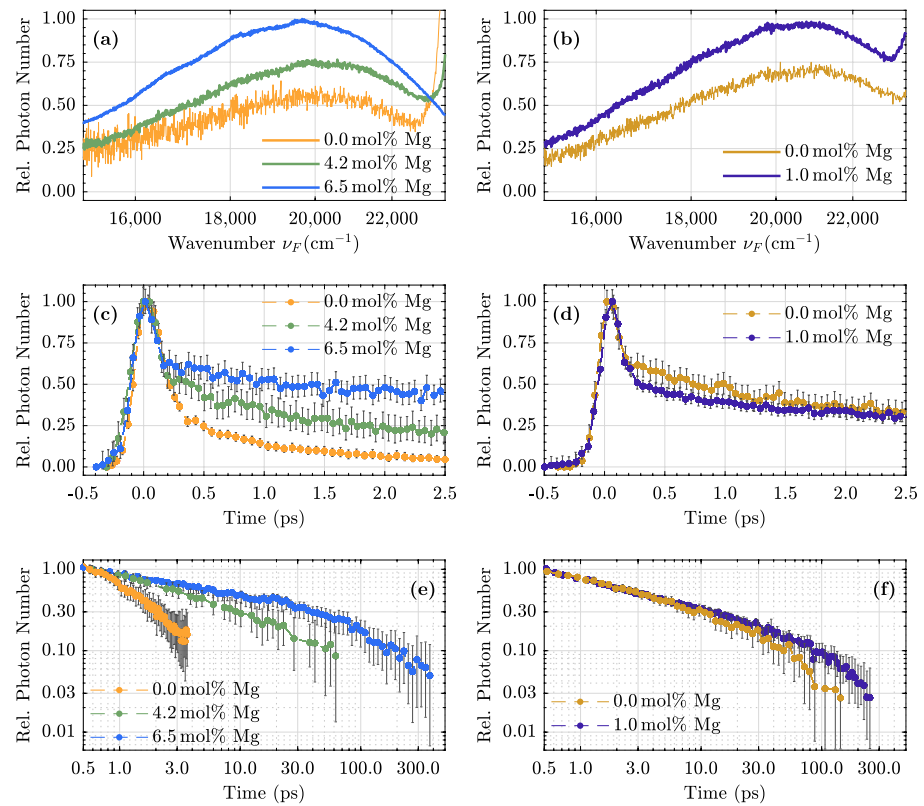
Figure 5. Steady state luminescence spectra (**a**) and (**b**), normalized short-time (**c**) and (**d**) and long-time kinetic traces (**e**) and (**f**) for lithium niobate samples with different stoichiometries/Mg-dopant concentrations. **Left column:** congruently melting crystals without Mg-doping (yellow), 4.2 mol% Mg (<ODRT, green) and 6.5 mol% Mg in the melt (>ODRT, blue). **Right column:** near-stoichiometric samples without Mg-doping (dark yellow) and 1 mol% Mg (>ODRT, dark blue).
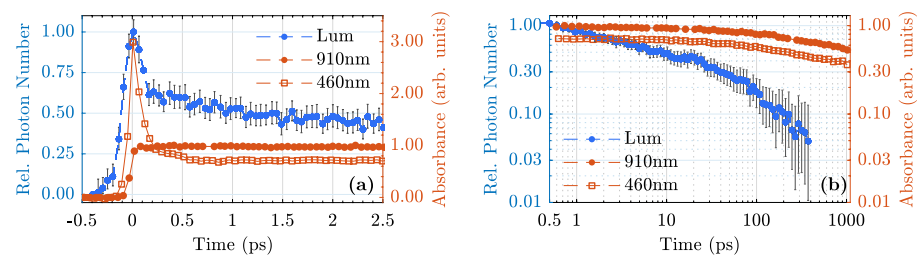

Figure 6. Transient absorbance of cLN:Mg (6.5 mol%) measured at probe wavelengths 910 nm and 460 nm (red dots and squares, respectively) compared with the transient spectrally integrated luminescence (blue dots). (**a**) Short-time behavior up to 2.5 ps, (**b**) Longer decay up to 1 ns.

Figure 6 shows the ultrafast transient absorbance of the cLN:Mg sample with a Mg concentration above the optical damage resistance threshold probed at 910 nm and 460 nm, corresponding to absorption bands typically associated with electron and hole polarons in lithium niobate. First, no short-time exponential decay is observed for the two wavelengths (Fig. 6a, red dots and squares). Figure 6b shows that the transient absorption is considerably longer than the luminescence decay (blue dots). On a time scale of a about 10 ps, it is more or less constant. This measurement is performed for the other samples as well. The results qualitatively confirm

once again, that no absorption feature corresponding the luminescence decay is observed in the blue-green and near infrared spectral range.

Discussion

For the first time, broadband femtosecond fluorescence upconversion spectroscopy has been successfully applied to the photoluminescence of lithium niobate single crystals. To the best of our knowledge, it is the first measurement of this kind on ABO_3 perovskite-like ferroelectrics. In comparison to former studies[24–26,31–34] this experimental approach uncloses the detection range for femtosecond/picosecond luminescence kinetics. In particular, it unlocks the room temperature sub-ns temporal behavior of lithium niobate single crystals with different stoichiometry and Mg-doping concentrations. Even congruently melting samples known as weak emitters can be examined. Their luminescence decay time has so far not been satisfactorily determined even at low temperatures[32]. We are therefore convinced that broadband fluorescence upconversion spectroscopy can also be applied on other (weakly) luminescing dielectrics with strong electron-phonon coupling of current interest, such as TiO_2 or $SrTiO_3$ and may provide new insights into carrier decay channels.

The necessity to use a broadband upconversion scheme arises as a potential time-dependent Stoke's shift of the luminescence feature could result in misleading kinetic traces observed for a single wavenumber. This experimental approach is preferred, e.g., to a streak camera, because in principle a much better temporal resolution can be achieved and a comparison to pump-probe transient absorption measurements on the fs-time scale might be easier.

In a first step we have shown that within the experimental error no temporal change of the luminescence band, which e.g. indicates a relaxation of hot carriers to an intermediate ground state, is observed (see Figs. 1 and 2). We like to remind that our experimental setup, although designed as a broadband scheme, has a limited access to the spectral shape of a very broad luminescence band. The steady state luminescence spectra exceed the spectral bandwidth (FWHM) of our setup by about a factor of two. Calculations showed that the peak position of such a broad spectrum can be determined with an error of ± 400 cm^{-1}. This means that two very broad emission bands shifted by ± 50 meV are difficult to distinguish within the current signal-to-noise ratio. Therefore, further analysis is limited to the temporal evolution of the luminescence intensity.

The observed pronounced luminescence maximum around time zero, which decays on the fs time scale (cf. Fig. 5c and d) is a rather surprising result, since it has the same spectral fingerprint as the longer decay components (cf. Fig. 1). Thus, upconverted scattered pump light at the origin of this decay, which could be the first assumption, is unlikely. In this case the influence on the observed kinetics would decrease with decreasing wavenumber. Furthermore, a closer examination reveals that the intensity peak is temporally broader than the cross correlation signal (FWHM 210 fs vs. ≤ 160 fs). Moreover, we like to point out that the low-energy part of the detected upconverted luminescence signal corresponds to wavelengths in the region of 540 nm, which is spectrally far away from a Gaussian-shaped laser pulse centered at 400 nm having a bandwidth of a few nm, even if a potential low energy shoulder is considered. However, we had the impression that the intensity ratio between the peak and the ps decay increases the longer the sample is illuminated. Therefore, we cannot exclude that the peak is related to surface degradation. Although, as we have argued above, it is rather unlikely that scattered pump light is responsible for this feature, we will postpone the discussion about the peak to later times. In the current experiment, the upconverted luminescence signal near time zero is 'caged' between pump scatter on the low energy side and upconverted pump scatter on the high energy side. Further experiments with a different pump wavelength, e.g., frequency-tripled laser pulses at 266 nm, might therefore clarify the luminescence behavior on the fs time scale, since in this case a spectral shoulder of the upconverted scattered pump light could definitely be excluded.

Luminescence features. In a more detailed discussion we focus on the two remaining ps-decay components IIa and IIb (cf. Fig. 3). Regarding its luminescence kinetics, congruently melting lithium niobate doped with Mg above the optical damage resistance threshold is a frequently investigated crystal composition[24,25,32,33]. We therefore begin our comparison to results reported in the literature with this sample composition. First, we present here the first fs-pulse induced data on luminescence kinetics at low temperatures (50 K – 200 K, cf. Fig. 4). They are in accordance with ns-pulse induced kinetics presented in the literature[24,25], which proves that the decay time, at least at lower temperatures, is not influenced by the pump pulse duration and intensity, which in our case is more than five orders of magnitude shorter and three order of magnitude higher, respectively. For a quantitative comparison of the decay shape, we determined τ and β using the previously applied first derivative of a stretched-exponential function[24,25] (not shown) resulting in the same fitting parameters for fs- and ns-pulse-induced luminescence kinetics.

However, such approach is based on the assumption that only a radiative decay channel is present, which is not reasonable for elevated temperatures. We therefore use an expression according to equation (3) as fitting function to compare the luminescence kinetics at low temperature and at room temperature. It is based on a recently proposed model that describes the low-temperature luminescence/absorption decay in lithium niobate considering STEs[25]. In particular, it is assumed that STEs have two decay channels, one local and radiative and one non-local, non-radiative, respectively. The latter describes STE migration through the crystal and pinning at defect sites. The complexes formed decay non-radiatively. As shown in Fig. 4a an excellent fit quality can be achieved. The radiative decay time turns out to be independent of temperature. The mean decay times as a function of temperature are shown in Fig. 4b. The inclusion of the mean decay time obtained from upconversion spectroscopy at room temperature (blue dot) in an Arrhenius fit leads to an activation energy of $E_a = (0.23 \pm 0.04)$ eV, which is larger than a recently published value obtained from low-temperature measurements on a sample with an Mg cocentration of 7 mol% in the melt ($E_a = (0.14 \pm 0.01)$ eV)[24]. The reason for this is the extended temperature range in
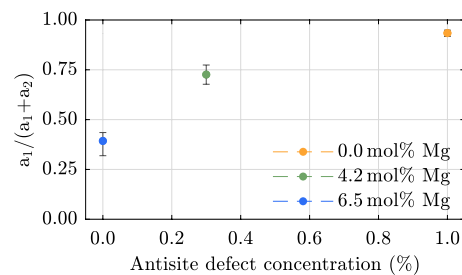
Figure 7. Amplitude ratio of the exponential (a_1) and non-exponential (a_2) decay in congruently melting lithium niobate samples as a function of antisite defect concentration. For short times the non-exponential decay is approximated by an offset. The antisite defect concentration for the samples with 4.2 mol% Mg in the melt is estimated from the results given in Ref.[41].

our experiment. Figure 4b shows that for temperatures below 160 K the mean decay time becomes increasingly temperature-independent. Since an Arrhenius function leads to an excellent fit of the temperature-dependent decay time, it is likely that the longer decay IIb at room temperature reported here corresponds to the commonly investigated μs luminescence decay in Mg-doped lithium niobate at low temperatures.

A change of the crystal composition, i.e., the stoichiometry and/or Mg-dopant concentration, largely influences the decay time of the longer component IIb as shown in Fig. 5e and f. The near-stoichiometric sample proves that the occurrence of this decay component is not related with Mg-dopants in the sample. The near-stoichiometric samples with and without Mg-doping have comparable decay times. The slightly shorter decay time of the undoped sample could be caused by impurity quenching due to residual antisite defects. This hypothesis is supported by the fact that the congruently melting sample with a Mg-doping just below the ODRT (4.2 mol%) has a very comparable decay time. In contrast, the congruently melting samples differ significantly from one another. With decreasing Mg concentration, the longer decay time decreases and the ratio between the short exponential (IIa) and the longer non-exponential component (IIb) at 1 ps after excitation increases. Since Mg-ions at the origin of this decay can be excluded, it seems likely that antisite defects, whose number density is anti-proportional to the Mg concentration, efficiently quench this long decay component. Anyhow, regardless of a concrete microscopic picture, the decay channel is considered to be of non-radiative nature, since the collected photon number of the longer component 1 ps after excitation is constant in all samples.

An even shorter decay component, corresponding to the exponential decay (IIa) in this work, was not observed by the two authors mentioned above. In contrast, Pankratov *et al.* reported a similar phenomenon in stoichiometric lithium niobate. They found a two-component decay over the entire luminescence spectrum. At liquid nitrogen temperatures, the two decay times were estimated to be < 20 ns and $2\,\mu$s, respectively[31]. Fischer *et al.* observed a second, very fast component in Zn-doped LN samples as well[32]. At the origin of this faster component, both suspected residual antisite defects in their samples, which are expected to accelerate the luminescence decay[26]. However, a systematic study of samples with different compositions was not performed by these authors. The data given in Fig. 5c and d also shows that the ratio between the short exponential decay and the longer non-exponential decay depends largely on the stoichiometry of the crystals. The higher the concentration of antisite defects, the more pronounced the short component appears. Figure 7 shows the amplitude ratio between the exponential decay component (a_1) and the longer one as a function of antisite defect concentration. For the very short time considered, the latter can be approximated as constant (a_2). The reason for the approximation is that a stretched-exponential function diverges for small arguments, which leads to unphysical results at very short times. The antisite defect concentration for the sample with 4.2 mol% Mg in the melt is estimated from the results given in Ref.[41]. However, the number of photons collected from the exponential decay channel is more or less the same in the three congruently melting samples, regardless of the Mg-doping. Since the number density of antisite defects and lithium vacancies varies greatly between these samples, we rather assume that the short exponential decay is related to the regular Nb-O-octahedra.

Microscopic picture. Light-induced phenomena in lithium niobate are often related to formation and transport of small polarons. A microscopic model describing transient photoluminescence data should therefore naturally take small polaron formation and decay into account. Since small polaron kinetics are usually studied by means of transient absorption spectroscopy, we report here on room temperature transient absorption data obtained under the same experimental condititons as the luminescence data. The transient absorption build-up and decay at a probe wavelength of 910 nm are in accordance with previously reported signals probed at 800 nm and in the NIR spectral range[19,21,23]. Both probe wavelengths reported here (910 nm and 460 nm) are time-locked probing the same decay mechanism, i.e., geminate electron and hole polaron annihilation. The sharp peak observed around time zero in the blue spectral range might be caused by two-photon absorption. A comparison with the luminescence decay (cf. Fig. 6), again clearly shows no correlation with the transient absorption kinetics, neither for the short exponential decay IIa nor for the longer non-exponential component

8

IIb. In particular, the large difference in the decay times at room temperature of one order of magnitude suggests that the luminescence decay kinetics on the ps-time scale is not influenced by small polaron absorption.

In the literature there are further indications leading to the conclusion that the blue-green photoluminescence in lithium niobate is not caused by geminate small polaron annihilation or radiative small polaron decay[18,25]. Instead, Messerschmidt *et al.* recently revived the idea of self-trapped excitons located at the Nb-O-octahedra at the origin of the luminescence[9,25–28], which has been supported by ESR studies indicating, that the X-ray induced luminescence is associated with electrons captured at Nb^{5+} and holes captured at O^- ions[42].

A possible explanation for a two component luminescence decay might then be found in two STE species with nearly identical spectroscopic fingerprints, which are directly generated by the pump pulse. Various kinds of intrinsic STEs are known in the literature, which differ in their location, e.g., on-center or off-center, or their multiplicity (see[43] and references therein). The latter can lead, for example, to singlet and triplet emission bands separated by a few tens of meV (rare gas solids) or a few eV (alkali halides). Typically, singlet and triplet STEs decay on very different time scales. For instance, triplet STE decay in rare gas solids is two to four orders of magnitude slower, depending on the temperature. In the wide-gap oxide Al_2O_3 very different decay times for singlet and triplet self-trapped excitons are found as well[44].

Transferred to the perovskite-like ferroelectric lithium niobate, the often observed luminescence of the intrinsic niobium-oxygen octahedra in LN might then be assigned to a triplet state, since it decays at cryogenic temperatures within a few hundred μs[25,26], which is a typical time scale for triplet STE decay (see[43] and references therein). In fact, photo-EPR studies on $KTa_{1-x}Nb_xO_3$ revealed the existence of triplet $Nb^{4+} - O^-$ polaronic excitons[45]. They share a common electronic structure with charge transfer vibronic excitons $Ta^{4+} - O^-$ and $Ti^{3+} - O^-$, whose triplet configurations are assumed to be their ground states and which are related with green luminescence in $KTaO_3$ and $SrTiO_3$, respectively[46–48]. Calculations furthermore revealed that the recombination of triplet charge transfer vibronic excitons at the niobium oxygen octahedra in $KNbO_3$ would lead to the experimentally observed blue/green luminescence as well[48,49]. In our samples, triplet STEs might survive long enough to migrate through the crystal until getting trapped/pinned at defect sites, which efficiently quenches the luminescence[25]. A distribution of distances to these defect sites would then manifest in a stretched-exponential decay behavior and the number density of defect centers influences the mean decay time. A high defect number density increases the pinning probability, resulting in shorter decay times, which would be consistent with our findings. A fitting function based on this idea (cf. equation (3)) leads to an excellent fit quality for very different temperatures. The additional short exponential decay component at room temperature might be attributed to locally decaying singlet STEs that cannot hop through the crystal lattice due to a very short intrinsic decay time.

From Fig. 5c and d it is immediately clear that the formation time of these quasi-particles is ≤ 200 fs. Such a time scale for STE formation is remarkably short and has been observed in polydiacetylen and SiO_2 as well[50–53]. At low temperatures, time constants on the ps time scale are often reported, e.g., in alkali halides[54,55], where self-trapping of excitons is hindered by a small energy barrier introduced by the short range coupling to acoustic phonons. Since our study is conducted at room temperature, such an energy barrier might be negligible, since typically only a few meV have to be surpassed[56]. However, this formation time is in the same range as the recently reported values for small polaron formation, which were estimated to lie between 1.5 fs and 300 fs[21–23]. As on the very short time scale the luminescence decay is again not accompanied by an increase of the transient absorption signal, this suggests that STEs do not break up into pairs of small polarons. Of course, the net absorption cross section of the small polaron pair could coincidentally correspond to that of the STE. But since this would be an unlikely accident, our investigation again indicates that both species are independent of each other.

Time-dependent density functional theory calculations might provide further insight into the microscopic processes responsible for the ultrafast luminescence decay behavior reported here and could help to verify whether our proposed model is justified.

In summary, this study reveals the sub-ns temporal dynamics of photoluminescence of the ABO_3 perovskite-like ferroelectric lithium niobate with ultrafast temporal resolution. To this end, it is shown that broadband fluorescence upconversion spectroscopy is feasible on such materials, although their luminescence is efficiently quenched at elevated temperatures. Within the error of our experiment, no temporal Stoke's shift is observed. Samples with different stoichiometries and Mg-dopant concentrations show a different long time behavior, which manifests itself in non-exponential decay kinetics. A larger number of antisite defects in the samples correlates with an efficient quenching of this longer component. On the other hand, a shorter exponential decay component is present regardless of the crystals composition.

Fs-transient absorption spectroscopy data on the same samples are qualitatively in accordance with already published kinetics and show that geminate small polaron annihilation can be excluded as microscopic mechanism for the blue-green luminescence of lithium niobate. Instead, a model based on self-trapped excitons is proposed. Both species seem to be independent of each other. For a complete and rigid microscopic picture, however, further experimental and theoretical investigations are required.

Methods

Experimental setup. Picosecond transient luminsecence kinetics of lithium niobate samples is investigated using broadband fluorescence upconversion spectroscopy (FLUPS)[35–37] adapted to the inspection of single crystals in reflection geometry. The samples are excited with frequency-doubled fs laser pulses (Coherent Inc. type *Astrella*, $\lambda = 400$ nm, $\tau = 60$ fs, $E = 65\,\mu J$) at a repetition rate of 1 kHz. A Cassegrain reflector collects the emitted fluorescence and images the fluorescing spot on a BBO crystal (Altechna, $d = 130\,\mu m$, $\theta_N = 40\,°$, $\phi = 0\,°$, front p-coating @ 400–1300 nm, backside p-coating @ 300–450 nm). There it is mixed under non-collinear Type II phase matching condition with NIR-gate pulses ($\lambda = 1340$ nm, $\tau = 45$ fs, $E = 50\,\mu J$). In order to compensate for pulse front mismatch introduced by the large mixing angle $\alpha \approx 19°$, the gate pulse fronts are

tilted by $\approx 20°$ by means of an equilateral N-SF11 prism and a demagnifying imaging of the spatial pulse profile on the BBO crystal. While the luminescence and gate pulses are blocked, the generated sum-frequency signal is imaged onto the entrance of an optical fiber connected to a spectrograph (Roper Scientific, type *IsoPlane* and *PIXIS 2K*). The sum-frequency signal of scattered pump light defines time zero and yields the temporal apparatus response function, which has a Gaussian shape with a full width at half maximum of < 160 fs. For each fixed time delay, the upconverted spectra are integrated for 5 s and averaged over 10 measurements (median), i.e., over 5,000 pump events.

A detailed description of the experimental setup as well as test measurements on the reference system Coumarin 153 solved in dymethyl-sulfoxide and a photometric correction, which extends the procedure established for a similar setup, are included in the supplementary information.

Samples.   Room temperature luminescence kinetics (ordinarily polarized part) and transient absorption are studied on plates of lithium niobate with different stoichiometries and Mg-doping concentrations.

The congruently melting samples (cLN) were grown by the Czochralski method from sintered mixtures of Li_2CO_3 and Nb_2O_5 with a Li/Nb molar ratio of 0.946 corresponding to the congruent composition. For doping, MgO was added to the starting mixture to obtain the specific molar Mg ratio in the melt (4.2 mol% and 6.5 mol%, respectively).

The undoped and Mg-doped stoichiometric samples (sLN) were grown by the high-temperature top-seeded solution growth (HTTSSG) method using K_2O flux of a concentration of ≈ 13 mol% (see[3]) from (doped) starting mixtures with the stoichiometric Li/Nb molar ratio. All crystals were grown, monodomenized close to the melting temperature, cut, and polished to optical quality at the WIGNER Research Centre for Physics, Budapest.

Data availability
The data that support the findings of this study are available from the corresponding author upon reasonable request.

References
1. Eerenstein, W., Mathur, N. D. & Scott, J. F. Multiferroic and magnetoelectric materials. *Nature* **442**, 759–765 (2006).
2. Zhu, S., Zhu, Y. & Ming, N. Quasi-phase-matched third-harmonic generation in a quasi-periodic optical superlattice. *Science* **278**, 843–846 (1997).
3. Lengyel, K. *et al.* Growth, defect structure, and THz application of stoichiometric lithium niobate. *Appl. Phys. Rev.* **2**, 040601 (2015).
4. He, J., Franchini, C. & Rondinelli, J. M. Lithium niobate-type oxides as visible light photovoltaic materials.*Chem. Mater.* **28**, 25–29 (2016).
5. Bellingeri, E., Pellegrino, L., Marré, D., Pallecchi, I. & Siri, A. S. All-SrTiO$_3$ field effect devices made by anodic oxidation of epitaxial semiconducting thin films. *J. Appl. Phys.* **94**, 5976 (2003).
6. Takashima, H. *et al.* Low-driving-voltage electroluminescence in perovskite films. *Adv. Mater.* **21**, 3699–3702 (2009).
7. Imlau, M., Badorreck, H. & Merschjann, C. Optical nonlinearities of small polarons in lithium niobate. *Appl. Phys. Rev.* **2**, 040606 (2015).
8. Williams, R. T. & Song, K. S. The self-trapped exciton. *J. Phys. Chem. Solids* **51**, 679–716 (1990).
9. Blasse, G. & Bril, A. The influence of crystal structure on the fluorescence of oxidic niobates and related compounds. *Z. Phys. Chem.* **57**, 187–202 (1968).
10. Leonelli, R. & Brebner, J. L. Time-resolved spectroscopy of the visible emission band in strontium titanate. *Phys. Rev. B* **33**, 8649–8656 (1986).
11. Yamada, Y. & Kanemitsu, Y. Photoluminescence spectra of perovskite oxide semiconductors. *J. Lumin.* **133**, 30–34 (2013).
12. Jermann, F., Simon, M., Bower, R., Krätzig, E. & Schirmer, O. F. Light-induced absorption changes in reduced lithium niobate. *Ferroelectrics* **165**, 319–327 (1995).
13. Berben, D., Buse, K. & Wevering, S. Lifetime of small polarons in iron-doped lithium-niobate crystals. *J. Appl. Phys.* **87**, 1034–1041 (2000).
14. Herth, P. *et al.* Evidence for Light-Induced Hole Polarons in LiNbO$_3$. *Phys. Rev. Lett.* **95**, 067404 (2005).
15. Beyer, O., Maxein, D., Woike, T. & Buse, K. Generation of small bound polarons in lithium niobate crystals on the subpicosecond time scale. *Appl. Phys. B* **83**, 527–530 (2006).
16. Merschjann, C., Berben, D., Imlau, M. & Wöhlecke, M. Evidence for two-path recombination of photoinduced small polarons in reduced LiNbO$_3$. *Phys. Rev. Lett.* **96**, 186404 (2006).
17. Merschjann, C., Schoke, B. & Imlau, M. Influence of chemical reduction on the particular number densities of light-induced small electron and hole polarons in nominally pure LiNbO$_3$. *Phys. Rev. B* **76**, 085114 (2007).
18. Conradi, D. *et al.* Influence of Mg doping on the behaviour of polaronic light-induced absorption in LiNbO$_3$. *Phys. Status Solidi* **2**, 284–286 (2008).
19. Maxein, D. *et al.* Polarons in magnesium-doped lithium niobate crystals induced by femtosecond light pulses. *Appl. Phys. B* **92**, 543–547 (2008).
20. Badorreck, H. *et al.* Scanning nonlinear absorption in lithium niobate over the time regime of small polaron formation.*Opt. Mater. Express* **5**, 2729–2741 (2015).
21. Sasamoto, S., Hirohashi, J. & Ashihara, S. Polaron dynamics in lithium niobate upon femtosecond pulse irradiation: Influence of magnesium doping and stoichiometry control. *J. Appl. Phys.* **105**, 083102 (2009).
22. Qiu, Y., Ucer, K. B. & Williams, R. T. Formation time of a small electron polaron in LiNbO$_3$: measurements and interpretation. *Phys. Status Solidi* **2**, 232–235 (2005).
23. Freytag, F. *et al.* Picosecond near-to-mid-infrared absorption of pulse-injected small polarons in magnesium doped lithium niobate. *Opt. Mater. Express* **8**, 1505–1514 (2018).
24. Kämpfe, T. *et al.* Time-resolved photoluminescence spectroscopy of Nb_{Nb}^{4+} and O^- polarons in LiNbO$_3$ single crystals. *Phys. Rev. B* **93**, 174116 (2016).
25. Messerschmidt, S. *et al.* The role of self-trapped excitons in polaronic recombination processes in lithium niobate. *J. Phys. Condens. Matter* **31**, 065701 (2019).

166

26. Krol, D. M., Blasse, G. & Powell, R. C. The influence of the Li/Nb ratio on the luminescence properties of LiNbO$_3$. *J. Chem. Phys.* **73**, 163–166 (1980).
27. Blasse, G. & De Haart, L. G. J. The nature of the luminescence of niobates MNbo$_3$ (M = Li, Na, K). *Mater. Chem. Phys.* **14**, 481–484 (1986).
28. Emond, M. H. J., Wiegel, M., Blasse, G. & Feigelson, R. Luminescence of stoichiometric lithium niobate crystals. *Mater. Res. Bull.* **28**, 1025–1028 (1993).
29. Wiegel, M., Emond, M. H. J., Stobbe, E. R. & Blasse, G. Luminescence of alkali tantalates and niobates. *J. Phys. Chem. Solids* **55**, 773–778 (1994).
30. Messerschmidt, S. *et al.* Pulse-induced transient blue absorption related with long-lived excitonic states in iron-doped lithium niobate. *Opt. Mater. Express* **9**, 2748–2760 (2019).
31. Prankratov, V., Grigorjeva, L., Millers, D., Corradi, G. & Polgár, K. Luminescence of ferroelectric crystals: LiNbO$_3$ and KNbO$_3$. *Ferroelectrics* **239**, 241–250 (2000).
32. Fischer, C., Wöhlecke, M., Volk, T. & Rubinina, N. Influence of the Damage Resistant Impurities Zn and Mg on the UV-Excited Luminescence in LiNbO$_3$. *Phys. Status Solidi A* **137**, 247–255 (1993).
33. Klose, F., Wöhlecke, M. & Kapphan, S. Uv-excited luminescence of LiNbO$_3$ and LiNbO$_3$:Mg. *Ferroelectrics* **92**, 181–187 (1989).
34. Powell, R. C. & Freed, E. E. Laser time-resolved studies of exciton migration in doped lithium niobate. *J. Chem. Phys.* **70**, 4681 (1979).
35. Gerecke, M., Bierhance, G., Gutmann, M., Ernsting, N. P. & Rosspeintner, A. Femtosecond broadband fluorescence upconversion spectroscopy: Spectral coverage versus efficiency. *Rev. Sci. Instrum.* **87**, 053115 (2016).
36. Zhao, L., Pérez Lustres, J. L., Farztdinov, V. & Ernsting, N. P. Femtosecond fluorescence spectroscopy by upconversion with tilted gate pulses. *Phys. Chem. Chem. Phys.* **7**, 1716–1725 (2005).
37. Zhang, X.-X. *et al.* Femtosecond broadband fluorescence upconversion spectroscopy: Improved setup and photometric correction. *Rev. Sci. Instrum.* **82**, 063108 (2011).
38. Shah, J., Damen, T. C. & Deveaud, B. Subpicosecond luminescence spectroscopy using sum frequency generation. *Appl. Phys. Lett.* **50**, 1307–1309 (1987).
39. Lemmetyinen, H. *et al.* Time-resolved fluorescence methods (IUPAC Technical Report). *Pure Appl. Chem.* **86**, 1969–1998 (2014).
40. Yan, M., Rothberg, L. J., Papadimitrakopoulos, F., Galvin, M. E. & Miller, T. M. Defect Quenching of Conjugated Polymer Luminescence. *Phys. Rev. Lett.* **73**, 744–747 (1994).
41. Iyi, N. *et al.* Defect Structure Model of MgO-Doped LiNbO$_3$. *J. Solid State Chem.* **118**, 148–152 (1995).
42. Koppitz, J., Schirmer, O. F., Wöhlecke, M., Kuznetsov, A. I. & Grabmaier, B. C. Threshold effects in LiNbO$_3$: Mg caused by change of electron-lattice coupling. *Ferroelectrics* **92**, 233–241 (1989).
43. Song, K. S. & Williams, R. T. Self-Trapped excitons (Springer, Berlin, 1993).
44. Lushchik, A., Kirm, M., Lushchik, C., Martinson, I. & Zimmerer, G. Luminescence of free and self-trapped excitons in wide-gap oxides. *J. Lumin.* **87–89**, 232–234 (2000).
45. Yusupov, R. V. *et al.* Experimental manifestations of the $Nb^{4+} - O^-$ polaronic excitons in $KTa_{0.988}Nb_{0.012}O_3$. *Phys. Rev. B* **84**, 174118 (2011).
46. Vikhnin, V. S. *et al.* Critical effects in optical response due to charge transfer vibronic excitons and their structure in perovskite-like systems. *J. Lumin.* **83–84**, 109–113 (1999).
47. Vikhnin, V. S., Eglitis, R. I., Kapphan, S. E., Kotomin, E. A. & Borstel, G. A new phase in ferroelectric oxides: the phase of charge transfer vibronic excitons. *EPL* **56**, 702–708 (2001).
48. Eglitis, R. I., Kotomin, E. A. & Borstel, G. Quantum chemical modelling of "green" luminescence in ABO$_3$ perovskites. *Eur. Phys. J. B* **27**, 483–486 (2002).
49. Kotomin, E. A., Eglitis, R. I. & Borstel, G. Quantum chemical modelling of electron polarons and excitons in ABO$_3$ perovskites. *J. Phys. Condens. Matter* **12**, L557 (2000).
50. Yoshizawa, M., Taiji, M. & Kobayashi, T. Relaxation dynamics of photoexcitations in polydiacetylene films. *IEEE J. Quantum Electron.* **25**, 2532–2539 (1989).
51. Kobayashi, T., Yoshizawa, M., Stamm, U., Taiji, M. & Hasegawa, M. Relaxation dynamics of photoexcitations in polydiacetylenes and polythiophene. *J. Opt. Soc. Am. B* **7**, 1558–1578 (1990).
52. Yoshizawa, M., Hattori, Y. & Kobayashi, T. Femtosecond time-resolved resonance Raman gain spectroscopy in polydiacetylene. *Phys. Rev. B* **49**, 13259(R) (1994).
53. Guizard, S. *et al.* Time-resolved studies of carriers dynamics in wide band gap materials. *Nucl. Instrum. Methods Phys. Res. B* **116**, 43–48 (1996).
54. Shibata, T. *et al.* Femtosecond spectroscopic studies of the lattice relaxation initiated by interacting electron-hole pairs under relaxation in alkali halides. *Phys. Rev. B* **49**, 13255(R) (1994).
55. Fujiwara, H., Suzuki, T. & Tanimura, K. Femtosecond time-resolved spectroscopy of the Frenkel-pair generation and self-trapped-exciton formation in KCl and RbCl. *J. Phys. Condens. Matter* **9**, 923–936 (1997).
56. Singh, J. Excitation energy transfer processes in condensed matter: theory and applications (Springer Science & Business Media, Berlin, 1994).

Acknowledgements

Author contributions

M.I, A.K and S.M. conceived the experiment. A.K. conducted the measurements. All authors discussed the results and provided input to the manuscript.

Competing interest

The authors declare no competing interests.

Additional information

167

www.nature.com/scientificreports/

Superposed picosecond luminescence kinetics in lithium niobate revealed by means of broadband fs-fluorescence upconversion spectroscopy

- Supplementary Information -

A. Krampf[1]**, S. Messerschmidt**[1]**, and M. Imlau***[1]

[1]School of Physics, Osnabrueck University, Barbarastraße 7, 49076 Osnabrueck, Germany
[*]mirco.imlau@uni-osnabrueck.de

Reflective broadband fluorescence upconversion spectrometer

Experimental Setup

The experimental setup for the investigation of the luminescence kinetics of solid samples (cf. Fig. S 1) follows the idea of a broadband upconversion scheme introduced by Ernsting *et al.* for the measurement of the luminescence of solved molecules[1]. A regeneratively amplified Ti-Sapphire laser ($\lambda = 800$ nm, $\tau = 35$ fs, Coherent Inc. type *Astrella*) delivers intense, frequency-doubled laser pulses ($\lambda = 400$ nm, $\tau = 60$ fs, $E = 65$ µJ) at a repetition rate of 1 kHz. After passing a motorized linear translation stage (travel distance of 300 mm), they are focused on the sample by a concave mirror (M_1, f = 250 mm).
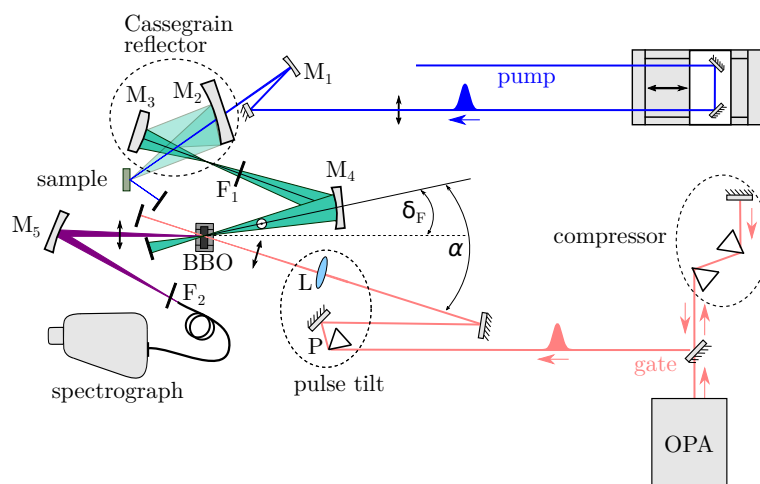

Figure S 1. Experimental setup used for broadband fluorescence upconversion spectroscopy of single crystals in reflection geometry. The sample is excited with a fs-laser pulse at a wavelength of 400 nm. The emitted luminescence is collected and imaged by an off-axis Cassegrain configuration onto a thin BBO crystal. There it is mixed with compressed and tilted gate pulses. The central ray of the luminescence cone and the gate pulses enclose an angle of $\alpha \approx 19°$. The generated sum frequency is imaged onto the input of an optical fiber and analyzed by a spectrograph. **F**: filter, **M**: spherical mirror, **L**: lens, **P**: prism.

The emitted luminescence is collected with a pair of spherical mirrors forming an off-axis Cassegrain reflector (M_2, R = -150 mm and M_3, R = 258.4 mm, magnification $\approx$3). It is designed to reduce astigmatism. The effects of such aberrations on the time resolution of our setup are negligible, which is checked considering ray optics. In contrast to the reference setup[1], the imaging of the fluorescent spot is realized in a reflective configuration. For this purpose the first, larger mirror of the Cassegrain reflector has a hole drilled in its center. Since two photon absorption decreases strongly with increasing penetration depth, the induced luminescence is predominantly emitted from a very thin subsurface layer. This geometry thus reduces a deterioration of the temporal resolution introduced by the relatively large group velocity dispersion in the relevant blue/green spectral range. While the specularly reflected pump light is blocked with a beam dump, pump light scattered from the sample surface is suppressed by a longpass filter with a cut-on wavelength of 422 nm (F_1, Asahi Spectra USA Inc. *ZUL0422*). Another concave mirror (M_4, R = -300 mm) then re-images the magnified image of the fluorescent spot without further magnification onto a BBO crystal with anti-reflection coatings on its front and backside (Altechna, d = 130 µm, $\theta_N = 40°$, $\phi = 0°$, front p-coating @ 400–1300 nm, backside p-coating @ 300–450 nm).

The luminescence is mixed under non-collinear Type II phase matching condition with NIR-gate-pulses ($\lambda = 1340$ nm, $\tau = 45$ fs, $E = 50$ µJ) generated by an optical parametric amplifier (Light Conversion type *TOPAS Prime*). Since we expect a very weak luminescence signal, we use the more efficient BBO orientation called "Case A" in Ref.[1], which converts a broad cone of incident light via angular tolerance phase matching. The large angle between the luminescence and the gate pulse ($\alpha \approx 19°$) naturally deteriorates the temporal resolution of the experiment for geometric reasons. To reduce this effect, the gate pulse fronts are tilted by $\approx 3.2°$ using an equilateral N-SF11 prism (P). The tilt angle is calculated using the description in Ref.[2]. A convex lens (L, f = 100 mm) on a dovetail translation stage images the gate pulses onto the BBO crystal with a demagnification of ≈ 6.5, stretching the tilt angle to $\approx 20°$. A prism-compressor compensates for the pulse broadening introduced by the group velocity dispersion in the N-SF11 prism.

The non-collinear wave mixing allows a spatial filtering of the generated from the fundamental waves. While the luminescence and gate signals are blocked, an UV-reflectance enhanced concave aluminum mirror (M_5, R = -200 mm) images

the sum-frequency with a small demagnification onto an optical fiber connected to a spectrograph with thermoelectrically cooled CCD (Roper Scientific, type *IsoPlane* and *PIXIS 2K*). With an additional long pass filter (F_2, Schott *WG335*) in front of the fiber, the sum-frequency signal of scattered pump light can be reduced around time zero if necessary. This signal defines time zero in the experiment as well as the apparatus response function, which has a Gaussian shape with a full width at half maximum of <160 fs.

The spectral region of efficient upconversion in a non-collinear fluorescence upconversion scheme depends largely on several parameters such as gate pulse wavelength, angles of incidence and BBO crystal thickness. Tuning the fluorescence angle δ_F by only a few degrees shifts this spectral region over the entire visible spectrum[1]. Therefore, before a measurement can be performed, spectral efficiency curves are calculated to find the fluorescence angle that provides the desired spectral region. To measure the luminescence kinetics of the lithium niobate samples, the fluorescence angle is set by turning the BBO crystal mounted on a calibrated, motorized rotation stage, so that the corresponding region of efficient upconversion is close to the room temperature steady state luminescence maximum near $\approx 20,000$ cm^{-1} (cf. Fig. 5 (a) and (b) in the manuscript). For each fixed time delay, the upconverted spectra are integrated for 5 s and averaged over 10 measurements (median), i.e., over 5,000 pump events.

Photometric Correction

Recently, Gerecke *et al.* compared photometric correction curves for their broadband fluorescence upconversion spectroscopy setup, which were obtained from upconverting different fluorescing dyes and SFG efficiency calculations, respectively[1]. For their efficiency curve generated in silico, they essentially considered the non-collinear geometry, i.e., the angles of the incident fluorescence and gate pulses, and the fluorescence divergence resulting from the large collection angle and the magnifying imaging on the nonlinear optical crystal. Including a single gate wavelength in their calculations, which reflects the central wavelength of the gate pulses, leads to a good agreement between both correction curves, especially in the wavelength region of (nearly) perfect phasematching. In a more recent study, however, they showed that relatively small changes in the gate wavelength have a large impact on the efficiency (correction) curve, showing that an accurate determination of the gate wavelength is imperative[3].

Therefore, we extend the calculation by including the spectral shape of the gate pulses, which is determined beforehand having a finite bandwidth of ≈ 50 nm (full width at half maximum). The spectral parts are taken into account according to their fraction of the total gate pulse energy. This naturally broadens the region of efficient sum frequency generation, since each spectral part of the gate pulse fulfills the condition of perfect phase matching for a different luminescence wavelength. The difference between finite and arbitrarily small gate bandwidth is illustrated in Fig. S 2. The same experimental parameters regarding crystal properties and geometry are used as in our measurement. The fluorescence angle is set to $\delta_F = 2.5°$, which is later used for the measurement of lithium niobate samples. The dashed blue line results when only a single wavelength at 1340 nm is considered. A maximum conversion efficiency is obtained for $\tilde{\nu}_F \approx 20,600$ cm^{-1} and an efficiency of more than 30% of the maximum value in the range of 18,060 cm^{-1}–22,350 cm^{-1}. The more realistic efficiency including the actual bandwidth of ≈ 50 nm of the gate pulses has its maximum again at $\tilde{\nu}_F \approx 20,600$ cm^{-1}, but is broadened (cf. orange line in Fig. S 2). If we again take a value of 30% of the maximum as a reference, the region of efficient upconversion is broadened by 670 cm^{-1}. Conversely, the correction curve assuming only a single wavelength is narrower, which leads to an overestimation of the fluorescence bandwidth. It should be noted that the absolute effect of the finite gate pulse bandwidth depends largely on the crystal thickness and the fluorescence angle. It is increased with thicker crystals and larger fluorescence angles.

Coumarin 153 solved in dimethyl-sulfoxide

To validate that our setup works as expected, we measured the luminescence of Coumarin 153 (*Aldrich*, CAS: 53518-18-6) solved in dimethyl-sulfoxide diluted to optical density ≤ 0.3 at 400 nm using our reflection geometry and compared the results with the steady state spectrum and literature. The filled volume of the cuvette is placed in the object plane of the Cassegrain reflector. In a first step, the measured spectra are corrected for the spectral response of the fiber and spectrograph determined with a standard light source (Bentham *CAL_CL2_100W*). The measured relative photon numbers $s(\lambda) = s(\lambda, t) - s(\lambda, t \ll t = 0)$ are converted to the energy scale according to the Jacobian transformation

$$s(\tilde{\nu}) = s(\lambda) \frac{d\lambda}{d\tilde{\nu}} = -s(\lambda) \lambda^2.$$

Figure S 3 shows the measured instantaneous upconverted fluorescence spectra of Coumarin 153 solved in DMSO 1 ps and 500 ps after excitation, recorded with our setup as blue and yellow dots, respectively. The fluorescence angle is set to $\delta_F = 3.5°$. The angle α is fixed.
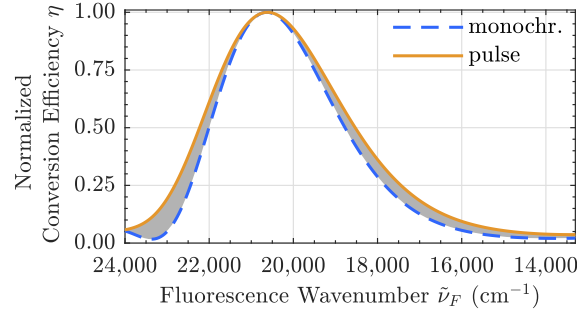
Figure S 2. Normalized spectral conversion efficiency of a thin BBO crystal (d = 130 μm, $\theta_N = 40°$, $\phi = 0°$) set to $\delta_F = 2.5°$ with (orange) and without (dashed blue) consideration of the gate pulse bandwidth of ≈ 50 nm (central wavelength 1340 nm). Both are normalized to their respective maximum. The external angle between fluorescence and gate pulse is $\alpha \approx 19°$. Type II phase matching is used.

To fit these data, a (test) fluorescence spectrum given by a lognorm function[1]

$$f(\tilde{\nu}_F) = \exp\left[-\ln(2)\left(\frac{\ln(1 + 2\gamma(\tilde{\nu}_F - \tilde{\nu}_0)/\Delta)}{\gamma}\right)^2\right] \tag{1}$$

with the peak, width and asymmetry parameters $\tilde{\nu}_0$, Δ, and γ is converted into the expected upconverted spectrum $f(\tilde{\nu}_U)$ by multiplication with the spectral conversion efficiency $\eta(\tilde{\nu}_F)$

$$f(\tilde{\nu}_U) = f(\tilde{\nu}_F)\,\eta(\tilde{\nu}_F). \tag{2}$$

The spectral response of our setup is compared with two reference spectra. Data recorded at large delay times can be compared with the steady state spectrum, since the time-dependent Stoke's shift of the luminescence spectrum appears within a few picoseconds[4]. For this purpose, the steady state luminescence spectrum is fitted with a sum of two lognorm functions. According to equation (2), the fit is multiplied by the spectral efficiency curve of our setup to obtain the distribution of UV-photons expected in an upconversion measurement. The result is shown in Fig. S 3 as a grey dashed line together with the data measured 500 ps after excitation. Obviously the peak positions and the high energy parts of the spectra are in perfect agreement, while a small deviation is observed on the low energy side. In a second step, the luminescence spectrum shortly after excitation can be compared with values given in literature, which are obtained with a broadband upconversion scheme using a transmission geometry[1]. The parameters of a test fluorescence spectrum given by a lognorm function are varied until a best fit to the data measured 1 ps after excitation is achieved (blue dots in Fig. S 3). This procedure is done using spectral efficiency curves with (red dashed line in Fig. S 3) and without finite gate bandwidth. The fitting parameters are shown in Tab. S 1.
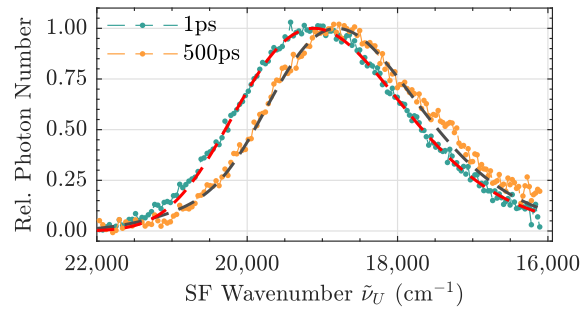

Figure S 3. Instantaneous luminescence spectra of Coumarin 153 solved in dimethyl-sulfoxide 1 ps (blue dots) and 500 ps (yellow dots) after excitation. The red line is a fit of an in silico upconverted lognormal function of equation (1) to the data, whereas the grey line reflects the steady state luminescence spectrum upconverted in silico.

Table S 1. Parameters obtained by fitting a lognorm function equation (1) to the luminescence spectrum of Coumarin 153 solved in dimethyl-sulfoxide 1ps after excitation. The photometric correction curve is calculated with and without consideration of the gate pulse bandwidth. The basic calculation using only the gate pulse central wavelength (Ref.[1]) is denoted with "monochr.". The extended calculation including the gate pulse bandwidth of ≈ 50 nm is denoted with "pulse". The first two rows compare parameters obtained with these two different calculation approaches. The third and fourth row give reference values reported in the literature[1], where the correction curves are calculated with a single gate wavelength.

	ν_0 (cm^{-1})	Δ (cm^{-1})	γ
pulse	19,000±150	3,300±200	-(0.3∓0.1)
monochr.	19,000±150	3,670±200	-(0.3∓0.1)
monochr.[1]	19,270	3,520	-0.29
	19,380	3,680	-0.34

It is evident that the parameters obtained by neglecting a finite gate bandwidth are very close to those given in literature, with the peak wavenumber being slightly smaller. This difference could stem from a lower coumarin concentration in Ref.[1], which leads to a lower self-absorption of the fluorescence in the blue spectral range. The table S 1 also shows that without taking the gate pulse width into account, the width of the spectrum is overestimated by $\approx 10\%$.

The striking agreement of our data with the steady state spectrum and results in the literature is remarkable. An additional experimental photometric correction using differently luminescing dyes as described in Ref.[1] is not required. This again proves that the theoretical photometric correction is very rigid, provided that the fluorescence and gate angles as well as the crystal thickness and gate pulse central wavelength are determined very thoroughly. For example, the angles are determined very accurately using the gate pulse reflected from the BBO crystal and a motorized rotation table. Pulses reflected directly back mark the gate angle zero. Then the crystal is rotated until the reflected gate pulse passes the off-axis Cassegrain reflector in such way that it is focused onto the sample, superimposing the pump pulse spot. The rotation angle now marks half the angle α. The gate pulse central wavelength and spectral width is characterized by a spectrometer sensitive to the near infrared spectral range (Ocean Optics *NIRQuest 512*). We like to note that the error margin given in Tab. S 1 reflects both the fitting error and the error in determining the angles used.

Additional optical elements in the beam path, such as the white glass filter used in the lithium niobate measurements, are also taken into account in the photometric correction by matrix multiplication.

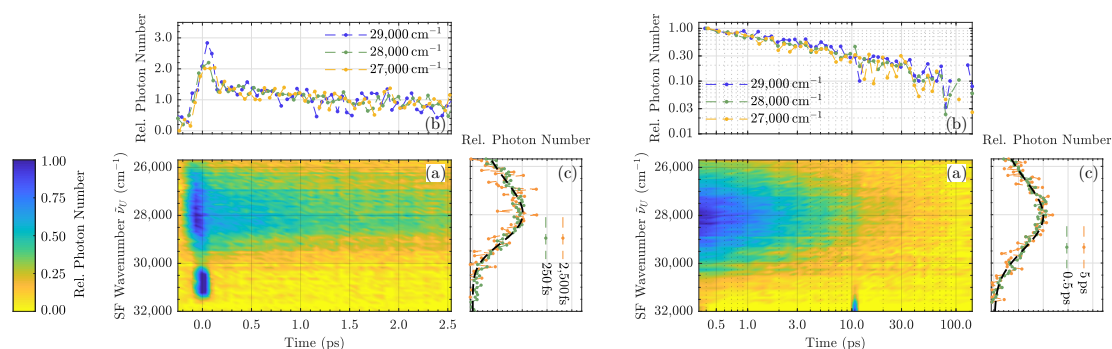## Broadband Fluorescence Upconversion Spectroscopy on different lithium niobate samples

Figure S 4. (a) Upconverted luminescence spectra of undoped near-stoichiometric LN as a function of time. (b) Normalized kinetic trace for three selected wavenumbers. (c) Detailed view of the spectra normalized to their maximum value for two fixed delay times. The black dashed line is the steady state spectrum upconverted in silico (cf. dark yellow curve in Fig. 5 (b) in the manuscript). **Left:** Up to 2.5 ps, **Right**: Up to 200 ps.
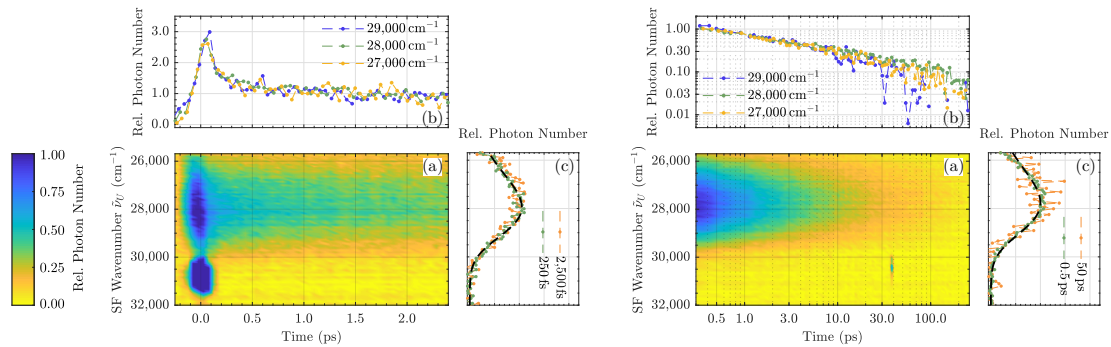
Figure S 5. (a) Upconverted luminescence spectra of Mg-doped (1 mol%) near-stoichiometric LN as a function of time. (b) Normalized kinetic trace for three selected wavenumbers. (c) Detailed view of the spectra normalized to their maximum value for two fixed delay times. The black dashed line is the steady state spectrum upconverted in silico (cf. dark blue curve in Fig. 5 (b) in the manuscript). **Left:** Up to 2.5 ps, **Right**: Up to 250 ps.
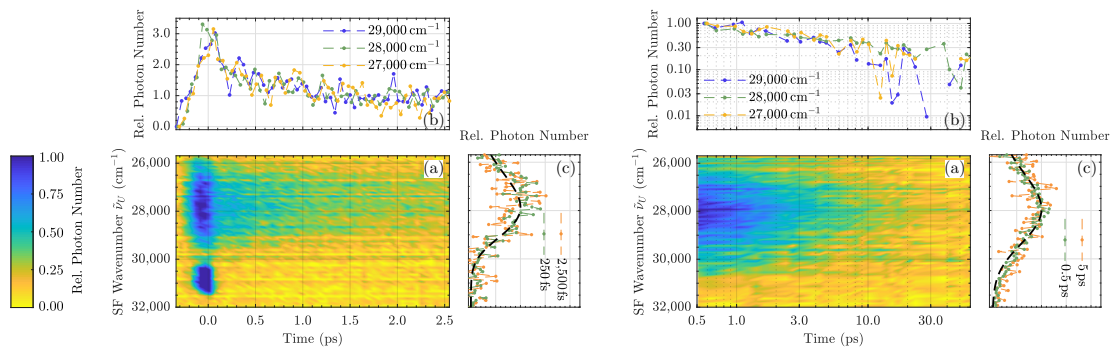

Figure S 6. (a) Upconverted luminescence spectra of Mg-doped (4.2 mol%) congruent LN as a function of time. (b) Normalized kinetic trace for three selected wavenumbers. (c) Detailed view of the spectra normalized to their maximum value for two fixed delay times. The black dashed line is the steady state spectrum upconverted in silico (cf. green curve in Fig. 5 (a) in the manuscript). **Left:** Up to 2.5 ps, **Right**: Up to 60 ps.
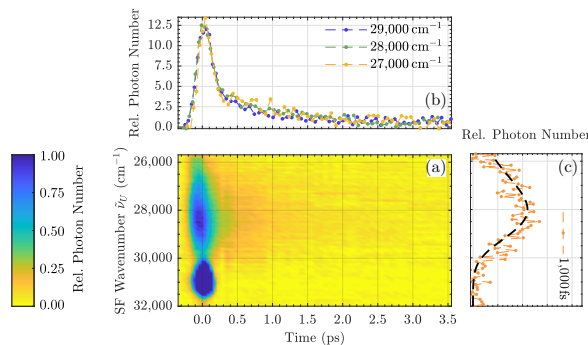

Figure S 7. (a) Upconverted luminescence spectra of undoped congruent LN as a function of time. (b) Normalized kinetic trace for three different wavenumbers. (c) Detailed view of the spectra normalized to their maximum value for two fixed delay times. The black dashed line is the steady state spectrum upconverted in silico (cf. yellow curve in Fig. 5 (a) in the manuscript)

References

1. Gerecke, M., Bierhance, G., Gutmann, M., Ernsting, N. P. & Rosspeintner, A. Femtosecond broadband fluorescence upconversion spectroscopy: Spectral coverage versus efficiency. *Rev. Sci. Instrum.* **87**, 053115 (2016).

2. Zhao, L., Lustres, J. L. P., Farztdinov, V. & Ernsting, N. P. Femtosecond fluorescence spectroscopy by upconversion with tilted gate pulses. *Phys. Chem. Chem. Phys.* **7**, 1716–1725 (2005).

3. Gerecke, M. *et al.* Effect of a Tertiary Butyl Group on Polar Solvation Dynamics in Aqueous Solution: Femtosecond Fluorescence Spectroscopy. *J. Phys. Chem. B* **121**, 9631–9638 (2017).

4. Martins, L. R., Tamashiro, A., Laria, D. & Skaf, M. S. Solvation dynamics of coumarin 153 in dimethylsulfoxide-water mixtures: Molecular dynamics simulations. *J. Chem. Phys.* **118**, 5955 (2003).

Danksagung

Zunächst geht an erster Stelle mein Dank an Herrn Prof. Dr. Mirco Imlau für die Aufnahme in die Arbeitsgruppe *Ultrakurzzeitphysik* sowie für die ausgezeichnete Betreuung und die konstruktiven Diskussionen während der gesamten Promotionszeit.

Weiterhin bedanke ich mich bei Herrn Prof. Dr. Simone Sanna von der Universität Gießen für die Begutachtung dieser Arbeit.

Ein großer Dank geht auch an alle Autoren, mit denen im Rahmen dieser Arbeit gemeinsame wissenschaftliche Publikationen entstanden sind. Besonders bedanken möchte ich mich bei Herrn Dr. Simon Messerschmidt für die enge Zusammenarbeit während des gesamten Studiums und der Promotionszeit. Herrn Dr. Stefan Nolte möchte ich sehr für die intensive Unterstützung mit seiner Expertise vor allem in der Anfangsphase meiner Labortätigkeit danken. Gleiches gilt für Herrn Dr. Christian Kijatkin, der immer ein offenes Ohr und viel Geduld bei der gemeinsamen Bewältigung von technischen Problemen hatte. Herrn Dr. Gábor Corradi danke ich dafür, dass er seine jahrzehntelange Erfahrung auf dem Gebiet der Polaronen in Lithiumniobat mit mir geteilt hat. Besonderer Dank gilt zudem Herrn Prof. Dr. Niko Ernsting für die Unterstützung beim Aufbau des FLUPS.

Bei allen aktuellen und ehemaligen Arbeitskollegen, allen voran meinen Büronachbarn Frau Gerda Cornelsen und Herr MSc. Yannic Toschke, möchte ich für das nette Klima während und abseits der Arbeit bedanken, ich hätte mich nicht wohler fühlen können.

Den Mitarbeitern der elektronischen und feinmechanischen Werkstatt danke ich für die Anfertigung und Reparatur verschiedenster Bauteile, ohne die viele Messungen nicht möglich gewesen wären. Herrn Werner Geisler danke ich für die geduldige Präparation und Reparatur der vielen in Mitleidenschaft gezogenen Kristalle.

Herzlich möchte ich mich schließlich bei meinen Eltern bedanken, deren Unterstützung ich mir in jeder Lebenslage sicher sein kann.

Erklärung über die Eigenständigkeit der erbrachten wissenschaftlichen Leistung

Ich erkläre hiermit, dass ich die vorliegende Arbeit ohne unzulässige Hilfe Dritter und ohne Benutzung anderer als der angegebenen Hilfsmittel angefertigt habe. Die aus anderen Quellen direkt oder indirekt übernommenen Daten und Konzepte sind unter Angaben der Quelle gekennzeichnet.

Weitere Personen waren an der inhaltlichen materiellen Erstellung der vorliegenden Arbeit nicht beteiligt. Insbesondere habe ich hierfür nicht die entgeltliche Hilfe von Vermittlungs- bzw. Beratungsdiensten (Promotionsberater oder andere Personen) in Anspruch genommen. Niemand hat von mir unmittelbar oder mittelbar geldwerte Leistungen für Arbeiten erhalten, die im Zusammenhang mit dem Inhalt der vorgelegten Dissertation stehen. Die Arbeit wurde bisher weder im In- noch im Ausland in gleicher oder ähnlicher Form einer anderen Prüfungsbehörde vorgelegt.

Osnabrück, den 06. Juli 2020